

超新星中微子实验的 若干问题研究

(申请清华大学理学博士学位论文)

培养单位：工程物理系

学 科：物理学

研 究 生：魏 瀚 宇

指导教师：陈 少 敏 教 授

二〇一六年十二月

Topical Experimental Studies on Supernova Neutrino Detection

Dissertation Submitted to

Tsinghua University

in partial fulfillment of the requirement

for the degree of

Doctor of Philosophy

in

Physics

by

WEI Hanyu

Dissertation Supervisor : Professor CHEN Shaomin

December, 2016

关于学位论文使用授权的说明

本人完全了解清华大学有关保留、使用学位论文的规定，即：

清华大学拥有在著作权法规定范围内学位论文的使用权，其中包括：(1) 已获学位的研究生必须按学校规定提交学位论文，学校可以采用影印、缩印或其他复制手段保存研究生上交的学位论文；(2) 为教学和科研目的，学校可以将公开的学位论文作为资料在图书馆、资料室等场所供校内师生阅读，或在校园网上供校内师生浏览部分内容；(3) 根据《中华人民共和国学位条例暂行实施办法》，向国家图书馆报送可以公开的学位论文。

本人保证遵守上述规定。

(保密的论文在解密后应遵守此规定)

作者签名：魏瀚宇

导师签名：陈少敏

日期：2016.10.27

日期：2016.10.27

摘要

核塌缩式超新星会释放大量各种味道的中微子，平均能量 10-20 MeV，携带约 99% 的超新星爆发能量。这些中微子不但对研究中微子属性和超出标准模型新物理有着不可替代的作用，而且蕴藏了大质量恒星演化过程的丰富信息。因此，探测超新星中微子对粒子物理、天体物理、核物理、以及宇宙学都具有重要意义。到目前为止，对超新星中微子的实验研究不仅针对爆发中微子，还包括弥散在整个宇宙空间由过往超新星爆发产生的遗迹中微子。本论文针对正在运行的大亚湾反应堆中微子实验和拟开展的锦屏中微子实验，利用超新星反电子中微子与探测器靶物质的反贝塔衰变 (IBD) 事例，进行了三个方面超新星中微子的实验研究。

1) 大亚湾中微子实验是目前世界上唯一具有空间分离的多个探测器的中微子实验。在该实验中，完成了设计，搭建，测试，及运行超新星中微子爆发在线触发系统。利用各个探测器上的 IBD 事例，通过构造概率密度函数，使该系统成为目前世界上响应最快，阈值最低的超新星触发系统，并对 20 kpc 以内的核塌缩式超新星爆发有 100% 的探测效率。该系统于 2013 年 8 月安装在大亚湾中微子实验中，于 2014 年 11 月正式联网国际超新星预警系统 (SNEWS)，并正常运行至今。

2) 分析了从 2011 年 12 月到 2013 年 11 月大亚湾采集的实验数据，对可能的超新星中微子爆发事例进行了寻找。进一步挖掘了可用于探测的中微子和碳-12 的中性流反应。高能量阈值 (10 MeV) 寻找对 25 kpc 范围内的核塌缩式超新星爆发有 100% 的效率。结合运行至今的在线触发系统，在 90% 置信水平给出了银河系内 0.53/年的核塌缩式超新星爆发率上限。低能量阈值 (0.7 MeV) 的寻找是目前世界上能量下限最低的超新星中微子实验研究之一，旨在进行不依赖于模型的搜寻；找到了两个可疑事例，概率上和能谱上均与本底预期一致。特别寻找了与超新星 SN2014J 和引力波 GW150914 关联的中微子事例，给出了相应的上限。

3) 对具有最深岩石覆盖和远离核电站的特点的锦屏中微子实验进行了计算研究。结果表明，千吨级的锦屏中微子探测器有望首次发现超新星遗迹中微子信号，主要本底仅由固有的大气中微子产生。其灵敏度可与未来万吨级普通液闪或者水切伦科夫探测器相当 (对超新星爆发灵敏度也是如此)，利用 20 千吨-年的数据，能在 99.95% 置信水平上发现当前 HBD 模型预言的超新星遗迹中微子信号。

关键词：超新星爆发中微子；超新星遗迹中微子；超新星预警；大亚湾中微子实验；锦屏中微子实验

Abstract

Core-collapse supernovae are the most energetic astrophysical events since the Big Bang. About 99% of the emitted energy is released by a tremendous number of neutrinos and antineutrinos of all flavors, with an average energy of 10-20 MeV. These neutrinos will play an irreplaceable role in studying the intrinsic properties of neutrinos and new phenomena beyond the standard model of particle physics. They also carry valuable information on supernova dynamics as well as stellar evolution. Hence, the detection of supernova neutrinos is an important interdisciplinary field of particle physics, astrophysics, nuclear physics, and cosmology. To date, the experimental studies on supernova neutrinos are not only for supernova burst neutrinos, but also for supernova relic neutrinos which are diffuse throughout the universe from all the past supernova explosions.

For the on-going Daya Bay reactor neutrino experiment and the proposed Jinping neutrino experiment, this thesis presents three experimental studies on supernova neutrinos, mainly using the inverse beta decay (IBD) interactions of supernova electron antineutrinos.

1) The design, implementation, testing, and operation of a supernova online trigger system were accomplished at Daya Bay, which has a unique feature of multiple detectors deployed at separate sites. Using IBD events from the multiple detectors, an effective algorithm was developed to let the trigger system to be the most prompt in the world and with the lowest energy threshold, and fully sensitive to core-collapse supernovae within 20 kpc. This trigger system was installed at Daya Bay in August 2013 and officially integrated into the worldwide Supernova Early Warning System in November 2014.

2) Supernova neutrino bursts were searched for using the Daya Bay data set acquired from 2011 December to 2013 November. The interaction of neutrino neutral-current excitation of ^{12}C was exploited for supernova neutrino detection, making best use of the target mass of the Daya Bay detectors. This search, with an energy threshold of 10 MeV, retains a 100% detection probability of core-collapse supernovae out to 25 kpc, which is comparable to that for the world-leading experiments. Combined with the currently-running online trigger system, the 90% C.L. upper limit on the rate of core-collapse supernovae is found to be 0.5/year. In addition, a search with a lower energy threshold of 0.7 MeV aims at a model-independent search for supernova neutrino bursts and allows

a detection of the full energy spectrum of supernova neutrinos. Two candidates were identified and attributed to the background based on their occurrence rate and energy spectrum. No coincident astronomical observations of supernovae were found. Two exotic searches for coincident neutrino events with SN2014J and GW150914 were also performed.

3) A computational study was carried out for the proposed Jinping neutrino experiment which would have the world's deepest overburden of rock and a long distance from nuclear power plants, thus providing an ultra-low cosmic-ray muon-induced background and reactor neutrino background. As a result, a kiloton-scale neutrino detector is promising to make the first discovery of supernova relic neutrinos, the backgrounds for which mainly originate from the atmospheric neutrinos. The potential sensitivity is found to be comparable to that of other proposed 10-kiloton-scale typical liquid scintillator detectors or water Cherenkov detectors (as is the sensitivity to supernova neutrino bursts). With a data set of 20 kt-year, the supernova relic neutrinos predicted by the HBD (Horiuchi, Beacom, and Dwek 2009) model can be discovered at a 99.95% confidence level at Jinping.

Key words: Supernova burst neutrinos; Daya Bay Reactor Neutrino Experiment; Supernova early warning; Supernova relic neutrinos; Jinping neutrino experiment

Contents

Chapter 1	Introduction	1
1.1	Supernova	1
1.1.1	What a supernova is	1
1.1.2	Supernova types	3
1.1.3	Core-collapse supernovae	4
1.1.4	Great significance of core-collapse supernovae	7
1.2	Supernova neutrinos	7
1.2.1	Importance of supernova neutrinos	8
1.2.2	SN1987A.....	9
1.2.3	Characteristics of supernova neutrinos	10
1.3	Detection of supernova neutrinos	12
1.3.1	Reactions and detector types	12
1.3.2	Expected number of supernova neutrino events.....	14
1.3.3	Applications.....	16
1.4	Supernova rate	18
1.5	Supernova relic neutrino.....	20
1.5.1	SRN formalism	20
1.5.2	Challenges in SRN detection.....	22
1.6	Current experimental status and this thesis work.....	24
1.6.1	Supernova burst neutrinos.....	24
1.6.2	Supernova relic neutrinos	26
Chapter 2	The Daya Bay Experiment	29
2.1	Experimental layout.....	29
2.2	Experimental overburden and muon flux	30
2.3	Antineutrino detector	31
2.4	Data taking	34
2.5	Main scientific goals and results	35
Chapter 3	Supernova trigger system at Daya Bay	36
3.1	Overview of the supernova trigger system.....	36
3.1.1	Online sub-system	36

3.1.2	Offline sub-system	38
3.1.3	Monitoring sub-system	41
3.1.4	Communication	42
3.2	Algorithm of the online trigger.....	42
3.2.1	IBD event selection	42
3.2.2	Supernova trigger	53
3.2.3	Detection probability	63
3.3	Test and performance	66
3.3.1	Tests on miscellaneous function	66
3.3.2	Tests on key functions	66
3.3.3	Capability test.....	67
3.3.4	Time latency of a supernova trigger	68
3.3.5	Operational test	69
3.4	Conclusion and outlook	71
Chapter 4 Offline search for supernova neutrino bursts at Daya Bay		72
4.1	Event reconstruction	72
4.2	Interaction channels.....	73
4.2.1	IBD channel.....	73
4.2.2	Neutral-current ^{12}C channel.....	79
4.3	Data sets for two types of analyses	89
4.4	Search for supernova neutrino bursts	89
4.4.1	Analysis A: high energy threshold (>10 MeV).....	92
4.4.2	Analysis B: low energy threshold	97
4.5	Search for low energy neutrinos associated with astrophysical bursts.....	103
4.5.1	SN2014J	104
4.5.2	GW150914.....	105
4.6	Summary	110
Chapter 5 Discovery potential for supernova relic neutrinos at Jinping		112
5.1	Jinping neutrino experiment.....	112
5.1.1	Experimental site	112
5.1.2	Cosmic-ray muon flux	114
5.1.3	Reactor neutrino flux	114
5.2	Supernova relic neutrino signal	114

Contents

5.2.1	Spectrum and flux	114
5.2.2	Detection techniques	114
5.3	Cosmic-ray muon-induced backgrounds.....	116
5.4	Reactor neutrino background.....	117
5.5	Challenging atmospheric neutrino backgrounds	117
5.5.1	Atmospheric $\bar{\nu}_\mu/\nu_\mu$ CC background	118
5.5.2	Atmospheric NC background	119
5.5.3	Summary	121
5.6	Slow liquid scintillator.....	121
5.6.1	Experimental study on LAB	121
5.6.2	Particle identification	123
5.7	Discovery potential study.....	127
5.7.1	SRN signal and selection.....	127
5.7.2	Atmospheric neutrino backgrounds.....	128
5.7.3	Summary	138
5.8	Comparison of different techniques	139
5.9	Supernova neutrino burst sensitivity	142
5.10	Conclusion and outlook	143
Chapter 6	Summary	145
References	148
Acknowledgments	157
Declaration	158
Appendix A	Statistics in overlapping windows	159
A.1	Probability distribution of N_{IBD} in sliding 10-second windows	159
A.2	Statistical uncertainty of the occurrence rate	160
A.3	Number of consecutive supernova triggers	164
Resume and Publications	166

Denotation

SN	Supernova
M_{\odot}	Solar mass
NS	Neutron star
BH	Black hole
PNS	Proto-neutron star
CCSN	Core-collapse supernova
MSW	Mikheev-Smirnov-Wolfenstein
PMNS	Pontecorvo-Maki-Nakagawa-Sakata
IBD	Inverse beta decay
LS	Liquid scintillator
SNEWS	Supernova Early Warning System
SBN	Supernova burst neutrinos
SRN	Supernova relic neutrinos
CSFH	Cosmic star formation history
IMF	Initial mass function
CC	Charged current
NC	Neutral current
DYB	Daya Bay
EH	Experimental hall
AD	Antineutrino detector
NPP	Nuclear power plant
IAV	Inner acrylic vessel
OAV	Outer acrylic vessel
GdLS	Liquid scintillator doped with gadolinium
SSV	Stainless steel vessel
MO	Mineral oil
PMT	Photomultiplier tubes
ACU	Automated calibration unit
LED	light-emitting diode
IWS	Inner water shield
OWS	Outer water shield

RPC	Resistive plate chamber
nGd	neutron capture on gadolinium
nH	neutron capture on hydrogen
NSI	Non-standard interaction
DAQ	Data acquisition
EFD	Event flow distributor
IS	Information sharing
DIM	Distributed information management
DNS	Dim name server
DCS	Detector control system
ADC	Analog to digital convertor
p.e.	Photoelectron
LAB	Linear alkyl benzene
FSI	Final state interaction
CJPL	China Jinping underground laboratory

Chapter 1 Introduction

This chapter will introduce general knowledge about supernovae (SNe) as well as supernova neutrinos, to clarify the motivation and the significance of detecting supernova neutrinos. As is relevant to the main contents of this thesis, the detection of supernova neutrinos and some applications are also succinctly described. Considering the relation between supernova rate and supernova distance to the Earth, supernova neutrino studies are basically categorized into two types. One is for supernova burst neutrinos (SBN) and the other is for supernova relic neutrinos (SRN) which diffuse in the universe from all the past supernovae. Supernova relic neutrinos are also known as the diffuse supernova neutrino background (DSNB). A relatively detailed introduction to SRN will be presented. The current experimental status on supernova neutrino detection will be shown.

1.1 Supernova

This section will introduce the necessary knowledge of supernovae, thus explaining the importance of supernova study. Some review of the explosions, mechanism, and neutrinos from supernovae are presented in Ref. [1–3].

1.1.1 What a supernova is

To explain what a supernova is, it is inevitable to start with the stellar evolution^[4,5]. Figure 1.1 makes an impressive illustration. A star is powered by its interior nuclear fusion and changes during its entire life, forming a kind of cycle from birth to death, and we call this stellar evolution. The processes and phases during the star's evolution strongly depend on the initial mass and the metallicity, and the lifetime varies from a few million years up to trillions of years. For massive stars (generally $>8 M_{\odot}$, solar mass), the star evolution goes through a protostar phase, a star phase, then a supergiant progenitor, and eventually a supernova explosion to a neutron star (NS) or a blackhole (BH) (possible for $>25 M_{\odot}$) which not only depends on the initial mass and the metallicity but also some other effects^[5]. The other remnants could form a nebula where a newly-born star could be raised. Low-mass stars, like the Sun, will transform into various dwarfs and different types of nebulae via a red or blue giant progenitor.

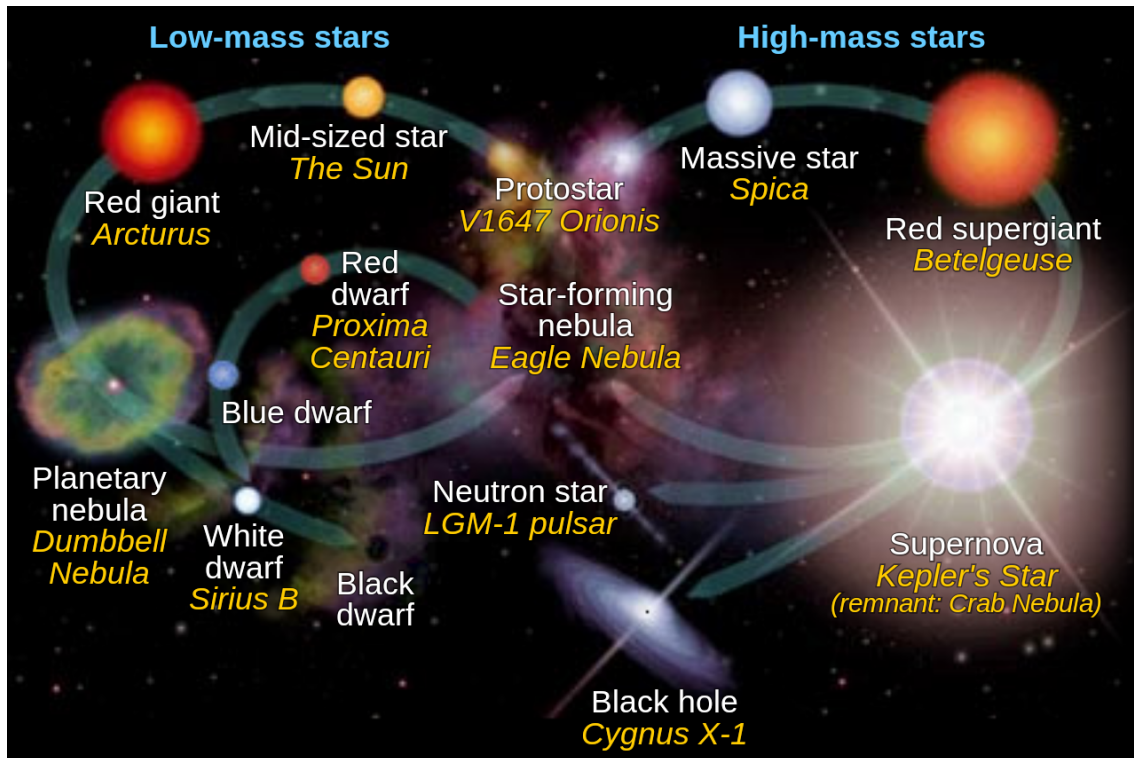


Figure 1.1 A schematic diagram of the stellar evolution. The italic yellow text refers to real examples from astronomical observations. (From wikimedia, see https://commons.wikimedia.org/wiki/File:Star_life_cycles_red_dwarf_en.svg. The background image from NASA's Goddard Space Flight Center.)

A core-collapse supernova is an explosion of an evolved massive star ($>8 M_{\odot}$), that marks the death of a massive star. Supernovae are some of the most energetic events in the universe since the Big Bang and they are more luminous than one billion Suns, fading away after a few weeks or months. Figure 1.2 shows an optical explosion from a supernova in M82 galaxy in January 2014, which is named SN2014J^①.

The material of the outer layers of a supernova will be blasted away, outwardly propagating at a velocity up to 10% of the speed of light. The shell of gas and dust will be expanded, resulting in a supernova remnant. The remnant is actually a kind of nebula. The core of the star after a supernova explosion will transform into a neutron star, or a black hole, as mentioned above. Figure 1.3 shows the supernova remnant of the earliest recorded SN1054, the records of which were provided by Chinese astronomers, and the supernova remnant of SN1987A, which is a milestone in supernova neutrino detection that will be explained in the next section.

^① The convention to name a supernova is “SN” followed by the year of discovery and then letters denoting the order of the supernova discovered in that year. The order is represented by one capital letter from A, B, ..., to Z, and then two lower-case letters from aa, ab, ..., to zz. At present, three-letter notation is not needed.

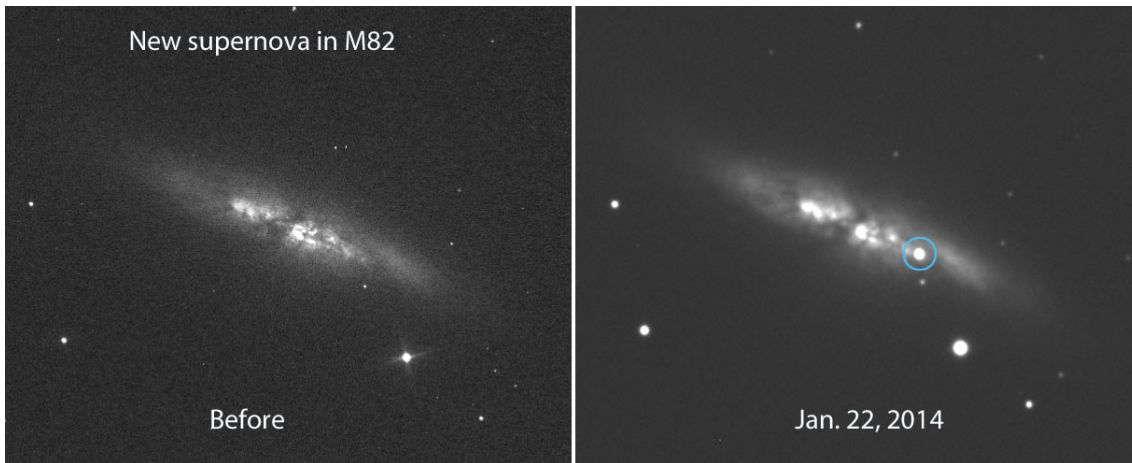


Figure 1.2 Before and after an optical explosion of a supernova in the M82 galaxy in January, 2014. Credit: UCL/University of London Observatory/Steve Fossey/Ben Cooke/Guy Pollack/Matthew Wilde/Thomas Wright, <http://www.ucl.ac.uk/mathematical-physical-sciences/news-events/maps-news-publication/maps1405>.

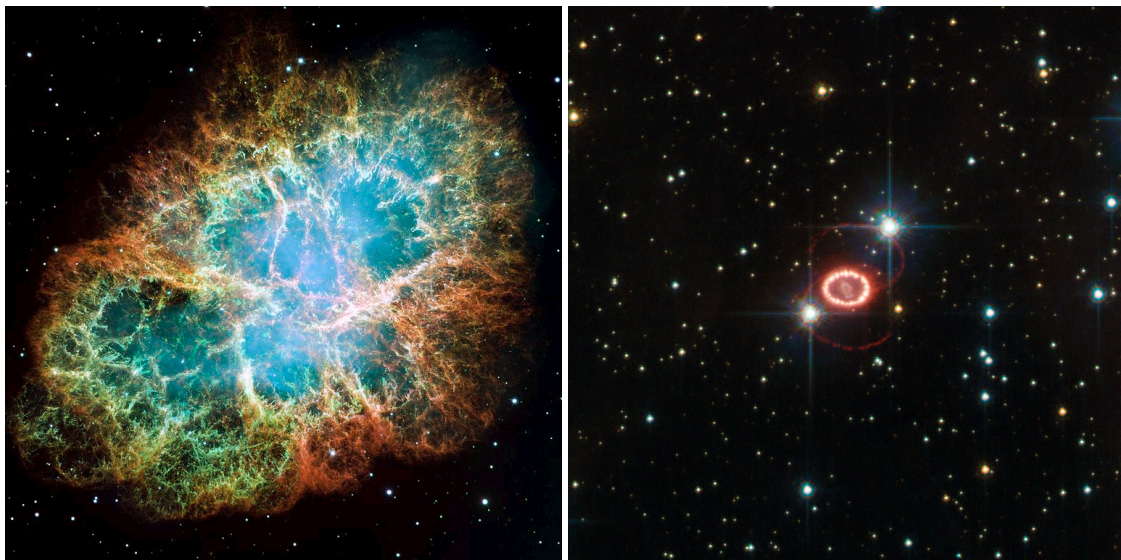


Figure 1.3 Left: The supernova remnant of SN1054 (Credit: NASA, ESA, J. Hester and A. Loll (Arizona State University), <http://hubblesite.org/gallery/album/pr2005037a/>). Right: SN1987A (Credit: ESA/Hubble & NASA, <http://www.spacetelescope.org/images/potw1142a/>).

1.1.2 Supernova types

For historical reasons, SNe are divided into different types (see Figure 1.4) and are characterized by their spectroscopic characteristics as well as the evolution properties of the light curve. These depend on the chemical elements of the envelope of the SN progenitor star. We will focus on core-collapse supernovae (CCSN) which represent about 70%^[7] of the supernova observations and which emit a tremendous number of neutrinos. Thermonuclear supernovae, e.g., type Ia, always occur in binary systems, with

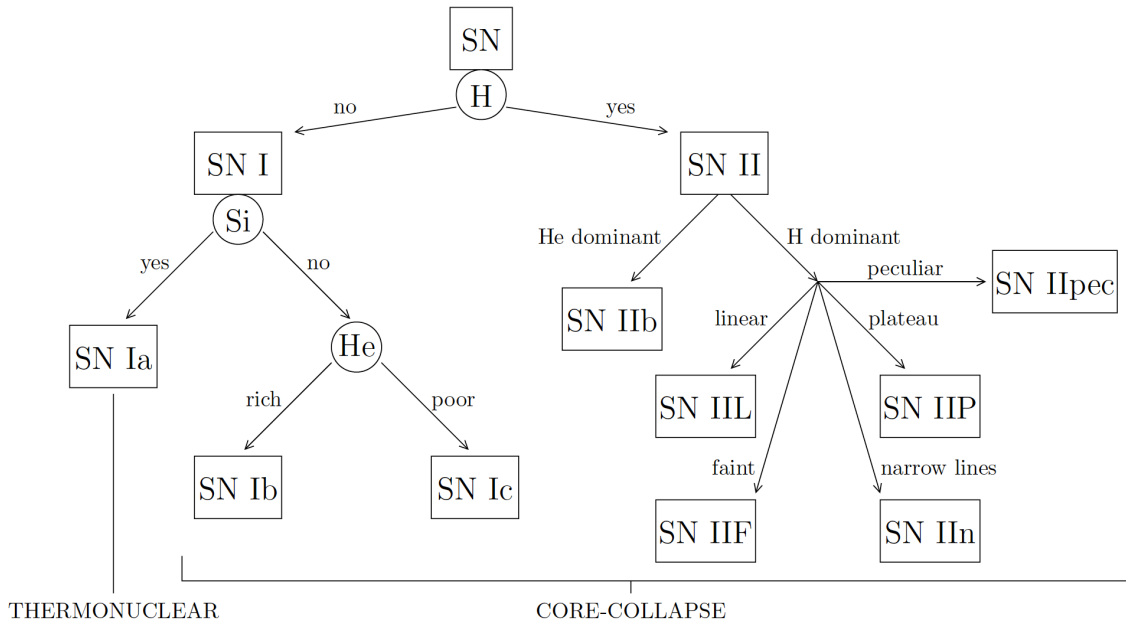


Figure 1.4 Classification of supernovae from Ref. [6].

insignificant neutrino emission with respect to CCSNe^[8,9]. Note that there are additional types of supernovae, e.g., type III, IV, and V, which based on a few examples cannot fit types I or II quite well. But these three types of supernovae are now regarded as likely to be core-collapse supernovae although some of them have unclear mechanisms.

1.1.3 Core-collapse supernovae

The core-collapse supernova (CCSN) mechanism and features referring to Ref. [3,6, 7,10] are presented in this subsection.

Explosion mechanism Taking type II SNe as an example, the CCSN mechanism is illustrated in Figure 1.5 and the main processes and neutrino emission are explained in accordance with the five sub-figures.

- a) Within a massive star, an iron core is formed from the fusions of the onion-like shells of elements. When the iron core reaches the Chandrasekhar-mass (a mass limit for the electron degeneracy pressure against the gravity), it starts to collapse.
- b) Protons combined with electrons in the core are compressed into neutrons with a rapid increase of the density. ν_e 's are produced but trapped by coherently enhanced elastic scattering on heavy nuclei at this moment.
- c) The core of neutrons is like a solid wall and would bounce back the infalling matter, forming an outward-propagating shock wave. When the shock reaches the outer

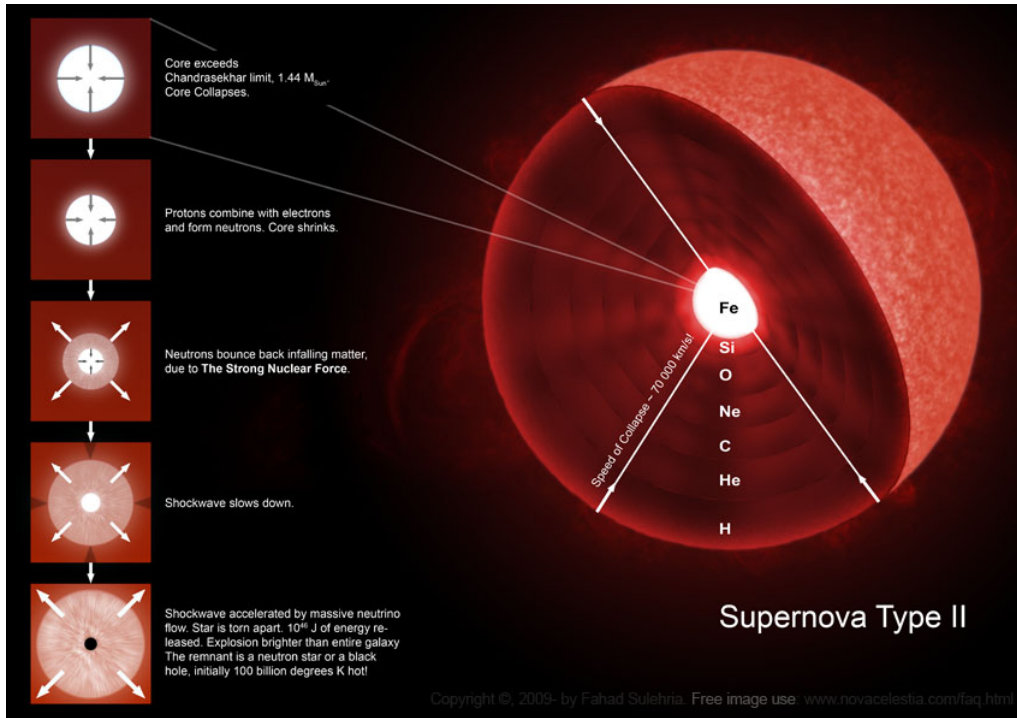
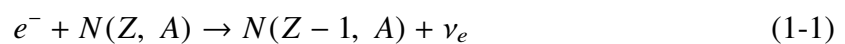


Figure 1.5 Illustration of a core-collapse supernova mechanism. (Free image use, http://www.novacelestia.com/images/stars_supernova_process_medium.jpg)

core, it produces a “prompt ν_e burst” within tens of milliseconds.

- d) The shock wave then runs out of pressure and stagnates. The neutrino streaming heats the material behind the shock wave, building up renewed pressure. The neutrino luminosity is dominated by $\nu_e/\bar{\nu}_e$ pairs in this phase within hundreds of milliseconds.
- e) After several hundreds milliseconds, the shock wave takes off and the overlying matter is expelled. The neutron star settles and cools by neutrino emission over seconds. Nucleosynthesis occurs in this phase, conceivably including the r -process (rapid neutron captures by heavy seed nuclei, e.g., ^{56}Fe in core-collapse supernovae) that produces about half of the heavier elements than iron, e.g., Pu and U^[11].

Neutrino emission All flavors of neutrinos produced in the core of a proto-neutron star undergo various interactions^[3,6,12] as listed below including electron capture,



positron capture,

$$e^+ + n \rightarrow p + \bar{\nu}_e, \quad (1-3)$$

electron-positron pair annihilation,

$$e^- + e^+ \rightarrow \nu + \bar{\nu}, \quad (1-4)$$

plasmon decay,

$$\gamma \rightarrow \nu + \bar{\nu}, \quad (1-5)$$

photo-annihilation,

$$e^\pm + \gamma \rightarrow e^\pm + \nu + \bar{\nu}, \quad (1-6)$$

electron-nucleon bremsstrahlung,

$$e^\pm + N \rightarrow e^\pm + N + \nu + \bar{\nu}, \quad (1-7)$$

and nucleon-nucleon bremsstrahlung,

$$N + N \rightarrow N + N + \nu + \bar{\nu}. \quad (1-8)$$

Failed supernova Recently, more attention^[13,14] has been drawn to the rarer stellar core collapse directly into a black hole (BH) with faint electromagnetic emission, i.e., failed supernovae. For massive stars ($>8 M_\odot$), the ordinary CCSN generally refers to the neutron star-forming core-collapses as implied by Equation (1-9). However, an explosion might also occur but is weaker for $M \sim (25 - 40)M_\odot$ with a black hole formed via fallback^[5]. Stars with $M \gtrsim 40M_\odot$ would directly collapse into a black hole with neither bounce-back shock propagating outside nor explosion. These black hole-forming core-collapses result in failed supernovae^[13,14] which would emit a more luminous and energetic neutrino flux in a shorter time than the ordinary CCSN and occupy a fraction of about 10-20%^[15] of the total CCSN. Though the total luminosity of an ordinary CCSN ($\sim 3 \times 10^{53}$ erg) is larger than

that from a failed supernova ($\sim 1.4 \times 10^{53}$ erg), the average energy (9-18 MeV) of neutrinos from an ordinary CCSN is smaller than that (20-24 MeV) from a failed supernova. As a result, the number of neutrino events from a failed supernova would be larger than that of an ordinary CCSN.

In this thesis, due to the large uncertainties in failed supernovae, we will use ordinary CCSN to demonstrate the supernova neutrino detection capability while the sensitivity to failed supernovae tends to be larger than that for ordinary CCSN.

1.1.4 Great significance of core-collapse supernovae

According to Refs. [3,6,7,10], deep insight into the core-collapse supernovae is of importance in many aspects which are summarized below.

1. Catastrophic end of massive stars in the stellar evolution leaving behind neutron stars or black holes.
2. Heavy element enrichment in the cosmos from the nucleosynthesis in the explosions, much relevant to the evolution of galaxies, stars, planets, and the origins of life.
3. Astronomical sources of neutrinos to unravelling the mysteries in supernova dynamics, as well as intrinsic properties of neutrinos.
4. Sources of gravitational waves predicted by Einstein's General Relativity.
5. Understanding of the long existing puzzles of the origins of gamma-ray bursts.
6. The most extreme physical environments with temperatures ranging from 10^9 K to 20 K and densities ranging from 10^{15} g cm $^{-3}$ to 10^{-23} g cm $^{-3}$.

The study of core-collapse supernovae is an interdisciplinary field of particle physics, astrophysics and astronomy, nuclear physics, and cosmology.

1.2 Supernova neutrinos

Supernova neutrinos are referred to as CCSN neutrinos in the following. Although modern telescopes, on the ground or in space, are now discovering and studying hundreds of supernovae each year spanning the electromagnetic spectrum from radio to gamma rays, supernova neutrinos would still play an irreplaceable role in supernova-related physics besides neutrino physics.

1.2.1 Importance of supernova neutrinos

CCSN would emit a tremendous number of neutrinos on a time scale of 10 seconds. These neutrinos in principle carry away $\sim 99\%$ of the gravitational binding energy released from the transformation of a stellar core into a neutron star. About $\sim 1\%$ of the gravitational binding energy is converted into kinetic energy and about 0.01% into the SN electromagnetic explosion that is visible by many kinds of telescopes^[7]. Moreover, the first electromagnetic outburst may occur several hours or even days later than the neutrino burst^[2]. In fact, CCSN neutrinos are really “messengers” conveying the information of CCSN explosions since the luminosity, energy, and flavor changing with time can tell us what exactly happens during the extremely powerful explosions as well as the stellar progenitor matter profile and so forth. This would provide a deep insight into the supernova dynamics and may answer the questions relevant to the failure of more sophisticated 3D numerical simulations nowadays of prompt bounce-shock mechanism^[16].

The fact that supernova neutrinos arrive a few hours or a day earlier than electromagnetic burst enables an early warning of a supernova explosion^[17,18], which is useful to the astronomy community for an observation of the supernova at a very early stage as well as for some experiments that cannot trigger by themselves. The data would be preserved immediately as well. Specifically, the bounce in a CCSN is strongly correlated to the strongest gravitational wave signal, and the supernova neutrinos would serve as a trigger for a joint search for gravitational wave from CCSN^[19–21].

From the detection point of view, neutrinos can travel much more freely than light in the universe since only weak interactions^① with matter are involved.

As an astronomical source of neutrinos, CCSN neutrinos can provide a wide range of limits on neutrino physics with the advantage of long travel distance, e.g., limits on neutrino mass, neutrino lifetime, neutrino magnetic moment, and neutrino electric charge^[6,22]. Specifically, due to the MSW^[23,24] (named after Mikheev, Smirnov, and Wolfenstein) effect, the neutrino flavor transitions (MSW resonance) in supernova dense matter are quite sensitive to the neutrino mass hierarchy, which is one of three remaining unknowns in neutrino mixing in the three-flavor framework^[25,26]. The phenomenology of self-induced flavor conversions originating from the large $\nu - \bar{\nu}$ interaction potential can also be studied^[27,28].

① Gravity is assumed to be a more essential interaction for everything resulting from geometric properties of space and time.

1.2.2 SN1987A

A milestone of the observation of supernova neutrinos is SN1987A which was the only time we measured some supernova neutrinos so far^[29–34]. This is a real example to validate the importance of supernova neutrinos, even though just two dozen neutrinos from SN1987A were observed.



Figure 1.6 Pictures of the blue supergiant star Sanduleak -69 202 before and after it exploded on 23 February 1987 (SN 1987A) in the Large Magellanic Cloud, 50 kpc away from the Earth. ©Australian Astronomical Observatory

Figure 1.6 shows the blue supergiant star in the Large Magellanic Cloud 50 kpc^① away from the Earth before and after it was observed to explode on 23 February 1987, i.e. SN1987A.

About two dozen neutrinos were observed by several neutrino detectors as shown in Figure 1.7. These two dozen neutrinos provided a crucial test for CCSN theory and basically the foundation of modern supernova models. As mentioned in Section 1.2.1, a wide range of limits were also provided on neutrino physics and properties, some of which are still the most stringent so far. A new era of *neutrino-astronomy* was opened by

① Parsec, abbrev. to pc, a unit of length to measure large distances beyond our Solar system. 1 pc equals about 3.26 light-years.

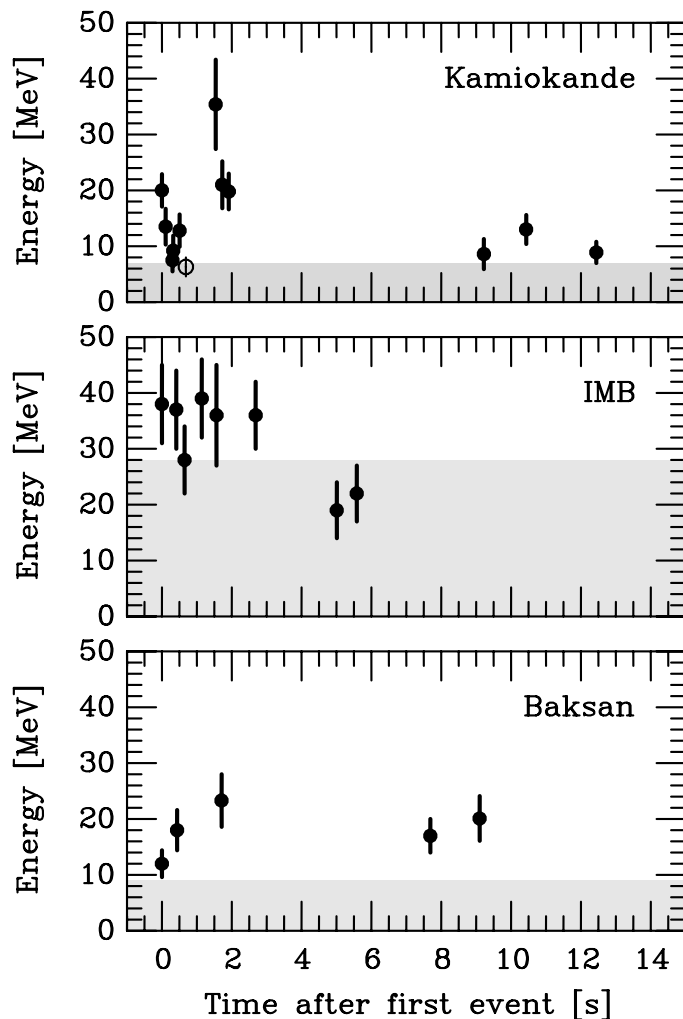


Figure 1.7 SN1987A neutrinos were observed at Kamiokande^[29,30], IMB^[31,32], and Baksan^[33,34] experiments. The energies represent the detected energy of positrons from inverse beta decay reactions. The shaded area corresponds to a trigger efficiency less than 30%. (From Ref. [7])

the detection of several SN1987A neutrinos and this work was awarded the Nobel Prize in Physics 2002.

1.2.3 Characteristics of supernova neutrinos

According to knowledge about the mass (Chandrasekhar limit $\sim 1.44 M_{\odot}$) and the radius (a few thousand kilometers) of a CCSN stellar core, the gravitational binding energy released from the stellar core to the neutron star during a CCSN explosion is estimated to be^[35]

$$E_{\text{bind}} \simeq E_{\nu}^{\text{tot}} = 3 \times 10^{53} \text{ erg} \times \left(\frac{M_{\text{NS}}}{1.4 M_{\odot}} \right)^2 \times \left(\frac{R_{\text{NS}}}{10 \text{ km}} \right)^{-1}, \quad (1-9)$$

where M_{NS} is the mass and R_{NS} is the radius of a neutron star. The mass is within the range of 1.2-1.6 M_{\odot} ^[36], while the radius is difficult to measure and is estimated to be ~ 10 km. A typical value of the total binding energy is 3×10^{53} erg^①, about $0.2 M_{\odot} c^2$ ^②. Considering the average energy of neutrinos (introduced below), $\sim 10^{58}$ neutrinos are emitted within a 10-s timescale.

The modern supernova theory and simulation has predicted the features of supernova neutrinos with time. Figure 1.8 shows curves of luminosity and average energy for different flavors of neutrinos changing with time. Three main phases are shown in Figure 1.8 upper

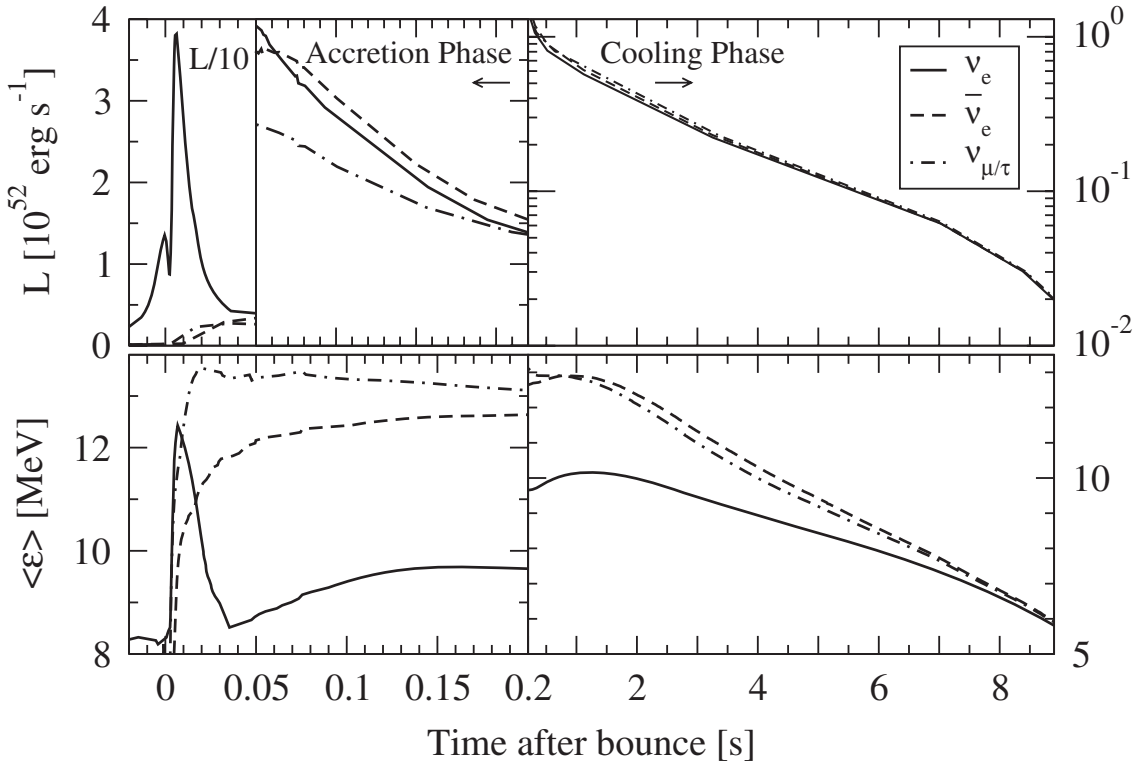


Figure 1.8 The luminosity and average energy of different flavors of neutrinos from a SN (progenitor mass 8.8 M_{\odot}) that explodes in a spherically symmetric simulation of the Garching group^[37].

panel: a prompt ν_e burst phase (luminosity divided by 10 in the figure), an accretion phase (dominated by $\nu_e/\bar{\nu}_e$ pairs production), and a cooling phase (by all flavors of neutrinos production). The phases coincide with the CCSN mechanism as already explained in Section 1.1.3.

Integrating luminosity over time, $L_{\nu_e} > L_{\bar{\nu}_e} > L_{\nu_x}$ ^③. $L_{\bar{\nu}_e}^{tot}$ is roughly 1/6 of the total

① 1 erg = 10^{-7} J = 624.15 GeV

② Equivalent solar mass. Not really mass loss, just gravitational energy conversion.

③ ν_x represents any one of $\nu_{\mu}, \bar{\nu}_{\mu}, \nu_{\tau}, \bar{\nu}_{\tau}$.

luminosity (time-integrated), which is about 5×10^{52} erg.

In the lower panel, the average energy is shown, $\langle E_{\nu_e} \rangle < \langle E_{\bar{\nu}_e} \rangle \leq \langle E_{\nu_x} \rangle$, which are about 10 MeV, 12 MeV, and 12 (20) MeV, respectively. Due to the absence of μ, τ neutrino observation, $\langle E_{\nu_x} \rangle$ has a large model-dependent uncertainty. The energy hierarchy is due to the different opacities (interactions) of the proto-neutron star for different flavors of neutrinos. The energy spectrum of supernova neutrinos follows a quasi-thermal distribution^[38,39],

$$f_\nu(E) \propto E^\alpha e^{-(\alpha+1)E/\langle E \rangle}, \quad (1-10)$$

where α is the pinching parameter (the spectrum will be narrower with larger α) and can be calculated from the moments of energy,

$$\frac{\langle E^2 \rangle}{\langle E \rangle^2} = \frac{2 + \alpha}{1 + \alpha}. \quad (1-11)$$

A Fermi-Dirac spectrum corresponds to $\alpha \approx 2.3$ with the degeneracy parameter $\eta = 0$ and a Maxwell-Boltzmann spectrum to $\alpha = 2$. The effective spectral temperature T is about $\frac{1}{3}\langle E \rangle$. Notice the pinching parameter α is undergoing evolution during the supernova explosion as a consequence of the varying moments of energy. The energy spectrum has a variation along with different SN models.

The shape of supernova neutrino energy spectrum integrated over time is illustrated in Figure 1.9, which is based on a dynamical collective calculation from Ref. [40]. The structure in the ν_e spectrum is accounted for by a collective effect of the prompt ν_e burst phase and the other two relatively placid phases (see Figure 1.8).

1.3 Detection of supernova neutrinos

In this section, the detection of supernova neutrinos is introduced, mainly considering the primary interactions, detector types, and a summary of the expected number of supernova neutrino events in present world-wide detectors.

1.3.1 Reactions and detector types

The key consideration for interaction channels for detection include the magnitude of the cross section (number of events), energy threshold (sensitive energy region), target

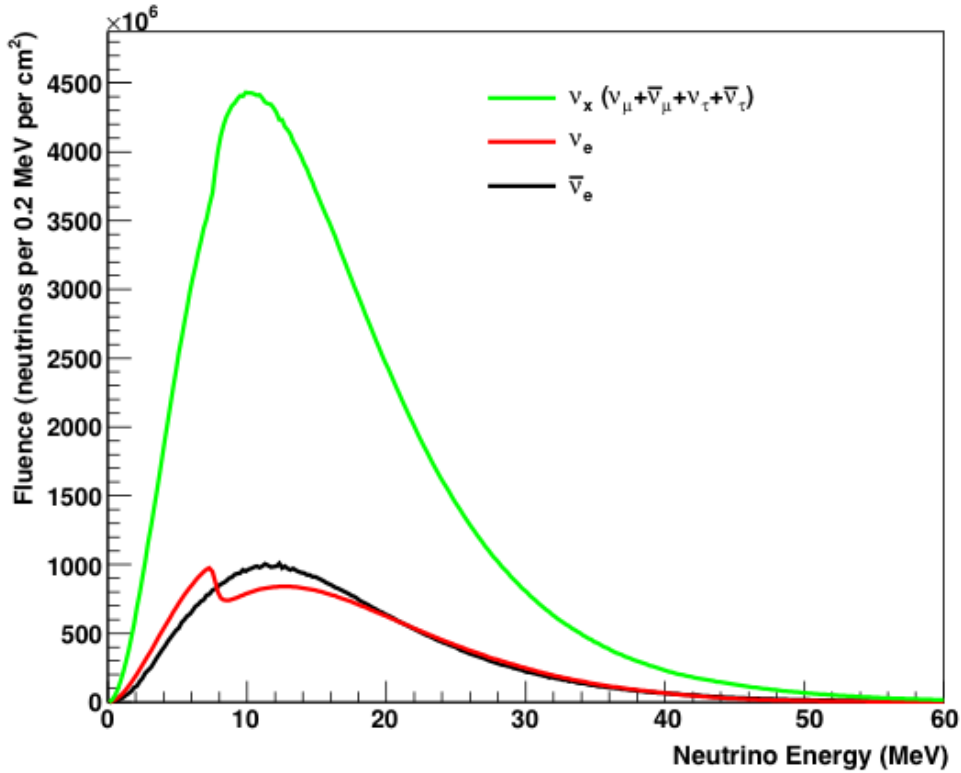


Figure 1.9 Example of energy spectra for all the flavors of supernova neutrinos integrated over 10 seconds from Ref. [41]. The calculation is based on the GKVM model of Ref. [40].

material, and reaction products (basis for detection technique and background suppression).

In liquid scintillator detectors, the supernova neutrinos (electron antineutrino) are primarily identified by the inverse beta decay (IBD) interactions^[42], $\bar{\nu}_e + p \rightarrow e^+ + n$. The interaction rates as a function of the supernova neutrino energy for various reactions are shown in Figure 1.10. The IBD interaction has a one order of magnitude larger cross section than other reactions as well as a low energy threshold of ~ 1.8 MeV. A roughly energy-independent shift from neutrino energy to positron kinetic energy, $T_{e^+} = E_\nu - 1.8/\text{MeV}$, can be derived from this interaction. Neutrinos (primarily $\bar{\nu}_e$) are detected through identifying e^+ or even a coincidence measurement from a prompt signal from e^+ and a delayed signal from neutron capture on nucleus. The coincidence measurement provides a distinct signature against backgrounds from accidentals, natural radioactivity, and other flavors of neutrinos from other sources.

In water Cherenkov detectors, the situation is quite similar to that in liquid scintillator detectors except for a little difference in neutrino interactions with oxygen nuclei instead of carbon nuclei. The neutron-tagging technique^[43] was recently developed to provide

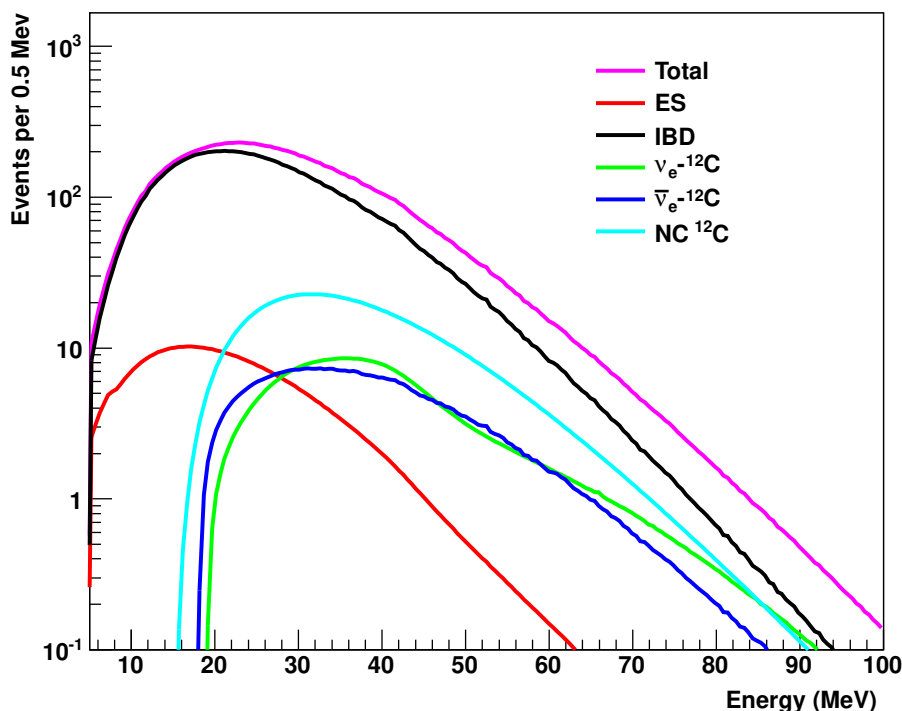


Figure 1.10 Interaction rates of supernova neutrinos as a function of the neutrino energy in 50 kt of liquid scintillator from Ref. [41]

a coincidence measurement of the IBD events, though in general the Cherenkov light is used merely to identify and reconstruct the IBD positrons.

$\nu - e$ scattering has a small cross section and usually can be ignored. However, for some large-volume detectors, e.g., Super-Kamiokande, this interaction is quite useful for identifying the direction of incident neutrinos.

In fact, coherent elastic neutrino-nucleus scattering has a relatively high cross section, but the detectable signal is from proton recoil or nucleus recoil, which has quite little visible energy in detectors^[44–46].

Some other types of detectors with different target materials have different scenarios to detect neutrinos. The future experiment DUNE^[47–50] (liquid argon time projection chamber detector) will make use of the neutrino interactions with argon nuclei to detect neutrinos and the ongoing experiment HALO^[51,52] uses neutrino interactions with lead.

1.3.2 Expected number of supernova neutrino events

In a liquid scintillator (LS) detector, the expected number of supernova neutrinos can be calculated. The approximate chemical composition of typical liquid scintillator is C_nH_{2n} ; thus 1 kiloton of liquid scintillator contains about 8.6×10^{31} protons. The IBD

cross section at leading-order^[42,53] is

$$\sigma_{\text{IBD}} = 9.42 \times 10^{-44} \text{cm}^2 (E_\nu/\text{MeV} - 1.3)^2. \quad (1-12)$$

As shown in Section 1.2.3, according to the luminosity (L) and average energy ($\langle E \rangle$) of $\bar{\nu}_e$ which is 5×10^{52} erg and 12 MeV, a total number of 2.6×10^{57} $\bar{\nu}_e$'s is emitted and the flux of $\bar{\nu}_e$ at Earth is

$$F_{\bar{\nu}_e} = 2.18 \times 10^{11} \text{cm}^{-2} \times \frac{L_{\bar{\nu}_e}}{5 \times 10^{52} \text{erg}} \times \frac{12 \text{MeV}}{\langle E_{\bar{\nu}_e} \rangle} \times \left(\frac{10 \text{kpc}}{D} \right)^2. \quad (1-13)$$

where D is the distance of a supernova to the Earth. Notice that $L_{\bar{\nu}_e}$ and $\langle E_{\bar{\nu}_e} \rangle$ are contingent upon supernova models and are known with precision.

Convoluting the energy spectrum ($\langle E_{\bar{\nu}_e} \rangle = 12 \text{MeV}$), the IBD cross section, the number of target protons, and the neutrino flux at Earth, the expected number of supernova neutrinos is estimated to be,

$$N = 300 \times \frac{L_{\bar{\nu}_e}}{5 \times 10^{52} \text{erg}} \times \left(\frac{10 \text{kpc}}{D} \right)^2 \times \left(\frac{\text{Mass}}{1 \text{kt}} \right), \quad (1-14)$$

where Mass refers to the target mass of a detector and other quantities have the same definition to those in Equation (1-13). No detector effect is involved here, and the neutrino oscillation effect is also ignored, specifically the complicated matter effect, in the dense proto-neutron star during a supernova explosion. Notice that the number N can be altered by different energy spectra as the cross section is energy-dependent.

For present and proposed SN neutrino detectors, the expected SN (at 10 kpc) neutrino event rates are summarized in Table 1.1 referring to Ref. [54].

A long-string detector refers to a long string water Cherenkov detector with an array of PMTs located in long vertical strings immersing in water or ice^[56,57], such as IceCube. There is no individual event reconstruction for neutrino type, energy, and direction of supernova neutrinos for IceCube^[58], as it detects supernova neutrinos (tens of MeV) via a collective effect of increase in the rates of all the PMTs caused by the Cherenkov light from produced charged particles. A surface detector refers to a detector at the surface of the Earth without adequate rock overburden and the SN neutrino signals may be buried by the large cosmic-ray muon-induced background. As a result, such kind of detectors have difficulty self-triggering, e.g., MiniBooNE^[59] and MicroBooNE^[60]. The other three

Table 1.1 Present and proposed SN neutrino detectors are listed with the expected number of SN (at 10 kpc) neutrino events. ‘Flavors’ indicates the primary detected flavor of neutrinos and other flavor components may be detectable/visible based on the target mass and the tagging quality. See text for more explanations of various superscripts.

Detector	Type	Mass (kt)	Location	Events	Flavors	Status
IceCube ^{*, S, T}	Long string	(600)	South Pole	(10 ⁶)	$\bar{\nu}_e$	Running
Super-Kamiokande ^{S, P}	Water	32	Japan	7,000	$\bar{\nu}_e$	Running
NO ν A [†]	LS	15	USA	4,000	$\bar{\nu}_e$	Running
LVD ^S	LS	1	Italy	300	$\bar{\nu}_e$	Running
KamLAND ^S	LS	1	Japan	300	$\bar{\nu}_e$	Running
MiniBooNE [†]	LS	0.7	USA	200	$\bar{\nu}_e$	Running
Daya Bay ^S	LS	0.33	China	100	$\bar{\nu}_e$	Running
Borexino ^S	LS	0.3	Italy	100	$\bar{\nu}_e$	Running
Baksan	LS	0.33	Russia	50	$\bar{\nu}_e$	Running
HALO ^S	Pb	0.08	Canada	30	ν_e, ν_x	Running
MicroBooNE ^{†, P}	Argon	0.17	USA	17	$\nu_e, \bar{\nu}_e$	Running
SNO+	LS	0.8	Canada	300	$\bar{\nu}_e$	Near future
PINGU ^{*, T}	Long string	(600)	South Pole	(10 ⁶)	$\bar{\nu}_e$	Proposed
Hyper-Kamiokande ^{P, T}	Water	560	Japan	110,000	$\bar{\nu}_e$	Proposed
LENA	LS	50	Europe	15,000	$\bar{\nu}_e$	Proposed
JUNO	LS	20	China	6,000	$\bar{\nu}_e$	Proposed
RENO-50	LS	18	Korea	5,400	$\bar{\nu}_e$	Proposed
DUNE ^P	Argon	34	USA	3,000	$\nu_e, \bar{\nu}_e$	Proposed

* No individual event reconstruction for tens of MeV neutrino event and the number of events is shown in parenthesis.

† Surface detectors, which may not be self-triggering due to background.

^S Collaborative detectors integrated in the world-wide Supernova Early Warning System (SNEWS)^[55].

^P Detectors with pointing ability.

^T Potential ability in measurement of the temporal features of SN neutrinos.

superscripts, “S”, “P”, and “T” will be explained in the following.

1.3.3 Applications

The applications of the detection of supernova neutrinos can be divided into several categories which are consistent with the importance of supernova neutrinos mentioned in Section 1.2.1.

Early warning of a supernova As introduced in Section 1.2.1, an early warning of a supernova explosion is an important application of the detection of supernova neutrinos. Particularly, the Supernova Early Warning System (SNEWS) is a world-wide network collaborating current supernova-neutrino-sensitive detectors, to provide a high-confidence early warning of a supernova occurrence^[17,18]. Seven detectors are involved in SNEWS^[55] at present and each of them is labeled with a superscript “S” (see Table 1.1).

Pointing to a supernova The direction of a supernova explosion is important for several reasons. For a supernova early warning, it is much more useful to provide the direction of a supernova explosion to let astronomers know where to look, allowing an observation at the very early stage. Furthermore, it is possible some CCSN may not result in a bright supernova electromagnetic explosion, e.g., failed supernova, and the direction information is helpful to locate the position of such kind of faint supernova explosion. Knowledge of distance and direction of a supernova explosion will help to determine the neutrino luminosity and the neutrino oscillation effects, for instance, matter effects through the Earth.

Generally, the determination of the SN direction in a single detector is contingent upon the intrinsic anisotropy of the neutrino interaction, and the detector capability of tracking the interaction products. Neutrino interactions with nuclei, have relatively weak energy-dependent anisotropy, for instance, the widely-used IBD interactions^[42]. But $\nu - e$ scattering does have a strongly-peaked forward distribution of electrons^[61]. With detector capability of tracking the interaction products, water Cherenkov detectors and liquid argon time projection chamber (LArTPC) detectors are able to determine the direction of incident neutrinos from $\nu - e$ interactions. The most common liquid scintillator detectors cannot determine the direction due to the high yield of isotropic scintillation light from IBD interactions, but a recent study shows that the direction information might be implied from the relative reconstructed positions of the IBD positron and the neutron events^[62]. Notice that $\nu - e$ scattering interactions only account for a few percent of the total number of interactions as seen in Figure 1.10.

Among the currently running detectors, Super-Kamiokande is the only experiment with pointing ability ($\sim 8^\circ$) and the ability will be improved ($\sim 3^\circ$) by the doped Gd to reduce the isotropic background from the IBD events^[63]. The future Hyper-Kamiokande^[64] would have a further improvement ($\sim 1^\circ$) by a large statistics. LArTPC detectors should also have a considerable pointing ability via lepton tracking. Such detectors with pointing

ability are labelled with a superscript “P” in Table 1.1.

Another method to determine the SN direction is via triangulation – the difference of the neutrino arriving time on detectors^[65]. But it needs the start time of the supernova burst neutrino signals, e.g., the rise time for large event statistics. IceCube and the future Hyper-Kamiokande may contribute to such kind of determination. In addition, a possible method is via the neutrino matter oscillation pattern^[66].

Temporal features The temporal development rather than a collective time-integrated effect of supernova neutrino signals will help to probe more sophisticated features of a supernova, e.g., the hydrodynamics. This is crucial to 3D SN simulation of supernova explosions. It is true that numerical 3D simulations of a supernova do not consistently explode. With enough statistics in tens of milliseconds, some super-large volume detectors, e.g., IceCube^[58] and Hyper-Kamiokande^[64], will be able to probe the subtle features in temporal development of $\bar{\nu}_e$. Such kind of detectors are labelled with a superscript “T” in Table 1.1. It is much anticipated that more flavor components can be detectable in the future.

Outlook The complete flavor measurement is the key point for the future to unravel more mysteries in supernova physics and to determine the unknown neutrino mass hierarchy as well as to probe more neutrino physics beyond the standard model^[54]. This requires large volume detectors with high quality flavor-tagging techniques.

1.4 Supernova rate

Though many interesting and important physics opportunities are associated with the detection of supernova neutrinos, how big a chance we have to detect supernova neutrinos is naturally the next question. According to the astronomical observations of supernovae, the supernova rate is shown in Figure 1.11 against the distance.

With increasing distance, the cumulative CCSN rate is increased; however the neutrino flux would naturally decrease significantly as shown in Equation (1-13). As a consequence, the sensitivity (detection probability) of a detector to supernova neutrinos gets worse for distant supernova explosions. Most of the current detectors on Earth are sensitive to Galactic (within several tens of kpc) supernova explosions, e.g., Mini-

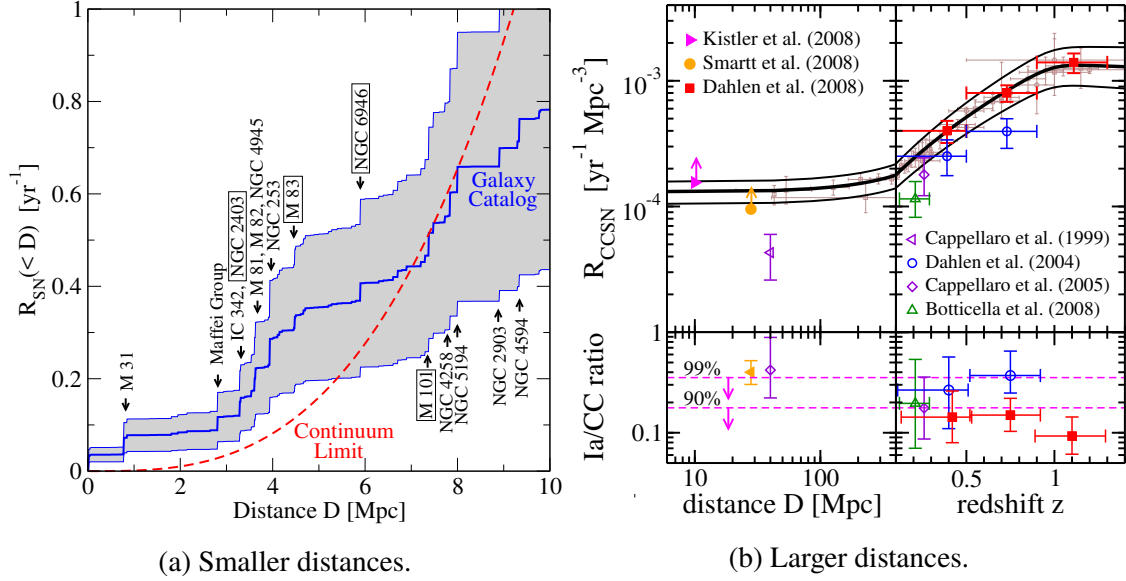


Figure 1.11 Supernova rate against distance. (a) Cumulative CCSN rate against distance for <10 Mpc from Ref. [67]. The dashed red line is a continuum limit based on the star formation rate (SFR) measurements and the stepped line is for local volume, where CCSN may vary among different galaxies. The band is the uncertainty. (b) Differential CCSN rate and Type Ia to CCSN ratio from Ref. [35] are shown in the top and bottom panel, respectively, against distances in Mpc and redshift $z > 0.1$. In the top panel, the solid curve represents the predictions with the error band from the SFR measurement (light brown squares in the background). In the bottom panel, the conservative upper limits are given by the dashed lines. Data are labeled with statistical errors.

BooNE^[59], LVD^[68], Daya Bay^[69], and even IceCube^{[58]①}, except for Super-K^[70] which has a relatively larger sensitivity up to hundreds of kpc.

Detecting supernova burst neutrinos is a once-in-a-lifetime opportunity. Within the Milky Way (the most distant edge is about 23.5 kpc away from the Earth), unfortunately the supernova rate is only a few per century. Even considering some large volume detectors, just a few more small galaxies which are actually satellites of the Milky Way would be taken into account, e.g., Large/Small Magellanic Clouds and the nearest major galaxy – Andromeda which is about 780 kpc away^[71]. Regarding the local effect of supernova explosions, the opportunity is not increased too much outside the Milky Way. Among the satellite galaxies of the Milky Way, the largest one with a relatively small distance to the Earth happens to be the Large Magellanic Cloud where SN1987A was observed.

Figure 1.11 shows that the differential supernova rate is roughly constant with distance (an increase from $z = 0.1$ and be stable from $z = 1$). Since the flux of neutrinos from a supernova explosion is proportional to the distance squares, it is conceivable that a

① Corresponds to a megaton scale detector; however, the sensitivity of triggering a supernova is reduced by the noise pedestal from digital optical modules for a given false trigger rate.

collective flux of the neutrinos from all the past supernova explosions across the universe exists. So far, regarding the supernova neutrino detection, this kind of supernova neutrinos are called **Supernova relic neutrinos** (SRN) which is also known as the diffuse supernova neutrino background (DSNB). In contrast, the neutrinos produced by a certain supernova explosion are designated as **Supernova burst neutrinos**.

1.5 Supernova relic neutrino

In this section, more details about the supernova relic neutrinos (SRN) are presented for its relevance to a collective effect involving large-scale cosmology.

1.5.1 SRN formalism

The differential SRN flux, $d\phi(E)/dE$, is computed by integrating the CCSN rate, $R_{\text{CCSN}}(z)$, and the neutrino emission spectrum, dN/dE' , over the redshift, z , and cosmic time, t ^[72]

$$\frac{d\phi(E)}{dE} = c \int R_{\text{CCSN}}(z) \frac{dN(E')}{dE'} (1+z) \left| \frac{dt}{dz} \right| dz \quad (1-15)$$

where $|dz/dt| = H_0(1+z)[\Omega_m(1+z)^3 + \Omega_\Lambda]^{1/2}$ and $E' = E(1+z)$. H_0 is the Hubble constant and Ω_m and Ω_Λ are cosmological parameters related to dark matter and dark energy. The R_{CCSN} is known with precision by astronomical theory and measurements, and is related to the initial mass and cosmic star formation. The neutrino emission spectrum is identical to the supernova burst neutrino spectrum. A few SRN models^[73–75] were constructed before SN1987A to predict both the flux and the shape. After SN1987A more sophisticated models^[15,35,76–80] were established, benefiting from the two dozen SN1987A neutrinos.

These modern models predict quite similar shapes of the SRN flux and one of the recent models from Horiuchi, Beacom and Dwek, HBD, in Ref. [35] is adopted in this thesis. The HBD model considers the effective neutrino temperature resulting from the initial temperature and mixing of the neutrinos. A typical temperature value of 6-MeV is used for supernova relic $\bar{\nu}_e$ in this thesis. Figure 1.12 compares the HBD model SRN flux and the neutrino emission spectrum. In general, the SRN flux in this thesis refers to the SRN $\bar{\nu}_e$ flux because the detection of supernova neutrinos mainly relies on the IBD interaction at present.

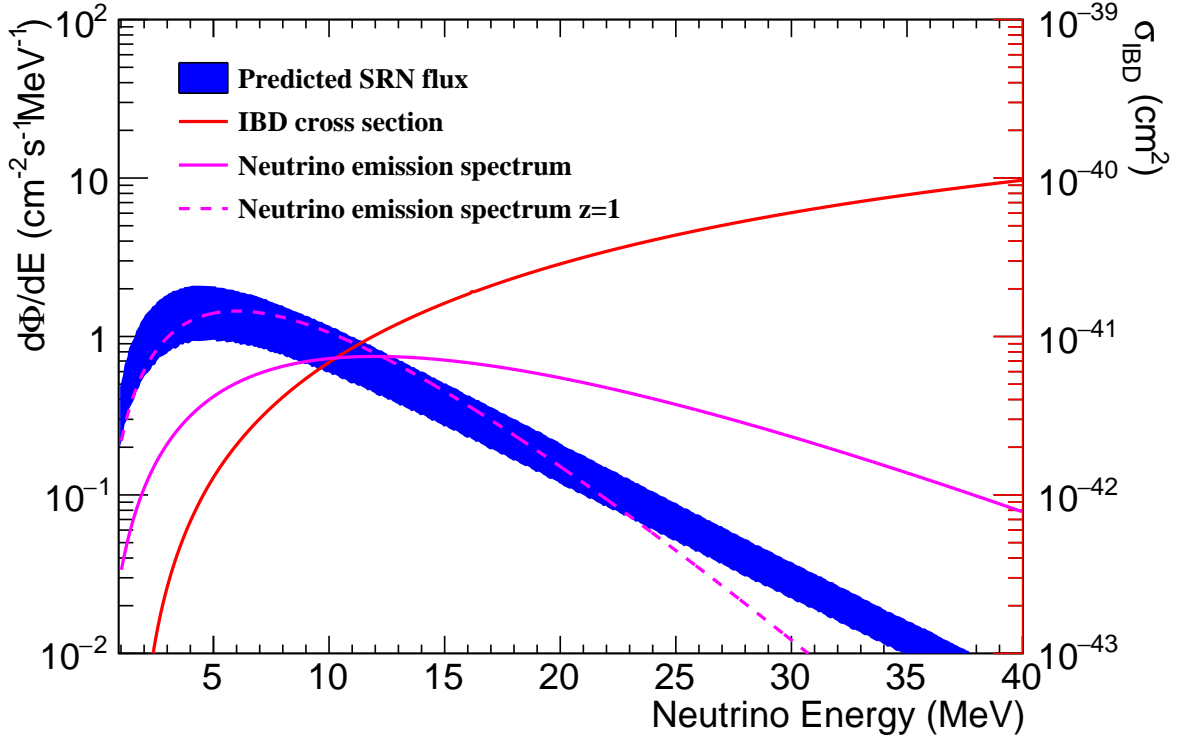


Figure 1.12 Predicted SRN flux (blue band) by HBD model^[35] with a 30-40% uncertainty due to astrophysical inputs. The IBD cross section is also plotted. To compare the shapes, two curves of the neutrino emission spectrum are shown and normalized with the SRN flux. The solid one is the normal neutrino emission spectrum from a supernova explosion approximately described by a Fermi-Dirac distribution. The dashed one additionally considers a constant redshift $z = 1$ on the normal neutrino emission spectrum, resulting in a shrinking (softening) of the spectrum. The neutrino emission spectrum and the HBD SRN flux both adopt a 6-MeV effective neutrino temperature.

The HBD SRN flux (blue band) has a 30-40% uncertainty due to astrophysical inputs, mainly from the R_{CCSN} uncertainty. The IBD cross section is also plotted.

Qualitatively, it is found that the neutrino emission with the redshift $z = 1$ is very roughly consistent with the SRN flux and the redshift $z = 1$ means a ~ 2.7 Gpc distance, 8.7 billion light-years, reflecting that the SRN flux has a large-scale effect, on average softened by a factor of ~ 2 . The neutrino emission spectrum and the HBD SRN flux both adopt a 6-MeV effective neutrino temperature.

Again, it should be emphasized that the effective neutrino ($\bar{\nu}_e$) temperature takes into account the initial neutrino temperature (4-5 MeV for $T_{\bar{\nu}_e}^{\text{ini}}$, 6-7 MeV for $T_{\bar{\nu}_x}^{\text{ini}}$) and neutrino mixing ($\bar{\nu}_e$ and $\bar{\nu}_x$ transition).

Since the collective effect of many CCSN explosions is involved in the SRN flux,

more physics can be probed by the SRN detection.

- An independent test on the stellar formation (supernova) rate.
- Failed supernovae (see Section 1.1.3) would contribute to the SRN^[15] flux and the detection of SRN can provide a constraint on the fraction of ordinary CCSN and failed supernovae, and thus on the fraction of neutron stars and black holes. This is valuable to test our current knowledge of CCSN, especially for failed supernovae only detectable via their neutrinos.

1.5.2 Challenges in SRN detection

Although supernova relic neutrinos have a softer spectrum than supernova burst neutrinos, the reaction channels and detection techniques are roughly the same except that the SRN flux is quite low. Efforts must be made to suppress the backgrounds.

In this thesis, the SRN events are detected via IBD interactions with a neutron tagging technique, in liquid scintillator detectors and even in water Cherenkov detectors^[81]. Therefore, the solar neutrino background from the solar *hep* reactions^[82] (with a flux two orders of magnitude larger than the SRN flux) which dominates $\lesssim 20$ MeV neutrino energy range is negligible.

Figure 1.13 shows the predicted SRN flux as seen in Figure 1.12 against the comparable atmospheric neutrino fluxes of $\bar{\nu}_e$, ν_e , $\bar{\nu}_\mu$, and ν_μ from Refs. [83,84]. The other main backgrounds, reactor neutrino background and muon-induced background in the SRN detection are also indicated.

Reactor neutrino background The reactor neutrino ($\bar{\nu}_e$) background is indistinguishable as the flavor is identical to the SRN flux. The reactor neutrino energy region is roughly less than 10 MeV^[85,86]. The location of the detectors would reduce the reactor neutrino background according to the inverse-square of distance.

Muon-induced backgrounds The cosmic-ray muon-induced backgrounds include the isotopes produced by the muon interacting with the detector target material, e.g., carbon or oxygen, and the spallation neutrons mainly from the muon interacting with the rock in the proximity of the detector^[87–89]. The muon-induced isotopes always have a decay or a cascade decay with a relatively long lifetime compared with the veto time window for a muon event. The spallation neutrons generated outside the detector would transport into the detector while the corresponding muon passes by. Therefore, such kind of neutrons

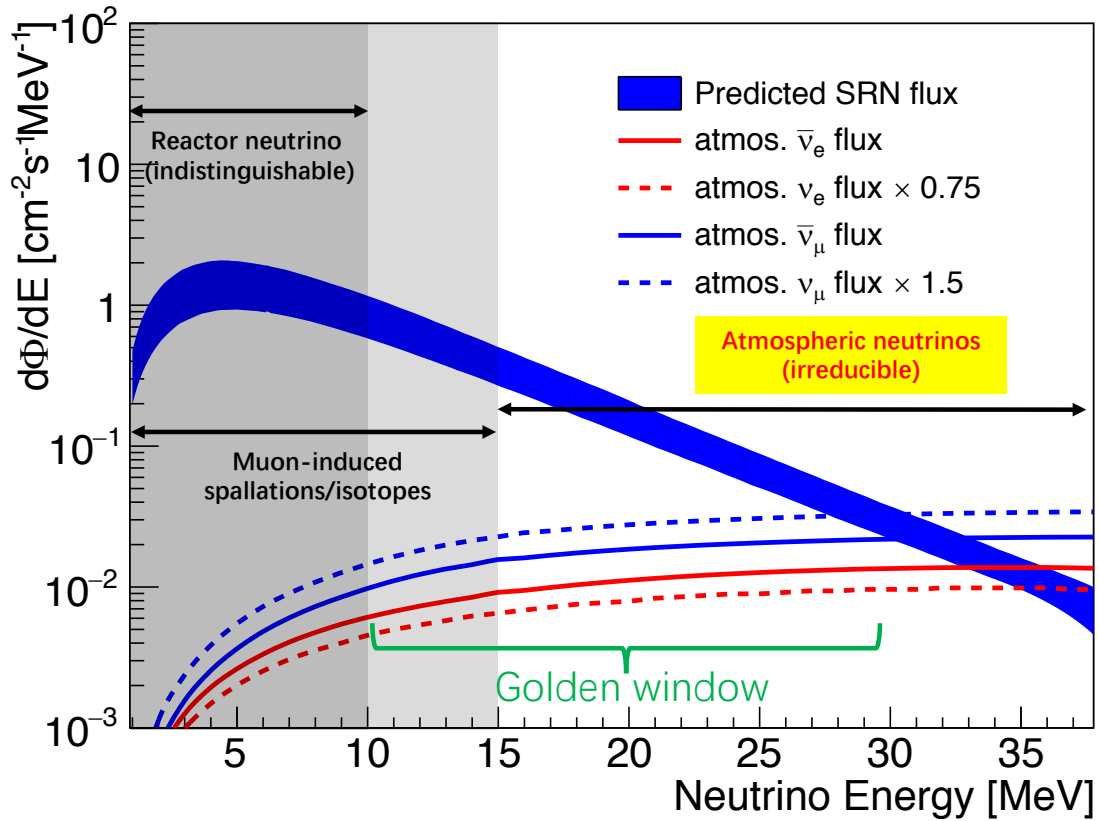


Figure 1.13 Predicted SRN flux versus backgrounds, especially the atmospheric neutrino flux. The dominant energy region of reactor neutrino backgrounds and muon-induced backgrounds are also shown. See text for more explanations.

cannot be removed by identifying the muon. Generally, the muon-induced backgrounds can be reduced significantly if the detector has a large overburden. In water Cherenkov detectors, spallation neutrino background would be further reduced due to the small yield of Cherenkov light. In liquid scintillator detectors, with neutron tagging the muon-induced isotope background is merely ${}^9\text{Li}/{}^8\text{He}$ which has a β decay to a neutron-unstable state. The energy region dominated by the muon-induced isotope background is roughly less than 15 MeV. A uniformly-distributed fast neutron background ranges from a few MeV to tens of MeV in liquid scintillator detectors.

Atmospheric neutrino background The atmospheric neutrino flux is irreducible for a detector on the Earth and cannot be suppressed by a specific experimental environment, unlike the reactor neutrino background and muon-induced background. Given the fact that the SRN flux is very low and the spectra overlap with the atmospheric neutrino spectra, the atmospheric neutrino background is the most challenging for SRN detection.

The atmospheric $\bar{\nu}_e$ background has the same flavor as the SRN ($\bar{\nu}_e$) flux, making it an intrinsic background for the SRN detection. Other flavors of atmospheric neutrinos are also backgrounds for the SRN detection, but with different mechanisms due to the different interactions and final states. The atmospheric neutrinos up to 1 GeV can still contribute to the background. More explanations and details can be seen in the related sections of the SRN study in this thesis.

According to the indistinguishable reactor neutrino background and the intrinsic atmospheric $\bar{\nu}_e$ background, a golden window for the SRN detection can be determined, which is about 10-30 MeV. Based on Figure 1.12, convoluting the SRN flux with the IBD cross section, just a few SRN events are expected in a 20 kilo-ton water or liquid scintillator detector per year.

1.6 Current experimental status and this thesis work

The current experimental status of supernova neutrino detection is shown in this section. The focus will be on the detectors relevant to the studies in this thesis.

1.6.1 Supernova burst neutrinos

From Table 1.1, we find many currently running detectors are sensitive to supernova neutrinos and some large-volume detectors, e.g., Super-Kamiokande and IceCube, are capable of detecting a large number of supernova neutrino events. However, the sensitivity strongly depends on the SN explosion distance to the Earth and only reaches Galactic supernova explosions nearby. Unfortunately, for the quite low supernova rate in our Milky Way or even including some satellite galaxies, no supernova explosions has ever been observed since SN1987A up to now. MiniBooNE^[59], Super-K^[70], and LVD^[68] searched for supernova neutrino bursts and gave upper limits of core-collapse supernova or failed supernova rates within 100%-sensitive distances (10 kpc for MiniBooNE, 25 kpc for LVD, and 100 kpc for Super-K). Other searches or studies of supernova neutrino bursts were also performed in SNO^[90], IceCube^[58], and KamLAND^[91,92].

The sensitivity of a neutrino detector to supernova burst neutrinos relies on both the expected number of supernova neutrino events and the background situation based on which to cut off the background events at an as-small-as-possible cost of supernova signal significance. In general, supernova burst neutrinos are identified via an increase of neutrino signals within a short duration, e.g., 10's of seconds. The specific algorithm may

vary with different detectors. Super-Kamiokande has a 100% sensitivity to supernova burst neutrinos of a supernova explosion out to 100 kpc and some sensitivity up to hundreds of kpc^[70]. IceCube is a megaton scale detector, but it has a sensitivity to trigger a supernova roughly within 50 kpc^[58] due to a large noise pedestal from thousands of digital optical modules. LVD has a 100% sensitivity within 25 kpc^[68] and provided the most stringent upper limit 0.114 per year at 90% C.L. of CCSN burst rate throughout the Milky Way using ~ 21 years of data. For some surface detectors, due to the large cosmic-ray muon-induced backgrounds, the sensitivity is not as good as expected for underground detectors.

To be well prepared for the next nearby Galactic supernova explosion, an early warning system was established for many detectors and a world-wide collaborative Supernova Early Warning System (SNEWS)^[55] emerged. Three “P”s (prompt, positive, pointing) are required for a supernova early warning^[17].

Seven experiments (see Table 1.1) are the participants of SNEWS at present, including the Daya Bay Reactor Neutrino Experiment (see Chapter 2), which is a sub-kiloton-scale reactor neutrino detector with 100% sensitivity to supernova explosions up to 25 kpc. The design, implementation, testing, and installation of the online (real-time) supernova trigger system at Daya Bay, which is also integrated into SNEWS, is one of the studies in this thesis. The motivation is explained below.

- 1) Daya Bay has a unique feature among the current neutrino experiments that 8 detectors are deployed in three experimental halls which are more than 1 km apart from each other. This makes the the trigger system at Daya Bay naturally robust against cosmic-ray muon events, enabling a *prompt* online analysis and a good control of false alert rate (*positive*).
- 2) Daya Bay detector is sensitive to low energy (>0.7 MeV) neutrino events, enabling a full detection of the supernova neutrino spectrum and a supernova trigger with low energy threshold.
- 3) More detectors involved in SNEWS would provide a more *positive* (low false alert rate) early warning.
- 4) In terms of recognition of a Galactic supernova explosion, the “effective” sensitivity which is convoluted with the supernova rate distribution over distance is actually not much worse than the current large-volume detector.
- 5) Daya Bay in principle to benefit the *pointing* of a supernova explosion using the

IBD events combining all liquid scintillator detectors^[62].

To have a more sensitive search for supernova neutrino bursts, offline analysis is always performed. Using the Daya Bay data taken from 2011 December to 2013 November, the first offline data analysis for supernova neutrino bursts at Daya Bay was carried out and the result is given in this thesis. In addition, this analysis covers the whole data set before the online trigger system was installed at Daya Bay. The possible neutrino event bursts associated with SN2014J^[93] (the closest known type Ia supernova so far) and GW150914^[94] (the first discovered gravitational wave event) were also searched.

More details and results of the supernova burst neutrino study at Daya Bay can be seen in Chapter 3 and Chapter 4.

1.6.2 Supernova relic neutrinos

Since the supernova relic neutrino flux is supposed to be quite low, so far there is no experimental evidence for supernova relic neutrinos. Super-Kamiokande without neutron tagging^[95] and with neutron tagging^[96], KamLAND^[97], SNO^[98], and Borexino^[99] experiments have provided upper limits on the SRN flux based on their data. From the literature, the most stringent upper limits are summarized in Figure 1.14 including the KamLAND 2012 result^[97] and the recent Super-Kamiokande results^[95,96,100].

From Figure 1.14, the KamLAND (hollow square) result reflects the capability of liquid scintillator for SRN detection. The upper limit is currently constrained by the muon-induced spallation background and ends at about 17 MeV due to the fatal atmospheric neutrino neutral current (NC) background, which is the key issue for liquid scintillators in the high energy region.

The SK-I/II/III (solid triangle) result reflects the capability of water Cherenkov detectors without neutron tagging. The upper limit begins from about 17 MeV, due to the large accidental background and muon-induced background in the low energy region. But the water Cherenkov detector has a much better sensitivity in the high energy region than liquid scintillators due to the significant reduction of atmospheric NC background.

The SK-IV (five-pointed stars and solid circles) results reflect the capability of water Cherenkov detectors with neutron tagging^①, in which case the upper limit is given for the low energy region by means of the double-coincidence signature of the IBD events based on the neutron tagging technique. For the high energy region, a large amount of Michel

① Neutron tagging is actually realized by the gamma tagging. A gamma or gamma cascade will be emitted by the excited isotope capturing a neutron.

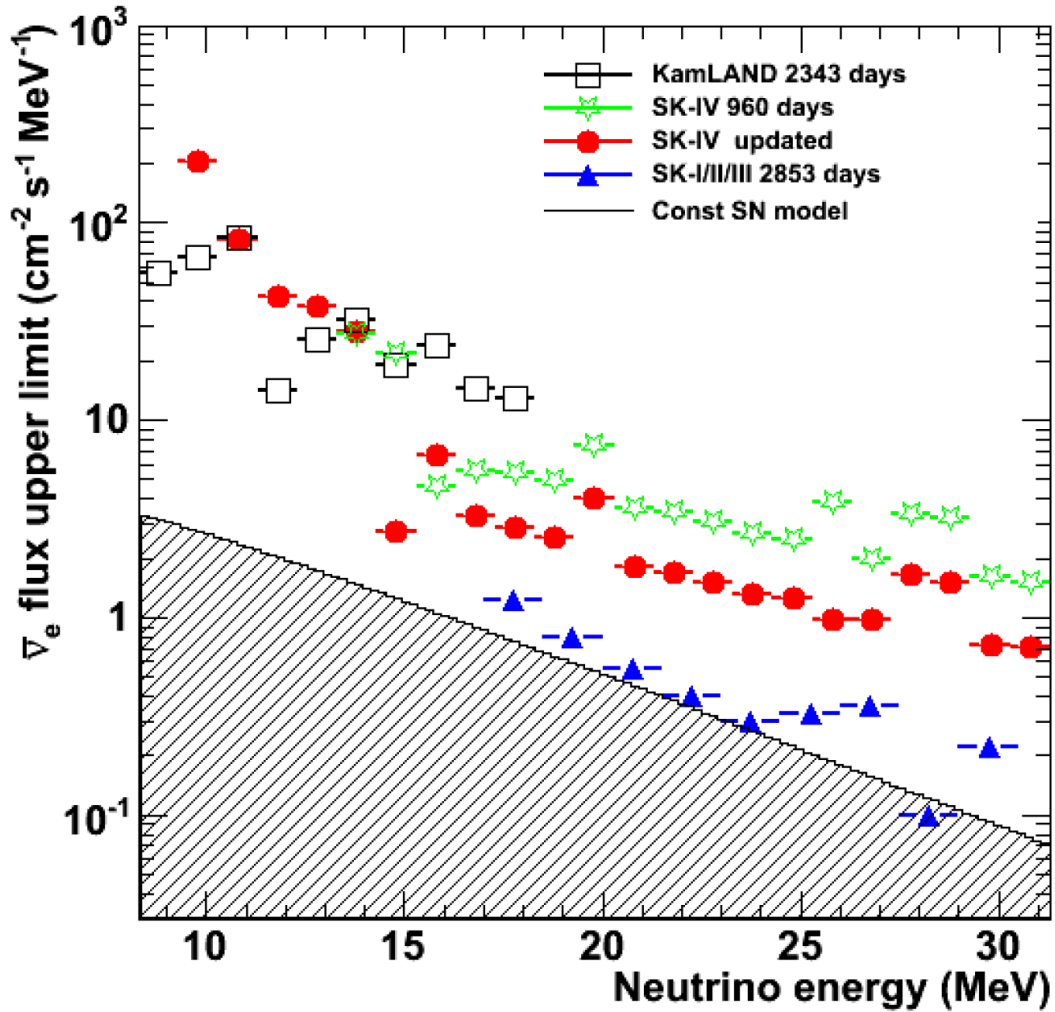


Figure 1.14 90% C.L. upper limits on SRN flux from KamLAND and Super-Kamiokande (SK) from Ref. [100]. Neutron tagging technique in water was used for SK-IV 960-day result and SK-IV updated (1890-day live time) result. SK-I/II/III 2853-day result is without neutron tagging. The SRN flux predicted by constant SN rate model is shown in the shaded area, which is for a comparison and roughly 2-3 times larger than the other recent SRN models.

electrons from the decays of invisible muons (below the Cherenkov threshold) produced by the atmospheric neutrino charged current (CC) interactions are the dominant background for water Cherenkov detectors. This background can be reduced significantly by the newly-developed neutron-tagging technique^[43] in the recent stage of the Super-K experiment with a forced trigger to search for a 2.2-MeV γ signal from neutron capture on hydrogen. The disadvantage at present for this technique is the low tagging efficiency $\sim 17\%$ but this would be increased to $\sim 90\%$ by a 0.2% gadolinium (Gd) compound-water solution^[43]. In the future, water doped with Gd is a proposed project in Super-Kamiokande^[81,101]. This will essentially increase the sensitivity of a water Cherenkov detector to discover the SRN.

In the future, except Gd-doped water Cherenkov detectors, large-volume liquid scintillator detectors with pulse shape discrimination for the scintillation light^[102–105] may contribute to this research. In liquid argon time projection chamber (LArTPC) detectors^[106–108], SRN events can be detected via neutrino CC and NC interactions with argon nuclei or extranuclear electrons. It is possible that the proposed DUNE experiment^[47] will have an opportunity to detect the SRN^[109] while more studies of the LArTPC detector response and cosmic-ray muon-induced backgrounds are essential and still underway.

To solve the key issues in the current SRN detection, the third study in this thesis is about the discovery potential for SRN in a proposed neutrino experiment^[110] at the world's most deepest China Jinping Underground Laboratory^[111]. For SRN detection, the lowest muon flux $\sim 2 \times 10^{-10}/\text{cm}^2/\text{s}$ and the lowest reactor neutrino flux $\sim 13 \times 10^5/\text{cm}^2/\text{s}$ at Jinping^[110] make it an ideal place across the world to do SRN study. Moreover, a kind of slow liquid scintillator would separate the scintillation and Cherenkov light via the time profile, allowing a significantly enhanced particle identification, thus suppressing the atmospheric neutrino CC and NC backgrounds dramatically. As a result, the search for SRN at Jinping would have a discovery potential for the entire range of 10-30 MeV golden window. The details are presented in Chapter 5.

Chapter 2 The Daya Bay Experiment

The Daya Bay Reactor Neutrino Experiment^[112] is described in this section, which is related to the first two studies in this thesis.

2.1 Experimental layout

Located in Shenzhen, Guangdong province, China, the Daya Bay experiment has three experimental halls (EH) with eight antineutrino detectors (AD), next to six reactor cores from three nuclear power plants (NPP)^[113]. In Figure 2.1, the layout of the experimental halls, antineutrino detectors, and the reactors are illustrated and labeled.

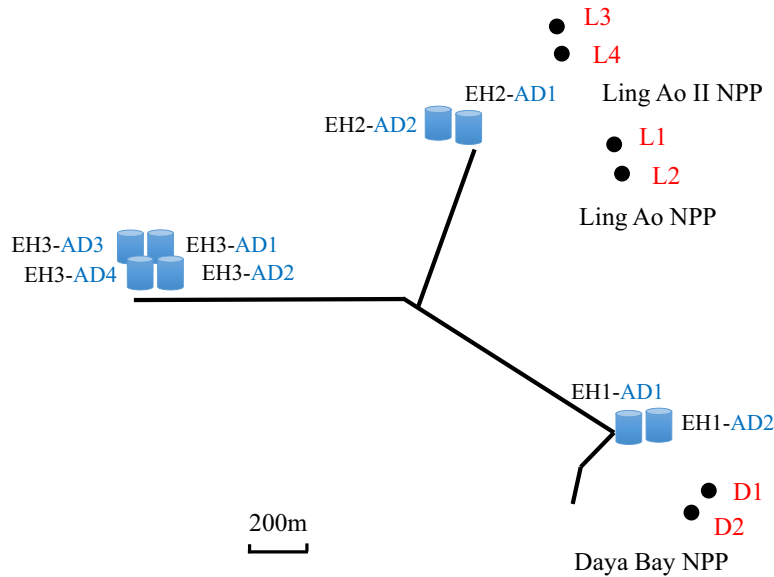


Figure 2.1 Experimental lay out of the detectors in Daya Bay and six reactor cores. The black line denotes the tunnels connecting the three experimental halls (EHs). Two near experimental halls (EH1 and EH2) each of which contains 2 antineutrino detectors (ADs) are located close to their nearest reactors – D1, D2 in Daya Bay NPP, and L1, L2, L3, L4 in Ling Ao and Ling Ao II NPPs. One far experimental hall (EH3) which contains 4 antineutrino detectors is located 1.52-1.93 km from all the six reactors.

The baselines^[114] from the geometric centers of the reactor cores to the detectors are

summarized in Table 2.1. Baselines are subtracted from the surveyed coordinates which were determined from a combined measurement of the station electronic theodolite and GPS. The precision is 18 mm.

Table 2.1 Baselines from the geometric centers of the reactor cores to the detectors. Unit: m

	D1	D2	L1	L2	L3	L4
EH1-AD1	362.38	371.76	903.47	817.16	1353.62	1265.32
EH1-AD2	357.94	368.41	903.35	816.90	1354.23	1265.89
EH2-AD1	1332.48	1358.15	467.57	489.58	557.58	499.21
EH2-AD2	1337.43	1362.88	472.97	495.35	558.71	501.07
EH3-AD1	1919.63	1894.34	1533.18	1533.63	1551.38	1524.94
EH3-AD2	1917.52	1891.98	1534.92	1535.03	1554.77	1528.05
EH3-AD3	1925.26	1899.86	1538.93	1539.47	1556.34	1530.08
EH3-AD4	1923.15	1897.51	1540.67	1540.87	1559.72	1533.18

2.2 Experimental overburden and muon flux

The experimental overburden is important in addition to the bird's-eye view, demonstrating the elevation profile of the mountain above the experimental halls. This is very relevant to the cosmic-ray muon flux, which is a main source of backgrounds in the neutrino detection. Figure 2.2 shows the elevation profile of the Daya Bay experiment from Ref. [115].

A summary of the muon flux, muon average energy, and overburden for each experimental hall^[116] is shown in Table 2.2.

Table 2.2 The muon flux and muon average energy from simulation. The uncertainty of the simulated flux is about 10%. M.w.e. stands for meter water equivalent.

EH	Overburden		Muon flux Hz/m ²	Average energy GeV
	m	m.w.e		
EH1	93	250	1.27	57
EH2	100	265	0.95	58
EH3	324	860	0.056	137

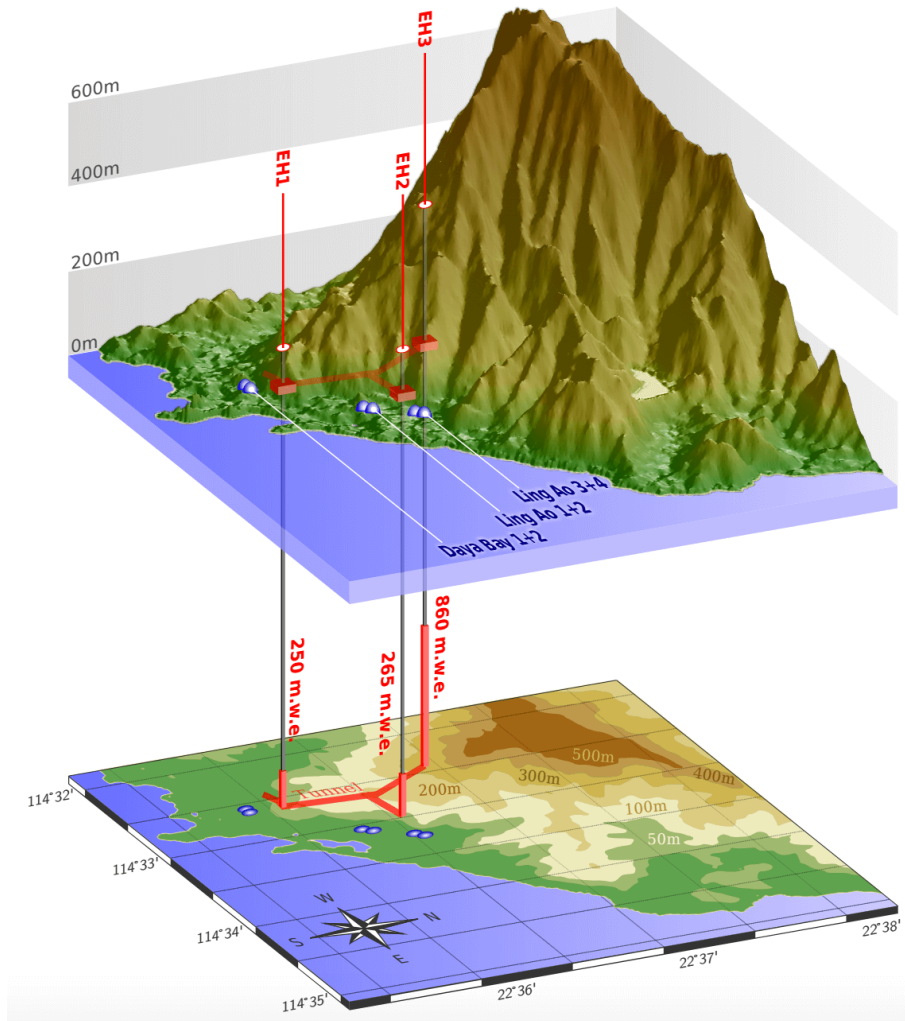


Figure 2.2 Experimental elevation profile of the mountain and the depth (meter water equivalent, m.w.e.) of each experimental hall. Figure by Marco Grassi, the Daya Bay Collaboration.

2.3 Antineutrino detector

The eight ADs^[113,114] were identically designed and assembled, each of which has a nested, coaxial cylindrical 3-zone structure as shown in Figure 2.3. An inner acrylic vessel (IAV) which is 3 m in both diameter and height, contains about 20 tons of gadolinium-doped (0.1% by mass) liquid scintillator (GdLS). An outer acrylic vessel (OAV) which is 4 m in both diameter and height contains about 22 tons of liquid scintillator (LS) originally to improve the tagging of γ 's that escape from the IAV. The stainless steel vessel (SSV) which is 5 m in both diameter and height contains about 36 tons of mineral oil (MO) to shield against the natural radiation from the PMTs and SSV. A total of 192 8-inch photomultiplier tubes (PMTs) were mounted in 24 columns and 8 rings on the inner surface of SSV, which were immersed in the MO. Top and bottom reflectors were

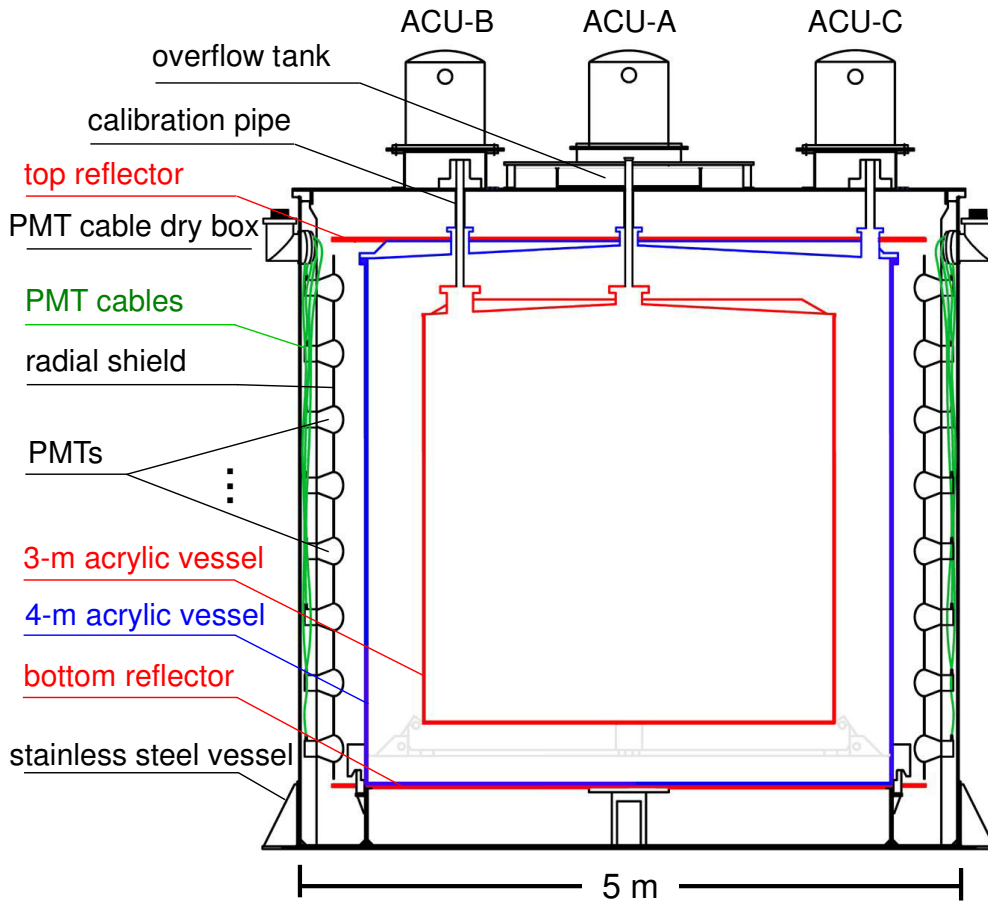


Figure 2.3 Schematic diagram of an antineutrino detector^[113].

installed to improve the light collection.

Three automated calibration units (ACUs) are installed on top of each AD, deploying light-emitting diodes (LEDs) and various radioactive sources (^{60}Co , ^{68}Ge , and $^{241}\text{Am-}^{13}\text{C}$) for the energy scale and position reconstruction calibration. They are at three different radial positions: the IAV center, the IAV edge, and the OAV edge.

All the ADs (2 in the near halls and 4 in the far hall) were submerged in a 2-zone water Cherenkov muon detector for the near (far) experimental hall, as shown in Figure 2.4. Tyvek sheeting was located, dividing the water pool into two zones, the inner water shields (IWS) and the outer water shields (OWS). There are 121 (160) and 167 (224) 8-inch PMTs mounted in IWS and OWS, respectively, in the near (far) experimental halls. A 4-layer resistive plate chamber (RPC) system covers the water pool, for further studies on the cosmic-ray muons. The water Cherenkov muon detector provides each AD with more than 2.5 m of shielding against the ambient radiation and muon-induced spallation products.

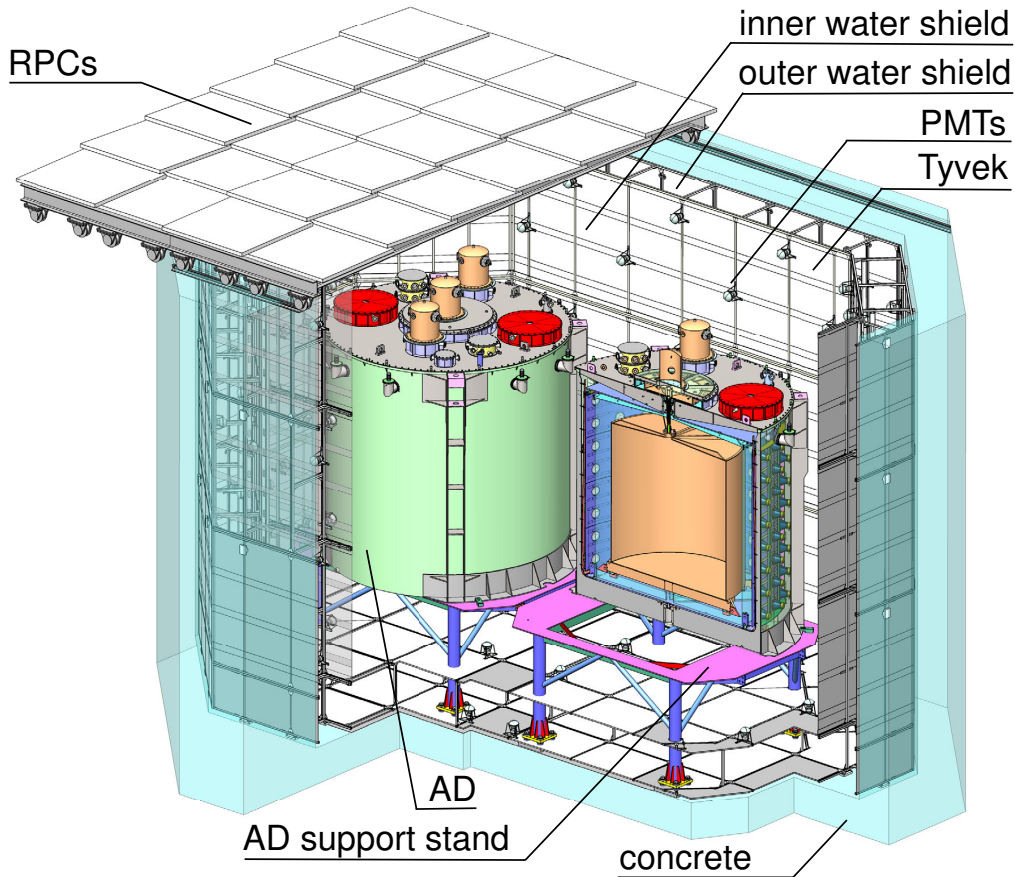


Figure 2.4 Diagram of the detector system in a near experimental hall^[113].

Any charged particle traversing the liquid scintillator would produce the scintillation photons via ionization depositing its kinetic energy; then to be collected by PMTs. Due to the different geometric acceptance for each PMT and the photon attenuation or scattering in the liquid scintillator, the detector response to the particle is generally non-uniform. Considering the Cherenkov light emission and scintillation quenching effect, there is fractional non-linearity effect in the conversion from deposited energy to number of scintillation photons. The scintillation photons hitting PMT will produce electrons via photo-electric effect, and the number of photoelectrons will be amplified with the high electric field in PMT, finally forming an electronic pulse. The energy and position of the charged particle will be reconstructed based on the PMTs' waveforms and the PMT hit pattern. The neutral particle, e.g., neutron or gamma, would produce scintillation photons by recoiling the protons or secondary electrons and positrons, respectively.

Electron antineutrinos are identified through IBD interactions ($\bar{\nu}_e + p \rightarrow e^+ + n$) in ADs at Daya Bay^[117–122]. Greater than 99% of the kinetic energy is carried away by e^+ . The e^+ deposits its kinetic energy within a few ns and then annihilates with an e^- . Two

back-to-back 0.511-MeV γ 's are produced in the annihilation and note that a few percent of the positrons annihilate in flight, with a sum of γ energy greater than 2×0.511 MeV. The neutron will be thermalized and then be captured by Gd (nGd) or H (nH)^①, emitting an approximately 8-MeV γ cascade or a single 2.2-MeV γ , respectively. The time from neutron production to capture is typically tens (hundreds) of μ s for nGd (nH). The time coincidence of the prompt positron and delayed neutron-capture signal provides a distinct IBD signature against the backgrounds.

2.4 Data taking

As seen in Figure 2.5, the data taking began on December 24, 2011, with two ADs in EH1, one in EH2, and three in EH3. It was paused on July 28, 2012, for the installation of one AD in EH2 and one AD in EH3. The data taking resumed with the eight ADs on October 19, 2012 and will continue until 2020. The data acquisition has an operational efficiency of better than 97% with occasional pauses for maintenance or power glitches and in the data acquisition time there is about 1% taken for the weekly calibration. The data quality is good with about 2% content of the problematic data.

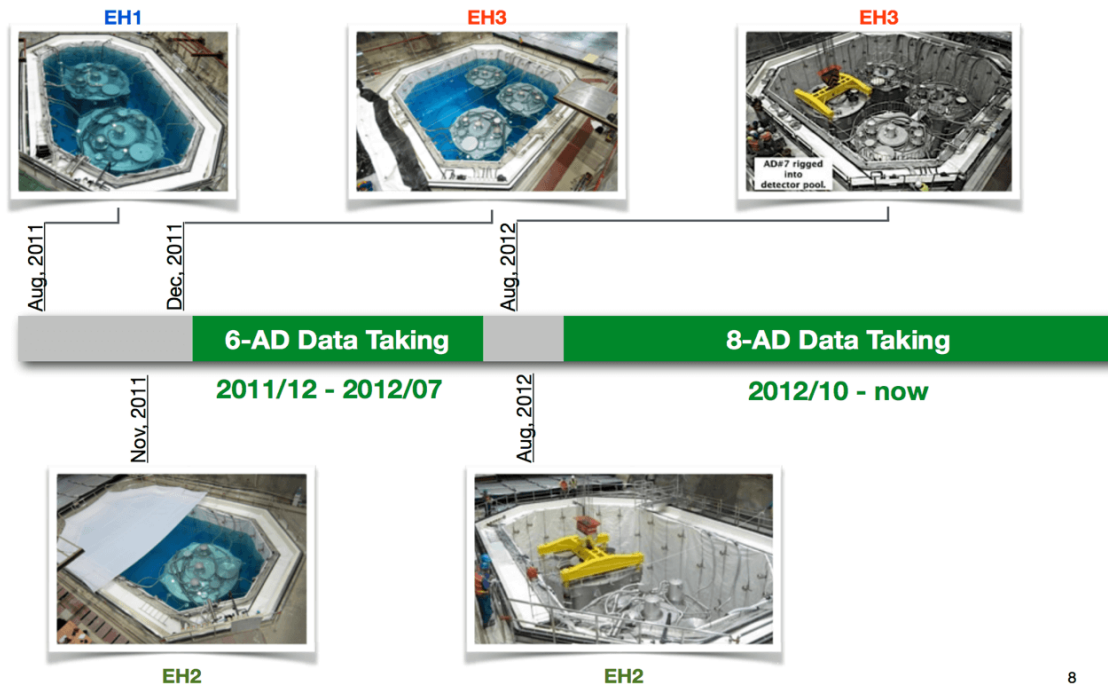


Figure 2.5 Important time nodes of the data taking and AD installation of the Daya Bay experiment.

^① Neutrons can be captured by other nuclei, e.g. carbon. In the GdLS volume, the nGd fraction is about 84% and the nH fraction is about 16%. In the LS volume, the nH fraction is about 96%.

2.5 Main scientific goals and results

The primary goal of the Daya Bay reactor neutrino experiment is to make a precise measurement of the neutrino mixing angle θ_{13} ^[117–122], using the neutrino flux from the six reactor cores, each producing a full thermal power of 2.9 GW. With 55 days of data, the Daya Bay experiment made the first discovery of the disappearance of reactor antineutrinos at 5.2σ excluding $\theta_{13} = 0$ ^[117]. The most precise measurement of θ_{13} across the world was also achieved by Daya Bay via neutron capture on gadolinium (nGd) ^[121]. With more statistics, the measurement of θ_{13} was improved as well as Δm_{ee}^2 (defined as $\cos^2\theta_{12}\Delta m_{31}^2 + \sin^2\theta_{12}\Delta m_{32}^2$, see Ref. [123]) via the shape analysis. In addition, an independent measurement of θ_{13} via neutron capture on hydrogen (nH) was published, validating the nGd result and providing the world’s most precise nH measurement ^[120,122].

An absolute measurement of the reactor neutrino flux and spectrum with high precision ^[124,125] was also done as Daya Bay has acquired the largest sample of reactor neutrino events in the world. A search for a light sterile neutrino ^[126–128] was also carried out recently. In addition, more exotic studies are being carried out, such as the decoherence effect ^[129], mass-varying neutrinos, Lorentz and CPT violation, and non-standard interactions (NSI), *etc.*

Chapter 3 Supernova trigger system at Daya Bay

As introduced in Chapter 1, an early warning of supernova explosions via neutrino signals is important in studying supernova dynamics as well as neutrino physics. Such a supernova online trigger system is strongly-motivated at Daya Bay (Section 1.6.1). This chapter will present the design, test, characterization, and sensitivity of the dedicated online supernova trigger system at Daya Bay, which has been integrated into the worldwide Supernova Early Warning System (SNEWS).

3.1 Overview of the supernova trigger system

A schematic diagram of the Daya Bay supernova trigger system is presented in Figure 3.1. The system is an entirely software framework, consisting of three sub-systems: online, offline, and monitoring.

3.1.1 Online sub-system

The online sub-system is embedded in the Event Flow Distributer (EFD, Figure 3.2) of the DAQ system^[130]. The EFD can access all the unpacked raw data, where a histogram filling program is running to provide the diagnostic histograms for the data quality monitoring. The reconstruction and selection of IBD events for each AD (see Section 3.2.1) are made along with the histogram filling program. The useful information of the selected IBD event is published to an information sharing (IS) server, which includes

- *Detector information*, including the experimental hall number and the AD number, e.g., EH1-AD1.
- *Run number*.
- *Trigger number*, which is exclusive for an event in a certain detector in a run.
- *Energy*.
- *Time stamp*, determined by GPS including two parts: second and nanosecond.
- *Vertex*, including three positions in x-, y-, z-axis.

Note that each IBD event includes a prompt sub-event and a delayed sub-event, with two sets of the last four items of information above.

Some programs are embedded in the IS server, in order to cache the IBD event information from all the ADs to a 2-min buffer. An online supernova trigger candidate

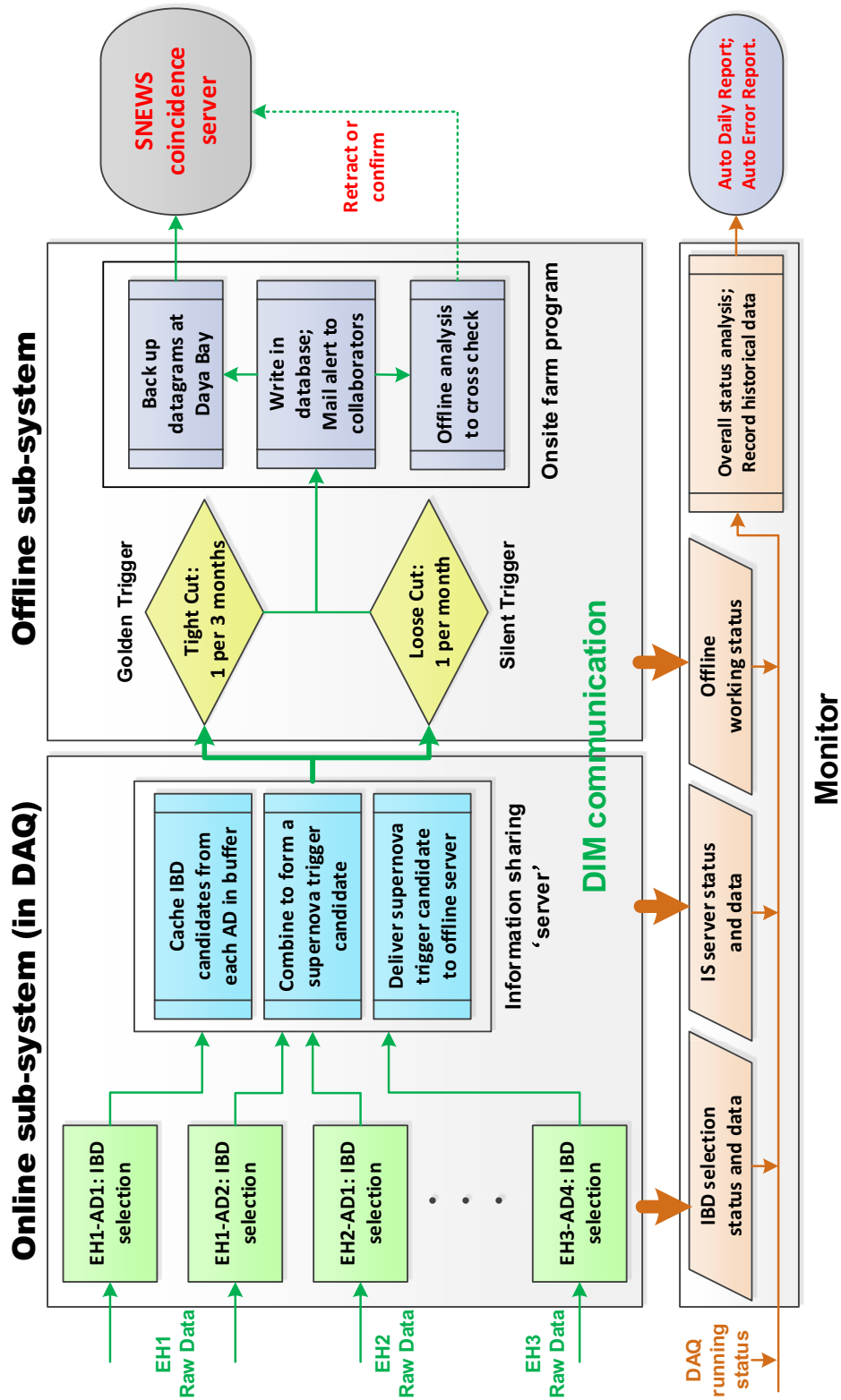
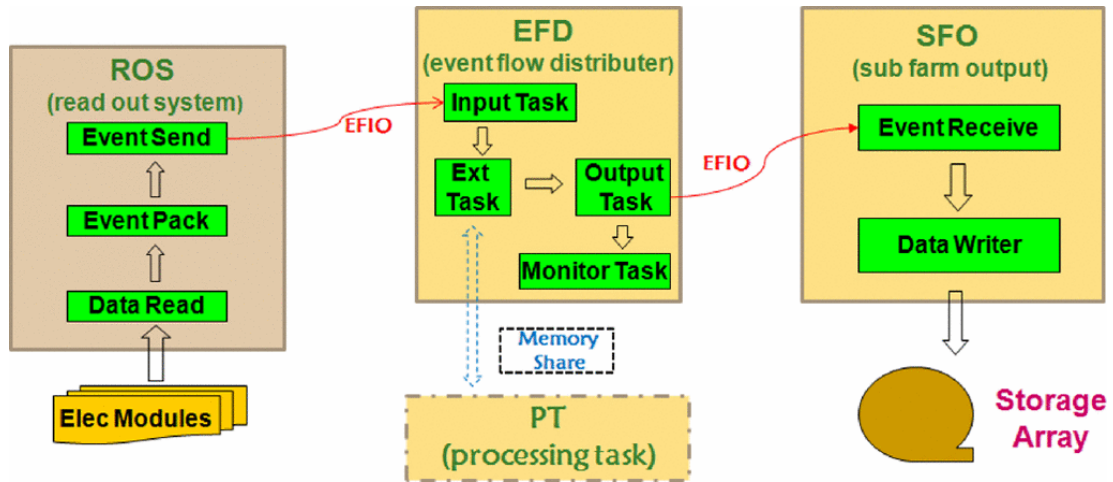


Figure 3.1 Schematic diagram of the Daya Bay supernova trigger system.

Figure 3.2 Diagram of the data flow components^[130].

will be formed every second based on the IBD events in the previous 10-second window, which can be represented as e.g., 1-2-3-4-5-6-7-8. The eight numbers denote the numbers of IBD events among EH1-AD1, EH1-AD2, ..., EH3-AD3, EH3-AD4 in the previous 10-second window. A Distributed Information Management (DIM, see Section 3.1.4) program will then deliver the online supernova trigger candidate to the offline sub-system, where a trigger decision will be made against the trigger threshold. IS here is one C++ package in the DAQ software^[130], serving to share information within the DAQ system.

3.1.2 Offline sub-system

The offline sub-system runs a couple of standalone programs on an onsite computer farm. It serves to make a trigger decision of the supernova trigger candidate released by the online sub-system (see Section 3.2.2). Supernova triggers are divided into two types: silent triggers (1 per month) and golden triggers (1 per 3 months). The golden trigger is more likely due to a real supernova neutrino burst and the silent trigger is to increase the acceptance of supernova neutrino bursts as well as to in principle serve as a heartbeat of the individual collaborative experiment to SNEWS.

Both types of the supernova triggers are written into a database which backs up the information of each supernova trigger. The database is also quite useful when testing the online supernova trigger system with a mass of supernova triggers at a quite low trigger threshold. The database function was implemented via *mysql*^①, and the database table structure is as follows in Figure 3.3. For each supernova trigger, there is a VID (valid-

① My S-Q-L (Structured Query Language), an open-source relational database management system^[131]

SUPERNOVA TRIGGER VID						
Field	Type	Collation	Attributes	Null	Default	extra description
SEQNO	int(11)			no	0	
TIMESTART	datetime			no	0000-00-00 00:00:00	Supernova Trigger start
TIMEEND	datetime			no	0000-00-00 00:00:00	Supernova Trigger end
SITEMASK	tinyint(4)			yes	NULL	
SIMMASK	tinyint(4)			yes	data	
SUBSITE	int(11)			yes	NULL	
TASK	int(11)			yes	NULL	0: SILENT / 1:GOLDEN / 2: TEST

SUPERNOVA TRIGGER						
Field	Type	Collation	Attributes	Null	Default	extra description
SEQNO	int(11)			no	0	
DETECTOR	tinyint(4)			no	0	offline convention
RUNNO	int(11)			yes	NULL	physics run number
FILENO	int(11)			yes	NULL	raw data file number of a certain physics run
pTRIGGERNO	int(11)			yes	NULL	prompt signal trigger number in the physics run
pENERGY	float			yes	NULL	prompt energy (MeV) after simple recon
pTIMESTAMP_sec	int(11)			yes	NULL	prompt trigger time second
pTIMESTAMP_nano	int(11)			yes	NULL	prompt trigger time nano second
pVERTEX_x	float			yes	NULL	prompt vertex x position (mm) after simple recon
pVERTEX_y	float			yes	NULL	prompt vertex y position (mm) after simple recon
pVERTEX_z	float			yes	NULL	prompt vertex z position (mm) after simple recon
dTRIGGERNO	int(11)			yes	NULL	delayed signal trigger number in the physics run
dENERGY	float			yes	NULL	delayed energy (MeV) after simple recon
dTIMESTAMP_sec	int(11)			yes	NULL	delayed trigger time second
dTIMESTAMP_nano	int(11)			yes	NULL	delayed trigger time nano second
dVERTEX_x	float			yes	NULL	delayed vertex x position (mm) after simple recon
dVERTEX_y	float			yes	NULL	delayed vertex y position (mm) after simple recon
dVERTEX_z	float			yes	NULL	delayed vertex z position (mm) after simple recon

Figure 3.3 The table structure of the database for a supernova trigger, including the VID table and the information table for each IBD event.

ity) table to describe the general information of this supernova trigger. ‘SITEMASK’, ‘SIMMASK’, and ‘SUBSITE’ are not used at present. ‘TASK’ represents if it is on a test status or a silent/golden trigger on an operational status. In general, a supernova trigger is composed of numerous IBD events. Each IBD event has an information table to list the useful information, with the primary key ‘SEQNO’ (sequence number) to indicate the order in a time sequence.

The datagram will be automatically sent to SNEWS through a dedicated SNEWS communication package with a secured OpenSSL certificate. Simultaneously, an email alert will be generated to Daya Bay collaborators, conveying the datagram of the supernova trigger. A screenshot of the datagram in an email alert is as below in Figure 3.4. The

```
Level: 2 (0=TEST 1=POSSIBLE 2=GOOD 3=CONFIRMED -1=RETRACTED)
Datetime[UTC]: 190816 225349 503740325 (DDMMYY HHMMSS NANO)
Datetime[Beijing]: 200816 65349 503740325 (DDMMYY HHMMSS NANO)
Significance: 0 (0=LOOSE 1=GOLDEN)
Duration: 10 seconds
Signal Number: 7
Distribution among ADs [AD1-AD8]: 0 4 1 0 1 0 0 1
Since last trigger: 31.737894 days
Since last golden trigger: 67.789780 days
```

Figure 3.4 The datagram in the email alert.

items are explained below.

- *Level*: the tag of the trigger to identify the status as described in the parenthesis.
- *Date time*: in format of ‘day-month-year hour-minute-second nanosecond’. The time of the first IBD event (prompt sub-event).
- *Significance*: the trigger type.
- *Duration*: the time from the first IBD event to the last one.
- *Signal number*: the number of the IBD events in this supernova trigger.
- *Distribution among ADs*: as indicated by the name.
- *Since last (golden) trigger*: time since the last silent (golden) trigger.

The trigger would be confirmed or retracted via an offline check, which is about 2 hours later due to the nominal KUP (keep up) reconstructed data^①.

^① The Daya Bay experiment has three types of data production: Keep up production (KUP), Physics production (PP), and Monte Carlo Production (MP). The first one is generally used for high-level data quality monitoring.

3.1.3 Monitoring sub-system

The real-time monitoring system is implemented as a set of distributed programs embedded into different parts of the supernova trigger system, communicating with the online and offline sub-systems as well as the existing DIM Name Server (DNS, see Section 3.1.4) in the Daya Bay Detector Control System (DCS)^[132]. The task of the monitoring system is to check the status of the IBD selection, the IS server, and the offline sub-system and provide necessary alerts. The communication among these portions is implemented via DIM (see Section 3.1.4).

In the DIM communication, a supernova (SN) *server* is registered along with the IS server to send a 1Hz heartbeat to each AD's IBD selection program to monitor the running status, to collect running information from the 8 ADs, and to reflect the IS server working status. If any AD stops data acquisition outside a tolerance of 2 minutes, a warning will be provided via email and the trigger system will ignore this 'dead' AD and keep operating with the other active ADs. If the 'dead' AD returns an active status (the 1 Hz heartbeat is sending to all the ADs uninterruptedly if the SN server is running), an email alert will also be sent.

A supernova (SN) *client* is instantiated in the offline sub-system and subscribed to the SN server, checking the IS server status and receiving real-time data from the 8 ADs. The SN client collects the experiment status from an existing DAQ Info server which is designed for ACU calibration. After checking the experimental status (Physics run or not) with the IS server status provided by the SN server, the SN client will automatically generate an error report via an email and sent it to experts if there is any abnormal state, e.g., the experiment is in a physics run while the IS server is not active. This ensures that the IS server of the online sub-system functions normally with the physics run.

As mentioned above, the SN client receives, records, and processes the real-time data, obtaining the IBD event rates from all the ADs, the number of unsolved errors or warnings, the number of supernova triggers, the network connection to SNEWS, and the working hours of the trigger system. A daily report is automatically generated to sent these information to the supernova trigger working group, serving as a daily check of the entire supernova trigger system.

3.1.4 Communication

The SN server or client mentioned above for communication is actually a virtual concept in DIM^[133] implemented in the C++ language. DIM is a light-weight and portable package for inter-process communication and the interaction mechanism of different components is shown in Figure 3.5.

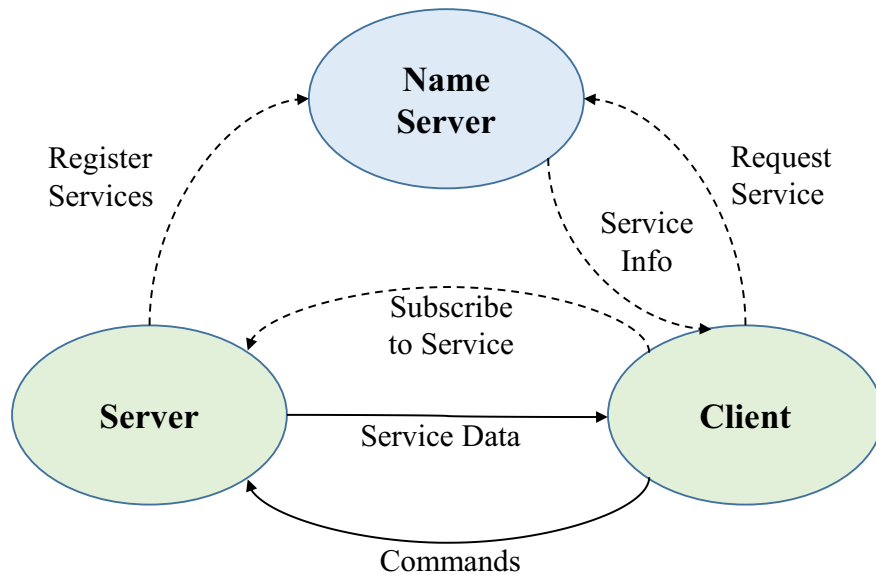


Figure 3.5 Schematic DIM component diagram.^[133]

3.2 Algorithm of the online trigger

The algorithm of the online supernova trigger is described in this section. The basic idea is to search for a simultaneous increase of IBD event rates from all the ADs within a 10-second window. The reconstruction and selection of IBD events will be introduced first, then followed by the determination of a supernova trigger. Finally, the packing of consecutive supernova triggers will be explained.

3.2.1 IBD event selection

The IBD events are reconstructed and then selected against the backgrounds, mainly including the accidental background, reactor neutrino background and the cosmic-ray muon-induced spallation (fast) neutron background.

3.2.1.1 Event time, energy and vertex

To achieve a *prompt* online supernova trigger and introduce negligible workload to the DAQ of the Daya Bay experiment, the event reconstruction is supposed to attain a balance between effectiveness and simplicity.

The trigger time of the IBD prompt sub-event is taken as the time of the IBD event. The GPS provides the trigger times with a <200 ns deviation from UTC time.

Energy is reconstructed following the formula below,

$$E = \frac{Q_{\text{Sum}}}{P \cdot S}, \quad (3-1)$$

where P is the average PMT gain, S the average energy scale, and Q_{Sum} the sum of ADC (analog to digital convertor) values from all the PMT channels with the baselines subtracted. The energy scale refers to the photoelectron (p.e.) yield by PMT photocathode from the collected scintillation photons per deposited energy in the liquid scintillator. The PMT gain here is a conversion factor from one photoelectron to the ADC value. P is calibrated by the PMT dark noise and the LED single photons. S is calibrated by the radioactive sources as well as the spallation neutrons detected in the liquid scintillator. P is typically equal to 19 [ADC value] per p.e. and S equal to 170 p.e./MeV. P has a slight upwards drift partially due to the change in temperature of the front-end electronics and S has a downward drift most likely due to the degradation of scintillation light transmission. The product of P and S is observed to vary less than 1% per year.

The vertex is reconstructed rapidly by a charge-weighting method utilizing the PMT charges and locations,

$$\vec{X} = \frac{\sum_{\text{PMT}} Q_{\text{PMT}} \cdot \vec{X}_{\text{PMT}}}{Q_{\text{Sum}}}, \quad (3-2)$$

where \vec{X} is the position vector, Q_{PMT} is the ADC value of a certain PMT, and Q_{Sum} is the sum of ADC values of all PMTs.

Primarily due to the geometric acceptance of the PMTs and the light attenuation in the detector, the vertex reconstruction has spatial non-uniformity. Compared with the energy reconstruction and vertex reconstruction above in Equation (3-1) and (3-2), the offline-level reconstruction of the Daya Bay experiment mainly has a position-dependent correction (a smooth position-dependent function or a pixel-wise template) to the reconstructed vertex,

then to the reconstructed energy based on the corrected vertex.

The bias of the the online reconstruction for the supernova trigger is evaluated to be about +10% and -40% for the energy and the prompt-delayed vertex distance, respectively. It should be stressed that the online reconstruction is adequately effective for the IBD event selection of the online supernova trigger.

3.2.1.2 IBD selection criteria

The Daya Bay selection procedures for the offline analysis have been described in publications^[117–122], the IBD event selection criteria for the supernova trigger were determined accordingly. Modifications were made in accordance with the scientific goal of the online supernova trigger rather than the reactor neutrino detection.

SN $\bar{\nu}_e$'s are identified by the ADs via the IBD interaction $\bar{\nu}_e + p \rightarrow e^+ + n$, then followed by the neutron capture $n + \text{H/Gd} \rightarrow \text{D/Gd} + \gamma/\gamma$'s, with an average capture time of $\sim 200/28 \mu\text{s}$. The IBD selection criteria for the online supernova trigger are described below in the sequence of usage.

AD trigger ADs are triggered based on a selection criterion written into the electronic trigger system. The time and charge information of each PMT channel are recorded to form a trigger when the number of PMTs (N_{PMT}) with charges above a threshold of ~ 0.25 photoelectron (p.e.) is at least 45 or the sum of PMT charges (Q_{Sum}) of all 192 PMTs is at least 65 p.e.. The trigger threshold corresponds to about 0.4 MeV and a 100% acceptance efficiency for IBD positrons with visible energy more than 0.7 MeV.

PMT flashes PMT flashes are caused by the spontaneous photon emission of the high-voltage divider of a PMT. Two quantities are defined to remove the PMT flashes. $Q_{\text{max}}/Q_{\text{Sum}}$ is the largest fraction of a single PMT's charge to the total charge in an AD. *Quadrant* is $Q_3/(Q_2 + Q_4)$ where Q_i is the total PMT charge in the i th azimuthal quadrant of an AD and Q_1 is roughly centered by the PMT with Q_{max} . The PMT flash event rate is comparable to the physics event rate in 5 - 10 MeV region (natural radioactivity dominant below the 5 MeV region) and the corresponding event energy is mainly 1-10 MeV but can be up to tens of MeV. The $Q_{\text{max}}/Q_{\text{Sum}}$ versus *Quadrant* plots for different event energy regions are shown in Figure 3.6. Note that the PMT flash event situations are diverse for different ADs due to the different numbers and locations of the actual “flasher” PMTs in an AD. But for all the ADs, the PMT flashes are in general suppressed significantly by

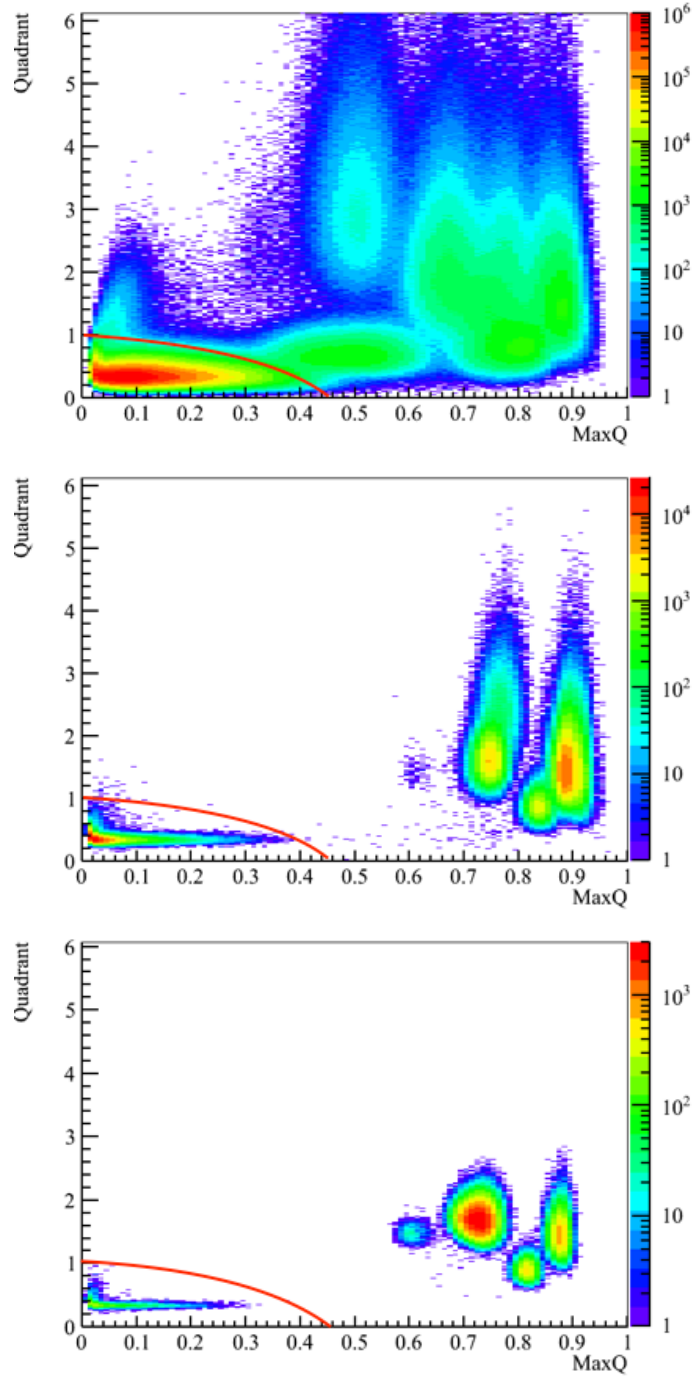


Figure 3.6 An example of $Quadrant$ in Y-axis vs. Q_{\max}/Q_{Sum} in X-axis^[134]. Top: event energy 1-5 MeV. Middle: event energy 5-12 MeV. Bottom: event energy >12 MeV. The left-bottom corner within a red curve is the physical signal region.

requiring $Q_{\max}/Q_{\text{Sum}} < 0.3$. $Quadrant$ is not used for the online supernova trigger but combined with Q_{\max}/Q_{Sum} to remove the PMT flashes in the offline analysis.

Muon vetoes Muon veto refers to a veto time window after a cosmogenic muon event, within which window all the AD events are excluded. This veto is to suppress the cosmogenic muon-induced background, e.g., spallation neutrons and isotopes. Spallation neutrons are produced instantaneously when a muon traverses the detector interacting with the carbon nuclei in the liquid scintillator; therefore a veto window of tens of nanoseconds is able to remove such spallation neutrons as long as the corresponding muon is identified. For the muon-induced isotopes, most of them are long-lived radioactive isotopes and ${}^9\text{Li}/{}^8\text{He}$ will have a β^- -neutron decay which can mimic the prompt and delayed subevents of an IBD event. The lifetimes of ${}^9\text{Li}$ and ${}^8\text{He}$ are 257.2 and 171.7 ms, respectively, which are both much longer than the 1-ms muon veto time window. Therefore, a second-timescale veto window is needed. Note that if a second-scale veto window is assigned after each muon event, there will be no live time for data acquisition at Daya Bay. Fortunately, most of the low energy cosmogenic muons are minimum ionizing in the liquid scintillator, producing quite few isotopes; therefore AD/shower muon events are defined to distinguish the minimum-ionizing muons and those that induce showers.

Since the energy of supernova burst neutrinos can be up to 50 MeV, an AD muon event for the online supernova trigger is defined to have a reconstructed energy greater than 50 MeV and the shower muon greater than 2.5 GeV. The veto window is 1 ms (1 s) for AD (shower) muons, which removes most of the muon spallations as well as any electronic follow-on triggers. Compared with the offline-level muon vetoes, the crucial difference is that the IWS, OWS, and RPC information are not utilized to provide a more effective identification of muon events, because they are not accessible to the current online supernova trigger system. The AD muon rates are about 20 Hz, 15 Hz, and 1 Hz for EH1, EH2, and EH3, respectively. The shower muon rates are about 0.3% and 0.5% of the total AD muon rates for EH1/2 and EH3, respectively. The IWS/OWS muon rates are about one order of magnitude larger.

Low-energy criterion All the AD events are required to have energy greater than 2 MeV for further processing by the online supernova trigger. This low-energy criterion is to remove the large amount of natural radioactivity signals originating from the ${}^{238}\text{U}/{}^{232}\text{Th}$ decay chains and ${}^{40}\text{K}$ decay in the liquid scintillator, PMT class, and SSV. Meanwhile, this criterion reduces the time consumption of data processing as it is applied before the substantive selection of the IBD events.

Coincidence time The average time difference between the prompt (e^+) and delayed (neutron capture) signals of an IBD event is about $30 \mu\text{s}$ and $200 \mu\text{s}$ for nGd and nH, respectively. A double-coincidence cut is applied to the IBD selection, which requires only two subevents within $[2, 400] \mu\text{s}$. The lower limit of coincidence time is determined by actual tests to remove the electronic noise.

Energy cuts The double coincidence events are selected from the data within $[2, 400] \mu\text{s}$ coincidence time after the PMT flash cut and the muon vetoes. The energy cuts are illustrated by the two red boxes in Figure 3.7. The double-coincidence events include reactor

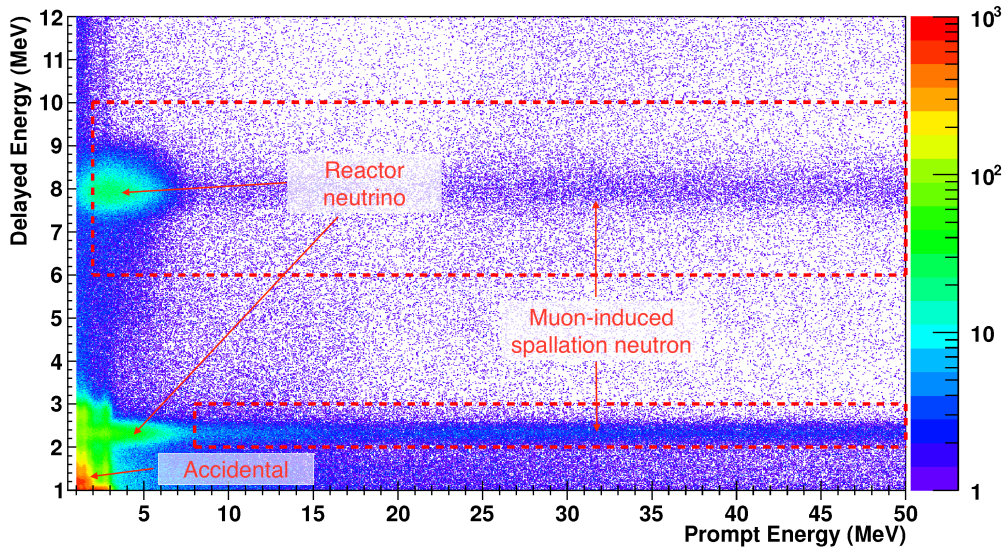


Figure 3.7 Prompt signal energy versus delayed signal energy of double-coincidence events. Two obvious bands with delayed energy $\sim 8 \text{ MeV}$ and $\sim 2.3 \text{ MeV}$ correspond to the IBD events with neutron captures on Gd and H. The three main backgrounds are indicated in this figure. Muon-induced spallation neutron background dominates the two horizontal neutron capture bands with prompt energy more than 8 MeV . Two clusters with prompt energy below 8 MeV correspond to the reactor neutrino background. The high event rates in the bottom-left corner correspond to the accidental background.

neutrino (real) IBD events and other IBD-like background events. Reactor neutrinos are mainly within $[1, 8] \text{ MeV}$ of the prompt energy and muon-induced fast neutrons dominate the higher prompt energy region. The areas of prompt energy and delayed energy below 3.5 MeV are dominated by the accidentals originating from natural radioactivity. Notice that all the double-coincidence events here are backgrounds for supernova $\bar{\nu}_e$ IBD signals, reasonably assuming there are no supernova burst neutrinos in the data.

The delayed signal from an IBD event is either a 2.2 MeV γ from nH, or an 8 MeV

γ 's cascade from nGd, so the delayed energy cut is 6-10 MeV for nGd or 2-3 MeV for nH. Considering the bias of the online energy reconstruction, to which the nH 2.2-MeV gamma selection is much more sensitive, 2-3 MeV (online reconstructed energy) actually corresponds to approximately 1.8-2.7 MeV (about $\pm 3\sigma$ of nH gamma peak). The prompt energy is required to be greater than 2 MeV and 8 MeV for the nH and the nGd events, respectively, in order to remove the majority of accidental backgrounds and possible electronic noise. The prompt energy is also required to be less than 50 MeV which is consistent with the AD muon definition.

Coincidence distance The prompt-delayed coincidence distance is required to be less than 800 mm which further suppresses the accidental background and electronic noise. Due to the bias of the online reconstruction of vertex, this value actually corresponds to about 1300 mm. With this cut, about 90% of the accidentals will be further rejected.

Table 3.1 IBD selection criteria for the online supernova trigger. All the values are based on the online event reconstruction. See text for more details.

	nH	nGd
AD trigger	$N_{\text{PMT}} \geq 45$ OR $Q_{\text{sum}} \geq 65$ p.e.	
20-cm PMT flash	$Q_{\text{max}}/Q_{\text{sum}} < 0.3$	
AD muon (μ_{AD})	> 50 MeV	
Showering AD muon (μ_{sh})	> 2.5 GeV	
AD muon veto	(0, 1) ms	
Shower muon veto	(0, 1) s	
Low energy	> 2 MeV	
coincidence time (t_c)	[2, 400] μs	
Prompt energy (E_p)	[8, 50] MeV	[2, 50] MeV
Delayed energy (E_d)	[2, 3] MeV	[6, 10] MeV
coincidence distance (d_c)	< 800 mm	

A summary of the IBD event selection criteria for the online supernova trigger is shown in Table 3.1. The online IBD event rates are measured to be 0.017, 0.013, and 0.0012 Hz per AD at EH1, EH2, and EH3, respectively. For these backgrounds, the reactor neutrinos contribute a fraction of 40%, 50%, and 66% at EH1, EH2 and EH3, respectively. The rest of the backgrounds are mainly muon-induced spallation neutrons. These single ADs' IBD event rates are basis of the false-alert control and the trigger

decision (see Section 3.2.2).

The flow chart of the IBD selection is shown in Figure 3.8.

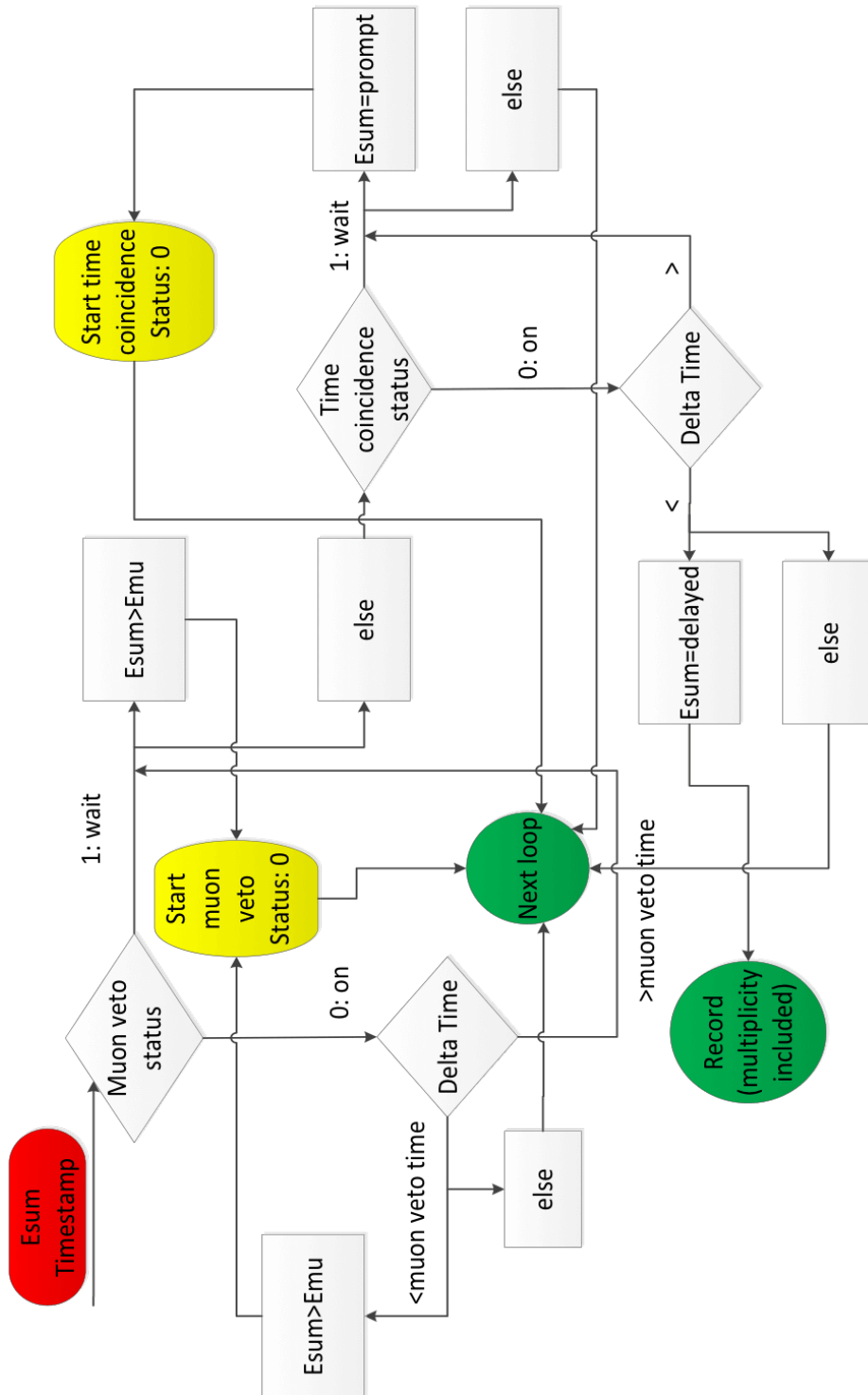


Figure 3.8 Flow chart of the IBD selection in the online supernova trigger system.

3.2.1.3 SN $\bar{\nu}_e$ IBD selection efficiency of a single AD

The IBD event selection efficiency of SN burst $\bar{\nu}_e$'s is evaluated from a Geant4-based simulation framework of the Daya Bay detectors. The spectrum of supernova burst neutrinos follows a quasi-thermal distribution as given in Equation (1-10), and is taken as the input of the simulation involving the IBD interaction. The two dominant parameters of the spectrum, $\langle E_{\bar{\nu}_e} \rangle$ and α are assumed to be 12 MeV and 2.6, respectively. The SN burst $\bar{\nu}_e$'s were separately simulated in the GdLS volume and LS volume of a Daya Bay AD. With the online event reconstruction and IBD selection criteria, the selected IBD events are shown in Figure 3.9. In the GdLS volume, the nGd fraction is about 84% and

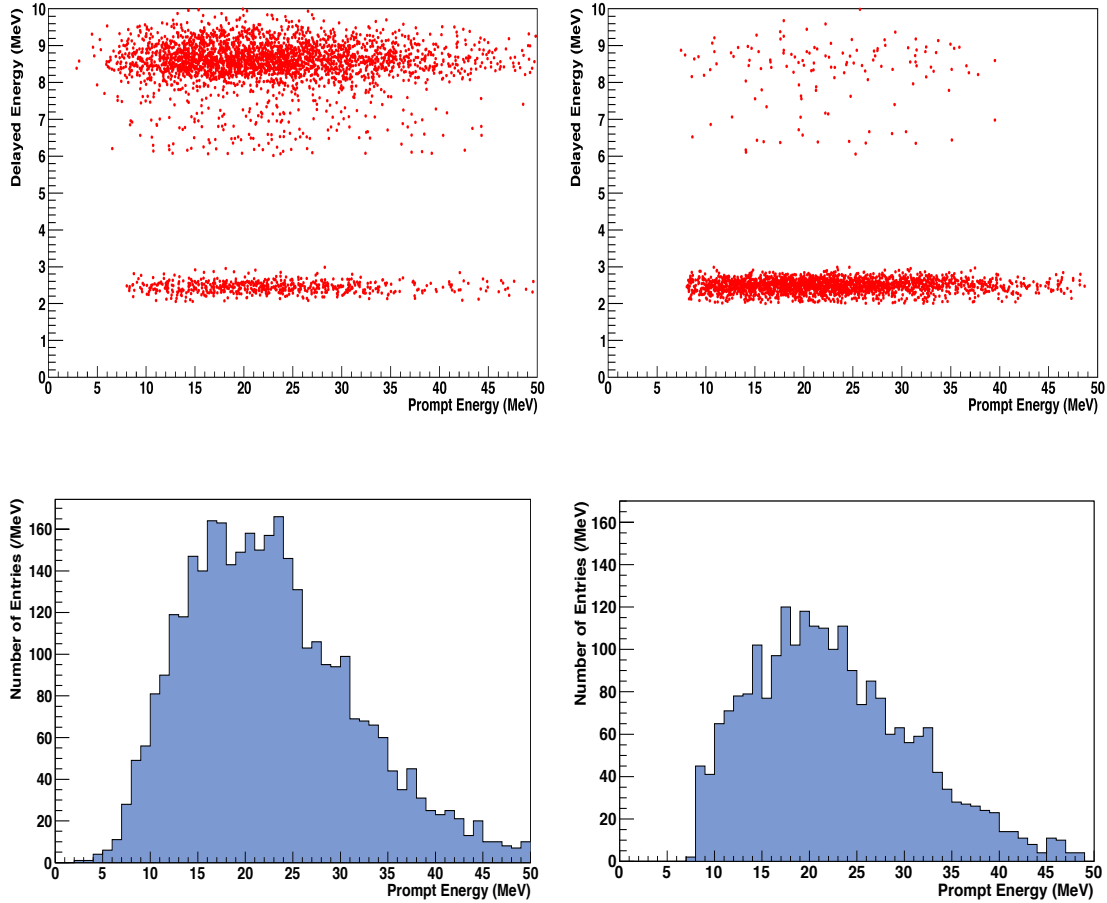


Figure 3.9 Energy distribution of the selected IBD events of supernova burst $\bar{\nu}_e$'s from a simulation. Top: 2-D plot of prompt signal energy vs. delayed signal energy. Bottom: Prompt signal energy spectrum. Left: Primary vertex in the Gd-LS volume. Right: Primary vertex in the LS volume.

the nH fraction is about 16%. That is why the GdLS 2-D plot has both obvious delayed nGd signals and nH signals. In the LS volume, the nH fraction is about 96%. Notice

that, the LS 2-D plot also has both the delayed nGd and nH signals; however, this is due to the fact that the neutron is produced in the LS volume but eventually captured in the GdLS volume. This can also happen for an IBD event in the GdLS volume. In liquid scintillators, neutron has a mean free path about 30-40 cm, and the neutron transport in-between the GdLS volume and the LS volume is called as the “spill-in” effect (net spill-in and spill-out). The spill-in effect is observed to be 105% in the GdLS volume. The spill-in effect from the MO can be ignored due to the absence of the prompt signals from the IBD positrons. Since the number of protons (target mass divided by the proton number density) and the selection efficiency in the acrylic vessels (IAV, OAV) are both one order of magnitude smaller than those in the LS volume, the simulation in acrylic vessels was ignored.

Table 3.2 The number of generated IBD events and selected IBD events in the simulation. Events were simulated in both the GdLS and LS volumes in EH1-AD1 and -AD2. The corresponding target mass and proton density are also listed.

	IBD triggered (N^{trig})	IBD selected (N^{sel})	Target mass [kg]	Proton density [10^{25} /kg]
AD1 GdLS	450	389	19941	7.169
AD1 LS	478	228	21574	7.116
AD2 GdLS	455	404	19967	7.169
AD2 LS	485	247	21520	7.116

The selection efficiency can be evaluated based on Table 3.2. The total selection efficiency (GdLS + LS) is calculated by,

$$\epsilon = \frac{N_{\text{LS}}^{\text{sel}} + N_{\text{GdLS}}^{\text{sel}} \cdot \omega}{N_{\text{LS}}^{\text{trig}} + N_{\text{GdLS}}^{\text{trig}} \cdot \omega}, \quad (3-3)$$

where ω is

$$\omega = \frac{N_{\text{LS}}^{\text{trig}}}{N_{\text{GdLS}}^{\text{trig}}} \cdot \frac{N_{\text{GdLS}}^{\text{proton}}}{N_{\text{LS}}^{\text{proton}}}. \quad (3-4)$$

The factor ω is to scale the IBD interactions in the GdLS volume according to the number of protons. As a result, the efficiencies were evaluated to be $66.2\% \pm 1.7\%$ and $69.1\% \pm 1.6\%$ for AD1 and AD2, respectively. The errors are statistical only.

The efficiencies of the selection criteria can also be estimated from the Daya Bay nGd analysis^[118] and nH analysis^[122], except for the selection efficiency of the prompt energy cut. Based on the energy spectrum of SN burst $\bar{\nu}_e$'s, the selection efficiency of the prompt energy cut is evaluated to be $\sim 96\%$ (93%) for the nH events (in GdLS volume) and $\sim 98\%$ for the nGd events. All the efficiencies of the selection criteria are summarized in Table 3.3, excluding the muon veto efficiency (ϵ_μ), multiplicity cut efficiency (ϵ_m), and PMT flash cut efficiency.

Table 3.3 Efficiencies of the IBD selection criteria. The spill-in/out effect of nH signals is included in the delayed energy efficiency. See text for more details.

	GdLS		LS
	nGd	nH	nH
Proton number (N_p)	1.43×10^{30}		1.54×10^{30}
neutron capture fraction	84%	16%	96%
Spill-in ($\epsilon_{\text{spill-in}}$)	105%	–	–
Prompt energy (ϵ_p)	98%	96%	93%
Delayed energy (ϵ_d)	92%	95%	67%
coincidence time (ϵ_t)	99%		85%
coincidence distance (ϵ_{dist})	99%		
Total selection efficiency	93%	89%	53%

Note that the spill-in effect of the nH signals is included in the delayed energy cut. The coincidence-time distribution of an IBD event is dominated by the neutron capture after the thermalization and it is same for nGd or nH signals in the GdLS volume. The coincidence-time efficiency is identical in a certain volume. The coincidence-distance distribution is dominated by the neutron thermalization primarily via hydrogen nuclei (free proton) recoiling, and is thus roughly the same for both the nGd and nH signals in both the GdLS and LS volumes. The coincidence-distance efficiencies are identical.

The total efficiency of the IBD selection criteria excluding the neutron capture fraction is also listed in Table 3.3. Considering the proton number and neutron capture fraction, the total efficiency of the IBD detection is 70% . Combining the estimates of the selection efficiency from the simulation and the existing analyses, 70% is used to be the nominal value.

The multiplicity cut (double-coincidence) is spontaneously applied with the

coincidence-time cut (coincidence time is T_c). The efficiency of the multiplicity cut (ϵ_m) is about 98%, which is mainly affected by the single event rate (R_s) and the muon event rate (R_μ). When $(R_s + R_\mu)T_c \ll 1$, $\epsilon_m \simeq e^{-R_s T_c} \cdot e^{-R_\mu T_c}$. In the online supernova trigger system at Daya Bay, R_s is about 20 Hz for all the ADs, and R_μ 's are about 20 Hz for EH1 and EH2, and 2 Hz for EH3, respectively.

The inefficiency of the PMT flash cut is negligible. The muon veto efficiencies depend on the muon flux, which are about 90%, 93%, and 99% for EH1, EH2, and EH3, respectively.

3.2.2 Supernova trigger

A supernova trigger is promptly determined each second by an analysis of the IBD events in the previous 10-second window from all the ADs. The occurrence rates of various distributions of IBD events among the ADs are predicted to set a false-alert rate, and to determine the trigger as well. The duration of 10-second window is determined according to the expected time scale of the supernova explosion. The packing of overlapping supernova triggers is also explained in this section.

3.2.2.1 Event combination and the prediction of occurrence rate

A trigger table is generated and initialized whenever the online supernova trigger system starts up. In the trigger table, all combinations of the IBD events in 8 ADs are listed and sorted according to their occurrence rates.

Table 3.4 Schematic trigger table for the online supernova trigger system. The combinations are sorted in a descending order of the occurrence rates.

EH1		EH2		EH3				Occurrence Rate (Hz)
AD1	AD2	AD1	AD2	AD1	AD2	AD3	AD4	($r_i \geq r_{i+1}$)
0	0	0	0	0	0	0	0	r_1
0	1	0	0	0	0	0	0	r_2
\vdots		\vdots				\vdots		\vdots
0	0	0	1	0	1	0	0	r_n
2	0	0	1	0	0	0	0	r_{n+1}
\vdots		\vdots				\vdots		\vdots

A schematic trigger table is shown in Table 3.4. All the combinations are enumerated

in each row with the numbers of IBD events in a 10-second window for each AD in each column. The number in the last column is the corresponding occurrence rate of the combination of IBD events in that row. The combinations are sorted in a descending order of the occurrence rate, i.e. $r_i \geq r_j$ when $i \leq j$. It is satisfied that P_i (occurrence probability) = r_i and $\sum_{i=1}^{\infty} r_i = 1$ (Hz) where i denotes the row number, as all the possible combinations are enumerated and the trigger decision is made every second. The derivation is shown below,

$$r_i \text{ (Hz)} = \frac{T \cdot n \cdot P_i}{T} = n \cdot P_i = P_i \text{ (if } n = 1/\text{second)},$$

where n is the frequency at which a trigger decision is made. Therefore,

$$\sum_{i=1}^{\infty} r_i = \sum_{i=1}^{\infty} P_i = 1.$$

The occurrence rates of all the combinations are predicted using the measured IBD event rates from all the ADs. It should be noted that the IBD events here are those selected online, and are all assumed to be backgrounds for the online supernova trigger. The possible supernova burst neutrinos were therefore ignored in the design of the trigger.

The IBD events from different ADs are uncorrelated (independent). However, in data there is some correlation observed between two ADs in the same experimental hall as indicated in Figure 3.10, where the pattern for uncorrelated IBD events should be like the right plot. It is now known that the correlation as shown in the left plot in Figure 3.10 is due to background contamination from the muon-induced spallations. For the online supernova trigger, this correlation is more significant than the offline analysis due to the absence of IWS and OWS information to identify the muon events. In the prediction of occurrence rates, the correlation between every two ADs in the same experimental hall was taken into account.

The prediction of the occurrence rate is presented below.

Firstly, for a single AD: The probability distribution of the number of IBD events (N_{IBD}) in a sliding 10-second window still follows a Poisson distribution, though the 10-second windows have an overlapping problem (see Figure 3.15). The derivation can be seen in Section A.1. The mean value of the Poisson distribution is $T_{\text{window}} \times R_{\text{IBD}}^i$, where R_{IBD}^i is the IBD event rate (Hz) of the i th AD.

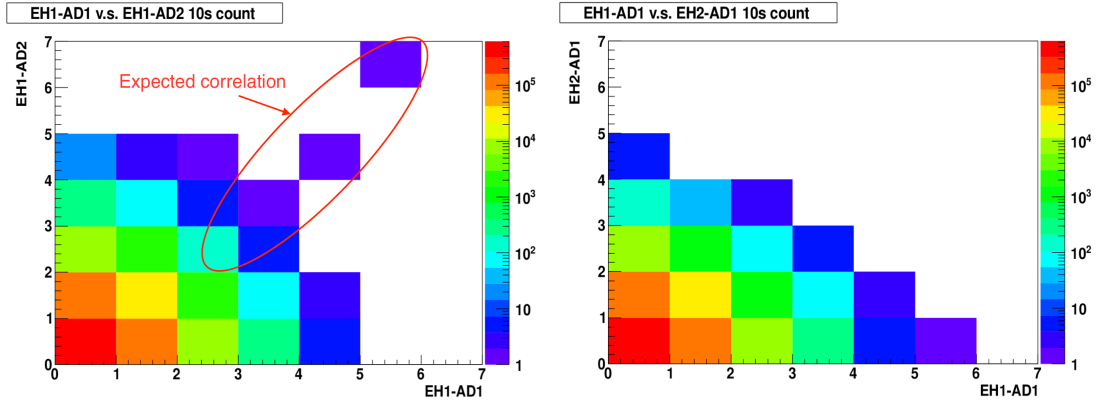


Figure 3.10 A demonstration of the correlation between two ADs. The numbers in X-axis/Y-axis mean the number of IBD events in 10-second windows. The Z-axis value (color palette) represents the count for a combination of the X- and Y-axis values. Left: Two ADs in EH1. Right: One AD in EH1 and one AD in EH2.

Secondly, for multiple ADs: The occurrence rate of a combination is predicted by a couple of mutually independent Poisson variables. Each AD owns a Poisson variable for the independent part and every two ADs share a Poisson variable for their correlated part. It is assumed the ADs from different experimental halls are mutually independent. The correlations between every two ADs in the same experimental hall are measured.

For the case of 2 ADs in the same experimental hall, for example, EH1 and EH2, three independent Poisson variables are needed: N_1 , N_2 , and N_{cor} . Then, the number of IBD events in a 10-second window for AD1 (AD2) is $N_{AD1} = N_1 + N_{cor}$ ($N_{AD2} = N_2 + N_{cor}$). The mean values of these Poisson variables can be derived from the measurements of $\mu(N_{AD1})$ ($\mu(N_{AD2})$), i.e. 10-s times $R_{IBD}^{AD1(AD2)}$ [Hz], and the covariance $Cov(N_{AD1}, N_{AD2})$:

$$\begin{aligned}
 \mu(N_{cor}) &= Cov(N_{cor}, N_{cor}) = Cov(N_1 + N_{cor}, N_2 + N_{cor}) \\
 &= Cov(N_{AD1}, N_{AD2}), \\
 \mu(N_1) &= \mu(N_{AD1}) - \mu(N_{cor}), \\
 \mu(N_2) &= \mu(N_{AD2}) - \mu(N_{cor}).
 \end{aligned} \tag{3-5}$$

Since each combination (N_{AD1}, N_{AD2}) can be decomposed into numerable combinations of (N_1, N_2, N_{cor}) , its probability can be calculated by summing over the numerable combinations:

$$\begin{aligned}
 P(N_{AD1}, N_{AD2}) \\
 = \sum_{i, j, k} \{ \text{Poisson}(\mu(N_{cor}), i) \cdot \text{Poisson}(\mu(N_1), j) \cdot \text{Poisson}(\mu(N_2), k) \},
 \end{aligned} \tag{3-6}$$

where i, j, k are non-negative integers which satisfy $i + j = N_{AD1}$, $i + k = N_{AD2}$.

For the case of 4 ADs in the same experimental hall, for example, EH3, assuming the correlation among three or four ADs can be ignored in comparison with the correlation between two ADs, 4 + 6 independent Poisson variables are needed: $N_1, N_2, N_3, N_4, N_{12}, N_{13}, N_{14}, N_{23}, N_{24}, N_{34}$, where N_i represents the independent part for the i th AD and N_{mn} represents the correlated part between the m th AD and the n th AD. The equations for deriving the occurrence rate in the case of 4 ADs are all listed below.

$$\begin{aligned}
 N_{AD1} &= N_1 + N_{12} + N_{13} + N_{14}, \\
 N_{AD2} &= N_2 + N_{12} + N_{23} + N_{24}, \\
 N_{AD3} &= N_3 + N_{13} + N_{23} + N_{34}, \\
 N_{AD4} &= N_4 + N_{14} + N_{24} + N_{34}.
 \end{aligned} \tag{3-7}$$

$$\begin{aligned}
 \mu(N_{mn}) &= Cov(N_{mn}, N_{mn}) = Cov(N_{ADm}, N_{ADn}), \\
 \mu(N_i) &= \mu(N_{ADi}) - \sum_{j \neq i}^{j \in \{1,2,3,4\}} \mu(N_{ij}) \quad (N_{ij} = N_{ji}),
 \end{aligned} \tag{3-8}$$

$$\text{where } \mu(N_{ADi}) = 10[\text{second}] \times R_{IBD}^{ADi}[\text{Hz}].$$

$$\begin{aligned}
 P(N_{AD1}, N_{AD2}, N_{AD3}, N_{AD4}) &= \sum_{k_{ij}} \left\{ \prod_{i \leq j}^{i,j \in \{1,2,3,4\}} \text{Poisson}(\mu(N_{ij}), k_{ij}) \right\} \quad (N_{ii} = N_i), \\
 N_{ADi} &= \sum_j^{j \in \{1,2,3,4\}} k_{ij} \quad (k_{ij} = k_{ji}).
 \end{aligned} \tag{3-9}$$

3.2.2.2 Measured IBD event rates and correlations

The measured IBD event rate for each AD (R_{IBD}^{ADi}) and the measured covariance of N_{IBD} in a 10-second window for every two ADs in the same experimental hall ($Cov(N_{ADm}, N_{ADn})$) are shown below in Table 3.5. Notice that the correlation coefficients between two ADs in EH3 are one order of magnitude smaller than those in EH1 or EH2 due to the smaller cosmic-ray muon flux. Consequently, the covariance values for EH3 in Table 3.5 are two orders of magnitude smaller than those in EH1 or EH2. The precision for the covariance measurement is $O(1e-6)$.

Table 3.5 The measured covariance of N_{IBD} in a 10-second window for every two ADs. The diagonal components are $10[\text{s}] \times R_{\text{IBD}}^{\text{AD}_i} [\text{Hz}]$. AD1 to AD8 denote EH1-AD1, EH1-AD2, ..., EH3-AD4. Only the lower triangular components are filled due to the symmetry of covariance matrix. All values are rounded to two digits in this table.

	EH1		EH2		EH3			
	AD1	AD2	AD3	AD4	AD5	AD6	AD7	AD8
AD1	0.16							
AD2	3.5e-4	0.16						
AD3	-	-	0.13					
AD4	-	-	2.4e-4	0.13				
AD5	-	-	-	-	0.013			
AD6	-	-	-	-	2.4e-6	0.013		
AD7	-	-	-	-	3.9e-6	6.5e-6	0.013	
AD8	-	-	-	-	2.6e-6	7.8e-6	1.9e-6	0.013

3.2.2.3 Uncertainty of the predicted occurrence rates of IBD event combinations

The uncertainty of the predicted occurrence rates (r_i) is statistically dominated, which is assigned to be

$$\sqrt{g} \cdot \sqrt{r_i(1-r_i)/N_{\text{window}}}. \quad (3-10)$$

The statistical uncertainty is in principle a binomial uncertainty with a factor g , which varies with different IBD event distributions among the ADs and on average is about 5. The errors originating from the measurements of the IBD event rates and the correlation between two ADs can be ignored. The complicated argument of the evaluation of this factor g is given in Section A.2, and a conservative estimation of the factor g is eventually adopted.

Based on the current estimation of the factor g , the predicted occurrence rates were compared with the measured ones using about 200-day data. From Figure 3.11, it was found that the predicted rates were well consistent with the measured ones, with $77\% < 1\sigma$, $97\% < 2\sigma$, and $99\% < 3\sigma$. This validates the prediction as well as the estimation of uncertainty. The statistical uncertainty is found to be dominated compared with the systematic uncertainty, for example, from the reactor power off, and is rationally

Measured Rate	Unertainty	Predicted Rate	Deviation(# σ)
0.63131593	0.00037725	0.63101173	0.806368183
0.09544838	0.00021058	0.09568180	1.108450487
0.09493778	0.00021007	0.09500536	0.321706594
0.07548105	0.00018932	0.07576684	1.509567536
0.01463010	0.00007685	0.01466437	0.445933637
0.01153820	0.00006835	0.01148871	0.724067301
0.01142295	0.00006801	0.01140748	0.227466549
0.00803414	0.00006398	0.00799168	0.663647575
0.00799862	0.00006383	0.00798879	0.153992736
0.00783317	0.00006317	0.00782250	0.168899785
0.00736947	0.00006129	0.00725423	1.880166087
0.00716079	0.00006043	0.00715202	0.145125903
0.00461789	0.00004858	0.00454874	1.423312596
0.00176542	0.00002321	0.00176078	0.19989536
0.00121276	0.00002228	0.00121136	0.062836625
0.00119820	0.00002214	0.00120323	0.227190605
0.00118940	0.00002206	0.00121180	1.015412511
0.00118659	0.00002203	0.00117776	0.400817068
0.00118414	0.00002201	0.00120280	0.847796456
0.00117332	0.00002191	0.00118614	0.585120949
0.00114171	0.00002161	0.00112339	0.847755669
0.00111364	0.00002135	0.00113139	0.831381733
0.00097069	0.00001993	0.00095958	0.557451079

Figure 3.11 A sample of the measured occurrence rates and the predicted occurrence rates. The deviation (multiple of σ) between the measurement and prediction is quantified by the estimated statistical uncertainty (σ). In the column of ‘Deviation’, the values between 1 and 2 are highlighted by yellow. The values between 2 and 3 (greater than 3) are highlighted by green (white), but do not show up in this figure due to the low frequency.

conservatively-estimated as expected.

The dominant systematic uncertainty for the predicted occurrence rates results from the reactor power-on and -off, which has a significant impact on R_{IBD} . From Figure 3.12, the IBD rate in θ_{13} analysis is observed to be quite consistent with the flux of reactor neutrinos, which is also an indication of the status (on or off) of reactors. The measured IBD event rate from the online supernova trigger is also plotted in Figure 3.13, which has a consistent variation with the status of the reactors in comparison with Figure 3.12. This is also a validation of the effective IBD selection in the online supernova trigger system. The contribution from nH signals in Figure 3.13 is insensitive to the reactor flux because of a prompt energy cut (>8 MeV). In addition, based on the deficit of the IBD event rate, the reactor neutrino contribution to our selected IBD events can be estimated.

To estimate the impact of reactor power-on and -off on the predicted occurrence rates, an upper/lower limit method was used. The upper/lower limit corresponds to the

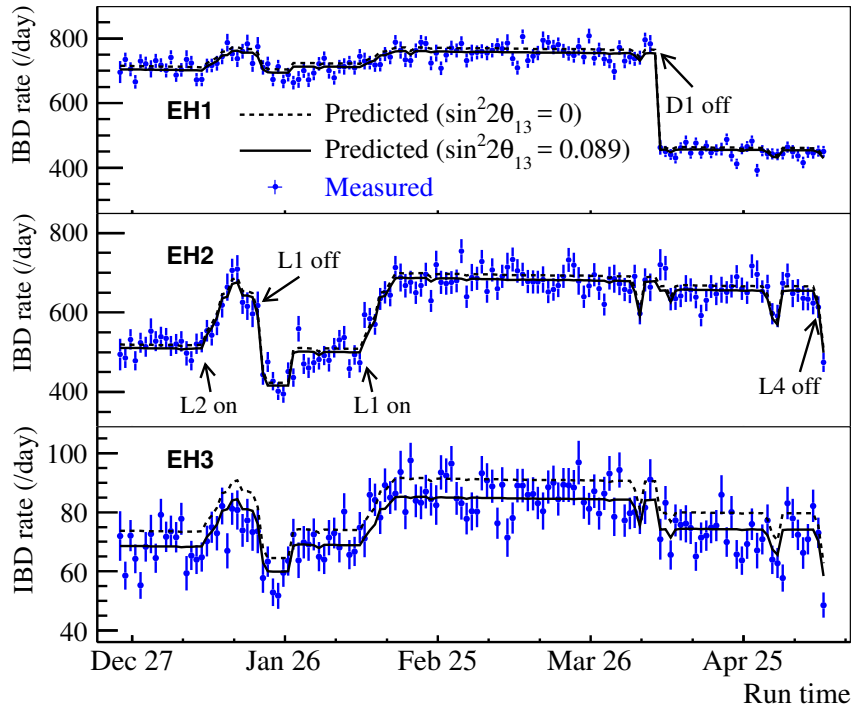


Figure 3.12 The measured IBD event rates per day in the three experimental halls are plotted along with time^[118]. The predicted line is based on reactor neutrino flux with two assumptions of θ_{13} . The reactor power-on and -off are indicated.

maximum/minimum reactor neutrino flux, and then the average difference between the upper and lower limits of the occurrence rates can be obtained. As a result, for 1 year of data taking, the occurrence rate of 1 per month (typical value of trigger rate threshold) has a $\sim 25\%$ ($\pm_{23\%}^{28\%}$) systematic uncertainty and a $\sim 75\%$ statistical uncertainty. For a long period, the statistical uncertainty decreases while the systematic uncertainty due to the reactor power-on and -off will be averaged out since the cycle of reactor refueling is about 1-1.5 years. As a consequence, the systematic uncertainty from the reactor power-on and -off can be ignored.

3.2.2.4 Trigger decision

The supernova trigger is determined against a false-alert rate threshold, which is set to be 1 per month or 1 per 3 months for the Daya Bay supernova trigger system.

The trigger table is invoked by the online trigger system to control the false-alert rate. Given a false-alert rate threshold P_{DYB} [Hz], the k th row would be found in the trigger

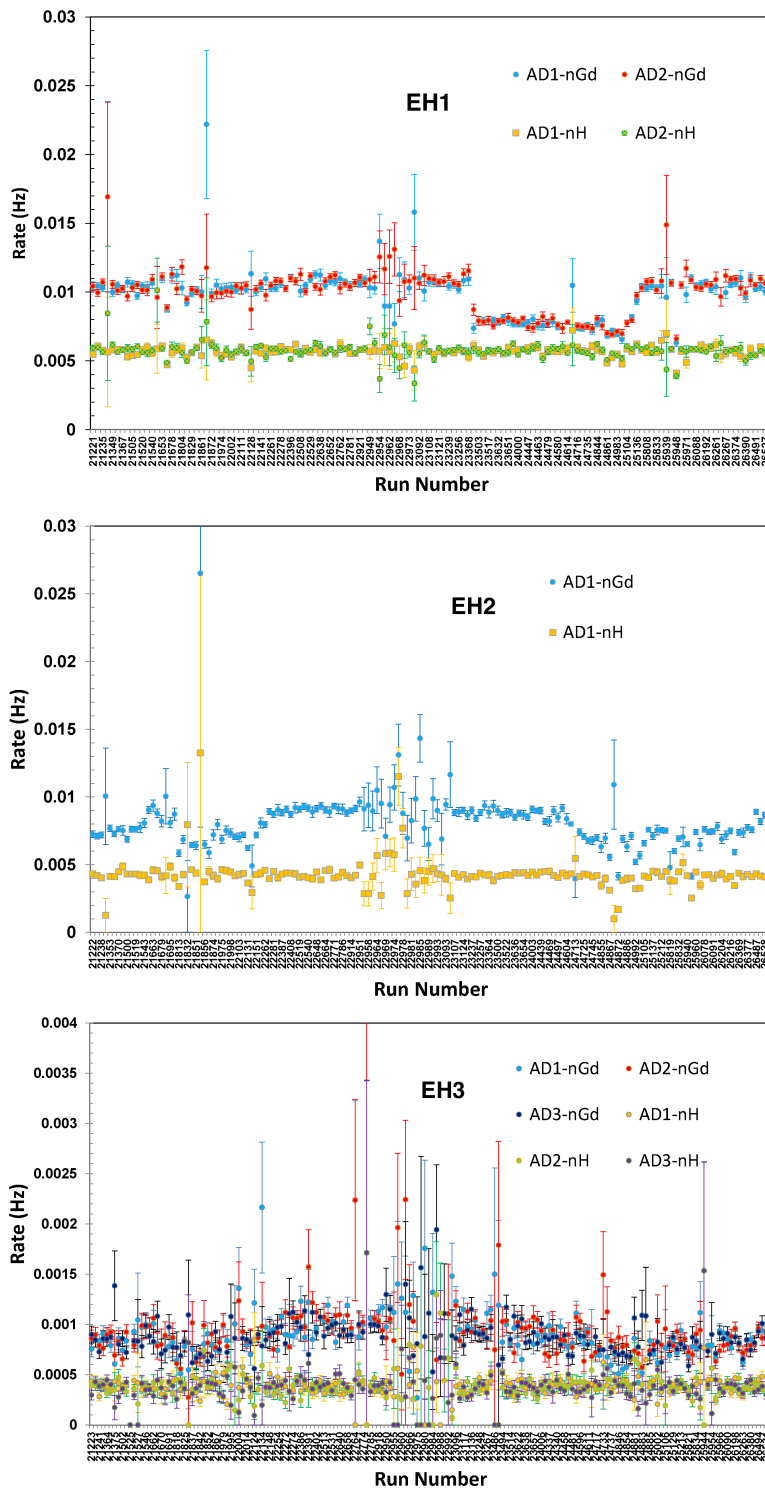


Figure 3.13 The measured IBD event rates from the online supernova trigger system in the three experimental halls are plotted with each run. The data were taken in the period of 6-AD configuration. The nH and nGd contributions are separated. The error bars are statistical for each physics run.

table that satisfies

$$\sum_{i=k+1}^{\infty} r_i \leq P_{\text{DYB}} \quad \text{and} \quad \sum_{i=k}^{\infty} r_i \geq P_{\text{DYB}}. \quad (3-11)$$

The rule for making a trigger decision is thus as follows – the combinations below the k th row are regarded as the supernova triggers. The trigger table with a trigger cut (the k th row) is illustrated in Figure 3.14.

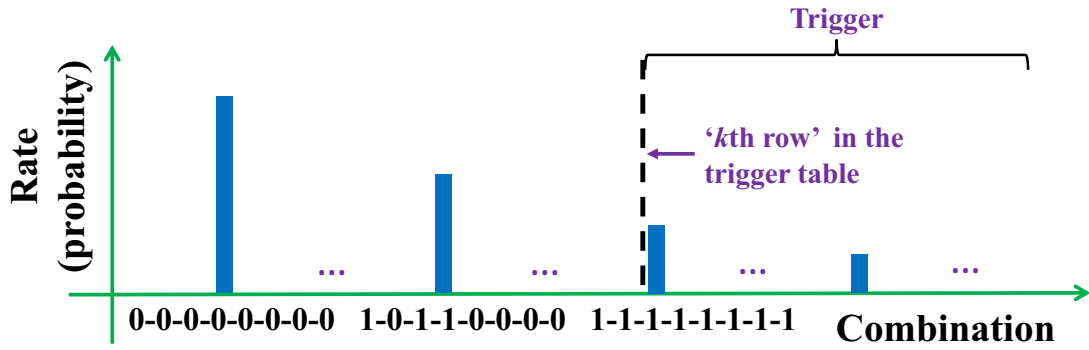


Figure 3.14 Illustration of the trigger decision using the trigger table given a false-alert rate threshold. All the combinations are enumerated in a descending order of their occurrence rates (trigger table). The trigger cut is represented by the dashed line (the k th row) which is determined based on the false-alert rate threshold. Sum of the occurrence rates of the triggers is just less than or equal to the required false-alert rate threshold.

In order to suppress the unexpected triggers, e.g., electronic noise, in a single AD or a single experimental hall, the goodness of the uniformity of the IBD events distributed in multiple ADs and different EHs were checked. A χ^2 based on the Poisson likelihood profile ratio was utilized to set a cut with negligible loss of sensitivity to supernova explosions,

$$\chi^2 = 2 \sum_{i=1}^N \begin{cases} \left(n_i \log \frac{n_i}{\lambda_i} + \lambda_i - n_i \right), & \text{if } n_i \neq 0, \\ \lambda_i, & \text{if } n_i = 0. \end{cases} \quad (3-12)$$

where

- 1) Case for multiple ADs: N is the number of ADs, equal to 6 or 8. n_i is the number of IBD events from the i th AD. $\lambda_i = \frac{\sum_{i=1}^N n_i}{N}$ for any i . The χ^2 is required to be less than 18.475 (99% C.L., n.d.f = 7, N=8).

- 2) Case for three EHs: N is the number of EHs, equal to 3. n_i is the number of IBD events from all the ADs in the i th EH. $\lambda_i = N_i^{\text{AD}} \cdot \frac{\sum_{i=1}^{N^{\text{AD}}} n_i}{N^{\text{AD}}}$. N_i^{AD} (N_i^{AD}) is the number of ADs from all EHs (the i th EH). The χ^2 is required to be less than 5.991 (95% C.L., n.d.f = 2).
- 3) Case for far and near site: N is 2. n_i is the number of IBD events from the near site ADs (4 ADs in EH1 and EH2) or the far site ADs (4 ADs in EH3). $\lambda = 0.5 \sum_{i=1}^N n_i$. The χ^2 is required to be less than 3.841 (95% C.L., n.d.f = 1).

The inefficiency introduced by the uniformity cut is negligible since the IBD events from supernova burst neutrinos corresponding to the most probable combinations are uniformly distributed among the ADs. This is validated in the computation of the detection probability (see Section 3.2.3).

3.2.2.5 Packing consecutive supernova triggers

The supernova trigger determinations are made second-by-second by analyses of the IBD events from all the ADs in the previous 10-second windows. Due to the strong correlation of the determinations from adjacent overlapping windows, e.g., A and B in Figure 3.15, it is very likely that a sequence of triggers consecutively occur at a time. To

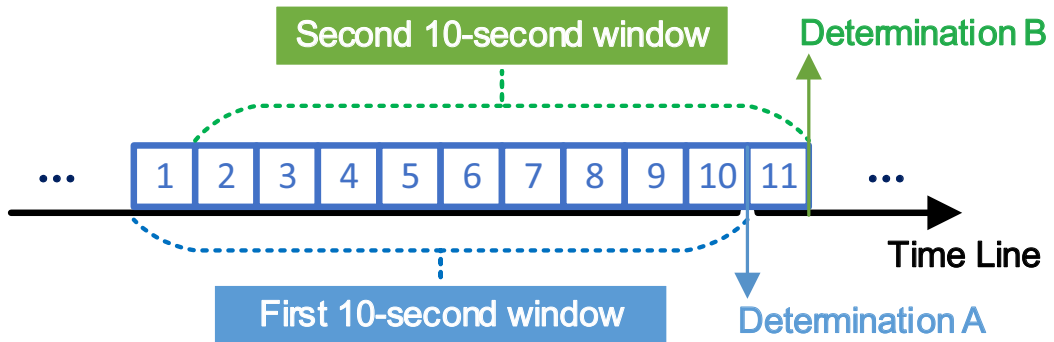


Figure 3.15 Illustration of two consecutive supernova trigger determinations in two overlapping 10-second windows.

avoid a redundant information to be sent out and to include as much as information once a supernova trigger occurs, such triggers are packed as a single supernova trigger and a single datagram for SNEWS. In the datagram (see Figure 3.4), the information of all the IBD events in these consecutive supernova triggers is extracted and summarized.

The real false-alert rate, P_{real} [Hz], must be converted to a Daya Bay trigger threshold P_{DYB} [Hz] as a consequence of the packing of consecutive supernova triggers. Then a trigger can be determined following the rule as explained in Section 3.2.2.4. The relation between P_{DYB} and P_{real} can be expressed as:

$$P_{\text{real}} = \frac{P_{\text{DYB}}}{\bar{N}}, \quad (3-13)$$

where \bar{N} is the average number of consecutive supernova triggers. Because it is difficult to analytically calculate and expensive to numerically simulate \bar{N} with a small ($\lesssim 10^{-6}$) P_{DYB} , an upper limit was estimated in Section A.3.

For the actual tests and operation, \bar{N} is set to be 3 based on the lower limit 1 and the upper limit 5.5. The value of \bar{N} can be tuned according to more observations in the operation. Up to now, $\bar{N} = 3$ has been effectively working as intended.

3.2.3 Detection probability

As shown in Equation (1-14), the expected number of SN burst $\bar{\nu}_e$ events can be determined by

$$N = 300 \times \epsilon_d \times \frac{L_{\bar{\nu}_e}}{5 \times 10^{52} \text{ erg}} \times \left(\frac{10 \text{ kpc}}{D}\right)^2 \times \left(\frac{\text{Mass}}{1 \text{ kt}}\right), \quad (3-14)$$

where D is the SN explosion distance to the Earth, $L_{\bar{\nu}_e}$ is the luminosity (expected to be 5×10^{52} erg) of emitted electron-antineutrinos, and Mass is the target mass of a single AD, which is about 42 ton. The total detection efficiencies (ϵ_d 's) are 62%, 64%, and 68% for EH1, EH2, and EH3, respectively. The number of expected SN $\bar{\nu}_e$ events at Daya Bay is expressed as,

$$\begin{aligned} N_1^{\text{AD}} &= 7.8 \times \left(\frac{10 \text{ kpc}}{D}\right)^2, \\ N_2^{\text{AD}} &= 8.0 \times \left(\frac{10 \text{ kpc}}{D}\right)^2, \\ N_3^{\text{AD}} &= 8.6 \times \left(\frac{10 \text{ kpc}}{D}\right)^2. \end{aligned} \quad (3-15)$$

where N_i^{AD} is the single AD's expected number of SN $\bar{\nu}_e$ events in a 10-second window in the EH*i*.

Based on N_i^{AD} shown in Equation (3-15), assuming the SN signals in different ADs are fully uncorrelated, the probability of each combination (of the number of IBD events

from all the ADs) from SN signals can be calculated.

The detection probability of a supernova explosion here is defined as the sum of the probabilities of the combinations over the trigger threshold. Three key quantities in the calculation of the detection probability is R_{IBD} (to determine the background trigger table), D (to determine the number of SN signals), and a false-alert rate threshold (to determine the trigger cut). Figure 3.16 shows the detection probability as a function of the SN explosion distance to the Earth under the condition of a false-alert rate threshold. Since the most distant edge of the Milky Way is about 24 kpc, the online supernova trigger system at Daya Bay is fully sensitive to the Galactic SN explosions.

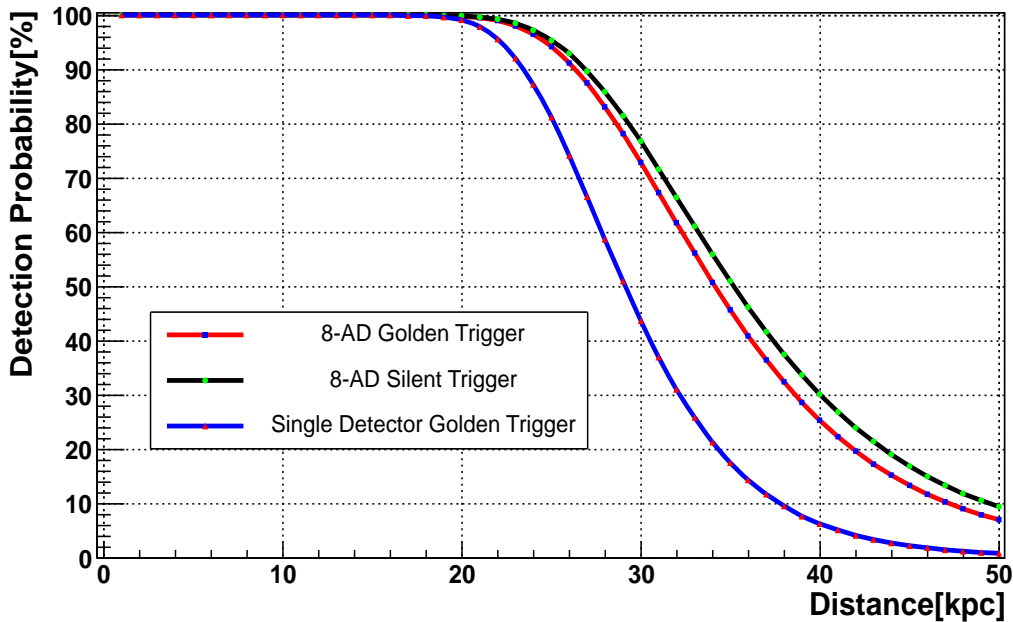


Figure 3.16 Detection probability of a supernova explosion given a false-alert rate threshold. “8-AD golden (silent) trigger” corresponds to a false-alert rate less than 1 per 3 (1) months. “Single Detector Golden” corresponds to the case in which the target masses from all the ADs are combined into a single detector, and with a false-alert rate less than 1 per 3 months.

The target masses of all the ADs are combined into a single detector with the sum of background rates, in order to illustrate the significant gain in the detection probability of multiple detectors over a mass-equivalent single detector. The blue curve and the red curve with the same false-alert rate threshold in Figure 3.16 give the comparison and the gain in the detection probability of multiple detectors is seen to be significant. It is found that the detection probability for the 8-AD case is equivalent to a single detector with as much as twice the target mass.

More curves of the detection probability are plotted in Figure 3.17 with different R_{IBD} values. Upper and lower limits of R_{IBD} are set to be R_{Gd} and $5 \times R_{Gd}$, where R_{Gd} is the measured rate of the IBD events with nGd delayed signals and dominated by reactor neutrinos. R_{Gd} is roughly 50% of the real R_{IBD} . Note that each AD uses its corresponding R_{Gd} .

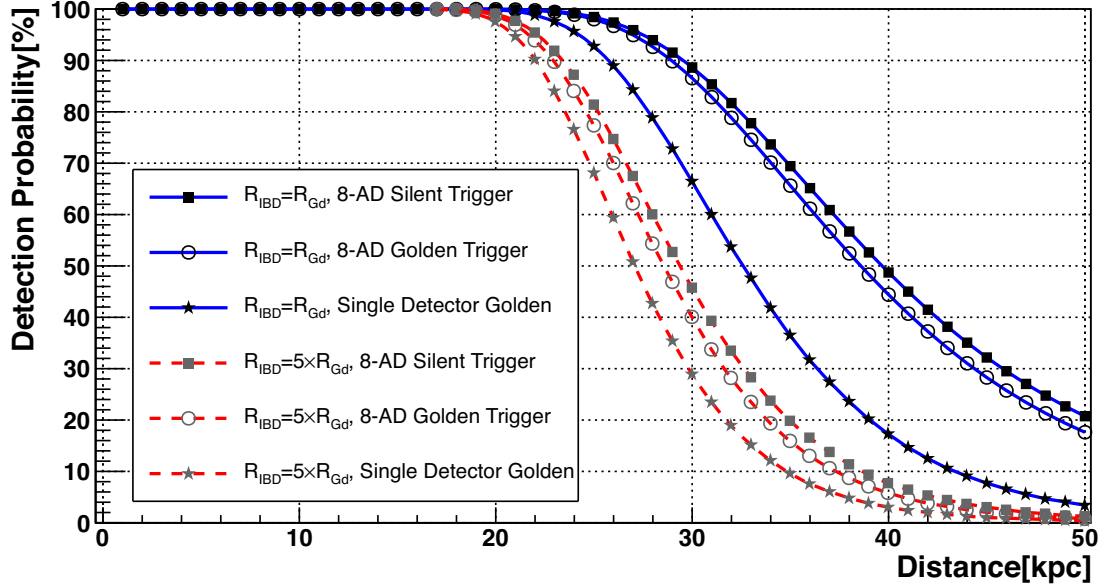


Figure 3.17 Detection probability of a supernova explosion given a false-alert rate threshold. “8-AD golden (silent) trigger” corresponds to a false-alert rate less than 1 per 3 (1) months. “Single Detector Golden” corresponds to the case in which the target masses from all the ADs are combined into a single detector, and with a false-alert rate less than 1 per 3 months.

Within the variation of R_{IBD} shown in Figure 3.17 and compared with Figure 3.16:

- 1) Regarding the detection probability of SN explosions within the Milky Way, the impact resulting from the variation of R_{IBD} can be ignored.
- 2) The gain in the detection probability of multiple detectors is roughly insensitive to the background rate as expected in such a large range of R_{IBD} .
- 3) The cost of increasing false-alert rate threshold is quite limited to the detection probability, even if the false-alert rate threshold changes from 1 per month to 1 per year (not shown).

Note that if the trigger table is generated based on a false-alert rate threshold as well as the measured R_{IBD} , and initialized in the online supernova trigger system, the detection probability is unchanged even if the real R_{IBD} changes. This is because the probability of the combinations over the trigger threshold are fixed.

3.3 Test and performance

Various kinds of tests were carried out on the online supernova trigger system, to ascertain the effectiveness of the design and implementation, the performance and the maximum capability, and the workload introduced to the existing DAQ.

3.3.1 Tests on miscellaneous function

The read-write operation of the database, email alert with the required datagram, and the daily/error/warning report and so forth in the monitoring system all worked smoothly and effectively during the tests and even during the entire period studied in this thesis.

3.3.2 Tests on key functions

The key functions of the online supernova trigger system are to select the IBD events and control the false-alert rate. A direct test of the IBD selection was performed as shown in both Figure 3.13 and Figure 3.20. The rises and falls are well consistent with the reactor power-on and -off, indicating the effectiveness of the IBD selection.

Table 3.6 Tests of the false-alert rate control. The threshold (offline/online) is the required false-alert rate threshold based on the offline/online-reconstruction. Due to the different IBD event rates from the online and offline reconstruction, the two thresholds are not identical but correspond to the same trigger rule (combinations surviving the cuts are fixed). The error of the threshold is statistical with the factor $g = 6.7$ (see Equation (3-10)) for 10^{-1} -Hz threshold and $g = 5.0$ for 10^{-3} -Hz threshold.

Trigger Type Rate (Hz)	14-min Test		1.25-h Test		18-h Test	
	Silent (10^{-1})	Golden (10^{-1})	Silent (10^{-3})	Golden (10^{-3})	Silent (10^{-3})	Golden (10^{-4})
Thresh. (offline)	2.76 ± 0.40	1.10 ± 0.28	3.33 ± 1.92	1.67 ± 1.36	1.67 ± 0.36	5.56 ± 2.1
Offline output	2.98	1.13	2.38	1.43	2.22	8.32
Thresh. (online)	3.43 ± 0.42	1.54 ± 0.32	7.84 ± 2.94	4.27 ± 2.18	4.27 ± 0.57	16.5 ± 3.6
Online output	3.51	1.42	6.93	4.77	4.92	23.5

A direct test of the false-alert rate control was done. The test result is summarized in Table 3.6. The IBD event rate from the online reconstruction is about 10-20% larger than that from the offline reconstruction. This is mainly due to the bias of the energy and vertex reconstruction, including more accidentals.

As given in Table 3.6, the IBD event rate in EH1-AD1 was 0.027 Hz, about 50% larger than the normal one. This was found to be due to a bug of the PMT cable map (relation between the geometric position and the electronic connector) in the database, which led to a more compact reconstruction of vertices, and thus introducing more accidentals. The problematic zones of the vertex reconstruction before and after this bug was fixed as shown in Figure 3.18.

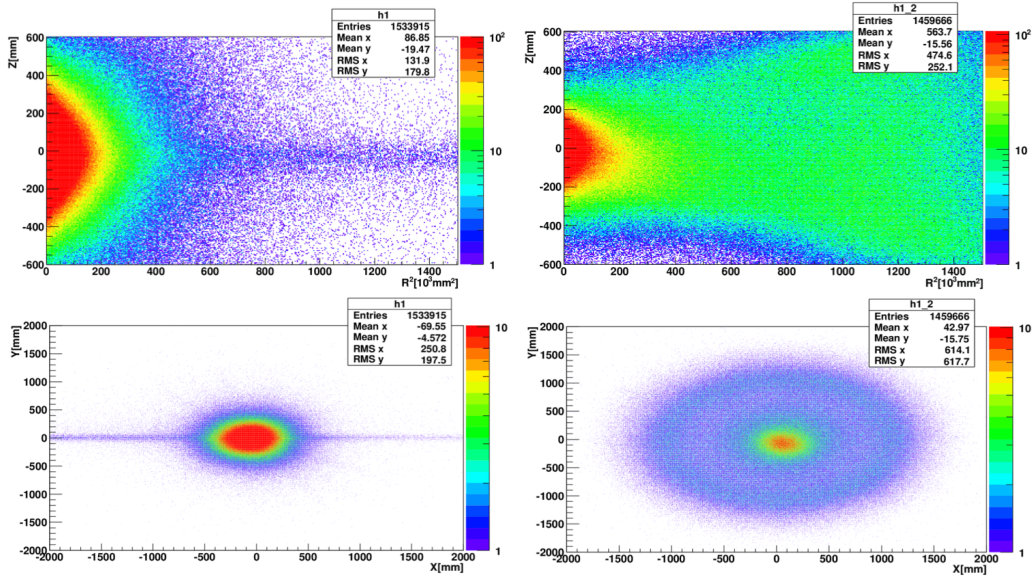


Figure 3.18 Problematic zones of the vertex (X, Y, Z) reconstruction before and after the bug of PMT cable map for EH1-AD1 was fixed. Top: Z versus R^2 . Bottom: X versus Y. Left: bug. Right: corrected.

3.3.3 Capability test

A test on the processing time of the IBD selection was done. 1629340 triggers were collected in a rate of 250 Hz. The IBD selection basically has two segments regarding the various selection criteria, and the processing is divided into two cases accordingly:

- A: The coincidence window (PMT flash, low-energy cut, muon veto, and prompt energy).
- B: The coincidence selection (delayed time, energy, and vertex).

A summary of such two types of triggers is shown in Table 3.7. The total fraction of the triggers is about 43.8% due to the trigger criteria of an AD as introduced in Section 3.2.1.2. The processing time is also plotted in Figure 3.19.

Considering the maximum capability of the DAQ in Daya Bay, the maximum rates

Table 3.7 Summary of time consumption regarding the two types of triggers in IBD selection.

Type	A	B	Total
Time range (ms)	< 0.1	0.1-1	< 1
Typical time (ms)	0.01	0.3	0.04
Fraction	42.4%	1.4%	43.8%

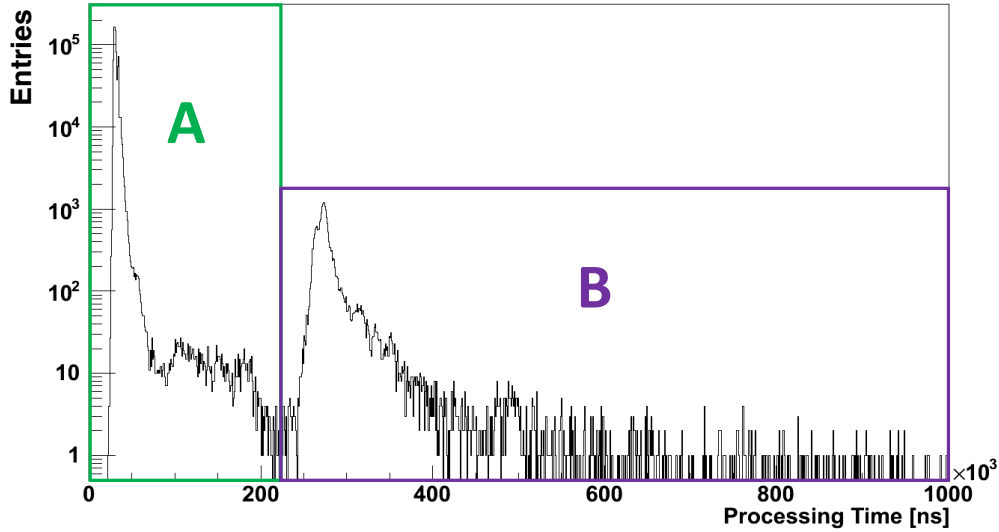


Figure 3.19 The IBD selection processing time. The two types of triggers are indicated.

are about 9 kHz and 2 kHz (including 4 kHz prompt + delayed triggers) for the acceptable single events and IBD events, respectively, of the IBD selection program. In a real physics run, the additional time consumption introduced by the IBD selection program is just about 8%.

A load test on the combination program of the online sub-system was carried out by artificially inputting 1 kHz triggers. It was observed that 500 Hz IBD events were perfectly selected and recorded at a cost of 70% CPU cores with additional 20% of the processing time. A conservative estimation of the maximum rate of the acceptable IBD events in the online trigger system is 1 kHz, which corresponds to a close SN explosion at 800 pc, 2600 light-years.

3.3.4 Time latency of a supernova trigger

The time latency of a supernova trigger from the beginning to recognition is less than 1 second (excluding the *duration* of the supernova trigger), while a few more seconds are needed from recognition to the completion of the email alert compilation and sending, as

well as a communication between the onsite computer farm and the SNEWS server (back up) at Brookhaven National Laboratory (Italian National Institute for Nuclear Physics). For the safe reliability, two standalone programs are responsible for the email alert to Daya Bay collaborators and the datagram to SNEWS, respectively.

3.3.5 Operational test

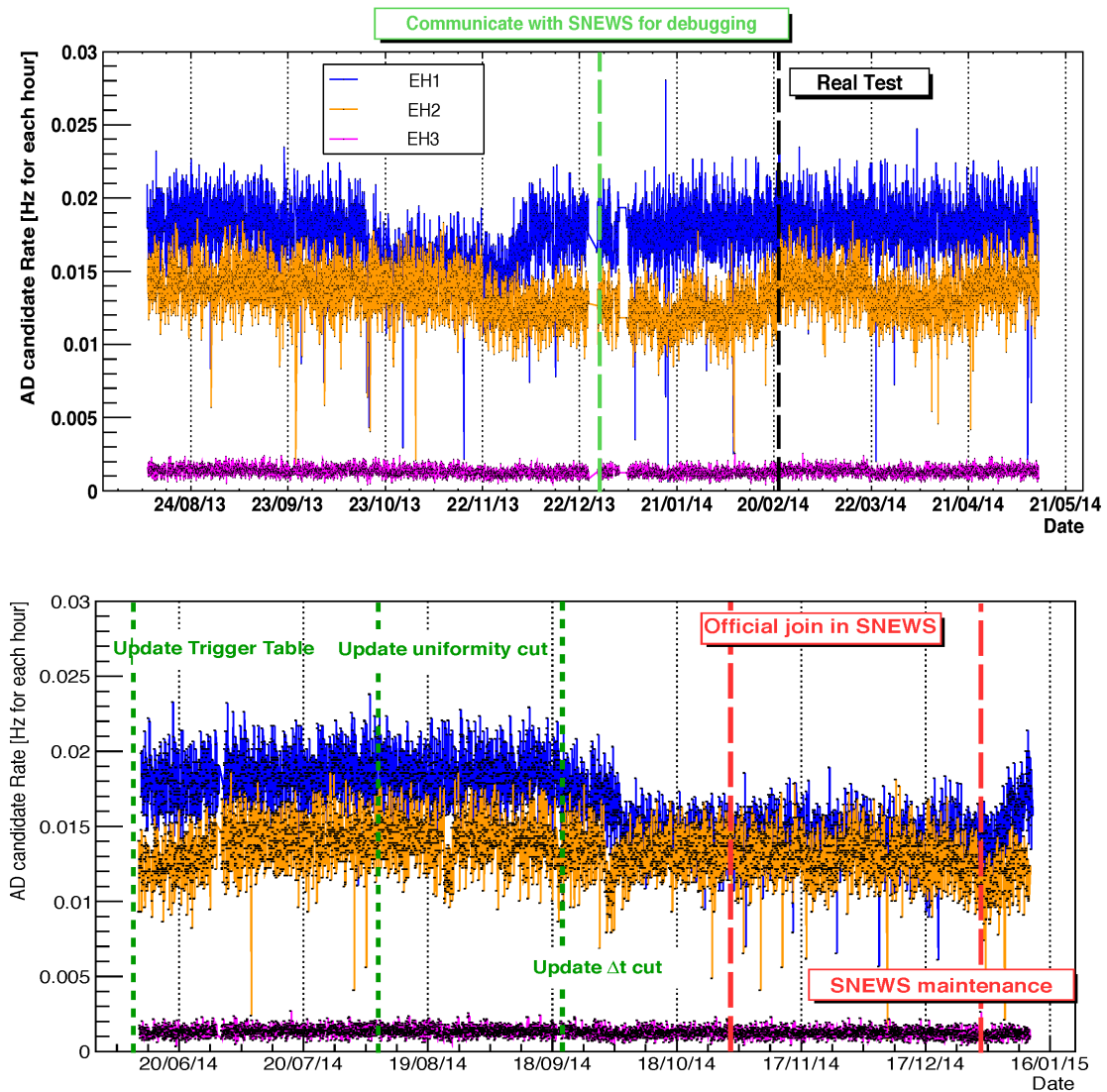


Figure 3.20 The single AD's IBD event rates for EH1, EH2, and EH3. Each point corresponds to an hour. The rate in EH1 is slightly higher than that in EH2, and the rate in EH3 is one order of magnitude smaller. The rises and falls are well consistent with the reactor power-off and -on. Some big events are also indicated in this figure.

The online supernova trigger system was installed at Daya Bay in August, 2013. The

tests on communication with SNEWS began in December, 2013. Then, the long-term “real test” was set out in February, 2014 during which the false-alert rate thresholds and all the other things were configured in compliance with SNEWS’s requirement. During this test, the trigger table was updated once according to the past 1-year measurement, the uniformity cut and coincidence-time cut were slightly augmented (tighten uniformity cut and T_c from 1-400 μs to 2-400 μs) to remove the observed unexpected electronic noise with negligible cost of sensitivity to SN explosions. Daya Bay officially joined SNEWS^[55] in November, 2014.

The online supernova trigger system has been running smoothly and effectively to date. The online trigger system is operating only for the DAQ physics runs with an operational efficiency of $\sim 97\%$.

There were twenty-seven triggers alerted in 2014 (roughly the “real test” period, with the silent trigger threshold of 1 per month and the golden trigger threshold of 1 per 3 months). Sixteen of them were found to be most likely abnormal triggers caused by the noise from the FEE board, the module trip on the water pool and RPC high voltage, or even a flash of lightning in the thunder storm (3 times). In principle, the online trigger system just utilizes the AD triggers and is supposed not to be affected by the high voltage module in the water pool and RPC as well as the lighting. More investigations about these abnormal triggers will be carried out in the future. In fact, the uniformity cut and coincidence-time cut were augmented according to the characteristics of these abnormal triggers (IBD events concentrated in one experimental hall or 1-2 μs coincidence time). The rest (normal) 11 triggers in 2014 are summarized in Figure 3.21 which coincide with the required false-alert rate. Note that the second to last trigger with a high confidence level in Figure 3.21 is probably abnormal due to the problematic PMT channels after a NPP power outage.

All the alerts online were ruled out by offline checks. Under the offline checks, most of the IBD events (about 30-40%) of the online triggers were removed, of which 20-30% were removed by the IWS/OWS muon vetoes that are not used in the online supernova trigger system as mentioned in Section 3.2.1.2, 10-20% by the precise energy and vertex reconstructions. It is estimated that an online supernova trigger which also survives the offline check would occur with a rate of a few per century.

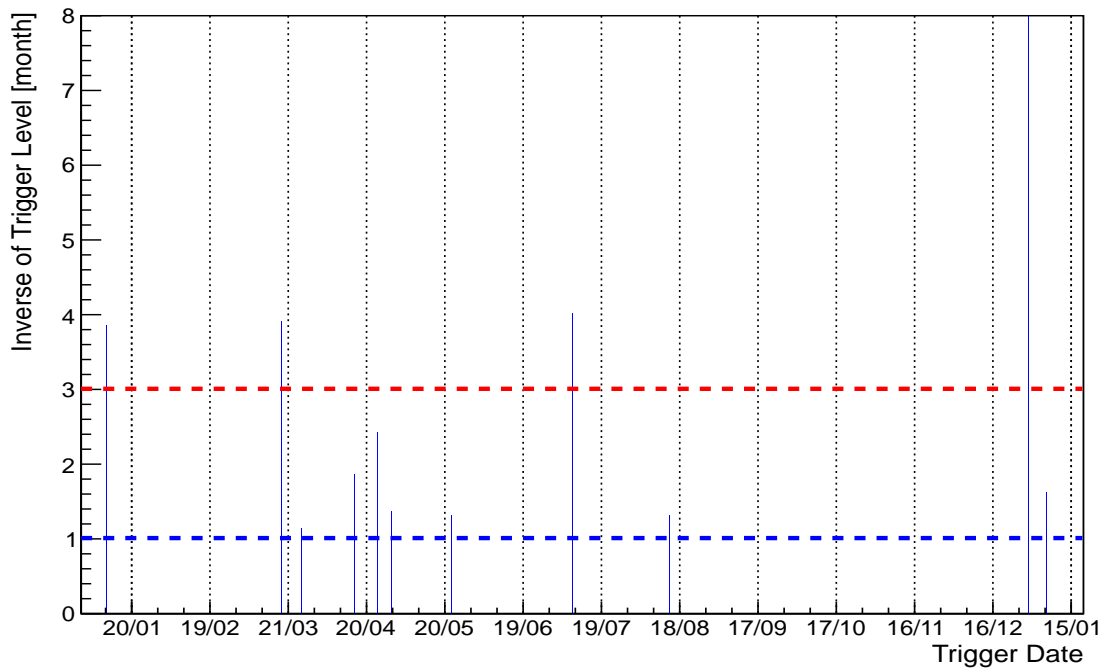


Figure 3.21 Normal triggers from January 2014 to January 2015 over the date. The Y-axis is the inverse of the corresponding false-alert rate threshold (see Section 3.2.2.4) in units of month, e.g., the red line corresponds to the false-alert rate threshold of 1 per 3 months and the blue line corresponds to the false-alert rate threshold of 1 per month.

3.4 Conclusion and outlook

An online supernova trigger system was designed, implemented, tested, and installed in the Daya Bay experiment. The unique feature that multiple ADs are deployed at a distance from each other in three separate experimental halls allows a rapid trigger algorithm with an effective control of the false-alert rate as well as a gain in the sensitivity to core-collapse supernovae. This online supernova trigger system is a very prompt (possibly the world's most prompt) supernova trigger system with the lowest energy threshold, and fully sensitive to the core-collapse supernovae throughout the Milky Way. This system was installed at Daya Bay in August 2013 and officially integrated into the worldwide Supernova Early Warning System (SNEWS) in November 2014. It has been smoothly running up to now with an operational efficiency of $\sim 97\%$.

Chapter 4 Offline search for supernova neutrino bursts at Daya Bay

Supernova burst neutrinos were searched for by an offline analysis at Daya Bay using about 1.5 years of data, including all the data before the online trigger system was installed. In addition, this is the first search for supernova neutrino bursts at Daya Bay and two types of analyses were performed: a high energy threshold (10 MeV) analysis and a low energy threshold (0.7 MeV) analysis.

The data correspond to two periods, a 6-AD period from December 24, 2011 to July 28, 2012 and a 8-AD period from October 19, 2012 to November 27, 2013.

The core algorithm of the trigger decision from the offline analysis is roughly the same as the online trigger. However, several aspects were improved as described below.

- 1) Good data sample after the data quality check, which should have few ‘abnormal’ events (e.g., electronic noise).
- 2) Offline reconstruction and optimized IBD selection, which considerably suppresses the muon-induced backgrounds and accidentals.
- 3) Lower energy threshold. The low energy threshold for nGd (nH) signals can be lowered to 0.7 (3.5) MeV compared with 2 (8) MeV from the online trigger.
- 4) More sophisticated investigations of the candidates, including the uniformity of the IBD events in multi-ADs, the energy spectrum against the backgrounds, and the coincidence with astronomical observations.

The improvements above allow a more confident recognition of supernova burst neutrinos as well as an enhanced sensitivity.

4.1 Event reconstruction

The offline search for supernova neutrino bursts utilized the Daya Bay official offline-reconstructed data. Compared with the online reconstruction (in Section 3.2.1.1), the crucial differences are that the charge-pattern templates from all the PMTs were derived from Monte Carlo simulation to correct the vertex reconstruction, and the position-dependent spatial non-uniformity of the energy scale was corrected for the energy reconstruction.

The charge-pattern (the average distribution of charge from all the PMTs) templates were determined for 9600 voxels within the OAV on a grid with 20 divisions in the r^2

direction, 20 in the z direction, and 24 in the ϕ direction (cylindrical coordinate with the z axis along with the cylindrical axis of the IAV/OAV). For a reconstructed position of each event, a χ^2 function based on the measured charge-pattern and the expected charge-pattern (from templates) was minimized, and interpolated using the nearest neighbor voxels around that with the smallest χ^2 value.

The energy scale in a single AD increased by 15% from the center to the edge in the radial direction, and decreased by 6% (2%) from the center to the top (bottom) in the axial direction which also depends on the radial position. The energy scale was corrected by a two-dimensional function (r, z) derived from spallation neutron captures in each AD. Slight differences (<3%) in the spatial non-uniformity were observed between the eight identically-designed ADs.

The energy resolution of the reconstructed energy (E_{rec}) was measured to be about $9\%/\sqrt{E_{\text{rec}}[\text{MeV}]}$ at the center of an AD and increased by about 20% on the edge of the OAV. In the LS volume, the position resolution of the reconstructed vertex was about 12 cm in the $r - \phi$ plane and 13 cm in the axial direction. From the center to the edge of an OAV, the position resolution increased by about 40% and vertically varied within a few percent.

4.2 Interaction channels

The offline reconstruction has more precise energy and vertex information as well as a better resolution. It is feasible that more interaction channels are utilized to do a physics analysis. In liquid scintillator detectors, the interaction rates for various reaction channels are shown in Figure 4.1.

The IBD interaction is obviously the dominant channel as mentioned in Section 1.3.1. An exotic channel – neutral-current (NC) excitation of ^{12}C interaction was exploited since it has a unique feature whose detected energy is a smeared mono-energetic de-excitation gamma (15.11 MeV) peak. As a result, a high signal-to-background ratio is expected.

4.2.1 IBD channel

4.2.1.1 IBD selection criteria

The IBD selection criteria are basically an improved version of the selection criteria for the online trigger. They are summarized in Table 4.1.

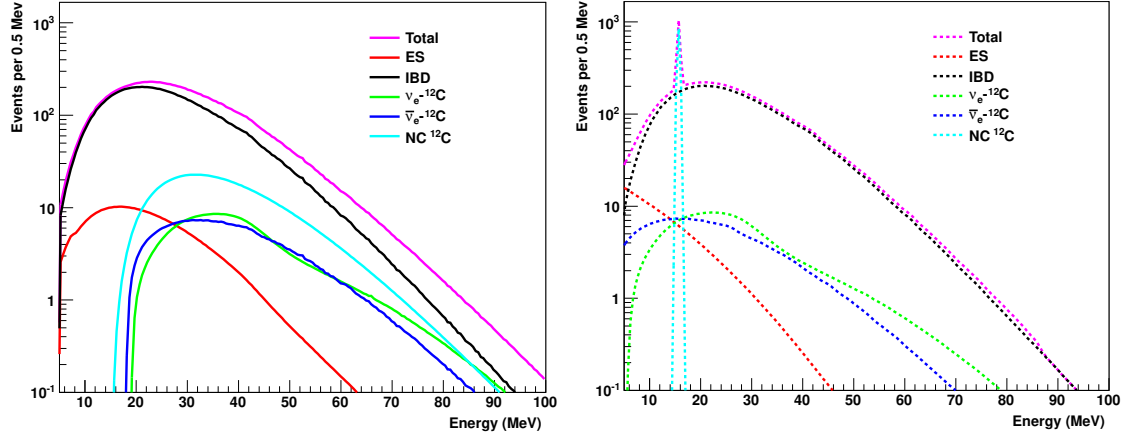


Figure 4.1 Event rates for supernova burst neutrinos (the GKVM model^[40]) in a 50-kt liquid scintillator detector from Ref. [41]. Left: interaction rates as a function of the neutrino energy. Right: smeared interaction rates as a function of the detected energy. ES: ν -e elastic scattering.

Table 4.1 IBD selection criteria for the offline search for supernova neutrino bursts. See text for more details.

	nH	nGd
AD trigger	$N_{\text{PMT}} \geq 45$ OR $Q_{\text{sum}} \geq 65$ p.e.	
20-cm PMT flash	$Ellipse < 1$	
5-cm PMT flash	$Q < 100$ p.e.	
Low energy	> 1.5 MeV	> 0.7 MeV
Detector latency	$< 2 \mu s$	
WS muon (μ_{WS}) [1ws/ows]	$N_{\text{PMT}} > 12/15$	
AD muon (μ_{AD})	> 50 MeV	
Showering AD muon (μ_{sh})	> 2.5 GeV	
WS muon veto	$(0, 400) \mu s$	
AD muon veto	$(0, 800) \mu s$	
Showering AD muon veto	$(0, 1) s$	
Coincidence time (t_c)	$[1, 400] \mu s$	$[1, 200] \mu s$
Prompt energy (E_p)	$[3.5, 50]$ MeV	$[0.7, 50]$ MeV
Delayed energy (E_d)	peak $\pm 3\sigma$	$[6, 12]$ MeV
Coincidence distance (d_c)	< 1000 mm	NA

For the PMT flash cut, the *Quadrant* (see Section 3.2.1.2) was combined with $q_{\text{max}} = Q_{\text{max}}/Q_{\text{Sum}}$ to determine a $Ellipse = \sqrt{Quadrant^2 + (q_{\text{max}}/0.45)^2}$ cut, which was required to be < 1 . In addition, flashes from three (three) 5-cm calibration PMTs installed near the top (bottom) reflectors were removed by requiring the charge to be < 100 p.e..

The low energy criterion to remove the natural radioactivity was lowered to 1.5 MeV

for the nH signals and 0.7 MeV for the nGd signals. 0.7 MeV is the lowest deposited energy corresponding to 100% acceptance of IBD positrons in an AD.

Since muon events from the ADs, IWS, and OWS may occur within a 2- μ s latency, the detector latency 2- μ s was used to group the muon events (earliest time and largest energy) to account for the cosmogenic muon-induced events. This grouping also removed the possible electronic re-triggers after a muon event.

In the offline analysis, the water pool locating the ADs is used to tag the muon events. A muon event was identified by the water shield (μ_{WS}) by requiring the number of triggered water pool PMTs $N_{\text{PMT}} > 12$ (15) in the IWS (OWS). An AD (showering) muon was required to be grouped with a μ_{WS} and satisfy the energy conditions – AD muon (μ_{AD}) if $50 \text{ MeV} < E_{\text{rec}} < 2.5 \text{ GeV}$ and showering muon (μ_{sh}) if $E_{\text{rec}} > 2.5 \text{ GeV}$. Three veto windows of 400 μ s, 800 μ s, and 1 s were applied to μ_{WS} , μ_{AD} , and μ_{sh} , respectively.

The coincidence time windows were 1-400 μ s and 1-200 μ s for the nH and nGd signals according to the different average neutron capture times. The energy threshold for the prompt signal was lowered from 8 MeV (2 MeV) to 3.5 MeV (0.7 MeV) for nH (nGd) signals. Delayed energy selection was within a $\mu \pm 3\sigma$ region for each AD where the mean value μ and the standard deviation σ were determined from the fit to the delayed energy spectrum of the 2.2-MeV γ using a Crystal Ball function. The $\mu \pm 3\sigma$ is approximately [1.90, 2.74] MeV for all the ADs. The coincidence distance was required to be less than 1000 mm for the nH signals, to further reject the accidentals by greater than 90%.

4.2.1.2 IBD selection efficiency

The coincidence selection efficiencies are summarized in Table 4.2. The total IBD selection efficiency is about 72% for the offline supernova search. This offline efficiency is found to be about 3% higher than that of the online trigger and due to the lower prompt energy threshold. This efficiency is model-dependent based on the supernova neutrino energy spectrum with an average energy $\langle E_{\bar{\nu}_e} \rangle = 12 \text{ MeV}$ and $\alpha = 2.3$. Actually, the efficiency changes within 1-2% with an average energy $\langle E_{\bar{\nu}_e} \rangle = 12\text{-}15 \text{ MeV}$ and $\alpha = 2.0\text{-}2.6$.

The PMT flash cut efficiency is about 100% and the multiplicity cut efficiency is 98%. The muon veto efficiencies for the three experimental halls are 82% (85%), 85% (88%), and 98% (99%) for nH (nGd) signals in EH1, EH2, and EH3, respectively.

Table 4.2 Efficiencies of the offline IBD selection criteria. Spill-in/out effect of the nH signals is included in the delayed energy efficiency. N_p corresponds to a single AD.

	GdLS		LS
	nGd	nH	nH
Proton number (N_p)	1.43×10^{30}		1.54×10^{30}
neutron capture fraction	84%	16%	96%
Spill-in ($\epsilon_{\text{spill-in}}$)	105%	–	–
Prompt energy (ϵ_p)	100%	98%	96%
Delayed energy (ϵ_d)	92%	95%	67%
Coincidence time (ϵ_t)	98%	99%	85%
Coincidence distance (ϵ_{dist})	NA	98%	98%
Total IBD selection efficiency	95%	91%	54%

4.2.1.3 Selected IBD events

The selected IBD event rates per hour corresponding to ~ 1.5 years of data are plotted in Figure 4.2. The variation of the IBD event rates is well consistent with the trend of the reactor neutrino flux changing with reactor power-off and -on. The IBD event rates are 0.0087 Hz per AD, 0.0080 Hz per AD, and 0.0012 Hz per AD, for EH1, EH2, and EH3, respectively.

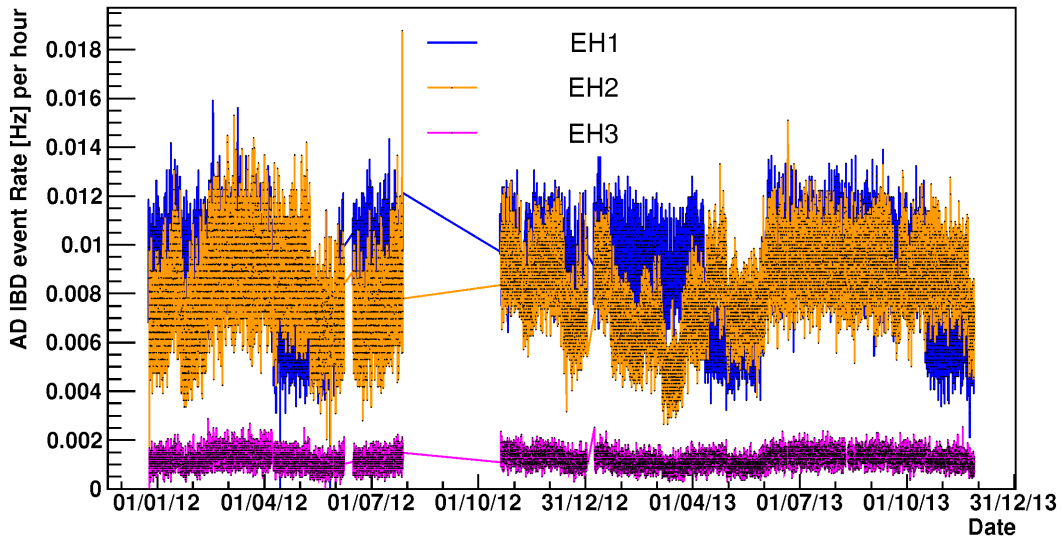
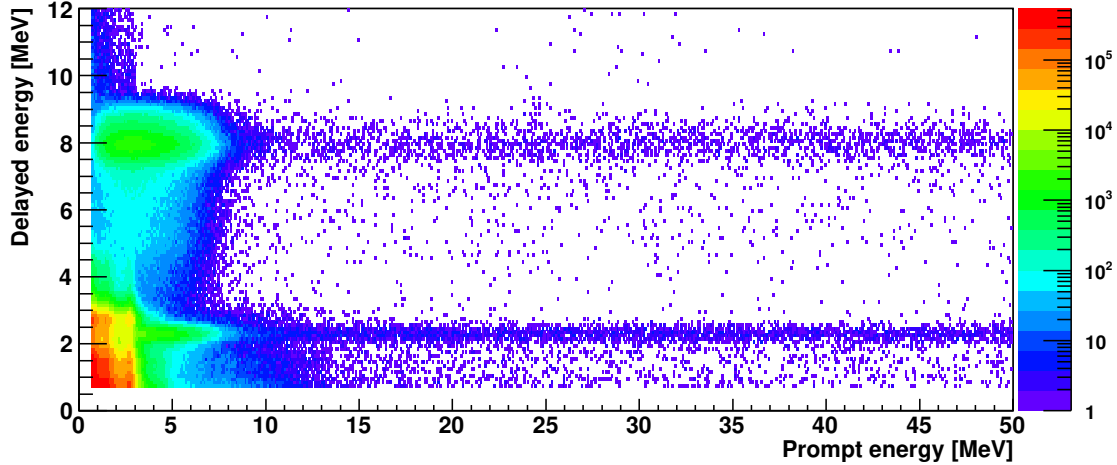
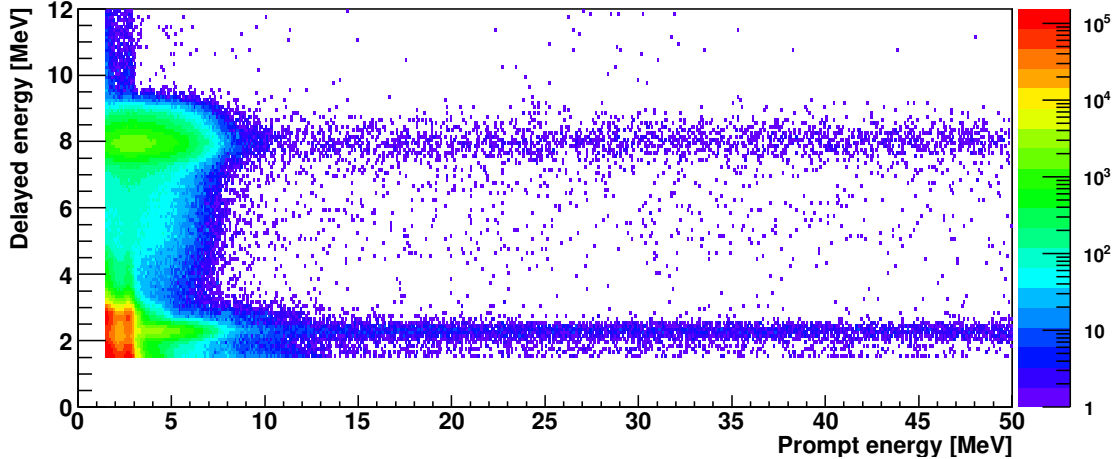


Figure 4.2 Average selected IBD event rates per hour in an AD for each experimental hall. The dates are in the format of day/month/year.

The prompt versus delayed signal energy distribution is shown in Figure 4.3. Clearly, a 3.5-MeV cut on prompt energy for the nH signals would remove the majority of the accidentals. A significant reduction of muon-induced spallation neutrons is due to the veto after the water shield muons in comparison with the online selected IBD events.



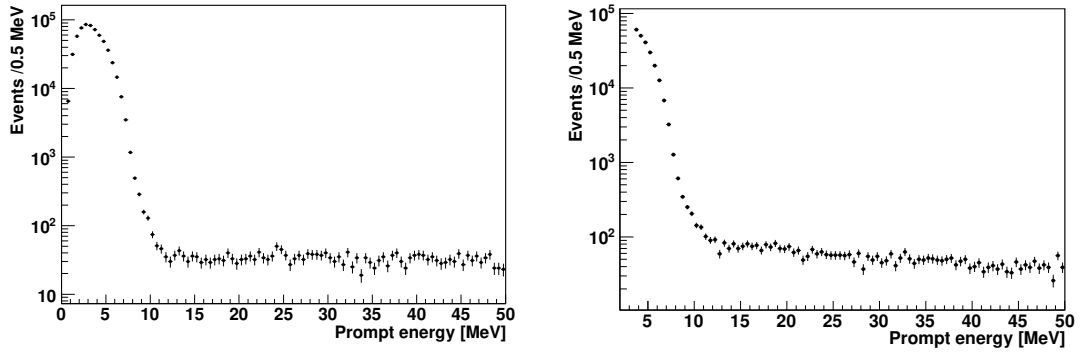
(a) Low energy criterion > 0.7 MeV and coincidence time 1-200 μs for the nGd signals.



(b) Low energy criterion > 1.5 MeV and coincidence time 1-400 μs for the nH signals.

Figure 4.3 Distribution of prompt versus delayed signal energy from the two ADs in EH1 without prompt and delayed energy cuts and coincidence distance cut. (a) for the nGd signals. (b) for the nH signals. (a) and (b) have quite similar distributions.

The prompt energy distributions for the nGd and nH signals with all the cuts are plotted in Figure 4.4. Both of the prompt energy spectra have two portions, one of which corresponds to the reactor neutrinos in < 10 MeV region and the other corresponds to the muon-induced spallation neutrons in > 10 MeV region. Slightly differences were observed between the prompt energy spectra of the muon-induced spallation neutrons from the nGd signals and the nH signals due to the spatial location of the LS volume

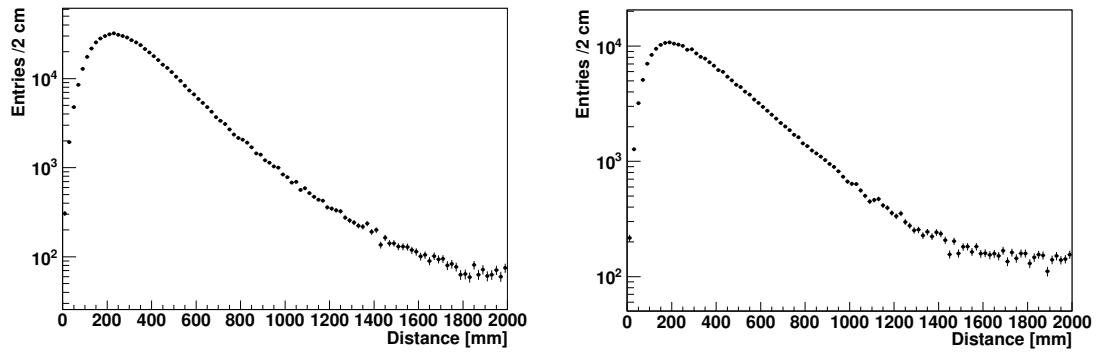


(a) From the nGd signals.

(b) From the nH signals.

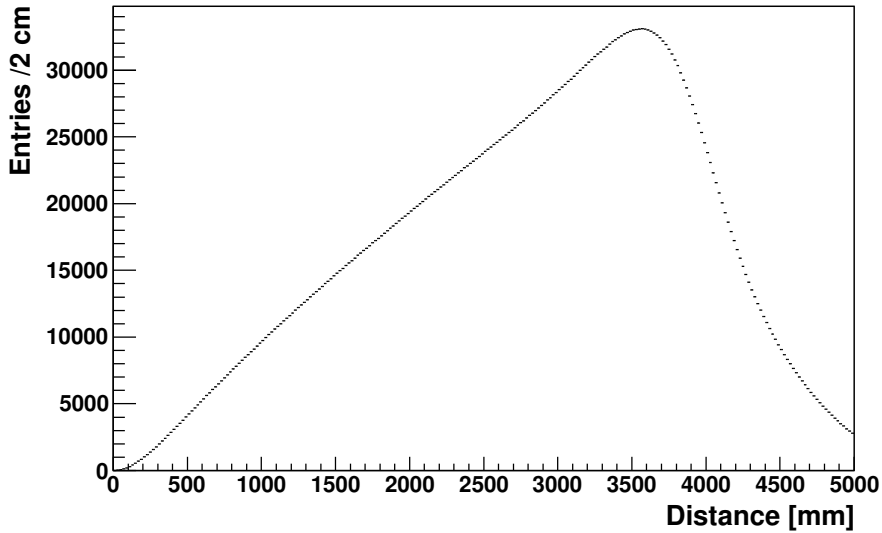
Figure 4.4 Prompt energy distribution from the two ADs in EH1 with all the cuts. (a) For the nGd signals. (b) For the nH signals. See text for more explanations.

(OAV) and the GdLS volume (IAV).



(a) From the nGd signals.

(b) From the nH signals.



(c) From accidentals.

Figure 4.5 Distance between the prompt and delayed signals after all the cuts except the coincidence distance cut.

Except the reactor neutrinos (indistinguishable from supernova neutrino signals) and muon-induced spallation neutrons (reduced significantly by water shield and AD muon vetoes), the accidentals are actually removed significantly by the other cuts even if the coincidence distance cut is not applied. From Figure 4.5, the accidentals are apparently removed significantly in both the nGd and nH signals considering the accidental distance distribution. Due to the larger fraction of the residual accidentals in the nH signals, a 1000-mm cut^[122] on the coincidence-distance was applied to the nH signals at the last step.

4.2.2 Neutral-current ^{12}C channel

4.2.2.1 Introduction to NC- ^{12}C interaction

The NC- ^{12}C interaction channel ($\nu + ^{12}\text{C} \rightarrow ^{12}\text{C}^* + \nu'$) was used in the search for supernova neutrino bursts to increase the rate analysis sensitivity. The $A = 12$ isobaric level scheme is shown in Figure 4.6, where the transitions from the ground state $^{12}\text{C}(0^+, 0)$ to the isotopic triad of $(1^+, 1)$ states $^{12}\text{N}_{\text{g.s.}}$, $^{12}\text{C}^*$ (15.11 MeV), and $^{12}\text{B}_{\text{g.s.}}$ are superallowed. These transitions give rise to the charged-current $\bar{\nu}_e/\nu_e$ captures by ^{12}C to ^{12}B and ^{12}N , and the neutral-current inelastic scattering of ν or $\bar{\nu}$ with ^{12}C to the excited state $^{12}\text{C}^*$ (15.11 MeV). The signal of NC- ^{12}C interaction thus results from the single 15.11-MeV de-excitation gamma.

The cross section of NC- ^{12}C interaction is given by^[135,136]:

$$\sigma = \frac{G_F^2}{\pi} \sum_i |M_i|^2 (E_\nu - E_i)^2, \quad (4-1)$$

where G_F is the Fermi constant, $|M_i|$ are the nuclear matrix elements and i 's are the indices of different spin states. The cross section of NC- ^{12}C (about $3 \times 10^{-42} \text{ cm}^2$ at $E_\nu = 29.8 \text{ MeV}$) was measured by the KARMEN experiment^[137-139] which is also in a good agreement with the theoretical prediction^[136].

4.2.2.2 NC- ^{12}C event selection

Selection criteria The NC- ^{12}C events were selected based on the selection criteria for the nH signals. The difference is that within the coincidence time window the one-fold (multiplicity = 1) events were selected with E_{rec} in the $\mu \pm 3\sigma$ region of the 15.11-MeV

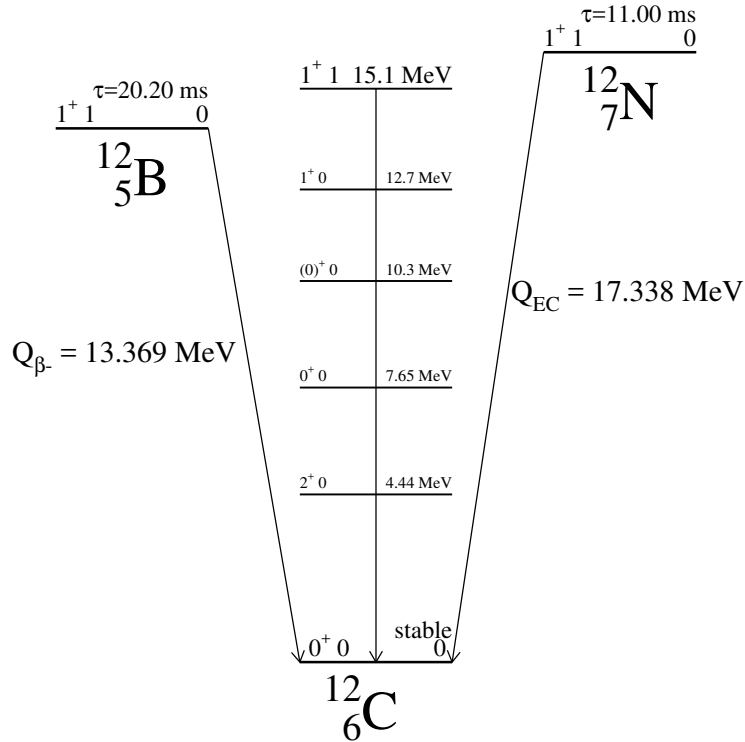


Figure 4.6 Isobaric level scheme of the isotopic triad ^{12}N , ^{12}C , ^{12}B .^[135]

γ peak. The selection criteria for the NC- ^{12}C events are summarized in Table 4.3. The energy cut for 15.11-MeV γ was determined by the simulation which is explained below.

Simulation of 15.11-MeV gamma The resulting NC- ^{12}C signal is studied by a simulation of 15.11-MeV gamma in an AD at Daya Bay prior to determining the energy cuts. 15.11-MeV γ 's were simulated in an AD with a uniform vertex distribution and a uniform direction distribution. The average time interval between two 15.11-MeV γ 's is set to be 3 seconds, which approximately corresponds to a NC- ^{12}C event rate from a typical supernova explosion at 10 kpc.

The reconstructed 15.11-MeV γ events from the simulation were selected with all the criteria in Table 4.3 except the energy cut. Notice that the simulation was performed in the full volume including the GdLS volume, LS volume, and MO volume. As mentioned before, the MO was ignored in the IBD selection since the IBD positrons produced in MO could rarely enter the scintillator and generally yield an insufficient amount of light to trigger an AD. However, a gamma particularly with a higher energy e.g., 15.11 MeV

Table 4.3 Selection criteria for the NC- ^{12}C events. See text for more explanations.

	NC- ^{12}C event
AD trigger	$N_{\text{PMT}} \geq 45$ OR $Q_{\text{sum}} \geq 65$ p.e.
20-cm PMT flash	$Ellipse < 1$
5-cm PMT flash	$Q < 100$ p.e.
Low energy	> 1.5 MeV
Detector latency	< 2 μs
WS muon (μ_{WS}) [IWS/OWS]	$N_{\text{PMT}} > 12/15$
AD muon (μ_{AD})	> 50 MeV
Showering AD muon (μ_{sh})	> 2.5 GeV
WS muon veto	(0, 400) μs
AD muon veto	(0, 800) μs
Showering AD muon veto	(0, 1) s
Coincidence time (t_c)	[1, 400] μs
Multiplicity	= 1
Energy	[14.5, 17.3] MeV

could enter the scintillator and even fully deposits its energy in the scintillator (GdLS + LS volumes). Figure 4.7 shows the reconstructed energy spectrum of 15.11-MeV gamma in the full volume. A simple Gaussian fit to the energy peak gives a mean value of 15.9 MeV and a standard deviation of 0.45 MeV. Similar to Figure 4.7, the spectrum corresponding to the MO volume is shown in Figure 4.8 where a simple Gaussian fit to the peak gives a mean value of 16.0 MeV and a standard deviation of 0.50 MeV.

The ratio of 15.89/15.11 \sim 1.05 can be accounted for by the 3% non-linearity effect of the reconstructed energy ($E_{\text{rec}}/E_{\text{true}}$ deviates from 1 due to the quenching effect in the scintillator adhering to the Birk's law, the non-linear Cherenkov light yield with deposited energy, and the non-linear electronic response) and about 2% residual non-uniformity effect (after the spatial non-uniformity correction) of the energy scale. The energy resolution 0.45 MeV in the full volume is about 10% larger than the predicted energy resolution 0.40 MeV in the center of an AD by the formula^[140],

$$\frac{\sigma_E}{E_{\text{rec}}} = \sqrt{0.016^2 + \frac{0.081^2}{E_{\text{rec}}/\text{MeV}} + \frac{0.026^2}{(E_{\text{rec}}/\text{MeV})^2}}. \quad (4-2)$$

As described in Section 4.1, the energy resolution changes by about 20% from the center to the wall of the OAV mainly due to the larger PMT geometric acceptance of scintillation

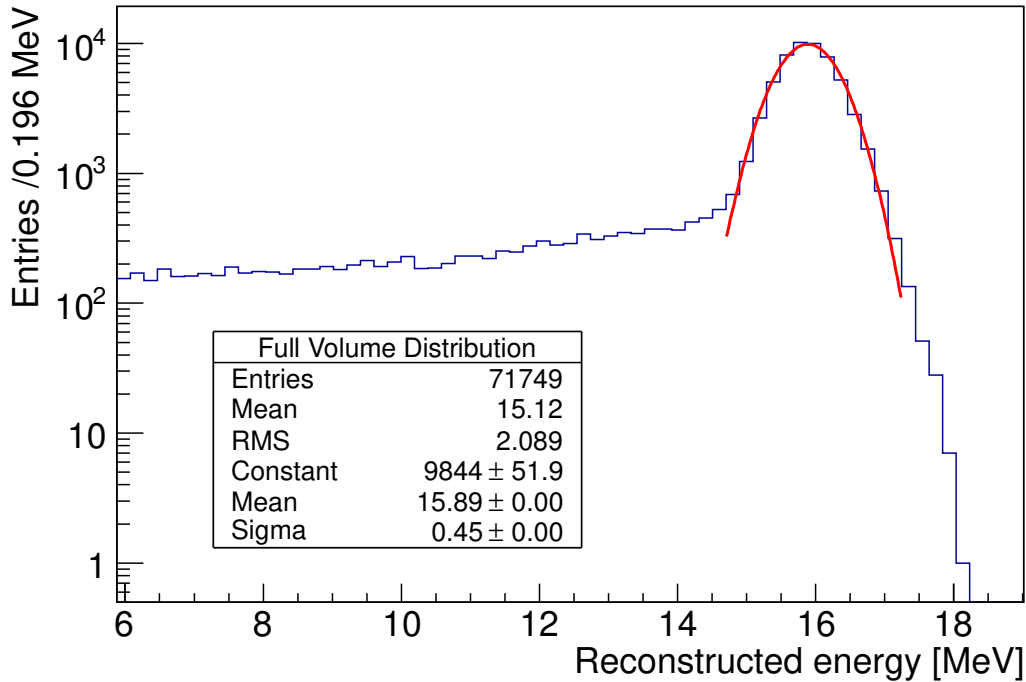


Figure 4.7 Reconstructed energy spectrum of simulated 15.11-MeV γ 's in the full volume after all selection criteria except the energy cut.

photons and the weaker light attenuation in the outmost space of an AD close to the PMTs. The energy resolution of 0.50 MeV in Figure 4.8 for the MO volume is 25% larger than 0.40 MeV.

To check the gamma leakage from the LS volume to the MO volume as well as that from the MO volume to the LS volume, the reconstructed vertices of the selected 15.11-MeV γ 's are shown in Figure 4.9 and Figure 4.10.

From Figure 4.9(a) and Figure 4.9(b), it is evident the gamma in the IAV almost deposits the full energy and the gamma on the edge of the OAV was a significant leakage problem. From Figure 4.10(a) and Figure 4.10(b), the gamma from the MO volume most likely enters the LS volume and deposits energy.

Selection efficiency The selection efficiency of the NC- ^{12}C events was also estimated by the simulation. The efficiencies for the different criteria are summarized in Table 4.4, including the AD trigger, low energy criterion (> 1.5 MeV), and the $\mu \pm 3\sigma$ energy cut.

The target masses of GdLS, LS, and MO are approximately 19.9 t, 21.5 t, and 36 t, respectively, for each AD. The energy scale uncertainty of 2% or the energy resolution uncertainty up to 10% would just introduce a 1% uncertainty to the energy cut efficiency.

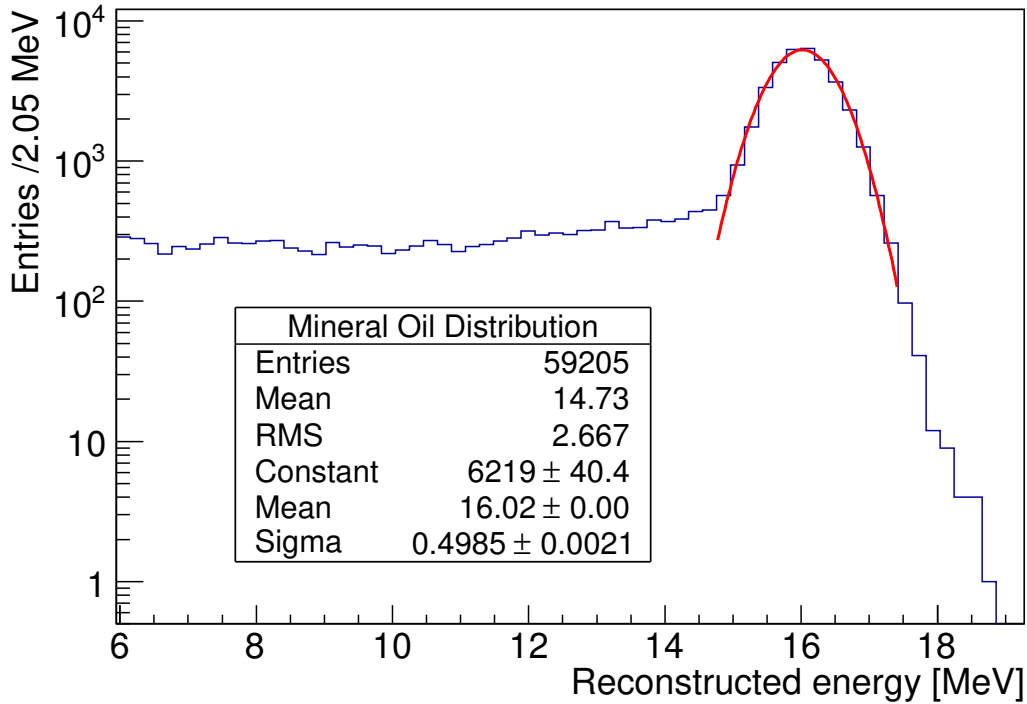
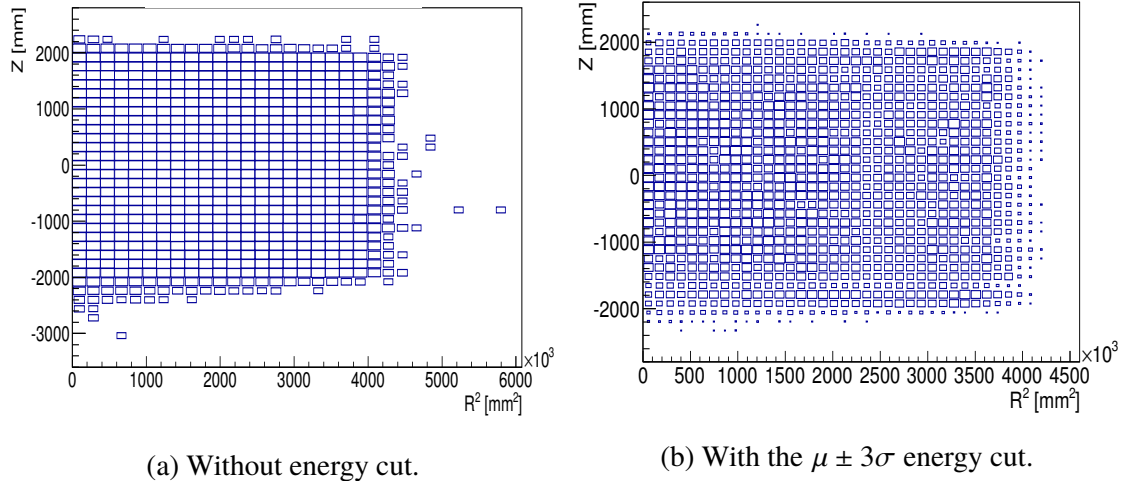


Figure 4.8 Reconstructed energy spectrum of simulated 15.11-MeV γ 's in the MO volume after all selection criteria except the energy cut.



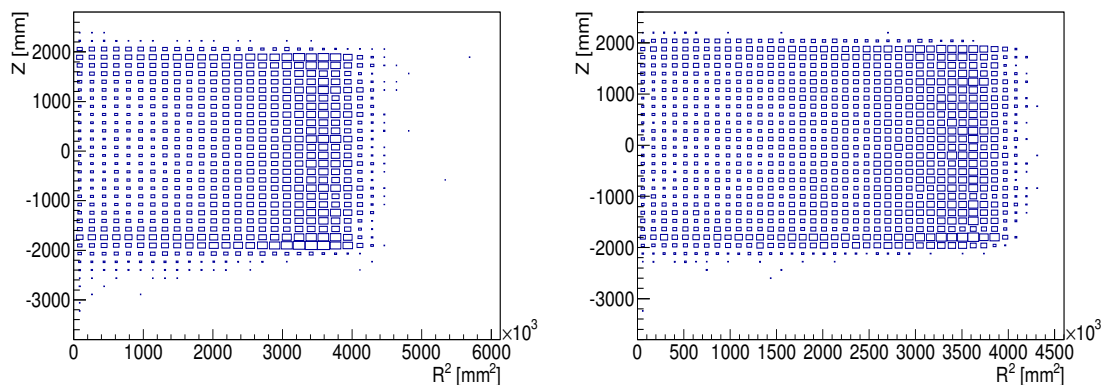
(a) Without energy cut.

(b) With the $\mu \pm 3\sigma$ energy cut.

Figure 4.9 Reconstructed vertex distribution of the selected 15.11-MeV γ 's in the full volume. (a) Without energy cut. (b) With the $\mu \pm 3\sigma$ energy cut. The size of the box indicates the number of entries.

The statistical uncertainty for the efficiency here is $< 1\%$. Considering the systematic uncertainty from the target masses of the three volumes, one can estimate the total absolute uncertainty of the efficiency to be about 2% .

The inefficiencies for different criteria are described below. Since a gamma may



(a) Without energy cut.

 (b) With the $\mu \pm 3\sigma$ energy cut.

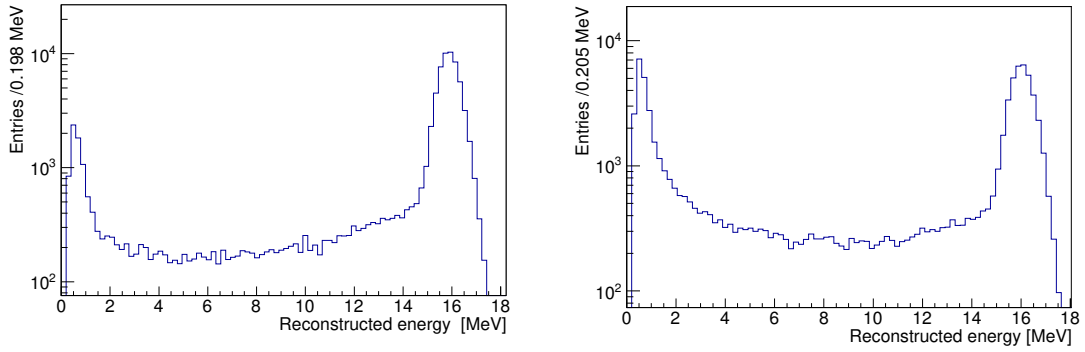
Figure 4.10 Reconstructed vertex distribution of the selected 15.11-MeV γ 's in the MO volume. (a) Without the energy cut. (b) With the $\mu \pm 3\sigma$ energy cut. The size of the box indicates the number of entries. The two plots have different scales.

Table 4.4 Efficiencies of the different selection criteria for the NC- ^{12}C (15.11-MeV γ) event step by step. In the parentheses are the inefficiencies due to the PMT flash cut. In the square brackets are the corresponding efficiencies for the 2.2-MeV γ .

Volume	AD trigger	> 1.5 MeV	[14.5, 17.3] MeV	Total
GdLS+LS	84%	95%	83%	65% [81%]
MO	26%	74% (5%)	64%	13% [6%]
Full	54%	91% (2%)	80%	40% [46%]

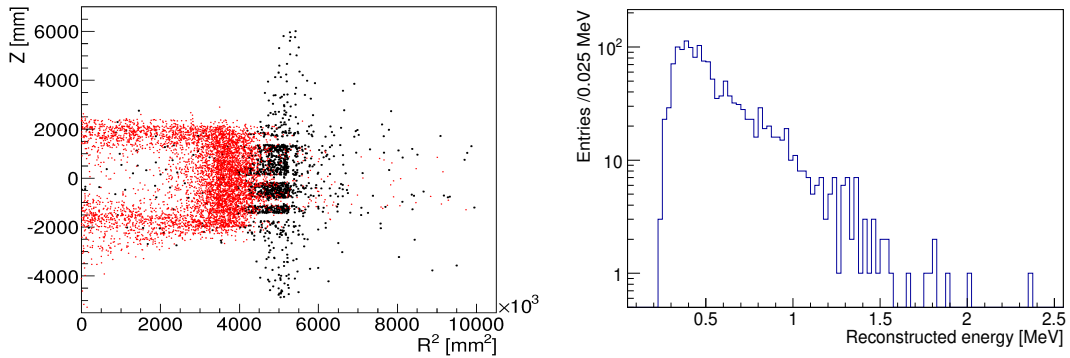
escape from the scintillator volume or just deposit quite a small fraction of its energy, it probably cannot satisfy the AD trigger criterion ($N_{\text{PMT}} \geq 45$ or $Q_{\text{sum}} \gtrsim 65$ p.e.) and would be ignored. As the gamma originating in the MO volume would more likely deposit a small fraction of its energy in the scintillator, the corresponding AD trigger efficiency is much worse. For the triggered events, the reconstructed energy spectra are shown in Figure 4.11.

For the events with $E_{\text{rec}} < 1.5$ MeV, most of them correspond to reconstructed vertices on the edge of the OAV where the gamma leakage or spill-in is easier. Particularly, some events were found to be like the PMT flashes which almost originate in the MO volume quite close to one or several PMTs. These flash-like events basically have $E_{\text{rec}} < 1.5$ MeV. The corresponding spectra or vertex distributions are shown in Figure 4.12. About 25% of the events originating in the MO volume with $E_{\text{rec}} < 1.5$ MeV are PMT flash-like. A negligible number of the PMT flash-like events originate in the scintillator volume.

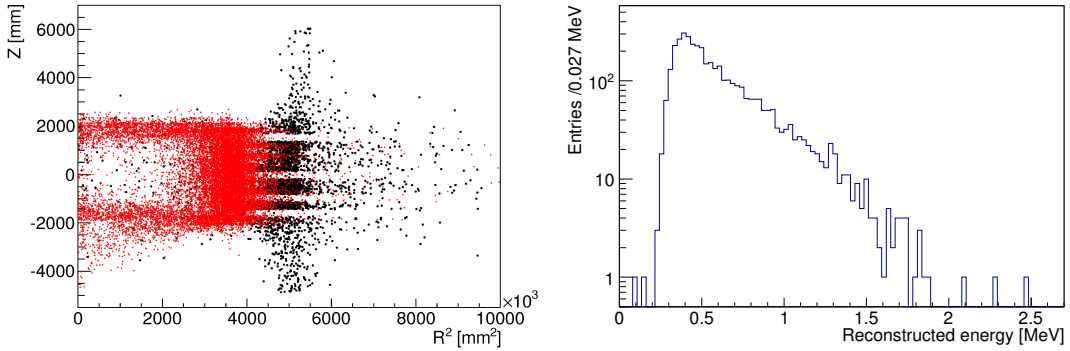


(a) Full volume.

(b) MO volume.

 Figure 4.11 Reconstructed energy spectra of the triggered 15.11-MeV γ events.


(a) Full volume.



(b) MO volume.

 Figure 4.12 $E_{\text{rec}} < 1.5$ MeV events. Left: vertex distribution where the black dots correspond to the PMT flash-like events and the red dots correspond to the rest events. Right: E_{rec} spectra of the PMT flash-like events.

The $\mu \pm 3\sigma$ energy cut was determined to be [14.5, 17.3] MeV for all the ADs. The efficiency depends on the size of the low energy tail of the full energy peak. Obviously, the tail is longer for the γ events originating in the MO volume.

The other selection criteria, e.g., muon vetoes, are the same as those for the nH

signals which have the identical veto efficiencies (82%, 85%, and 98% for EH1, EH2, and EH3). The coincidence cut (multiplicity = 1) efficiency (without the appearance of any other single event before or after within the coincidence time window) is still dominated by the single event rate and is basically the same as that for the IBD selection (without the appearance of any other single event to interrupt the existing IBD double coincidence). The value is approximately $e^{-R_s T_c} \cdot e^{-R_s T_c} \sim 98\%$.

4.2.2.3 Supernova neutrino NC- ^{12}C event rates

The NC- ^{12}C interaction rate for a supernova explosion at 10 kpc is estimated from the supernova neutrino spectra for different flavors, the cross section which is introduced in Equation (4-1), and the integrated luminosity (flux) of each flavor. A typical SN model is used here with $\langle E_{\nu_e} \rangle = 10$ MeV, $\langle E_{\bar{\nu}_e} \rangle = 12$ MeV, $\langle E_{\nu_x} \rangle = 20$ MeV, $\alpha = 2.3$, $F_{\nu_e}^0 : F_{\bar{\nu}_e}^0 : F_{\nu_x}^0 = 2.4:1.6:1.0$, and $L_{\text{total}} = 3 \times 10^{53}$ erg. The results are summarized in Table 4.5.

Table 4.5 The expected number of supernova neutrino NC- ^{12}C events in all the ADs (full volume including GdLS, LS, and MO) at Daya Bay from a supernova at 10 kpc with the typical parameters shown in text. $\langle \sigma \rangle$ is the averaged cross section considering the energy spectrum (up to 50 MeV) of supernova burst neutrinos.

Flavor	$\langle E_{\nu} \rangle$ (MeV)	$\langle \sigma \rangle$ (cm 2)	N_{event}
ν_e	10	0.79×10^{-43}	0.5
$\bar{\nu}_e$	12	2.1×10^{-43}	0.9
ν_x ($\times 4$)	20	1.4×10^{-42}	16.0
Total			17.4

As the cross section of NC- ^{12}C is approximately proportional to the neutrino energy squared, the fraction of supernova neutrinos with energy greater than 15.11 MeV dominates the averaged cross section in Table 4.5 as illustrated in Figure 4.13. Note that various SN models on ν_x (never observed to date) parameters (e.g., $\langle E_{\nu_x} \rangle$) would introduce a variation up to a factor of 2 on the N_{event} for the NC- ^{12}C interactions.

Considering the selection efficiency $\sim 40\%$, one can estimate that about 1 NC- ^{12}C event is expected in a single AD at Daya Bay for a supernova at 10 kpc.

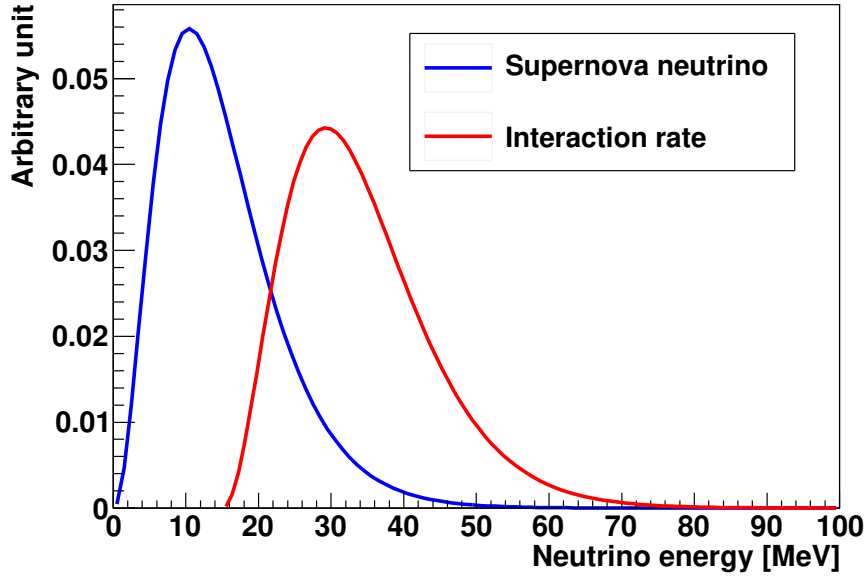


Figure 4.13 Normalized spectra of supernova neutrinos before and after convoluting with the NC- ^{12}C cross section. Blue: an example of supernova burst neutrino energy spectrum. Red: corresponding NC- ^{12}C interaction rates.

4.2.2.4 Selected NC- ^{12}C events (Backgrounds)

Since ~ 1 NC- ^{12}C event is expected in an AD for a supernova at 10 kpc, the magnitude of the expected number of background must be measured for a comparison. The rate per day of the selected NC- ^{12}C events (backgrounds) using the criteria in Table 4.3 is shown in Figure 4.14. The background event rates in a single AD are 8×10^{-5} Hz, 6×10^{-5} Hz, and 6×10^{-6} Hz for EH1, EH2, and EH3, respectively.

The E_{rec} spectra of the backgrounds are shown in Figure 4.15. Below 5 MeV, the background events are dominated by natural radioactivity. A bump in the 5-14 MeV region comes from the muon-induced ^{12}B which has a beta decay with $Q \sim 13.4$ MeV and $\tau \sim 29.1$ ms. Luckily, the NC- ^{12}C events are not contaminated by the muon-induced ^{12}B . Beyond 15 MeV, the background events are mainly from the muon-induced spallation neutrons (see vertex distribution in Figure 4.16).

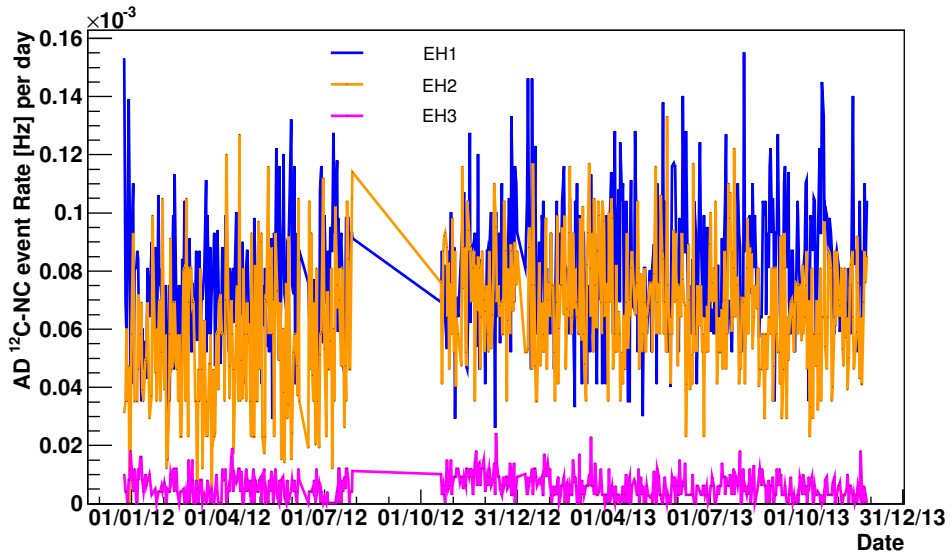
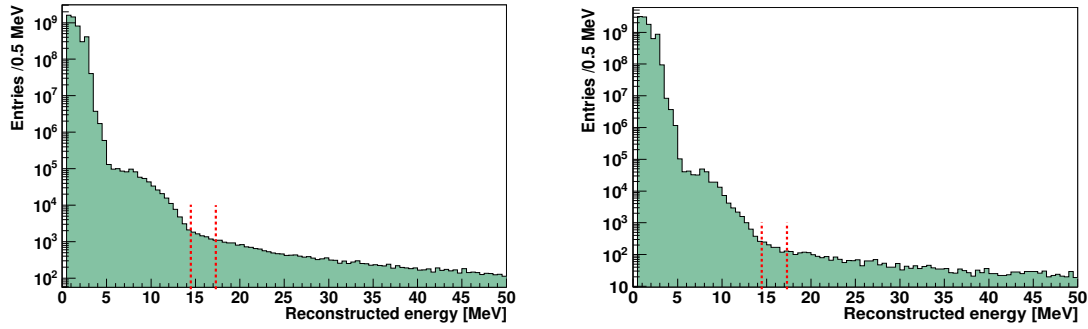


Figure 4.14 Average rates in a single AD of the selected NC- ^{12}C events (backgrounds) per day for each experimental hall. The dates are in the format of day/month/year.



(a) From the near site EH1.

(b) From the far site EH3.

Figure 4.15 Reconstructed energy spectra of 1-fold (single) backgrounds without the energy cut in EH1 and EH3. The energy cut is indicated by the two dashed lines.

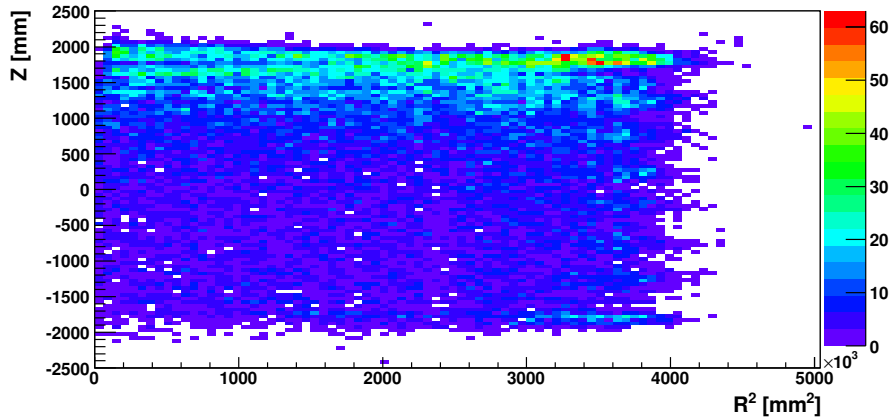


Figure 4.16 Reconstructed vertex distribution of 1-fold (single) backgrounds within 12-20 MeV.

4.3 Data sets for two types of analyses

The data sets for the search for supernova neutrino bursts are three independent data samples which are summarized in Figure 4.17.

Two types of analyses were performed which have different energy thresholds.

- A) A high energy threshold (> 10 MeV) analysis utilized the data samples in Figure 4.17(a) (in the red box with a 10-MeV cut) + Figure 4.17(b) (in the red box with a 10-MeV cut) + Figure 4.17(c) (within the vertical lines for 15.11-MeV gamma). This high energy threshold analysis would have a better signal-to-background ratio and a high sensitivity. The 10-MeV cut reduces the event rates from the two IBD samples by greater than two orders of magnitude.
- B) A low energy threshold analysis utilized the data samples in Figure 4.17(a) (in the red box) + Figure 4.17(b) (in the red box) to cover the low energy supernova neutrinos and perform a model-independent search.

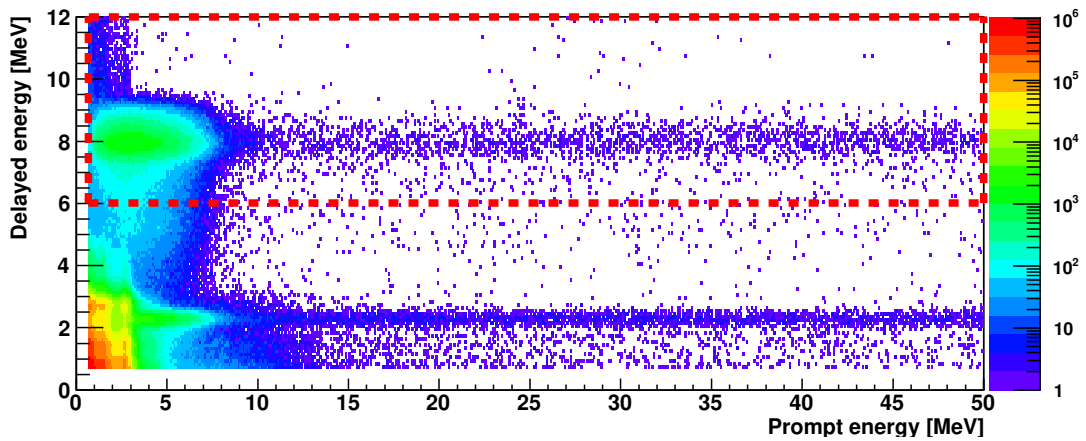
The events from the different analysis data samples are directly combined for each second to search for supernova neutrino bursts in a rate analysis. The directly-used event rates for each AD are all summarized below. In the offline analysis, the correlation caused by muon-induced spallations between two ADs can be ignored since a powerful water shield muon veto was applied in comparison with the online trigger. In analysis A the correlation was reduced by four orders of magnitude and in analysis B the correlation was reduced by two orders of magnitude.

The measured event rates are shown in Table 4.6 and Table 4.7. A few percent difference was observed between the two ADs in EH1 or EH2 in the analysis B mainly caused by the different numbers of reactor neutrino IBD events due to the different baselines from the ADs to the reactor cores.

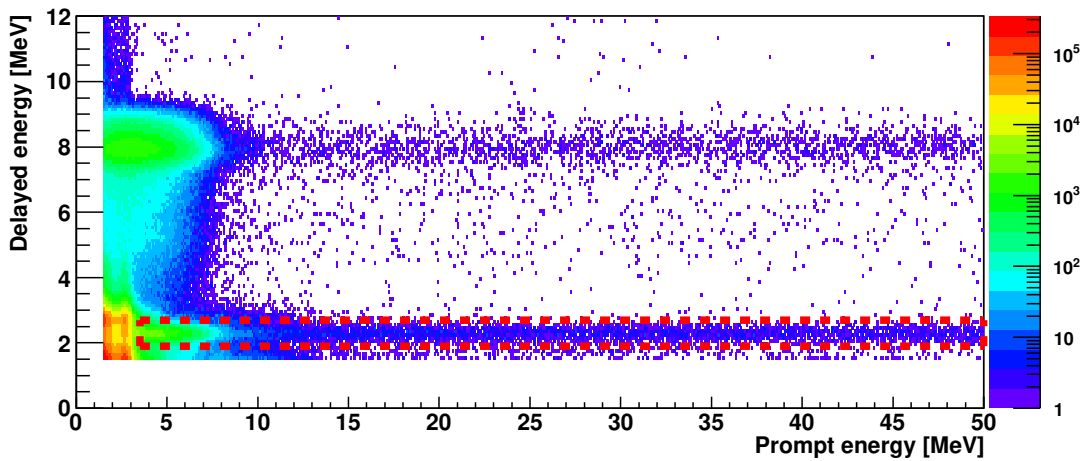
4.4 Search for supernova neutrino bursts

The search for supernova neutrino bursts has basically the same principle as that for the online supernova trigger. In general, two steps should be done:

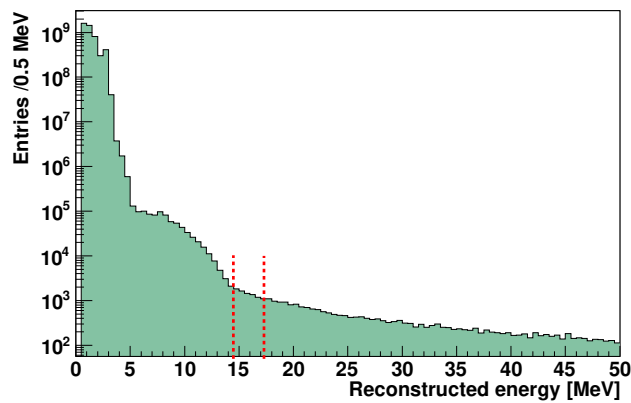
- 1) Search for any increases in the multi-AD event rates within the sliding 10-second windows.
- 2) Check the “event burst” in Step 1 against the additional features of supernova burst neutrinos as well as a coincidence inspection with astronomical observations.



(a) IBD nGd sample in the dashed red box.



(b) IBD nH sample in the dashed red box.



(c) NC- ^{12}C 15.11-MeV gamma sample between the two dashed lines.

Figure 4.17 Example of the three independent samples (the IBD nGd events, IBD nH events, and NC- ^{12}C events) for the search for supernova neutrino bursts at Daya Bay. Each AD has a set of the three data samples.

Table 4.6 The 6-AD period background event rates for analysis A and B. Simultaneous seconds: 16078630, about 98% of the total DAQ time.

Unit: 10^{-4} Hz		EH1		EH2		EH3	
		AD1	AD2	AD3	AD4	AD5	AD6
Analysis A	Rate	1.40	1.47	1.08	0.096	0.113	0.121
	Error	0.030	0.030	0.026	0.0077	0.0084	0.0087
Analysis B	Rate	85.5	86.7	79.5	11.9	11.7	11.8
	Error	0.23	0.23	0.22	0.09	0.09	0.09

Table 4.7 The 8-AD period background event rates for analysis A and B. Simultaneous seconds: 31322831, about 97% of the total DAQ time.

Unit: 10^{-4} Hz		EH1		EH2			EH3		
		AD1	AD2	AD3	AD4	AD5	AD6	AD7	AD8
Analysis A	Rate	1.62	1.52	1.27	1.29	0.118	0.117	0.112	0.125
	Error	0.023	0.022	0.020	0.020	0.0061	0.0061	0.0060	0.0063
Analysis B	Rate	86.8	88.2	82.2	80.6	12.0	11.9	11.9	11.9
	Error	0.17	0.17	0.16	0.16	0.06	0.06	0.06	0.06

The strategy of the offline search for supernova neutrino bursts is a little different with that of the online trigger. The false-alert^① rate threshold is not set to something like 1 per month but 1 per century which is comparable to the CCSN rate within the Milky Way. A high confidence search is intended instead. As supplementary, a false-alert rate threshold of 1 per year would be set to collect the suspicious candidates and the detailed information would be provided after all the checks in Step 2.

The supernova neutrino bursts were searched individually in the 6-AD period and 8-AD period. All the necessary definitions, mathematics and statistics have been described in Chapter 3.

① The false-alert here refers to the false determination of a supernova burst. To have consistent concepts in this thesis, this designation will be used consistently in this chapter.

4.4.1 Analysis A: high energy threshold (>10 MeV)

4.4.1.1 Results

Intuitive plots were used to determine the supernova neutrino bursts as shown in Figure 4.18. The plots present the measured rates versus predicted rates for all the observed combinations. The supernova neutrino burst candidates can be directly recognized with the marked false-alert rate threshold in this plot and the validation of the prediction is as well demonstrated. Any ‘abnormal’ event far away from the ‘normal’ cluster can be realized easily.

It should be emphasized that the background significance could be changed very much from 1 per months to 1 per century; however, the total number of the background events from all the ADs may just increase by 1 with different distributions among the ADs. As mentioned before, due to the low background event rate, any observed event would be treated as a golden one while the detection probability (sensitivity) of supernova explosions is slightly decreased (see Figure 4.20).

The $\pm 1\sigma$ statistical uncertainty was estimated using Equation (3-10) where the factor g is elaborated in Section A.2. Note that g is not monotonic with the occurrence rate r and also depends on the event distribution in multi-ADs, hence the $\pm 1\sigma$ limits of the predicted rates are kind of sawtoothed locally.

It was found that a false-alert rate threshold of 1 per 120 days (the next adjacent threshold is about 1 per 200 days) would remove all the combinations and no supernova neutrino burst was observed. A data-driven statistical interpretation of the results can be achieved, to illustrate why there was no fake supernova neutrino burst mimicked by background fluctuations with a false-alert rate of 1 per 120 days. Three fake supernova bursts are expected in the 8-AD period (~ 360 days).

The bottom plot of Figure 4.18 shows the combinations with the predicted rates around $10^{-6.77} = 1 / 68\text{-day}$ just on the vertical line of 1 per 120 days threshold, while the distribution of the counts for these combinations are shown in Figure 4.19. Each entry represents a combination and this figure is an imitation of a dozen of the numbers of the fake supernova bursts to appear in the 8-AD period with the probability (rate) of 1 per 68 days. The expected value is $362 \text{ days} \times 1/68\text{-day} = 5.3$ and the statistical derivation

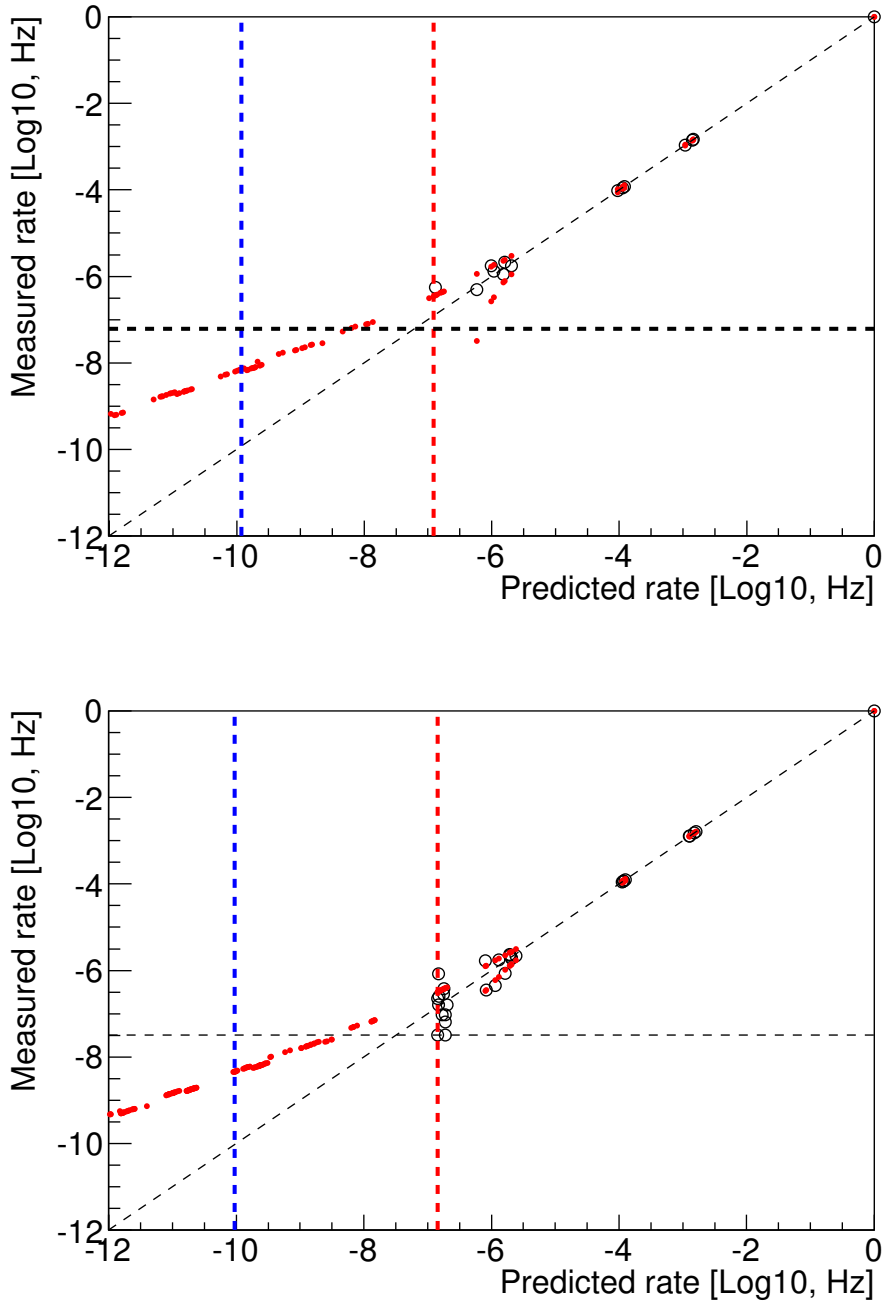


Figure 4.18 The measured rates versus predicted rates of all the observed combinations (represented by circles) in the data. The diagonal line refers to identical measured rates and predicted rates. The horizontal line indicates the minimum measured rate caused by the finite data sample size. The two vertical lines correspond to the false-alert rate thresholds of 1 per century (blue) and 1 per 120 days (red). The red dots denote the estimated $\pm 1\sigma$ limits for the measured rates. The combinations and the rates are discrete. Top: 6-AD period. Bottom: 8-AD period. See text for more explanations.

(uncertainty) is estimated to be

$$\sqrt{6.7 \times 31322831 \times \frac{1 \text{ sec}}{68 \text{ days}} \times \left(1 - \frac{1 \text{ sec}}{68 \text{ days}}\right)} = 6.0,$$

where 6.7 is the factor g and 31322831 is the number of seconds (10-s windows), i.e. statistical tests, in 8-AD period. Apparently, Figure 4.19 has consistent mean value and RMS with our estimation. And about 30% of the entries have zero counts. Analogously, the number of the fake supernova neutrino bursts with a false-alert rate threshold of 1 per 120 days would have a larger probability than 30% to be zero since the combinations beyond the false-alert rate threshold have smaller occurrence rates than 1 per 68 days.

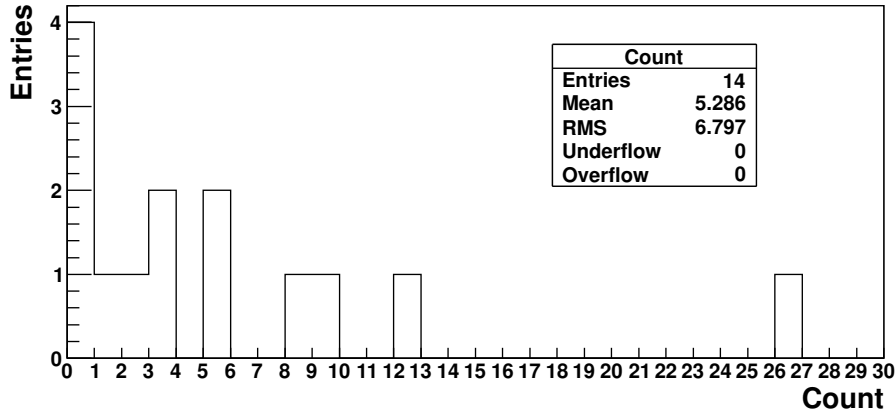


Figure 4.19 Distribution of the counts (in 8-AD period) of the combinations (14 in total) with a quite similar occurrence rate of 1 per 68 days.

4.4.1.2 Detection probability

To evaluate the detection probability (sensitivity) of the offline search, three quantities (background rate, a false-alert threshold, and the number of supernova neutrino signals) were calculated based on the previous sections.

- 1) Background rate: Table 4.6 and Table 4.7.
- 2) False-alert threshold: 1 per century and 1 per 120 days.
- 3) Number of supernova neutrino signals: ~ 10 (1 from NC- ^{12}C interaction) in an AD for a supernova at 10 kpc, which considers the detection efficiencies (64% for the IBD signals with a target mass of 42 t, and 40% for the NC- ^{12}C signals with a target mass of 78 t). In addition, the muon veto efficiencies and the multiplicity cut

efficiency should also be included. The 64% selection efficiency for the IBD signals is smaller than the efficiency of 72% as introduced in Section 4.2.1.2 mainly due to the 10-MeV prompt energy cut.

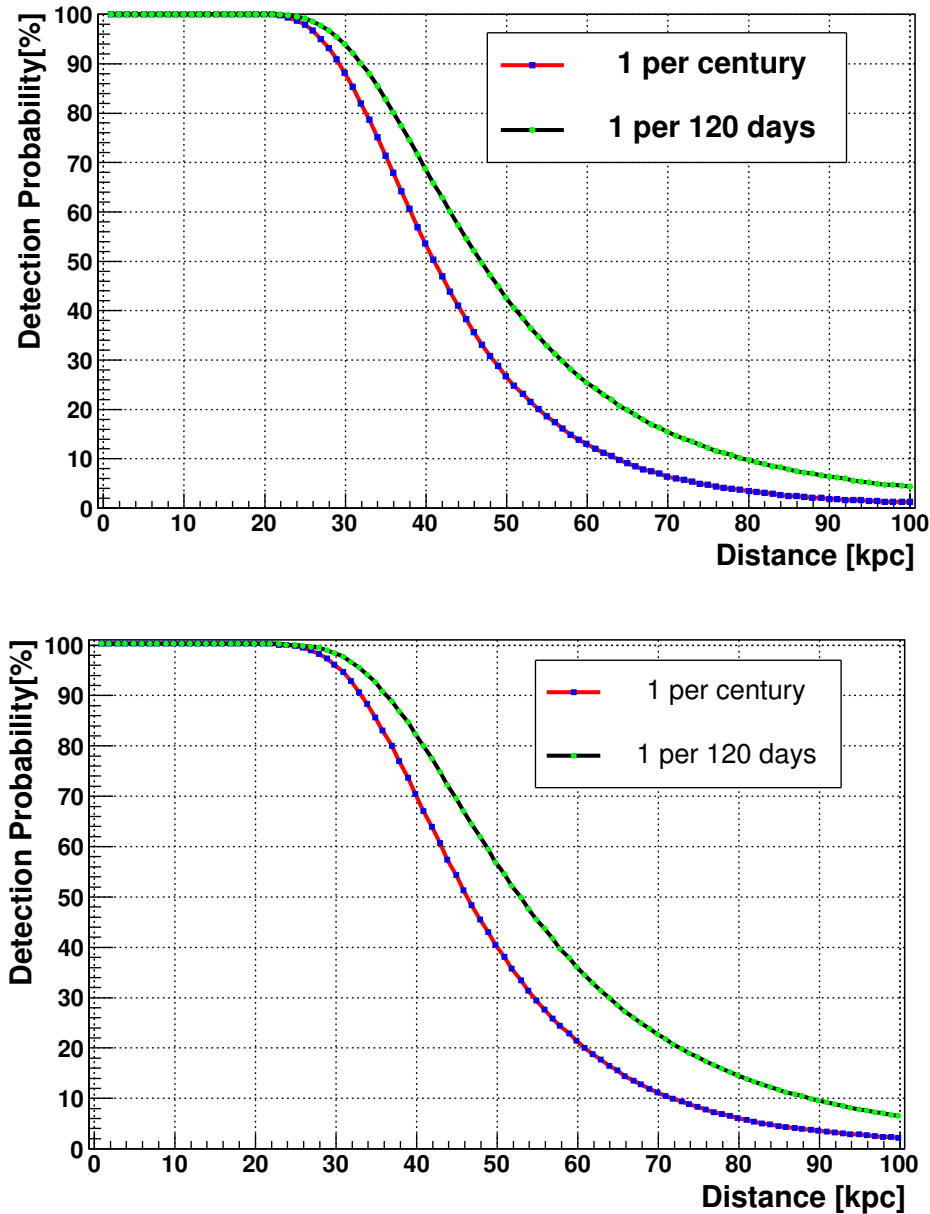


Figure 4.20 Detection probability of supernova explosions as a function of the distance to the Earth. Top: 6-AD period. Bottom: 8-AD period. The two lines in the plot correspond to the false-alert rate thresholds of 1 per century and 1 per 120 days.

The detection probability increases significantly with respect to that for the online trigger especially for the larger distances. Due to the quite high signal-to-background ratio, a small gain from the multi-AD configuration is obtained in the detection probability. But

for a large distance, this gain becomes considerable with a relatively small signal-to-background ratio.

The detection probability with the full configuration of 8 ADs is also compared with that from the LVD experiment which has 1 kiloton liquid scintillator and 0.85 kiloton iron tanks (840 counters/tanks in total). LVD did the search for supernova neutrino bursts with a trigger-level analysis including all possible interaction channels with the energy threshold at 10 MeV. The results are shown in Figure 4.21.

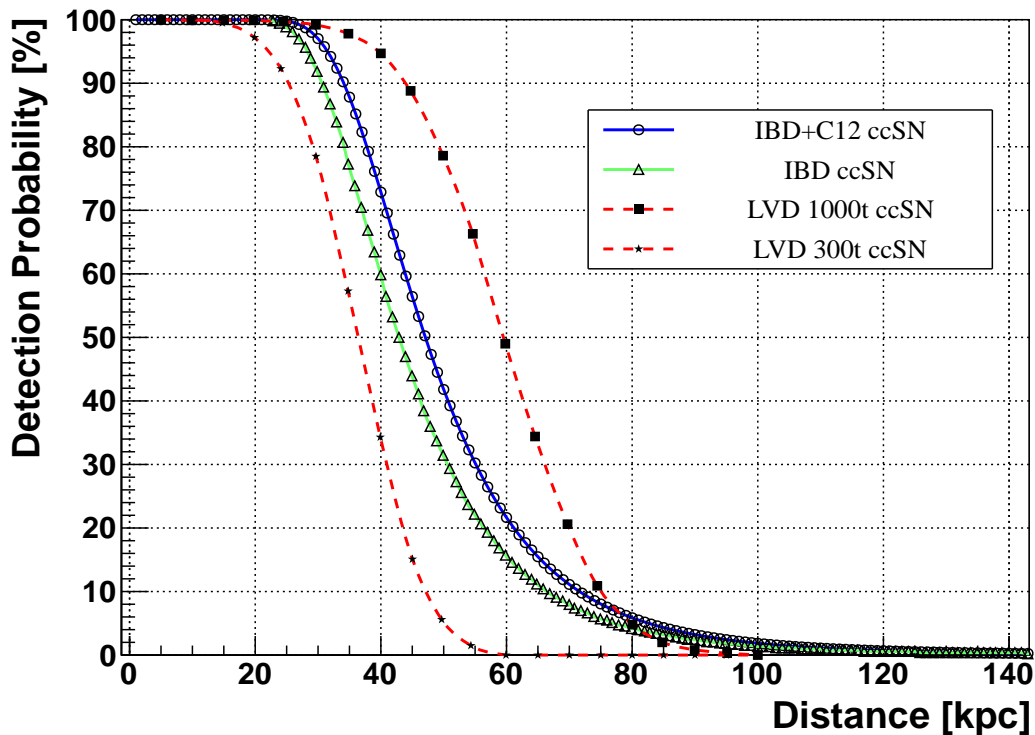


Figure 4.21 Detection probabilities for the Daya Bay and the LVD experiments, both of which have a type of 1 per century false-alert rate threshold. The two lines for the LVD experiment correspond to a 300 t liquid scintillator period at the beginning and a 1000 t liquid scintillator period later up to now. The contribution of the NC- ^{12}C channel at Daya Bay is also indicated by an IBD-only curve.

The LVD 300-t curve corresponds to roughly the same target mass as Daya Bay including the iron tanks. A significantly larger detection probability at Daya Bay was obtained mainly due to the low background rate and the multi-AD configuration in the three experimental halls. It is noted that the low background rate is not attributable to cosmogenic muons since LVD has a 3600 m.w.e. overburden. The background rate is reduced mainly due to the detector capability with a sophisticated analysis method.

The gain in sensitivity stemming from the NC- ^{12}C events ($\sim 10\%$ of the IBD events) is indicated in Figure 4.21. As shown in Table 4.5, the event rate strongly depends on ν_x ($x = \mu, \tau$) neutrinos, the average energy of which is quite uncertain up to now. The event rate of NC- ^{12}C has a large variation which can be increased by a factor of 2 or even more.

4.4.1.3 Upper limit on the rate of CCSN

Since no supernova neutrino bursts were observed within the 549 days (DAQ time) of data, a 90% C.L. upper limit on the rate of CCSN within the Milky Way (100% sensitivity) is calculated by

$$\frac{2.3}{549 \text{ days}} \simeq 1.5 \text{ yr}^{-1}.$$

As the online supernova trigger system is also fully sensitive to the CCSN within the Milky Way, the 90% C.L. upper limit can be lowered to 0.53 /yr including the live time of the online supernova trigger system to date.

The current most stringent upper limit on the rate of CCSN out to 25 kpc was given by the LVD experiment from 21 years of data. The upper limit is just proportional to the inverse of the data time within 100%-sensitive distances.

4.4.2 Analysis B: low energy threshold

4.4.2.1 Results

The measured rates versus the predicted rates of all the combinations for the low energy threshold analysis are plotted in Figure 4.22.

For the false-alert rate threshold of 1 per year, two candidates in total were observed for the 6-AD period (1 candidate) and the 8-AD period (1 candidate) as shown in Figure 4.22. We will provide the detailed information of such kind of candidates (see Section 4.4.2.3) after all the checks even though a solid conclusion is difficult to make.

4.4.2.2 Detection probability

The detection probabilities are shown in Figure 4.23.

Compared with the online supernova trigger, the detection probability is just slightly increased since the background event rates in EH1 and EH2 are reduced by a factor of 2 but the live time is as well decreased by about 10% due to the IWS/OWS muon veto. The

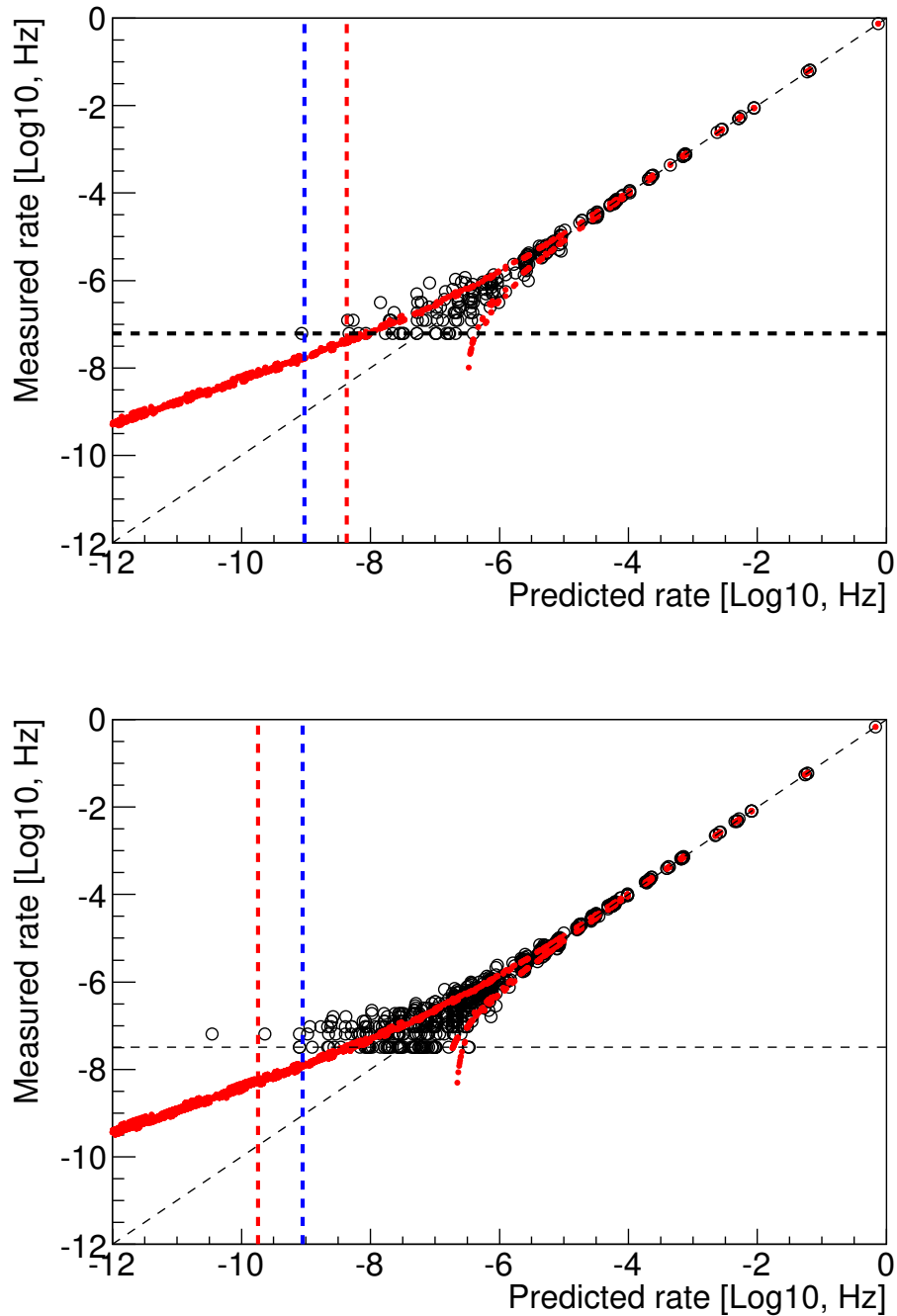


Figure 4.22 The measured rates versus predicted rates of all the observed combinations (represented by circles) in the data. The diagonal line refers to the identical measured rates and predicted rates. The horizontal line indicates the minimum measured rate caused by the finite data sample size. The two vertical lines correspond to the false-alert rate thresholds of 1 per year and 1 per 3 months, respectively. The red dots denote the estimated $\pm 1\sigma$ limits for the measured rates. The combinations and the rates are discrete. Top: 6-AD period. Bottom: 8-AD period. See text for more explanations.

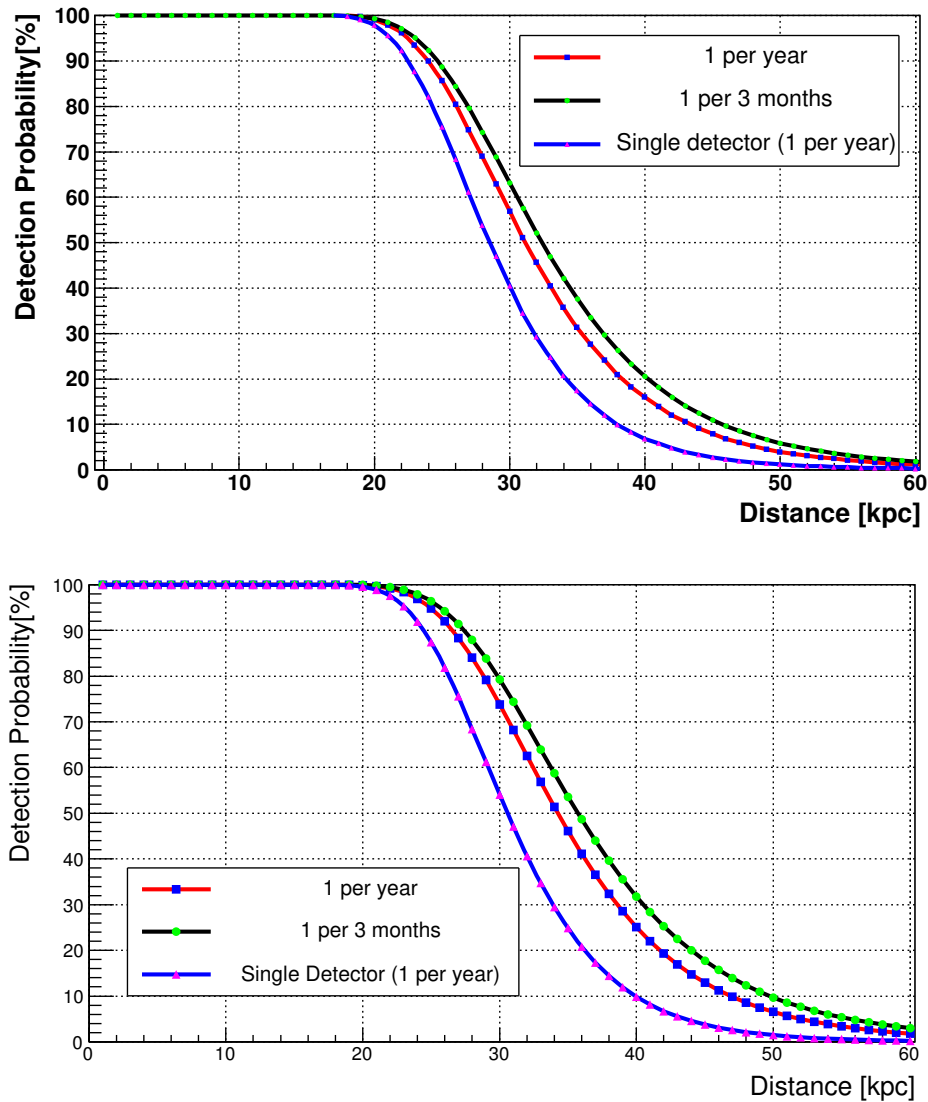


Figure 4.23 Detection probability of supernova explosions as a function of the distance to the Earth. Top: 6-AD period. Bottom: 8-AD period. The three lines in either plot from top to bottom correspond to the multi-AD cases with the false-alert rate thresholds of 1 per 3 months and 1 per year, and the case of a mass-equivalent single detector for comparison with the false-alert rate threshold of 1 per year.

detection probability is calculated based on the typical supernova model; however, the motivation/advantage of the low energy threshold analysis is to cover the neutrino energy region below 10 MeV. In this region, no supernova neutrinos have been observed so far, and the model is still quite uncertain.

4.4.2.3 Two candidates

Two candidates were observed in the offline analysis with a low energy threshold. After a careful data quality check on the two candidates, no obvious unphysical issues were found. They are all far from the preceding muons and the characteristics of the prompt and delayed signals (prompt-delayed vertex distance and time difference) also indicate that the two candidates are overall IBD-like.

The uniformity checks based on Equation (3-12) are ignored as a consequence of the good data quality. A significance level for the candidate as a real supernova neutrino burst was calculated using the probability of each combination. The number of the supernova burst neutrinos in a single AD was fitted with the method of maximum-likelihood. In this fit, the EH-dependent muon veto efficiencies and the expected background rates in each AD are included. The significance level of signal is defined as

$$S = \sum_i P_i(P_i \leq P_s), \quad (4-3)$$

where i indicate different combinations of the number of events and P_s is the probability of the candidate which is assumed to be a real supernova neutrino burst.

Similarly, assuming these events are all from the background, a significance level of background can also be defined using an expression like Equation (4-3) which is equivalent to the false-alert rate threshold.

Detailed information about the two candidates is shown below.

Candidate 1 This candidate appeared in the 6-AD period (186 days) with a total number of 7 IBD events. The significance level of signal (Equation 4-3) is 21%. The significance level of background is 0.91 yr^{-1} (1 per 401 days). The time chart of the events in this candidate is shown in Table 4.8. The prompt vs. delayed signal energy distribution is shown in Figure 4.24.

The prompt energy spectrum of the events is shown in Figure 4.25. Based on the measured background spectra for the nH sample and nGd sample in each experimental hall, the events are expected to be from the background. A sum of several normalized background spectra corresponding to each event in the candidate is shown as the expected spectrum. For each event, the normalized spectrum is prepared according to its experimental hall and data sample (nGd or nH). A jump of the “background spectrum” in

Table 4.8 Time chart of the events in Candidate 1. The nH signals are marked. Indices denote the order in the time sequence which are also indicated in Figure 4.24.

		Start time: 1332547520 (unix time), 08:05:20 Mar. 24, 2012 (Beijing time)									
		1 s	2 s	3 s	4 s	5 s	6 s	7 s	8 s	9 s	10 s
EH1	AD1	1									1
	AD2			1 (nH)			1				
EH2	AD3			2 (nH)							1 (nH)
	AD4										
EH1	AD5										
	AD6										
Index		1		2-4			5				6-7

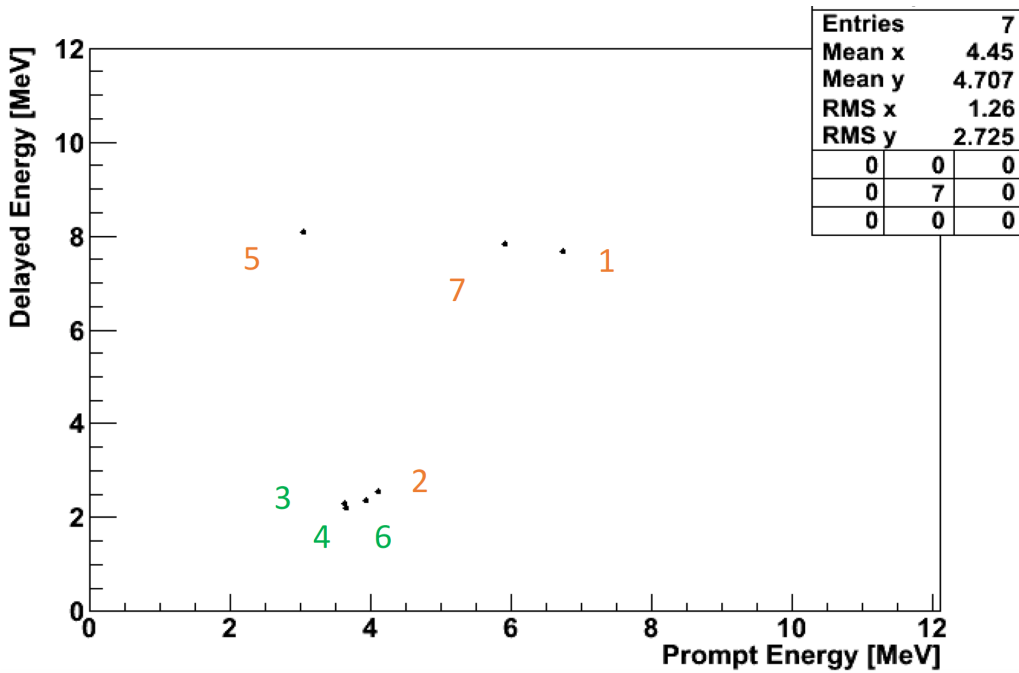


Figure 4.24 The prompt vs. delayed signal energy distribution of the events in Candidate 1. Time indices are indicated. One color corresponds to one experimental hall.

Figure 4.25 is due to the 3.5-MeV cut on the nH sample. In addition, the prompt energy spectrum in was fitted to the supernova neutrino spectrum with a floating $\langle E \rangle$. The fit result is shown in the statistics label. Due to the low statistics of the events, the fit of supernova neutrino spectrum makes little sense except to obtain fitted $\langle E \rangle$ of these events.

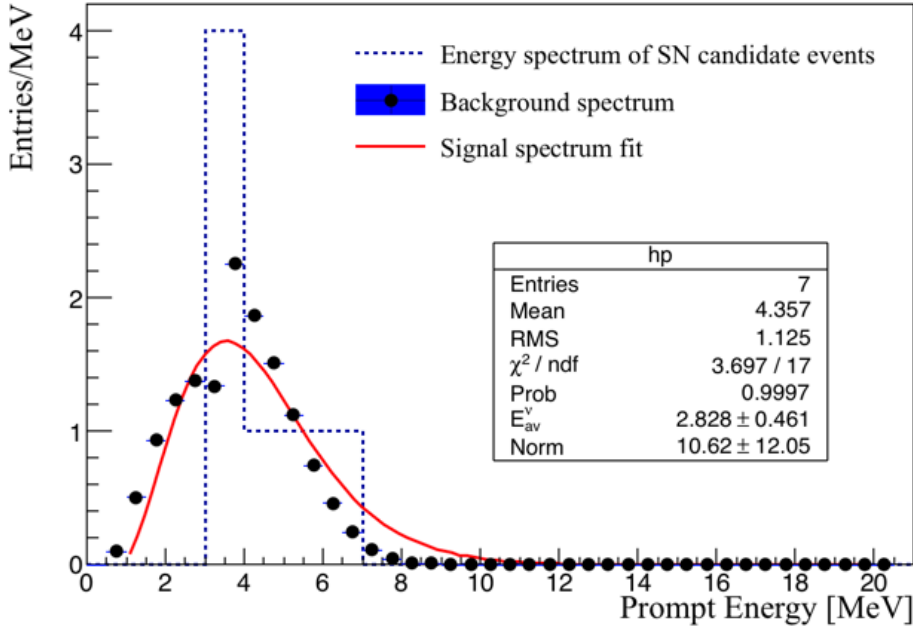


Figure 4.25 Prompt energy spectrum of the events in Candidate 1 (dashed histogram). The black dots represent the expected spectrum assuming the events are all from the background. The red curve is the fit of the supernova neutrino energy spectrum. See text for more explanations.

Candidate 2 This candidate appeared in the 8-AD period (362 days) with a total number of 7 IBD events. The significance level of signal is 25%. The significance level of background is 0.27 yr^{-1} (1 per 1335 days). The time chart of the events in this candidate is shown in Table 4.9. The prompt vs. delayed signal energy distribution is shown in Figure 4.26. The prompt energy spectrum of the events is shown in Figure 4.27. More explanations can be referred to the text for Candidate 1.

4.4.2.4 Coincident supernovae with the two candidates

A coincidence inspection of the astronomical observations was also performed using the two supernova catalogs – Asiago (<http://graspa.oapd.inaf.it/>) and Rochester (<http://rochesterastronomy.org/supernova.html>). No coincident supernova was found in the two catalogues. The filter conditions are:

- 1) CCSN type.
- 2) Distance $< 1 \text{ Mpc}$ or supernova apparent magnitude (brightness as seen by an observer on the Earth) < 10 (~ 100 times dimmer than SN1987A).
- 4) Date ± 2 months.

Table 4.9 Time chart of the events in Candidate 2. The nH signals are marked. Indices denote the order in the time sequence which are also indicated in Figure 4.26.

		Start time: 1377578263 (unix time), 12:37:43 Aug. 27, 2013 (Beijing time)									
		1 s	2 s	3 s	4 s	5 s	6 s	7 s	8 s	9 s	10 s
EH1	AD1										
	AD2		1							1	
EH2	AD3						1	1 (nH)	1		
	AD4										
EH3	AD5										
	AD6										
	AD7	1									
	AD8			1							
Index	1	2	3				4	5	6	7	

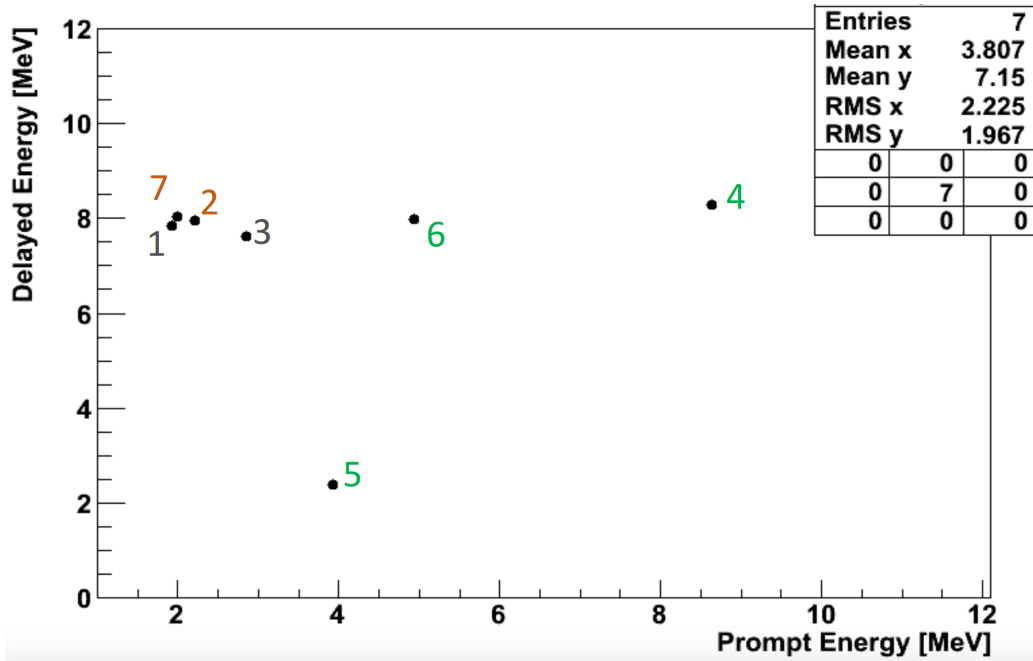


Figure 4.26 The prompt vs. delayed signal energy distribution of the events in Candidate 2. Time indices are indicated. One color corresponds to one experimental hall.

4.5 Search for low energy neutrinos associated with astrophysical bursts

This section will briefly present two special efforts to search for low energy neutrinos in Daya Bay associated with SN2014J in 2014 and the gravitational-wave event GW150914 in 2015, in addition to the search for supernova neutrino bursts using the Daya Bay data

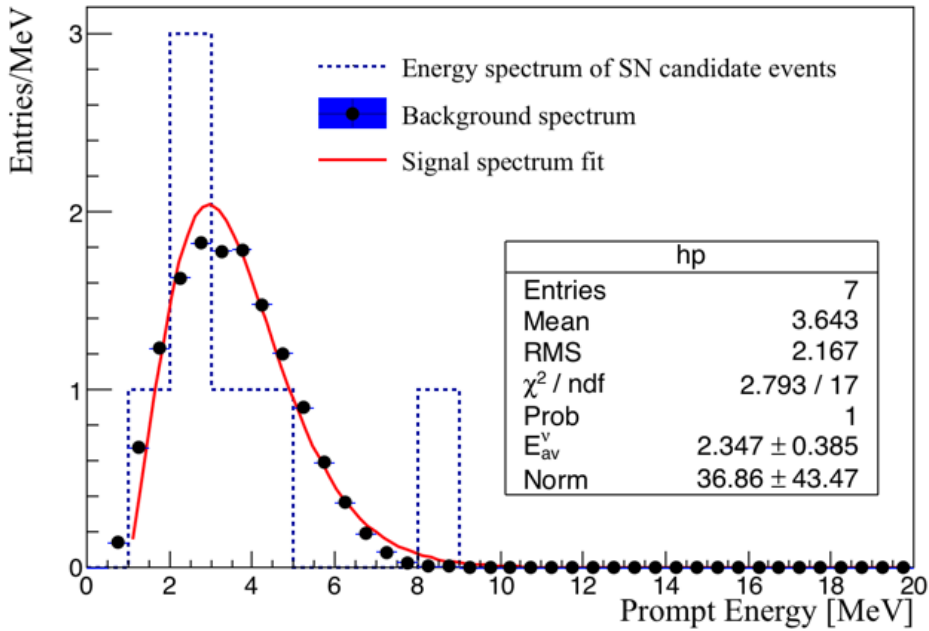


Figure 4.27 Prompt energy spectrum of the events in Candidate 2 (dashed histogram). The black dots represent the expected spectrum assuming the events are all from the background. The red curve is the fit of the supernova neutrino energy spectrum. See text for more explanations.

set acquired from 2011 December to 2013 November. The conclusion is that there is no implication of any neutrino bursts associated with the two astrophysical bursts.

4.5.1 SN2014J

SN2014J is a type Ia supernova in the ‘Cigar Galaxy’, M82, discovered by Steve Fossey on January 21, 2014. It is special among the hundreds of known supernovae (see Asiago supernova catalog) because it was the closest (~ 3.5 Mpc) type Ia supernova discovered so far, reaching an apparent magnitude of ~ 11 which is roughly 100 times dimmer than SN1987A^① but still bright enough for amateur astronomers to observe. The gamma emission from SN2014J was detected near the maximum optical light curve on January 31, 2014^[141]. Figure 1.2 in Chapter 1 just shows the images for SN2014J.

Few neutrino events would be expected to be associated with SN2014J because

- In theory, quite a few neutrinos can be emitted by a type Ia supernova since the explosion is driven by thermal nuclear interactions.
- This supernova is 3.5 Mpc away and far beyond the sensitive distance of the Daya

^① In general, a type Ia supernova is roughly 100 times brighter than a core-collapse supernova. Therefore, a type Ia supernova at 3.5 Mpc (SN2014J) could just be 100 times dimmer than a type II supernova at 50 kpc (SN1987A).

Bay experiment.

However, regarding the particularity of SN2014J as mentioned above, an effort was still made to search for potential low energy neutrinos associated with this supernova using the acquired data from 2013 December to 2014 February. The method and algorithm are the same as that of searching for supernova neutrino bursts. No neutrino event bursts were identified given a false-alert rate threshold of 1 per year with a total number of IBD events in 8 ADs of 6^①.

The time range for such a search is quite uncertain because of the unknown start time of the supernova explosion according to the observation of electromagnetic explosion.

4.5.2 GW150914

4.5.2.1 Introduction

The first gravitational wave event (GW150914) was observed by LIGO on September 14 2015 at 09:50:45 UTC^[94], at a significance of greater than 5.1σ . This event was suggested to be due to a merger of two black holes (BH-BH merger) with masses $36_{-4}^{+5}M_{\odot}$ and $29_{-4}^{+4}M_{\odot}$. The final black hole mass is $62_{-4}^{+4}M_{\odot}$, radiating $3_{-0.5}^{+0.5}M_{\odot}c^2$ in gravitational waves. The coalescence of the two black holes occurs at a luminosity distance of 410_{-180}^{+160} Mpc within about 0.2 s.

There is no mechanism so far proposed for neutrino or electromagnetic emission from a BH-BH merger. Though both neutrinos and gamma-ray bursts can be emitted from the accretion disk of a black hole^[142,143], it is most likely that an accretion disk is not allowed during a BH-BH merger. Therefore, neither neutrino signals nor gamma-ray bursts are expected. However, a weak gamma-ray burst was reported coincidentally 0.4 s after GW150914 by the *Fermi* Gamma-ray Burst Monitor^[144]. This result may imply that some accretion disk appears or some other mechanisms, thus motivating a search for neutrino signals associated with it.

Within the time window [-500, 500] s relative to the gravitational wave events, ANTARES and IceCube^[145] searched for the neutrino signals above ~ 100 GeV associated with GW150914 and KamLAND^[146] searched for the neutrino signals below ~ 100 MeV associated with GW150914 and GW151226. No coincident neutrino events were identified. Super-Kamiokande searched for both the high energy neutrino events and the low energy neutrino events^[147] with null results.

① Precisely, the IBD event distribution in multi-ADs is considered for a candidate decision.

4.5.2.2 Coincident search

The IBD events with prompt signal energies < 50 MeV were used to search for coincident electron antineutrino signals at Daya Bay with GW150914. Selection criteria are the same as the search for supernova neutrino bursts with the low energy threshold (analysis B), since the neutrino spectrum emitted by an accretion disk of a black hole is expected to approximately have a Fermi-Dirac distribution with an average energy of ~ 10 MeV^[142,143]. Single events are not used for electron neutrino signals due to the low signal-to-background ratio as well as the absence of corresponding sophisticated detector response model so far.

The neutrino signals are assumed to be within $[-500, 750]$ s around the GW detection time, which results from the time difference $[-500, 500]$ s between GW emission and high energy neutrino emission predicted by Ref. [148] and the time-of-flight delay of a massive neutrino $[0, 250]$ s. The time-of-flight delay can be expressed as^[6]

$$\Delta t = \frac{D}{v} - D \simeq \frac{m^2}{2E^2} D = 5.15 \text{ ms} \left(\frac{m}{\text{eV}} \right)^2 \left(\frac{E}{10 \text{ MeV}} \right)^{-2} \frac{D}{10 \text{ kpc}}, \quad (4-4)$$

where D is distance, v is neutrino velocity, E is neutrino energy, and m is neutrino mass which is assumed to be ~ 1 eV. For $E = 10$ MeV, $\Delta t \approx 250$ s.

The IBD events with prompt energies in $[0.7, 50]$ MeV of the nGd signals and $[3.5, 50]$ MeV of the nH signals were searched for in the time window $[-500, 750]$ s, and the results are shown in Figure 4.28. The stationarity of the IBD event rate in the $[-10, 40]$ hours window was checked and the event rate was statistically consistent. The number of IBD events in the $[-1500, 1750]$ s window is also consistent with the measured IBD event rate.

Due to the reactor neutrino background mainly below 8 MeV, a 8-MeV energy cut was accordingly applied to the selected IBD data sample. The residual background rates were found to be $(1.6 \pm 0.3) \times 10^{-4}$ Hz, $(1.3 \pm 0.3) \times 10^{-4}$ Hz, and $(5.7 \pm 1.8) \times 10^{-5}$ Hz for EH1, EH2, and EH3, respectively. The expected number of background in the $[-500, 750]$ s is calculated, which is 0.43 from all the ADs in the three experimental halls. Since no events were found (applying a 8-MeV energy cut) within the $[-500, 750]$ s window of GW151904, the 90% C.L. upper limit on the IBD events is calculated to be $N_{90} = 2.01$ using the Feldman-Cousins method^[149].

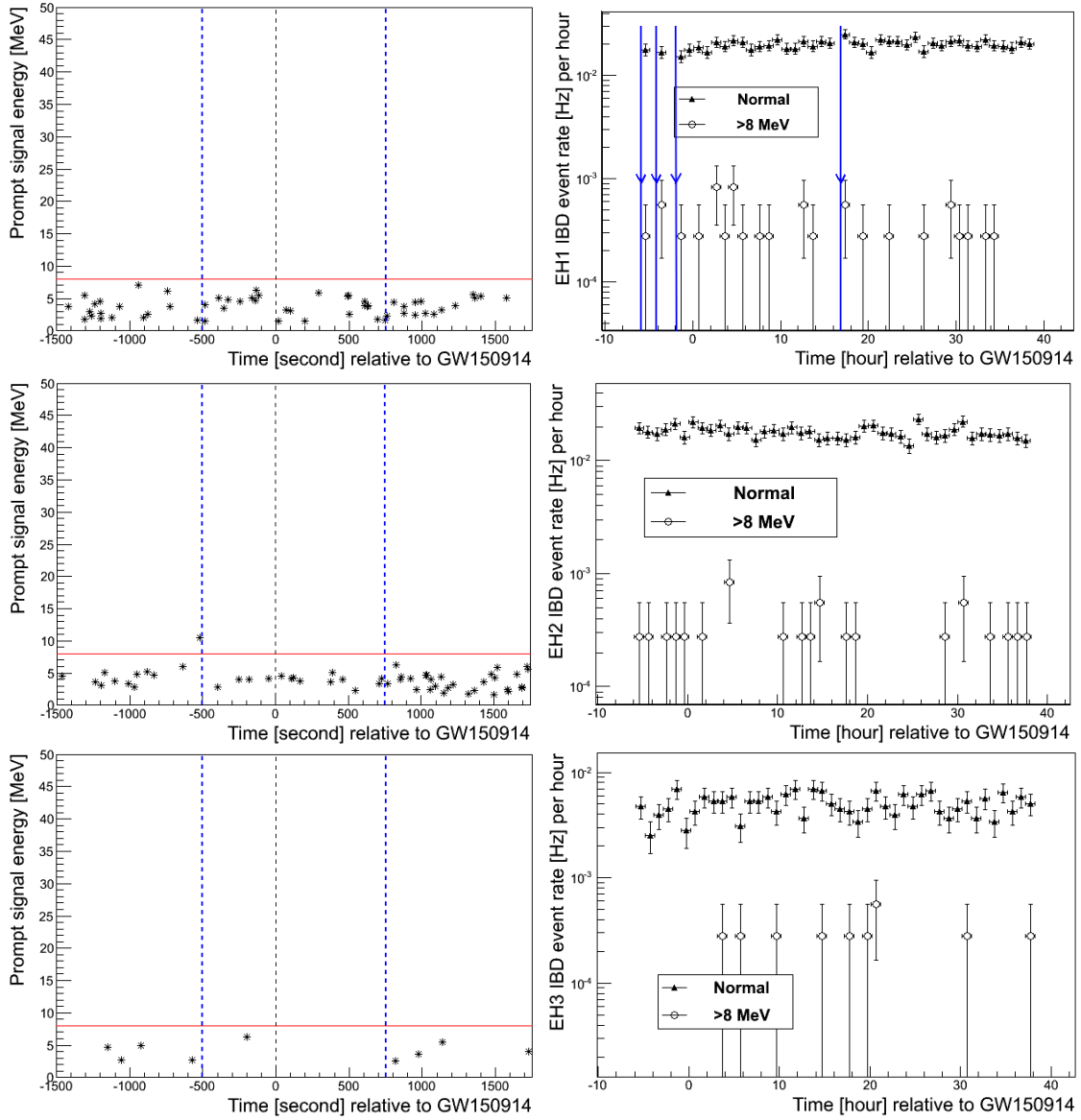


Figure 4.28 The IBD events around GW150914 from the three experimental halls (EH1, EH2, EH3 from top to bottom). Left: Prompt signal energies of the IBD events in the $[-1500, 1750]$ s window to GW150914 (time = 0, indicated by dashed black line). Two blue dashed lines indicate the $[-500, 750]$ s window. The horizontal red line corresponds to 8 MeV energy cut. Right: IBD event rate (Hz) per hour for each experimental hall. ‘Normal’ represents the results without additional energy cut. ‘>8 MeV’ represents the results with a 8-MeV energy cut (red line in the left plot). The absence of some ‘>8 MeV’ points is due to the zero event rate in that hour. Three vertical blue arrow lines indicate the start times of different physics runs merely for EH1.

4.5.2.3 Fluence and Luminosity

The fluence upper limit, F_{90} , of electron anti-neutrinos at the detector is calculated based on N_{90} , the total number of target protons N_p , the live time efficiency ϵ_{live} (due to the muon veto and multiplicity cut efficiencies), the detection efficiency ϵ_d , the normalized

neutrino energy spectrum $\lambda(E_\nu)$, and the IBD cross section $\sigma(E_\nu)$,

$$F_{90} = \frac{N_{90}}{N_p \int \sigma(E_\nu) \lambda(E_\nu) dE_\nu \epsilon_{\text{live}} \epsilon_d}, \quad (4-5)$$

which is translated into the upper limit of luminosity.

In Daya Bay, ϵ_{live} is different for each experimental hall. N_p and all the other efficiencies except the 8-MeV prompt energy cut efficiency can be seen in Table 4.2 or the text in Section 4.2.1.2. In the calculation, the nGd signals, the nH signals in GdLS volume, and the nH signals in LS volume are considered individually.

The normalized neutrino spectrum $\lambda(E_\nu)$ in tens of MeV is assumed to be a Fermi-Dirac distribution^[142,143], which can be expressed as Equation (1-10) with $\alpha \approx 2.3$. The other parameter $\langle E_\nu \rangle$ is going to be scanned from 1 MeV to 50 MeV, resulting in a varying prompt energy cut efficiency. Without neutrino oscillation, the resulting F_{90} as a function of the average energy $\langle E_\nu \rangle$ is shown in Figure 4.29 as well as the upper limits on the total luminosity at 410 Mpc.

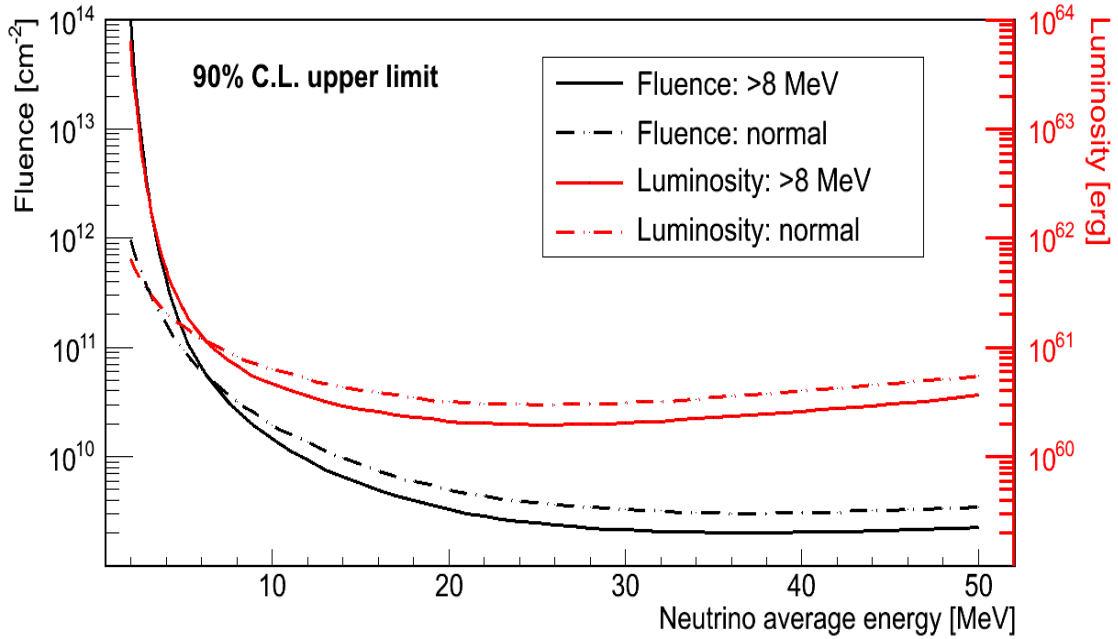


Figure 4.29 The 90% C.L. upper limits on $\bar{\nu}_e$ fluence at the detector and the translated luminosity at 410 Mpc as a function of the average energy of Fermi-Dirac distribution. The black lines (below) correspond to the fluence upper limits. The red lines (above) correspond to the luminosity upper limits. The dashed dot lines correspond to the normal selection without additional 8-MeV cut. The solid lines correspond to the augmented selection with 8-MeV prompt energy cut.

The upper limit increases rapidly in the low energy region for the ‘normal’ lines due to the decreasing efficiency by the 8-MeV cut. Analogously, a slight upward trend of the fluence upper limits with the increasing energy in tens of MeV due to the 50-MeV truncation of the prompt energy selection. This trend is obvious for the luminosity upper limits due to the presence of another E_ν term in the translation.

Based on Figure 4.28, the IBD event rates with the normal selection criteria are $(1.96 \pm 0.36) \times 10^{-2}$ Hz, $(1.76 \pm 0.33) \times 10^{-2}$ Hz, and $(4.64 \pm 1.71) \times 10^{-3}$ Hz for EH1, EH2, and EH3, respectively. The expected number of background events in [-500, 750] s window is ~ 52 . Luckily, the observed number of background events in this time window with respect to GW150914 was 39 in total, which is about 2σ smaller than expected. As a consequence, the 90% C.L. upper limit of 3.08 can be obtained by the Feldman-Cousins method^① which is still consistent with the case with an additional 8-MeV prompt energy cut.

With an assumption that the neutrino energy spectrum is a δ -function $\delta(E - E_\nu)$, F_{90} in Equation (4-5) can be rephrased as

$$F_{90}(E_\nu) = \frac{N_{90}}{N_p \int \sigma(E_\nu) g(E_{\text{rec}}, E_\nu) dE_{\text{rec}} \epsilon_{\text{live}} \epsilon_d}, \quad (4-6)$$

where $g(E_{\text{rec}}, E_\nu)$ is the detector energy response to E_ν . Here just the energy resolution is considered. The resulting F_{90} is shown in Figure 4.30. The steps of the curves are all attributable to energy cuts at some points.

Due to the uncertainty of the distance for GW150914, the luminosity can be thus given by

$$L_{\text{tot}} \leq L_{90} \left(\frac{D_{\text{GW}}}{410 \text{ Mpc}} \right)^2 \text{ erg}, \quad (4-7)$$

where L_{90} is the upper limits shown in Figure 4.29 and Figure 4.30.

4.5.2.4 Conclusion

Low energy electron anti-neutrinos associated with the first-discovered GW150914 were searched for at Daya Bay. No coincident IBD events were identified. Given two assumptions of the neutrino energy spectrum, a monochromatic or a Fermi-Dirac distri-

^① The upper limit can also deviate due to the background fluctuation. See Ref. [150].

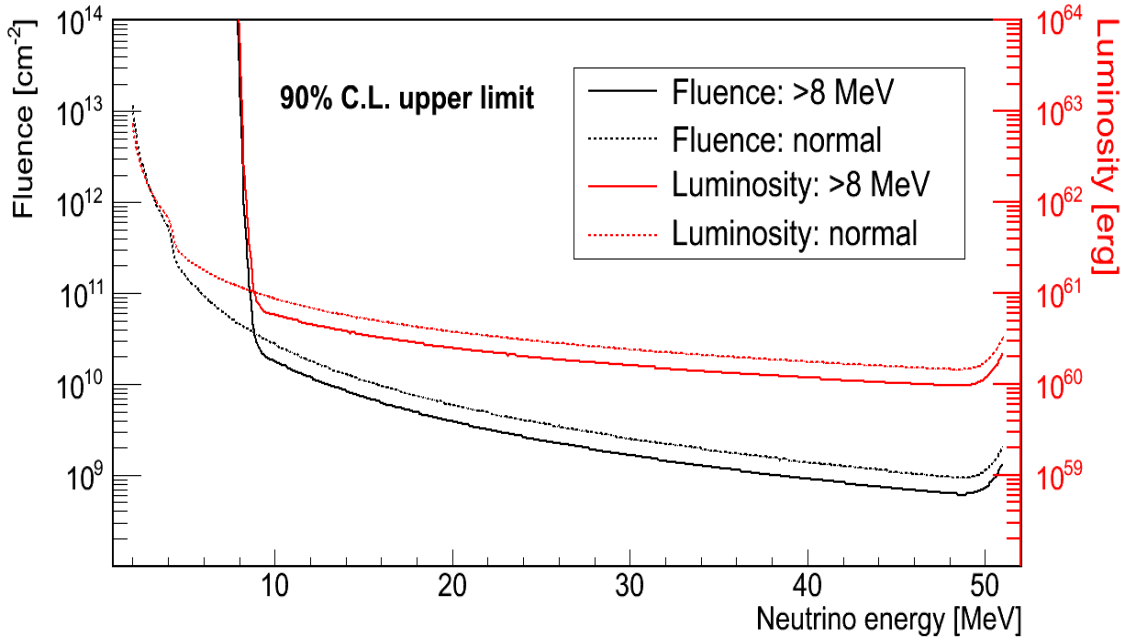


Figure 4.30 The 90% C.L. upper limits on $\bar{\nu}_e$ fluence at the detector and the translated luminosity at 410 Mpc as a function of the neutrino energy assuming a monochromatic spectrum. The black lines (below) correspond to the fluence upper limits. The red lines (above) correspond to the luminosity upper limits. The dashed dot lines correspond to the normal selection without the additional 8-MeV cut. The solid lines correspond to the augmented selection with the 8-MeV prompt energy cut.

bution, the 90% C.L. upper limits were provided on the fluence of the neutrinos at the detector as well as the total luminosity at 410 Mpc for GW150914. Due to the far distance to the Daya Bay detectors, a relatively loose constraint was provided on the neutrino emission of the gravitational waves. In the future, more opportunities are expected and more efforts will be made to explore the unknown physics associated with black holes as well as other exclusive astrophysical events through neutrinos.

4.6 Summary

An offline search for supernova neutrino bursts has been presented in this chapter using ~ 1.5 years of data in the Daya Bay experiment. The detection channels include the commonly-used IBD interaction as well as the newly-used neutrino neutral-current excitation of ^{12}C . The latter channel basically increases the fiducial target mass of the Daya Bay detector by which the mineral oil (γ shielding on purpose) could contribute to the neutrino detection.

The search for supernova neutrino burst was based on any increases in the multi-AD signals within the sliding 10-second windows and a rate of the fake supernova neutrino burst imitated by the background fluctuation (consistently defined as false-alert rate threshold which is used in the online supernova trigger) was set to be 1 per century in this search. Additional features of the supernova neutrino burst candidate were checked to further increase the confidence level of the search. Two types of analyses were performed: a high energy threshold of 10 MeV adopting IBD channel plus NC- ^{12}C channel, and a low energy threshold of 0.7 MeV for IBD nGd signals and 3.5 MeV for IBD nH signals.

The search with a high energy threshold has a high sensitivity to core-collapse supernovae (typical model) which retains 100% out to 25 kpc covering the whole Milky Way. The sensitivity is increased by a factor of 2 for the extragalactic region compared with the online supernova trigger. Since no supernova neutrino bursts were observed in this analysis, a 90% C.L. upper limit on the rate of core-collapse supernovae (including failed SN) within the Milky Way was estimated to be 1.5 yr^{-1} . As the offline search covered the whole data set before the online trigger system was installed, this upper limit is lowered to 0.53 yr^{-1} in conjunction with the fact that no supernova trigger has been confirmed from the running online trigger system to date.

The search with a low energy threshold was intended to be model-independent, allowing a detection of the full energy spectrum of supernova neutrinos. As a result, no neutrino bursts were found with a false-alert rate threshold of 1 per century but two candidates were identified with a false-alert rate threshold of 1 per year. Based on their occurrence rate and the energy spectrum, the two candidates are most likely attributable to the background. The detailed information of the two candidates (with an average energy of ~ 4 MeV) are provided after the checks to rule out the high possibility of being unphysical, accidental, or muon-induced. No coincident astronomical observations of supernovae were found within the two supernova catalogs (Asiago and Rochester).

In addition, two exotic searches were performed for the coincident neutrino signals with the so far closest type Ia SN2014J and the first discovered gravitational wave event GW150914. There is no positive evidence of any coincident neutrino signals. The corresponding upper limits on the $\bar{\nu}_e$ fluence and total energy are given for GW150914.

Chapter 5 Discovery potential for supernova relic neutrinos at Jinping

Supernova relic neutrinos have been introduced in Section 1.5 including the formalism and the challenging backgrounds regarding the detection – muon-induced background, reactor neutrino background, and atmospheric neutrino background. The present experimental status is also reviewed in Section 1.6.2 and only upper limits on the SRN flux can be given by the present experiments, mainly hydrogen-rich detectors – liquid scintillator detectors and water Cherenkov detectors.

This chapter will present a study of discovery potential for supernova relic neutrinos at Jinping, where the muon-induced background and reactor neutrino background can be suppressed significantly. The sensitivities of kilo-ton scale detectors are estimated for liquid scintillator, water, and gadolinium-doped water detectors, respectively. Specifically, for the high energy SRN detection, the capability of a kilo-ton scale detector would be maximized using a type of slow liquid scintillator, e.g., linear alkyl benzene, LAB, which can have a good separation of the Cherenkov and scintillation light. Based on this ability of LAB, the particle identification in such a detector is significantly enhanced, thus dramatically reducing the challenging atmospheric neutrino background in present experiments including 1) charged-current (CC) background of atmospheric neutrinos in water Cherenkov detectors, and 2) neutral-current (NC) background of atmospheric neutrinos in liquid scintillator detectors.

5.1 Jinping neutrino experiment

5.1.1 Experimental site

The Jinping neutrino experiment is proposed to be located in China Jinping underground Laboratory (CJPL)^[111] in Jinping Mountain, Sichuan Province, China (see Figure 5.1). China Yalong River Hydropower Development Company has built the Jinping II Hydropower Station, including two traffic tunnels, four headrace tunnels, and one drainage tunnel across the Jinping Mountain (see Figure 5.2), with a maximum overburden of 2,400 m rock (~7000 meter water equivalent).

The first phase of CJPL (CJPL I) was constructed beside the middle of the traffic tun-



Figure 5.1 Location of CJPL in Jinping Mountain surrounded by Yalong River as the solid blue line. The dashed line indicates the Jinping tunnels. The two hours' drive to the closest Xichang Airport. (From Ref. [110])

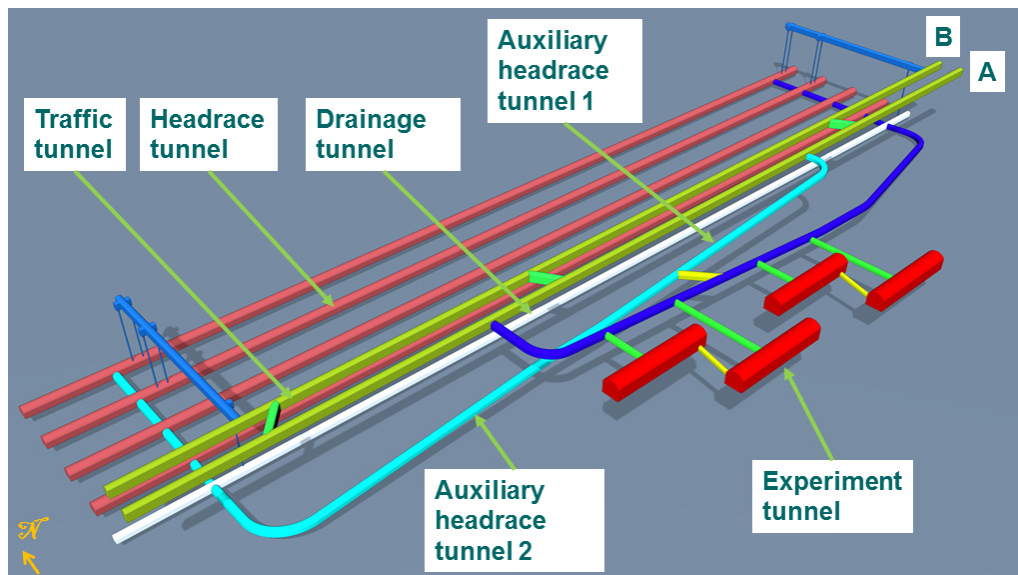


Figure 5.2 Schematic diagram of Jinping tunnels and Jinping phase II laboratories^[110].

nels in the end of 2009. Two dark matter experiments, CDEX^[151,152] and PandaX^[153,154], have been carried out in the lab of CJPL I with fruitful achievements. The second phase of CJPL (CJPL II) started in the end of 2014 and it is planned to build four 150 m long tunnels close to the traffic tunnels as shown in Figure 5.2.

The Jinping neutrino experiment^[110] is proposed to use one of the newly-built four tunnels to install one or two neutrino detectors with a fiducial target mass of 2×1 kilo-ton for solar neutrino physics, and 2×1.5 kilo-ton for geo-neutrino and supernova relic neutrino physics, adopting liquid scintillator techniques as a baseline design and with a possible extension to slow liquid scintillator (see Section 5.6).

5.1.2 Cosmic-ray muon flux

The cosmic-ray flux was measured to be about $2.0 \times 10^{-10}/(\text{cm}^2 \cdot \text{s})$ at CJPL^[155]. A summary of the muon fluxes from the underground laboratories in the world can be seen in Figure 5.3.

5.1.3 Reactor neutrino flux

Jinping is also a thousand kilometers away from the nearest nuclear power plants. Taking into account all the running and proposed nuclear power plants^[156], one can estimate the reactor neutrino flux to be $1.3 \times 10^6/(\text{cm}^2 \cdot \text{s})$. The reactor neutrino fluxes and the muon fluxes for other underground laboratories in the world are also shown in Figure 5.3.

5.2 Supernova relic neutrino signal

5.2.1 Spectrum and flux

As shown in Figure 1.13, the HBD (6-MeV) model is used to predict the SRN signal, then to demonstrate the discovery potential. About 5 IBD interactions are expected with an exposure of 20 kt-year liquid scintillator in $[10, 30]$ MeV of neutrino energy.

5.2.2 Detection techniques

In a hydrogen-rich detector, supernova relic neutrinos, as well as supernova burst neutrinos, are primarily detected via inverse beta decay, IBD, $\bar{\nu}_e + p \rightarrow n + e^+$ as mentioned in Section 1.3.1.

Liquid scintillator (LS): An IBD event is generally identified by a prompt-delayed coincident signature in LS, based on the scintillation photons from charged particles' deposited energy. The prompt signal is from the kinetic energy of the positron and its annihilation gammas. The delayed signal is from the emission of gamma(s) through

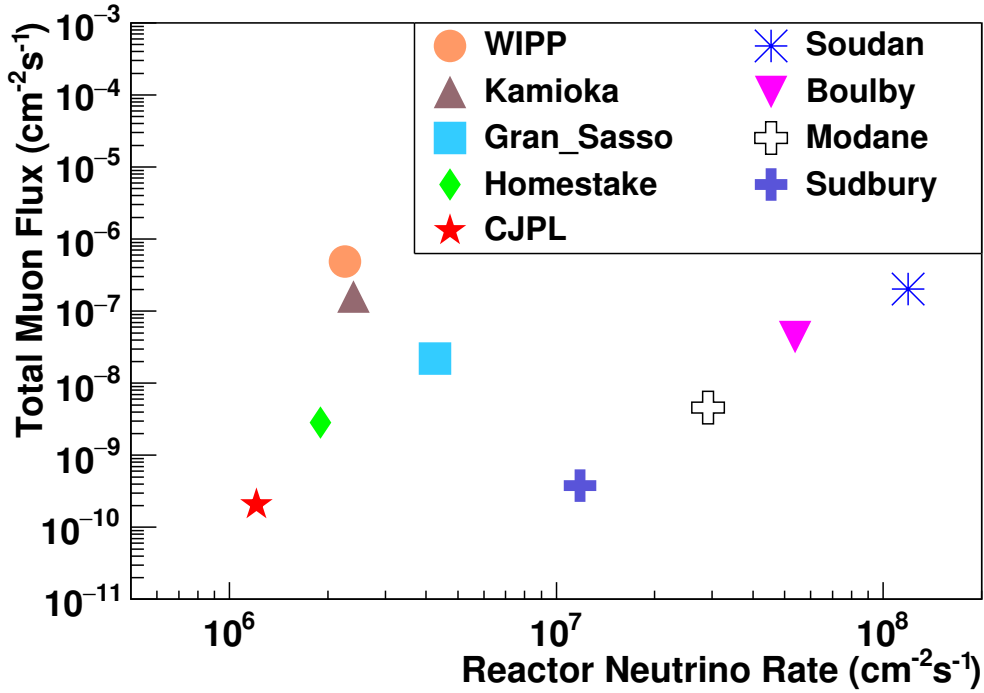


Figure 5.3 Muon flux vs. reactor neutrino flux for underground laboratories in the world^[110]. The star with the lowest muon flux and reactor neutrino flux corresponds to Jinping.

neutron capture on hydrogen or doped isotope, e.g., gadolinium. The relation of prompt signal energy (E_p) and neutrino energy (E_ν) is $E_\nu \simeq E_p + 0.8$ MeV.

Water: An IBD event is identified by the Cherenkov photons radiated by the IBD positrons in water Cherenkov detector. In the early stage, a prompt-delayed coincidence measurement was not applicable in water Cherenkov detectors since the 2.2-MeV gamma from the neutron capture on hydrogen is hard to detect. However, the neutron tagging technique was developed for a later stage of Super-K data following to the upgrade of the electronic trigger boards. A delayed signal from neutron capture on hydrogen can be tagged^[43,96], allowing a powerful coincidence measurement of IBD events based on Cherenkov photons despite a low tagging efficiency. The relation of IBD positron energy (E_{e^+}) and neutrino energy (E_ν) is $E_\nu \simeq E_{e^+} + 1.3$ MeV.

Water doped with gadolinium (Gd-water): For Gd-doped water Cherenkov detector, the total energy of the gamma cascade from the neutron capture on Gd is ~ 8 MeV, providing a much more efficient neutron tagging in comparison with the 2.2-MeV gamma from neutron capture on hydrogen. A high neutron tagging efficiency of about 90% can be obtained with a 0.2% of Gd compound-water solution^[43].

In this chapter, the detection technique of SRN is a coincidence measurement of

the IBD prompt positrons and the delayed neutron captures in both liquid scintillator and water Cherenkov detectors.

5.3 Cosmic-ray muon-induced backgrounds

A heavy overburden of ~ 7000 m.w.e. at Jinping provides an ultra-low cosmic-ray muon flux of $2 \times 10^{-10}/\text{cm}^2/\text{s}$ with an average muon energy ~ 351 GeV^[110]. KamLAND has an overburden of ~ 2700 m.w.e. and the cosmic-ray muon flux is about three orders of magnitude larger than that at Jinping with an average energy of 260 GeV. Therefore, the muon rate in a kiloton-scale detector at Jinping is estimated to be about 0.0003 Hz. The spallation background is about $(351/260)^{0.77}/1000 \sim 1.3 \times 10^{-3}$ times smaller than KamLAND according to the power law of the muon spallation yield.

For many muon-induced isotopes (see Figure 5.4), due to the longer life times of the corresponding decays, many of them could still contaminate the signal selection even if a muon veto is applied. The muon veto efficiency for muon-induced isotopes and the introduction dead time are to be balanced. However, this is not a big issue at Jinping since a much longer veto window can be applied for each muon e.g., 10-20 s, which can thoroughly remove all the isotopes induced by cosmic-ray muons (associated with other selection criteria). Negligible dead time 0.3-0.6% would be introduced.

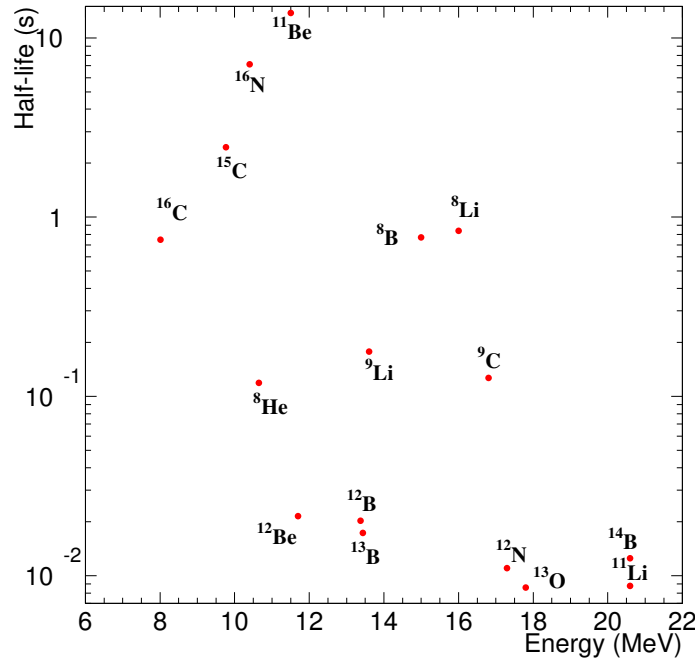


Figure 5.4 Half-lives and end-point energies for primary muon-induced isotopes. The figure is from Super-K 2012 SRN paper [95].

Fast neutrons (in liquid scintillator detectors) are basically generated by cosmic-ray muons in close proximity to the detector and so could migrate into the detector. Such background cannot be vetoed as the corresponding muon most likely does not traverse the detector. However, with the ultra low muon flux, this background can be ignored for the SRN study at Jinping which is estimated to be at least one order of magnitude smaller than the intrinsic atmospheric $\bar{\nu}_e$ background.

Accidental backgrounds are basically formed coincidentally by two uncorrelated events in a detector that satisfies the IBD selection criteria in time, energy and space. In a neutrino detector, the events in the 7.5-30 MeV range primarily originate from the muon-induced ^{12}B and fast neutrons; therefore with the Jinping assumption, the accidental background can be ignored, as it is a second order effect of the rare backgrounds from cosmic-ray muons.

5.4 Reactor neutrino background

The reactor neutrino flux at Jinping is estimated to be $\sim 1.3 \times 10^6 / \text{cm}^2 / \text{s}$ ^[110] taking into account all the running and proposed nuclear power plants. Though this reactor neutrino flux is smaller than all the other experiments across the world, the suppression is still not as much as the cosmic-ray muon flux at Jinping and the reactor neutrino background is still comparable with the SRN flux.

The reactor neutrino background with at least 7.5 MeV of prompt signal energy was evaluated to be ~ 4.8 with an exposure of 20 kt-year liquid scintillator. A reactor neutrino energy spectrum based on the Huber-Muller model^[85,86] was used. The energy resolution accounts for 10-20% of the reactor neutrino background. As a consequence, the lower prompt/neutrino energy threshold for the SRN study is increased to 10.0/10.8 MeV to remove the reactor neutrino background, getting in a better discovery sensitivity.

5.5 Challenging atmospheric neutrino backgrounds

Regarding the irreducible atmospheric neutrino backgrounds, except for the intrinsic atmospheric $\bar{\nu}_e$ background and the negligible atmospheric ν_e background, the atmospheric $\bar{\nu}_\mu / \nu_\mu$ CC background and the atmospheric neutrino NC background are the ultimate obstacles in the way of the optimum SRN discovery at Jinping as explained in detail below.

5.5.1 Atmospheric $\bar{\nu}_\mu/\nu_\mu$ CC background

The atmospheric $\bar{\nu}_\mu/\nu_\mu$ CC background originates from the atmospheric $\bar{\nu}_\mu/\nu_\mu$ CC interactions with the detector target material. Here we are taking the liquid scintillator as an example to demonstrate the background mechanism, the atmospheric neutrinos interact with carbon nuclei and hydrogen nuclei. In water Cherenkov detectors the atmospheric neutrinos interact with oxygen instead of carbon nuclei with roughly the same background mechanism.

The atmospheric $\bar{\nu}_\mu/\nu_\mu$ fluxes and the corresponding cross sections (from GENIE^[157], the same below) are shown in Figure 5.5.

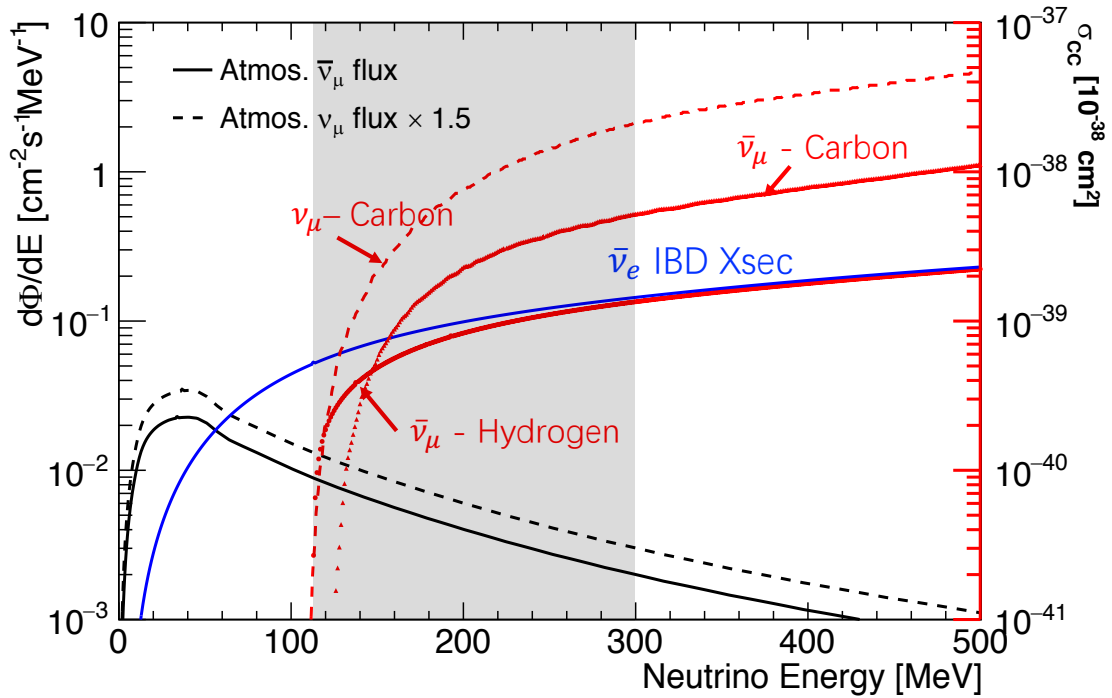


Figure 5.5 Demonstration of atmospheric $\bar{\nu}_\mu/\nu_\mu$ CC background in liquid scintillator. CC interaction cross sections are plotted with the right-sided axis as a function of the neutrino energy and indicated for various channels. The $\bar{\nu}_e$ IBD interaction cross section is plotted for comparison. The fluxes of atmospheric $\bar{\nu}_\mu/\nu_\mu$ are plotted along with the left-sided axis. The atmospheric $\bar{\nu}_\mu/\nu_\mu$ CC background for about 10-30 MeV SRN detection is mainly contributed to by the interactions in the shaded area.

The cross section is the total CC interaction cross section is dominated by the quasi-elastic scattering (QES) for <500 MeV neutrinos. The primary reactions are shown

below.

$$\bar{\nu}_\mu + p \rightarrow \mu^+ + n \quad (5-1)$$

$$\bar{\nu}_\mu + {}^{12}\text{C} \rightarrow \mu^+ + n + {}^{11}\text{B}(+\gamma) \quad (5-2)$$

$$\nu_\mu + {}^{12}\text{C} \rightarrow \mu^- + n + {}^{11}\text{N} \quad (5-3)$$

$$\bar{\nu}_\mu + {}^{12}\text{C} \rightarrow \mu^+ + n + {}^7\text{Li} + \alpha \quad (5-4)$$

In liquid scintillator detectors, these reactions would mimic the IBD interactions via a prompt signal from μ and a delayed signal from neutron capture. However, in liquid scintillator, μ can be identified to some extent by the Michel electrons of μ decays. Therefore, a triple coincidence of a prompt signal from the μ ionization and two delayed signals from the Michel electron of μ decay ($\tau \sim 2 \mu\text{s}$) and the neutron capture ($\tau \sim 30/200 \mu\text{s}$ for nGd/nH) would reduce such CC background by a factor of about 10. Note that a fraction of negative muons would be captured by nuclei (generally with an emission of γ) rather than decay.

In water Cherenkov detectors, it is difficult to do the same thing as liquid scintillator detectors since μ 's below the Cherenkov threshold ($<54 \text{ MeV}$ kinetic energy with an index of refraction $4/3$) are invisible in the water Cherenkov detectors and the Michel electrons would mimic the IBD prompt signals from a wide energy range of atmospheric neutrinos. Hence, the atmospheric $\bar{\nu}_\mu/\nu_\mu$ CC background is the most challenging background in water Cherenkov detectors though neutron tagging could reduce this background by a factor of 5.

If the liquid scintillator detector can identify the Cherenkov light, it can further remove the atmospheric CC background based on the absence of Cherenkov light from the untagged muon events.

5.5.2 Atmospheric NC background

The atmospheric NC background originates from the atmospheric neutrino NC interactions with the detector target material. As for the atmospheric $\bar{\nu}_\mu/\nu_\mu$ CC background, the liquid scintillator is utilized to demonstrate the background mechanism.

The atmospheric $\bar{\nu}_\mu, \nu_\mu, \bar{\nu}_e, \nu_e$ fluxes and the corresponding cross sections are shown in Figure 5.6.

The cross section is the total NC interaction cross section which is dominated by

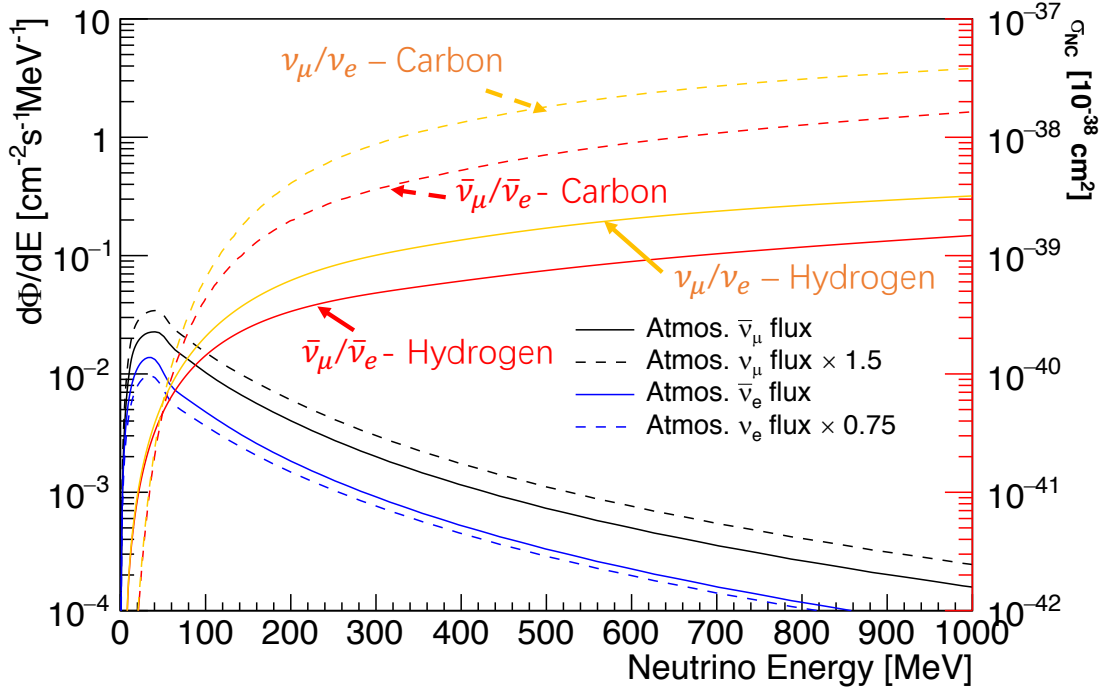


Figure 5.6 Demonstration of atmospheric NC background in liquid scintillator. NC interaction cross sections are plotted along with the right-sided axis as a function of the neutrino energy and indicated for various channels. The fluxes of atmospheric $\bar{\nu}_\mu$, $\nu_\mu, \bar{\nu}_e, \nu_e$ are plotted along with the left-sided axis. The atmospheric NC background for about 10-30 MeV SRN detection can be contributed by the interactions with a neutrino energy up to ~ 1 GeV.

the (quasi-)elastic scattering (QES) and a few percent by resonant/coherent single π production and the neutrino-electron scattering. The primary reactions are shown below. Note that the final states of the NC interaction might be much more complicated due to the hadron intranuclear transport and final state interaction (FSI).

$$\nu(\bar{\nu}) + {}^{12}\text{C} \rightarrow \nu(\bar{\nu}) + n + {}^{11}\text{C} + \gamma \quad (5-5)$$

$$\nu(\bar{\nu}) + {}^{12}\text{C} \rightarrow \nu(\bar{\nu}) + n + {}^{10}\text{B} + p \quad (5-6)$$

$$\nu(\bar{\nu}) + {}^{12}\text{C} \rightarrow \nu(\bar{\nu}) + n + {}^6\text{Li} + \alpha + p \quad (5-7)$$

In liquid scintillator detectors, the energetic neutrons from atmospheric NC interactions would deposit energy mainly through recoiling protons and inelastically scatter with carbon nuclei. But only a small fraction of the neutron energy is visible in the liquid scintillator due to the strong quenching effect following the Birk's law. After the neutron thermalization (depositing energy) by which the IBD prompt signal is mimicked, a delayed neutron capture naturally occurs. Such background is fatal to the liquid scintillator

detectors since atmospheric neutrinos over a large energy range from all flavors would contribute.

In water Cherenkov detectors, the situation becomes much better as a neutron cannot emit Cherenkov light on its own. Some Cherenkov light produced by the secondary γ of the inelastic scattering with carbon would also be reduced by the Cherenkov hit pattern (the directionality and the number of Cherenkov rings).

If the water Cherenkov detector can be mixed with liquid scintillator, it can further remove the atmospheric NC background based on the visible energy of the NC events.

5.5.3 Summary

The challenging atmospheric $\bar{\nu}_\mu/\nu_\mu$ CC background and the atmospheric NC background are the key issues in current hydrogen-rich detectors compared with the quite low SRN flux; however, a feasible solution was found, which is to use both scintillation and Cherenkov light in one detector, dramatically reducing these atmospheric neutrino backgrounds with an enhanced particle identification.

5.6 Slow liquid scintillator

Slow liquid scintillator is a type of liquid scintillator with a much slower emission of scintillation light than Cherenkov light as well as the time response of common PMTs. The concept is proposed to be water-based liquid scintillator^[158,159] or oil-like liquid scintillator^[160,161]. A recent experimental study demonstrated the ability of linear alkyl benzene to separate the Cherenkov and scintillation light using time, which can be one candidate or one ingredient of the slow liquid scintillator and is used to study the discovery potential for SRN. Linear alkyl benzene, LAB, is the common solvent of liquid scintillator which is always mixed with other fluors like some kind of wavelength shifters.

5.6.1 Experimental study on LAB

An experiment was set up (as shown in Figure 5.7) to study the LAB scintillation light emission using plastic scintillator modules assembled with PMTs to collect the cosmic-ray muon signals. Based on the anti-coincidence requirements for the PMT signals at different locations, the vertically downward-going muons were selected and the corresponding waveforms from the top and the bottom PMTs above and below the container of LAB were integrated and fitted. The LAB container was a cuboid acrylic

vessel located vertically along the 40-cm side and with the other two sides of 30 cm and 15 cm length.

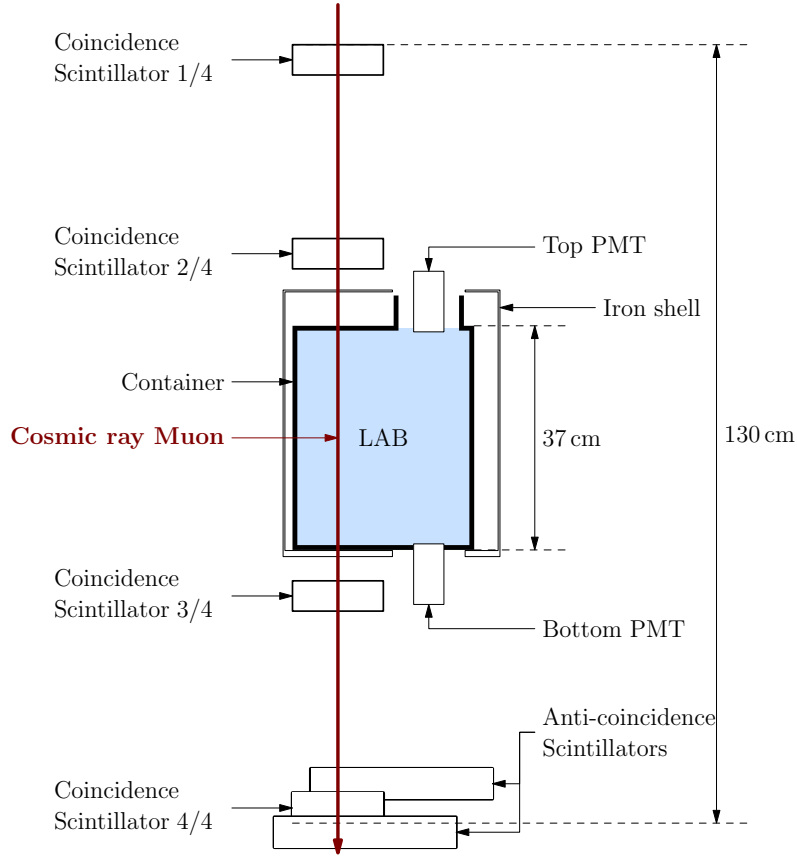


Figure 5.7 Schematic diagram of the experimental set-up from the front view^[160].

As seen in Figure 5.8, the top PMT could just collect the scintillation light and the bottom PMT would collect both the Cherenkov and scintillation light from the downward-going muons. A clear separation of the Cherenkov and scintillation light was observed from the muons with an average energy of 4 GeV and an average deposited energy of about 70 MeV.

The time profile of the scintillation light can be modeled by the formula below,

$$n(t) = \frac{\tau_r + \tau_d}{\tau_d^2} (1 - e^{-t/\tau_r}) \cdot e^{-t/\tau_d}, \quad t > 0, \quad (5-8)$$

where $n(t)$ is the normalized number of scintillation photons over time, τ_r is the rising time, and τ_d is the decay time. The Cherenkov emission is assumed to be instantaneous modeled by a δ function. And the waveforms were fitted with the time profile convoluted with a Gaussian time response of the PMT.

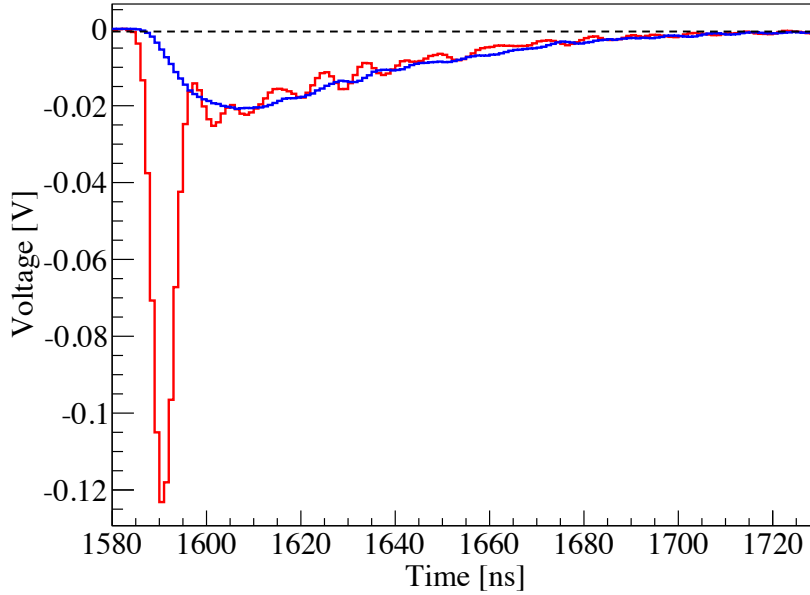


Figure 5.8 Average waveforms from the top (blue curve) and the bottom (red curve) PMTs^[160]. Due to the large charge collected by the bottom channel from Cherenkov peak, the red curve has a stronger ringing effect along with the tail of the waveforms. The ringing effect on the top channel is averaged out.

As a result, the fit to Figure 5.8 shows that the rise time and the decay time of scintillation emission are (7.7 ± 3.0) ns and (36.6 ± 2.4) ns, respectively. The time resolution dominated by the PMT response is about 2 ns.

The scintillation light yield was also compared to the simulation including the collection efficiency and the quantum efficiency of the PMTs. The result is ~ 1000 photons/MeV which is one order of magnitude smaller than the liquid scintillator.

A more relevant illustration of the waveforms from a 10-MeV electron is shown in Figure 5.9 in which case the ratio of Cherenkov light over scintillation light is ~ 0.2 .

5.6.2 Particle identification

Different particles in a target material would have different yields of Cherenkov and scintillation light which depend on both the particle kinetic energy and particle species. This is the origin of the particle identification using Cherenkov and scintillation light.

5.6.2.1 Light yield of scintillation photons

The light yield of scintillation photons depends approximately linearly on the particle's kinetic energy, but different particles would have different quenching effects accord-

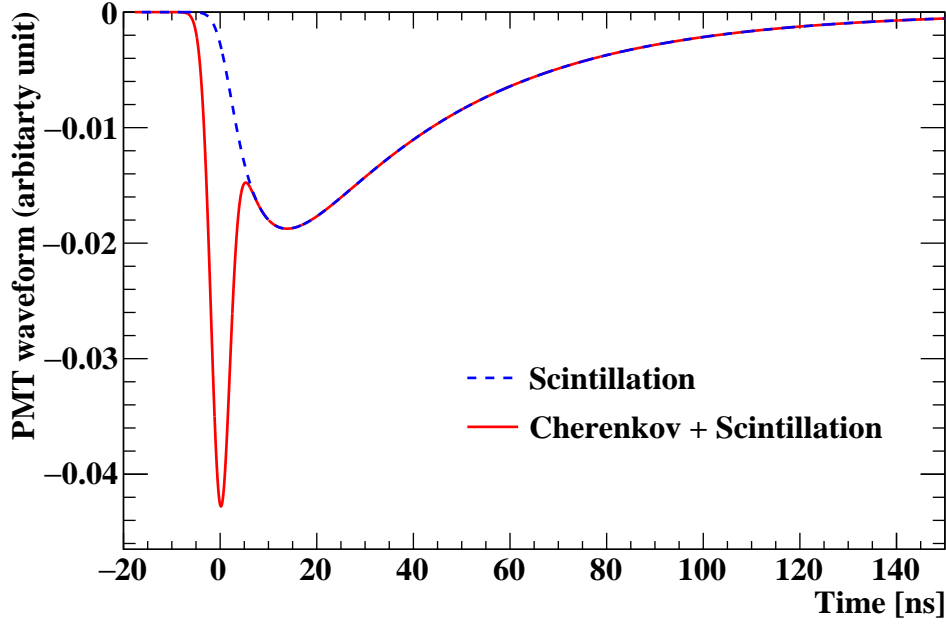


Figure 5.9 PMT waveforms of Cherenkov and scintillation light of a 10-MeV electron in LAB. No detection efficiencies are involved. The dashed blue curve denotes only the scintillation light and the red solid curve denotes the sum of Cherenkov and scintillation light.

ing to Birk's law^[162] which is modeled by an empirical formula in Equation (5-9). The larger the energy loss per path length, the heavier the quenching effect is.

$$\frac{dL}{dx} = \frac{dL_0}{dx} \cdot \frac{1}{1 + k_B \frac{dE}{dx}}, \quad (5-9)$$

where L is the light yield, $\frac{dE}{dx}$ is the energy loss of a certain particle per path length, k_B is the Birk's constant which depends on the material. k_B is about 0.13 mm/MeV for liquid scintillators. The quenching effect is the second item in Equation (5-9). The scintillation emission of LAB is mainly distributed in the wavelength range of 300-400 nm.

5.6.2.2 Light yield of Cherenkov photons

The light yield of Cherenkov photons can be theoretically calculated by the electrodynamics as shown in Equation (5-10),

$$\frac{d^2N}{dx d\lambda} = \frac{2\pi\alpha z^2}{\lambda^2} \left(1 - \frac{1}{\beta^2 n^2(\lambda)} \right), \quad (5-10)$$

where N is the number of Cherenkov photons, x is the path length of a charged particle in a medium, λ is the photon wavelength, z is the electric charge of the particle, β is the speed (over vacuum light speed c) of the particle, $n(\lambda)$ is the index of refraction corresponding to the wavelength λ , and α is the fine structure constant. Regardless of the material, the Cherenkov light yield depends on the speed of the charged particle which is actually subject to the particle kinetic energy and the particle rest mass (species). Note that Equation (5-10) holds when $\beta n > 1$. This means a charged particle with a speed greater than the light speed in this medium would emit Cherenkov light. The Cherenkov angle (between the direction of the particle and the Cherenkov light) can be derived from the wave front analysis which satisfies

$$\cos \theta_c = \frac{1}{\beta n(\lambda)}.$$

5.6.2.3 Particle identification of LAB

The particle identification of LAB is demonstrated with a Geant4^[163] simulation for γ , e^- , μ^- , and p in a large detector filled with LAB. Other related particles in the SRN detection would indirectly or identically emit Cherenkov photons via these charged particles. The scintillation time profile of LAB is implemented and the quenching effect is about 96%, 85% and 56% on average for e^- , μ^- , and p in the interesting energy range for SRN detection.

The number of Cherenkov photons vs. the number of scintillation photons is are plotted in the upper panel of Figure 5.10(a). The Cherenkov and scintillation photons are collected in a wavelength range of [300, 500] nm, within which the PMTs are assumed to have a detection efficiency of $\sim 10\%$ including the quantum efficiency and the collection efficiency. The true accepted scintillation and Cherenkov photons are used without any other detection efficiencies or optical effects. Accordingly, the fractional difference of the number of Cherenkov photons to the mean value of a gamma is plotted in the lower panel of Figure 5.10(a).

For a more realistic case shown in Figure 5.10(b), the attenuation of optical photons in LAB in Ref. [164] is considered in which case the attenuation is conservatively taken as absorption without any re-emission and the attenuation length ranges from 10 cm to 10 m with the wavelength from 300 nm to 400 nm. The attenuation length is about 1-2 m for the average wavelength of the scintillation emission of LAB which is about 340 nm.

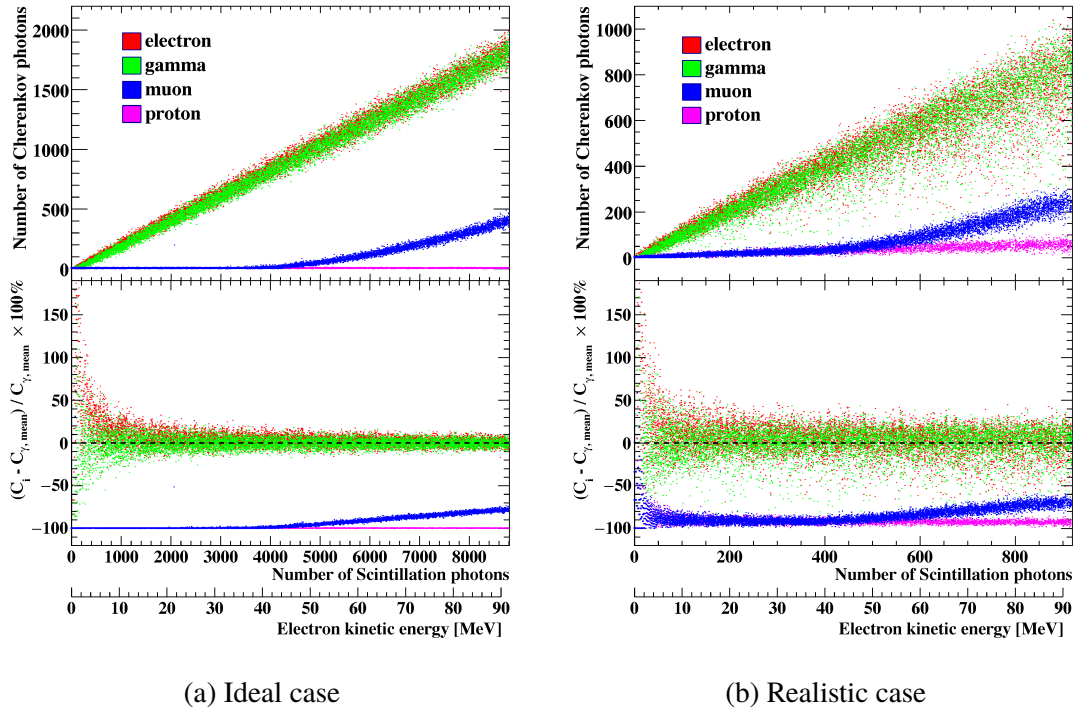


Figure 5.10 The number of Cherenkov photons vs. the number of scintillation photons within a wavelength range of [300, 500] nm for various particles in a LAB detector from simulation. The scintillation light yield is 1000/MeV and the quenching effect is involved. A $\sim 10\%$ PMT detection efficiency is assumed. (a) An ideal case, true accepted scintillation and Cherenkov photons without any other detection efficiencies or optical effects. (b) A more realistic case, considering the attenuation of optical photons in LAB according to Ref. [164] and the contamination of the identification between the Cherenkov and the scintillation photons. X-axis is the number of scintillation photons with a converted electron kinetic energy. Upper panel: Y-axis is the number of Cherenkov photons. Lower panel: Y-axis is the fractional difference of the number of Cherenkov photons to the mean value of a gamma.

For a kiloton-scale detector filled with LAB whose radius is ~ 10 -m level, the remaining Cherenkov and scintillation photons are about 50% and 10% if considering the optical attenuation in LAB assuming two uniform distributions of the vertex and the direction of the incident particle. The scintillation emission spectrum follows Ref. [160] and the Cherenkov wavelength spectrum results from Equation (5-10).

In Figure 5.10(b), the contamination in the identification of the Cherenkov and scintillation light is also considered using the time profile. Such two types of light were simply separated by a time cut. The photons within the first beginning 10-ns window were treated as the Cherenkov photons and the rest treated as the scintillation photons. This is actually a conservative method as the pulse shape could be fitted for a more sophisticated discrimination. In the lower panel of Figure 5.10(b), the upwarping structure of μ and

p bands in the lower energy region is just due to this treatment, since an e or γ has a small fraction of the Cherenkov light over the scintillation light which is comparable to the scintillation photons of a μ or p treated as the Cherenkov photons.

A distinct separation between $e(\gamma)$ and μ, p can be observed even for the realistic case in Figure 5.10. A separation of μ and p is doable when the muons pass the Cherenkov threshold. For a single γ , the Cherenkov light is emitted by its secondary electrons and positrons, the yield of which would be lower than an e with the same initial kinetic energy, especially for <10 MeV region with about 1σ discrepancy on average. For a neutron, the Cherenkov light possibly is produced by the secondary γ from its inelastic scattering with a carbon nucleus. The Cherenkov light hit pattern will be used to further distinguish a neutron (γ) from an electron or a positron.

5.7 Discovery potential study

This section will present the discovery potential for supernova relic neutrinos in [10.8, 30.8] MeV using a kiloton-scale LAB detector at Jinping. The backgrounds are assumed to originate from atmospheric neutrinos. A comparison of different detection techniques for the SRN detection would be shown in the next section.

It should be noted that the particle identification presented in Figure 5.10(b) is actually the detector response for various final state particles of the corresponding interactions.

5.7.1 SRN signal and selection

The SRN flux predicted by the HBD model was adopted. A SRN event is identified by a prompt-delayed coincident signature from the IBD interaction. The selection criteria will fully utilize the ability of the particle identification based on the number of Cherenkov photons (N_{Ch}) and the number of scintillation photons (N_{Sc}), significantly reducing the backgrounds at a small cost of the efficiency of selecting SRN signals. All the selection criteria are described below.

1. A double coincidence within the prompt-delayed time interval, 0.2-1000 μs .
2. A cut on N_{Sc} of the prompt signal, which is required to be within [70, 294] counts corresponding to the golden window of SRN $\bar{\nu}_e$ energy (8.3-30.8 MeV $\bar{\nu}_e$ energy, 7.5-30.0 MeV prompt signal energy).
3. A cut on $N_{\text{Ch}}/N_{\text{Sc}}$ of the prompt signal, which is required to be >0.65 to suppress the backgrounds with about 2% inefficiency of the SRN events. [98%]

4. A delayed energy cut on the gamma from neutron captures. [95%]
5. A vertex distance cut to further reduce the accidental background. [99%]
6. A check of the Cherenkov hit pattern (the directionality and number of visible Cherenkov rings), mainly for the atmospheric neutrino NC background. [98%]

As a result, a 90% efficiency for the SRN signal within [8.3, 30.8] MeV of the neutrino energy can be obtained from the product of the rationally estimated efficiencies in the square brackets. The inefficiency of the multiplicity cut within the coincidence time is negligible since the low energy criterion of the SRN detection can be greater than 8 MeV, based on which the event rate mainly from the natural radioactivity is quite low, e.g., less than 1 Hz with an efficiency greater than 99.8%. The muon veto efficiency is not considered because of the low muon flux.

5.7.2 Atmospheric neutrino backgrounds

The atmospheric neutrino backgrounds are estimated by a simulation convoluting the atmospheric neutrino flux, GENIE^[157] neutrino interaction cross sections and final states, and the Geant4-based^[163] detector response which enables the study of the particle identification in Figure 5.10(b).

5.7.2.1 Atmospheric neutrino flux

There are several atmospheric neutrino flux models calculated by M. Honda et al. (Honda flux), G. Battistoni et al. (Fluka flux) and G. Barr et al. (Barr flux). Honda flux^[84] was adopted in this thesis. The atmospheric neutrino flux is a convolution of the primary cosmic ray flux at the top of the atmosphere with the yield of neutrinos per primary particle. In addition, the filter effect of the geomagnetic field on the primary particles is also involved^[84] and the atmospheric neutrino flux would have to consider the turbulence of solar activities at lower energies. In this study, we used the atmospheric neutrino flux for the solar minimum activity (larger flux) at mountain levels at Kamioka, averaging them over all the arrival azimuthal directions.

The fluxes of four flavors of atmospheric neutrinos can be seen in Figure 1.13, Figure 5.5 and Figure 5.6. A clean plot of the four atmospheric neutrino fluxes is shown here in Figure 5.11 integrating all the zenith and azimuthal directions.

In fact, considering the matter effect (MSW-PMNS) on the neutrino oscillation, a 2D flux of the atmospheric neutrinos with the zenith angle against the neutrino energy is

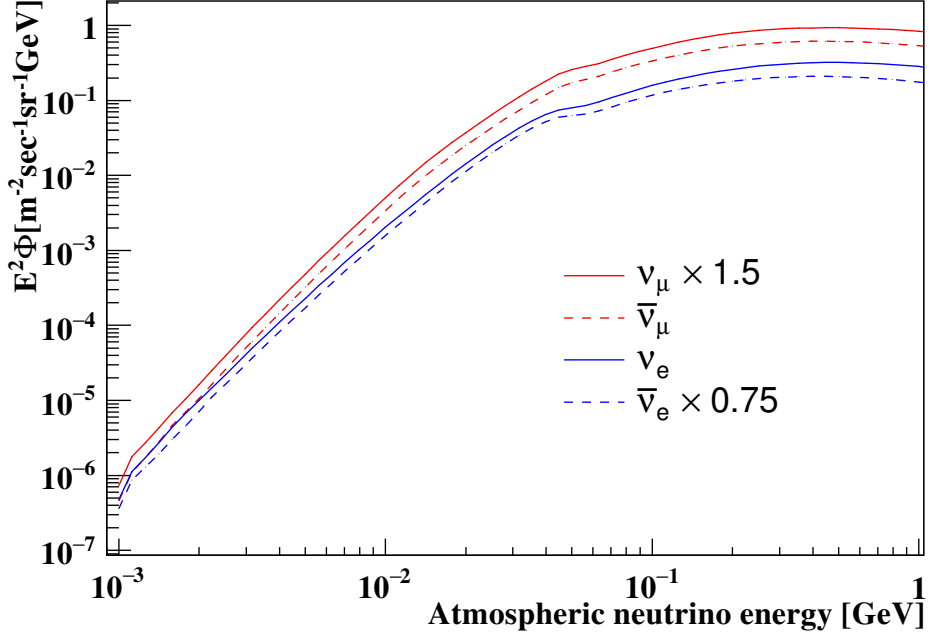


Figure 5.11 Atmospheric neutrino fluxes (Honda flux) for four flavors of neutrinos integrating all the zenith and azimuthal directions. Note that the Y-axis is multiplied by E^2 . Some neutrino fluxes are scaled since the electron (muon) neutrino and anti-neutrino have roughly identical fluxes. The muon-neutrino flux is about twice the electron-neutrino flux.

needed. They are also shown here in Figure 5.12.

Neutrino oscillation in matter As mentioned above, the atmospheric neutrino flux in the detector must involve the matter effect on the neutrino oscillation since the atmospheric neutrinos could traverse the Earth. In the matter effect, the W -boson exchange interaction between the electron-neutrinos and the electrons in matter is considered. Due to such neutrino coupling with electrons, the matter is opaque for neutrinos as if the mass eigenstates change and the oscillation framework should be altered accordingly.

A simple analytical approximation to the neutrino oscillation probabilities in matter is presented in Ref. [165] at a large value of θ_{13} recently measured by the reactor neutrino experiment Daya Bay and RENO. The approximation, which is applicable to all oscillation channels at all the relevant energies and baselines, works well for large θ_{13} . The accuracy of the approximation is demonstrated by comparing it to the exact numerical result, as well as some other approximation results. As a consequence, the neutrino oscillation probabilities expressed in Ref. [165] are used in this study.

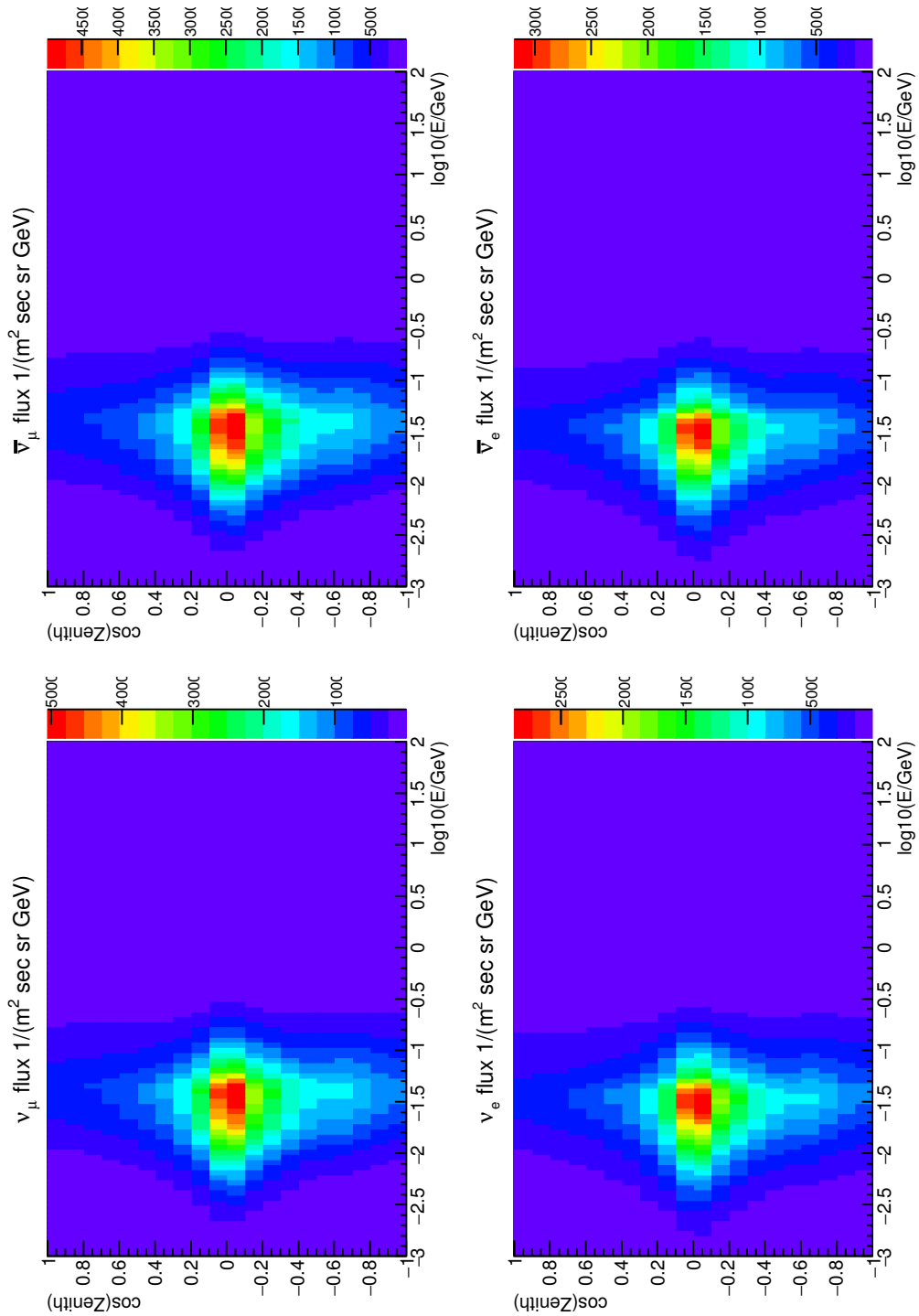


Figure 5.12 The 2D plots for atmospheric neutrino fluxes of all flavors with the zenith angle against the neutrino energy. The $\cos(\text{Zenith})$ is 1 when the direction is downward-going and the negative $\cos(\text{Zenith})$ implies the neutrinos traverse the Earth and will undergo the oscillation with matter effect.

Earth matter profile The Earth matter profile has to be considered in the matter effect of the atmospheric neutrino oscillation. The model in Ref. [166] was used to describe the Earth internal composition as shown in Figure 5.13. This model is well approximated by a number of layers with constant densities. The solid curve in Figure 5.13 shows the Earth profile according to the data in Ref. [167] and the dotted curve represents the adopted approximation, which has five layers with constant densities $\rho_{i=1,\dots,5} = 13.0, 11.3, 5.0, 3.9, 3.0 \text{ g/cm}^3$, electron number densities $N_{i=1,\dots,5} = 6.15, 5.36, 2.47, 1.93, 1.50 N_A \text{ cm}^{-3}$, and maximum radii $r_{i=1,\dots,5} = 1221, 3480, 5701, 5971, 6371 \text{ km}$. An additional layer from the top of atmosphere to the surface of the Earth is set to be 15 km with zero electron number density.

Combining the matter effect and the Earth matter profile, the oscillation probabilities of atmospheric neutrinos with a certain zenith angle on the surface of the Earth are calculated and presented in Figure 5.14. The mass hierarchy is assumed to be normal and the other oscillation parameters are set in accordance with PDG^[168]. For neutrino (anti-neutrino) case, there is a resonance of the electron-neutrino oscillation probability assuming a normal (inverted) hierarchy in which case the matter effect parameter about the strength of electron-neutrino coupling with electrons coincides with the Δm_{13}^2 providing a large effective neutrino mixing angle θ'_{13} .

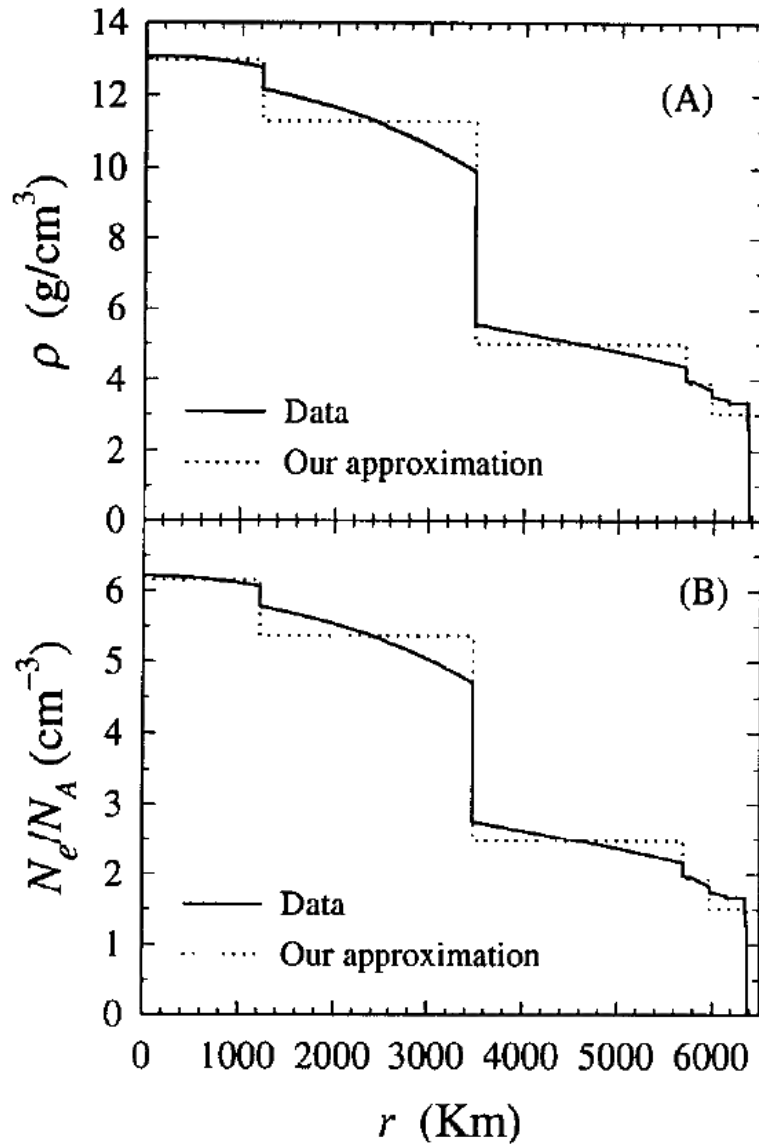


Figure 5.13 (A) The matter density ρ and (B) the electron number density of the Earth as a function of the radius r .

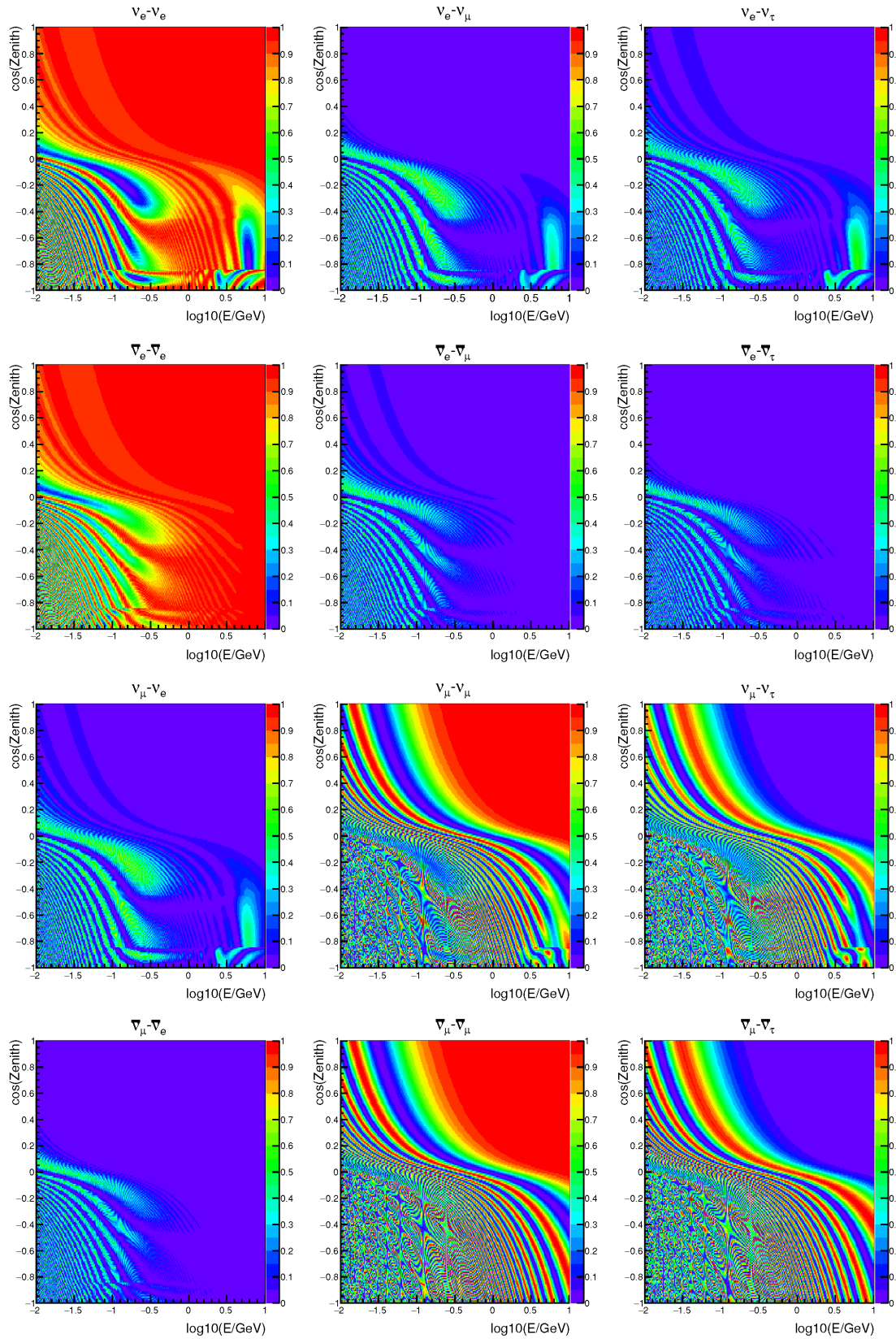


Figure 5.14 Atmospheric neutrino oscillation probabilities with the matter effect in the Earth. The negative $\cos(\text{Zenith})$ correspond to the atmospheric neutrinos traversing the Earth.

Based on the neutrino oscillation in the Earth, the atmospheric neutrino flux would be, e.g.

$$\Phi_e^{\text{Osc}} = \Phi_e^0 \cdot P(e \rightarrow e) + \Phi_\mu^0 \cdot P(\mu \rightarrow e), \quad (5-11)$$

where Φ^0 is the non-oscillation atmospheric neutrino flux and P is the oscillation probability.

The ratios of the atmospheric neutrino fluxes with and without oscillation (i.e. Φ^{Osc}/Φ^0) for each flavor are shown in Figure 5.15. The ratios are quite similar for atmospheric $\bar{\nu}_\mu/\nu_\mu$ and significantly different for >1 GeV $\bar{\nu}_e/\nu_e$ due to the resonance of ν_e oscillation assuming a normal hierarchy.

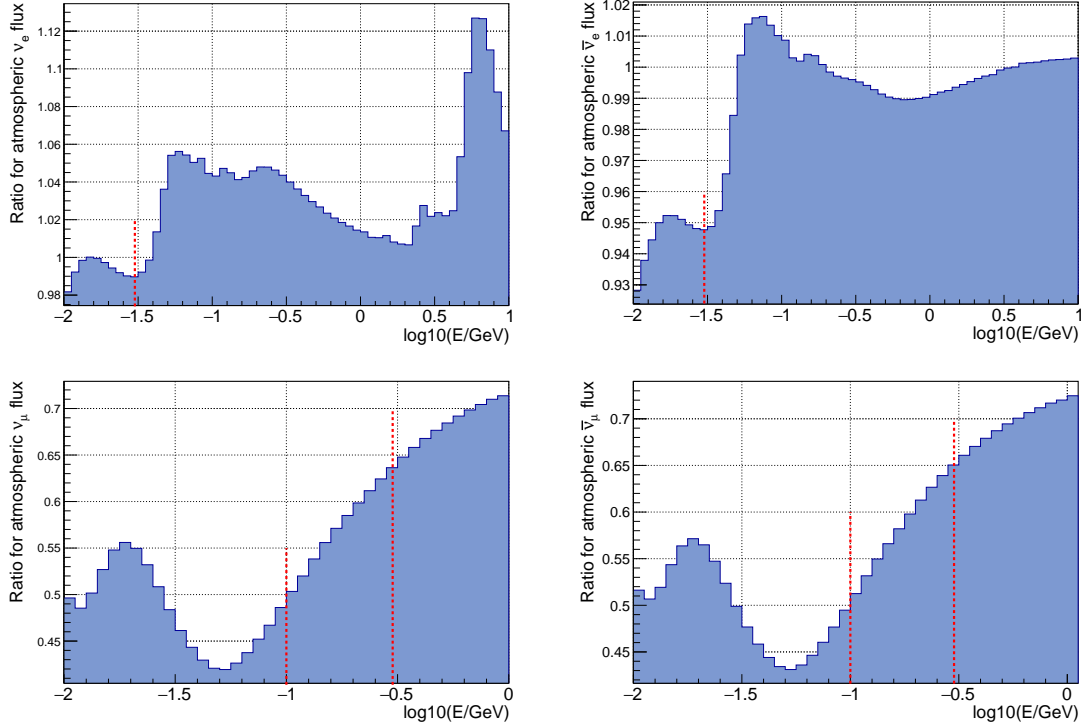


Figure 5.15 Ratio of the atmospheric neutrino flux with and without oscillation. Four flavors ν_e , $\bar{\nu}_e$, ν_μ , $\bar{\nu}_\mu$ from left (neutrino) to right (anti-neutrino) and then top (electron-neutrino) to bottom (muon-neutrino). The X-axis is the neutrino energy and the Y-axis is the value of the ratio. Dashed vertical lines correspond to 30 MeV for electron-neutrino and 100, 300 MeV for muon-neutrino.

In a summary, the matter effect has a large impact (30-50%) on the atmospheric $\bar{\nu}_\mu/\nu_\mu$ fluxes and a small impact (a few percent) on the atmospheric $\bar{\nu}_e/\nu_e$ fluxes with regard to the energy range for SRN study.

5.7.2.2 Cross sections

The recent version 2.10.0 of GENIE^[169] with the complicated intranuclear hadron transport and final state interaction (FSI) in heavy nuclei is used. The cross sections have been shown in Figure 5.5 and Figure 5.6.

5.7.2.3 Estimates of atmospheric neutrino backgrounds

Event rates The event rates can be calculated following the formula below, which convolutes the atmospheric fluxes, the oscillation probabilities, the exposure of the target material, and the corresponding cross sections with the selection efficiencies,

$$\begin{aligned}
N(\nu_f) [1/(\text{kt} \cdot \text{year})] = & \\
& \sum_i \left\{ \text{Flux}(E, \theta_{\text{zen}}, \nu_i) [1/(\text{GeV} \cdot \text{sr} \cdot \text{s} \cdot \text{m}^2)] \right. \\
& \times P(\theta_{\text{zen}}, \nu_i \rightarrow \nu_f, \text{Mass Hierarchy}) \left. \right\} \\
& \times 2\pi \cdot d\cos\theta_{\text{zen}} [\text{sr}] \times dE [\text{GeV}] \\
& \times T [60 \cdot 60 \cdot 24 \cdot 365 \text{ s / year}] \\
& \times \sum \left\{ \sigma(\text{nucleus}, E, \nu_f) [\text{m}^2] \cdot N_{\text{nuclei}} [/\text{kt}] \times \epsilon \right\}.
\end{aligned} \tag{5-12}$$

The θ_{zen} denotes the zenith angle, E is the neutrino energy, $\nu_{i/f}$ denotes the initial/final flavor of neutrinos, P is the oscillation probability, σ is the cross section of a certain nucleus, and ϵ is the selection efficiency. The unit conversion is also indicated in the square brackets.

Atmospheric $\bar{\nu}_e$ CC background The atmospheric $\bar{\nu}_e$ CC background is the intrinsic background for the SRN detection, which is estimated to be 0.013/kton-year with the same efficiency for SRN events.

Atmospheric $\bar{\nu}_\mu/\nu_\mu$ CC background

The cross sections and typical interactions of this background can be seen in Section 5.5.1.

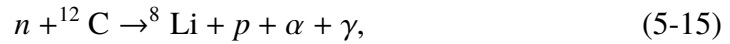
With the double-coincidence cut, $\sim 10\%$ of the atmospheric $\bar{\nu}_\mu/\nu_\mu$ CC background survives in which case the muons do not decay within 0.2-1000 μs . From the N_{Sc} cut to the $N_{\text{Ch}}/N_{\text{Sc}}$ cut, less than 2% of the events remain, in which case the Cherenkov photons are generated mainly by some Michel electrons from the muon decays within 0.2 μs . As a result, the atmospheric $\bar{\nu}_\mu/\nu_\mu$ CC background is about one order of magnitude smaller

than the intrinsic atmospheric $\bar{\nu}_e$ background. About 20% of this background originates from the atmospheric ν_μ .

Atmospheric neutrino NC background

The cross sections and typical interactions of this background can be seen in Section 5.5.2.

Due to the complicated final states of the atmospheric neutrino NC interactions with carbon nuclei (break-up) as well as the neutron inelastic scattering with carbon nuclei, the event with one neutron produced in the final state would be selected regardless of whether there is any delayed neutron capture. It is possible that the neutron is ‘absorbed’ immediately by a carbon nucleus following the interactions, e.g.,



and so forth. The isotopes produced by these interactions basically have much longer half-lives than 1000 μs . Coincidentally, such interaction in Equation (5-13) would emit a relatively high energy γ or γ cascade which generate adequate Cherenkov light surviving our cuts. With $N_{\text{Ch}}/N_{\text{Sc}}$ cut, about 1/5 of the NC backgrounds after N_{Sc} cut will survive.

Note that a fraction of neutron events removed by the $N_{\text{Ch}}/N_{\text{Sc}}$ cut is due to the PMT waveforms though they may be associated with adequate Cherenkov light. In Figure 5.16, several typical PMT waveforms of a neutron event are presented. With our current simple 10-ns cut to separate Cherenkov and scintillation light, the delayed Cherenkov light which depends on the neutron interactions with the target material would be treated as scintillation light. Using a subtle pulse shape discrimination, these events will be more effectively removed. A neutron event can also have an expected PMT waveform of a SRN signal. In Figure 5.17, the expected waveforms from a neutron and a positron are shown.

The Cherenkov light hit patterns were additionally checked as mentioned in Section 5.7.1. The typical Cherenkov hit pattern indicated by a 50-m radius spherical shell can be seen in Figure 5.18. Clearly, the Cherenkov light from a neutron is more likely isotropic due to the multiple secondary γ ’s or multiple electrons or positrons generated by a single γ . The directionality and the number of significant (visible) Cherenkov rings

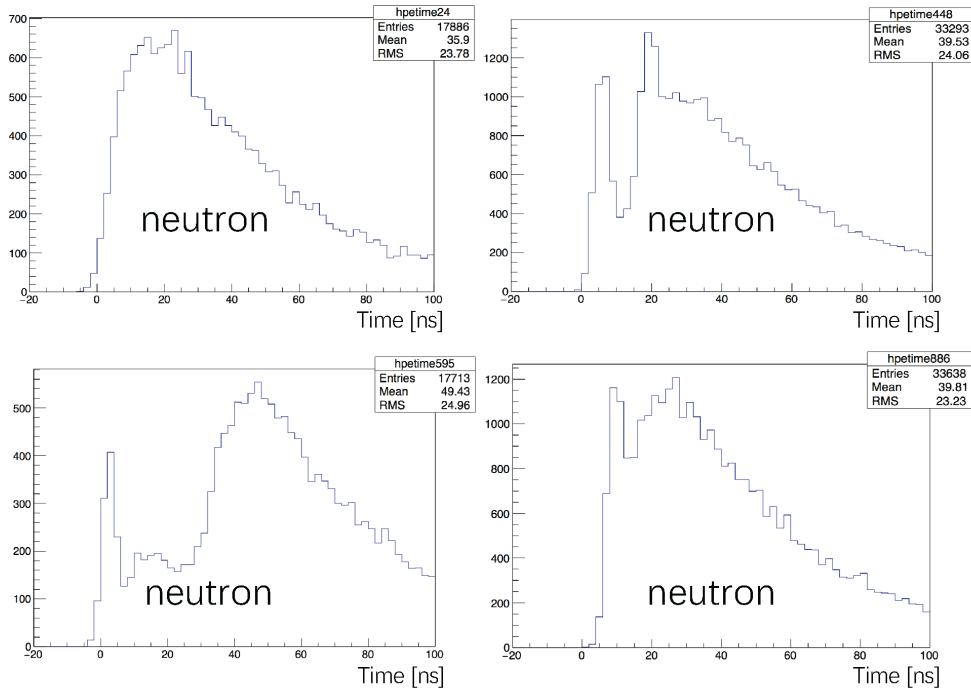


Figure 5.16 Several typical PMT waveforms of neutron events in LAB. X-axis is time. Y-axis is in an arbitrary unit.

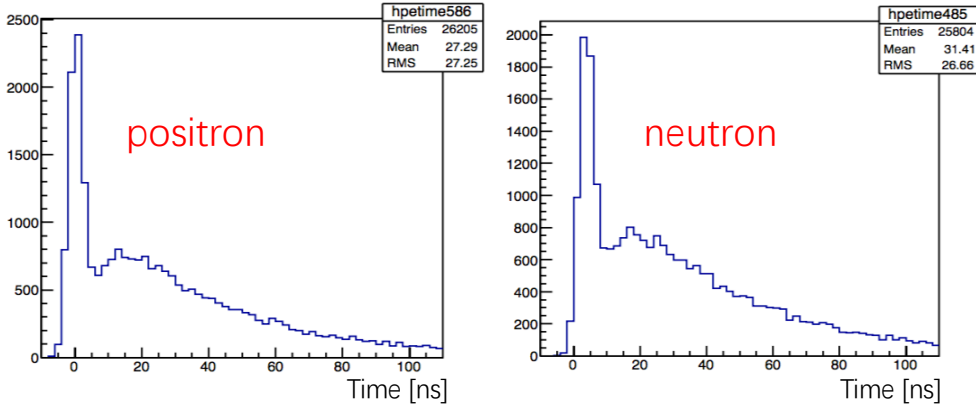


Figure 5.17 Expected PMT waveform of a SRN prompt signal. One is from a real IBD positron and the other is from a neutron. X-axis is time. Y-axis is in an arbitrary unit.

are the discriminators to further suppress the NC background. As a result, about 3% of the neutron events after all the other cuts are left.

The NC background from the atmospheric neutrinos is estimated to be 0.018/kton-year which is roughly the same as the intrinsic atmospheric $\bar{\nu}_e$ background. This background is almost equally contributed by the electron- and muon-neutrinos (roughly the

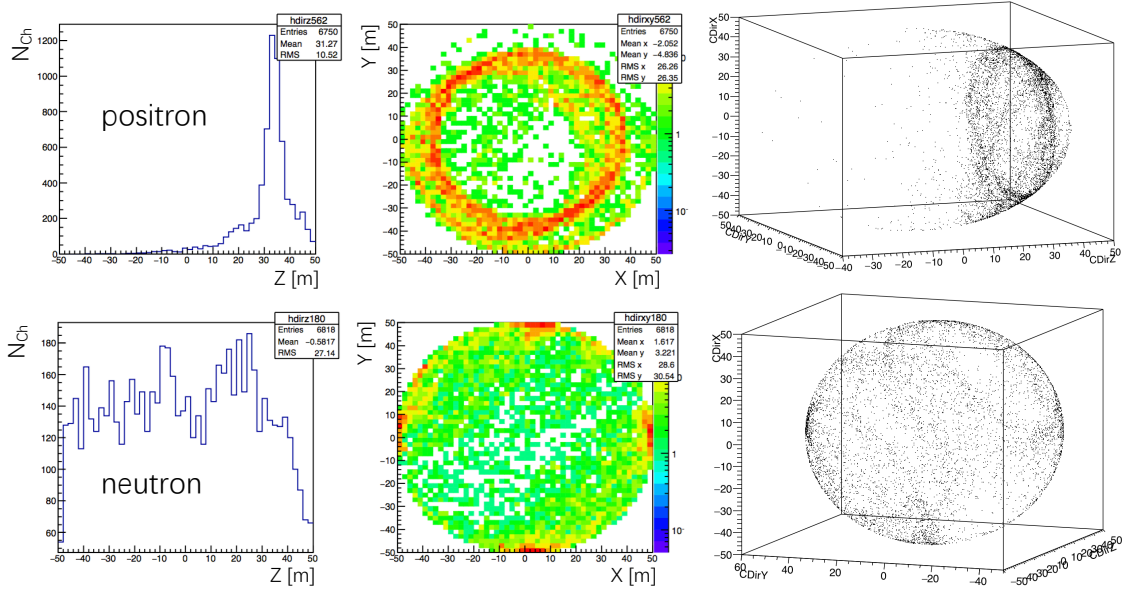


Figure 5.18 Typical Cherenkov hit pattern indicated by a 50-m radius spherical shell. The incident direction of the positron or the neutron is along with the Z-axis. Left: Cherenkov light distribution over the Z-axis. Middle: Cherenkov light distribution in the X-Y plane. Right: A 3-D scatter plots of the Cherenkov light on the spherical shell.

same cross sections and the identical fluxes considering 30-50% reduction of the atmospheric $\bar{\nu}_\mu/\nu_\mu$ fluxes due to the neutrino oscillation). And the contribution from neutrinos is about twice that from anti-neutrinos.

5.7.3 Summary

The prompt signal energy spectra of the backgrounds and the predicted SRN events are presented in Figure 5.19 with an exposure of 20 kton-year of LAB at Jinping. Note that the reactor neutrino background is larger than the liquid scintillator by a factor of 5 due to the relatively poor energy resolution. The SRN events originate from the SRN flux predicted by the HBD (6-MeV) model. In the prompt energy range of 10-30 MeV, the expected number of background events is about 0.1 per bin on average, in which case any event would be regarded as a “golden” event. In a kiloton-scale LAB detector at Jinping, a 99.95% confidence-level ($\sim 3.5\sigma$) discovery of the SRN flux within [10.8, 30.8] MeV will be obtained with an exposure of 20 kton-years.

Additional systematic uncertainties are not considered in this sensitivity study since the conclusion would not be essentially changed due to a very good signal-to-background ratio.

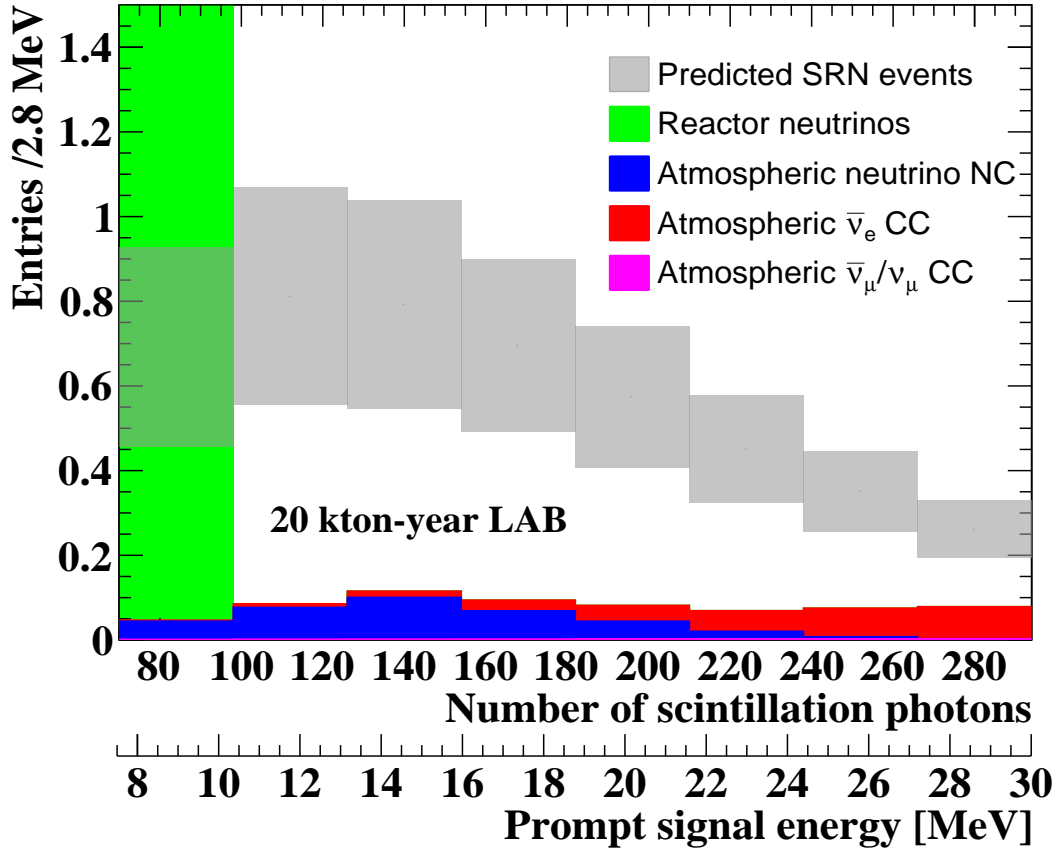


Figure 5.19 Prompt signal energy spectra of the backgrounds and the predicted SRN events in LAB with an exposure of 20 kton-year at Jinping.

5.8 Comparison of different techniques

The expected numbers of various backgrounds and SRN signals are summarized in Table 5.1 corresponding to an exposure of 20 kton-year of water, Gd-doped water, liquid scintillator, and slow liquid scintillator (LAB as a candidate) at Jinping. The neutrino energy range for the SRN detection is 10.8-30.8 MeV. The backgrounds for water and Gd-doped water were estimated based on the SRN analysis at SK^[43,96,100]. Note that the spallation cut with a signal efficiency of about 80% would be not needed at Jinping. The estimates of the backgrounds in liquid scintillator are consistent with the KamLAND SRN study^[97]. The total number of backgrounds, the signal selection efficiency, and the signal-to-background ratio are also presented accordingly.

Neutron tagging is assumed to be implemented for the (Gd-doped) water Cherenkov detectors. A low tagging efficiency $\sim 17\%$ of a 2.2-MeV γ from the neutron capture on hydrogen would be increased to 92%^[43] merely for a tagging of 8-MeV γ cascade from

Table 5.1 Summary of the expected number of backgrounds and SRN signals in the neutrino energy of 10.8-30.8 MeV with an exposure of 20 kton-year of water, Gd-doped water, liquid scintillator, and slow liquid scintillator (LAB) at Jinping.

20 kton-year	water ^a	Gd-w ^a	LS	slow LS
Atmospheric $\bar{\nu}_e$ CC	0.04	0.22	0.28	0.26
Atmospheric $\bar{\nu}_\mu/\nu_\mu$ CC	0.41	2.3	3.6	0.025
Atmospheric neutrino NC	0.12	0.61	62	0.35
Total backgrounds	0.58	3.2	66	0.64
Signal ^b	0.68	3.6	4.2	4.1
Signal efficiency	16%	85%	92%	90%
S/B	1.2	1.1	0.064	6.4

^a with neutron tagging.

^b by HBD (6-MeV) model; the number of signals in (Gd-) water is corrected by a factor of 0.9 due to the different fraction of free protons in water from that in LAB.

the neutron capture on gadolinium. In addition, the neutron capture fraction is about 90% with a 0.2% of the Gd compound-water solution.

The expected number of SRN events versus the exposure for several different types of detectors is shown in Figure 5.20. The background-only 68.3% confidence intervals (σ_{up} and σ_{low}) based on Table 5.1 are also drawn from which the sensitivities are indicated. Three predicted points for KamLAND (liquid scintillator detector) and Super-K experiments (water Cherenkov detector with neutron tagging) with data to the end of 2015 are shown according to Ref. [97] and Ref. [100]. The SK* point for the 15-30 MeV SRN neutrino energy range (negligible muon-induced backgrounds) is also plotted by the SK point with the same exposure. Note that the sensitivity of the current Super-K SRN analysis without neutron tagging would be better than that with neutron tagging in the region above 15 MeV by a factor of 2-3. This is mainly caused by the higher signal efficiency $\sim 75\%$ though the dominant Michel electron background from the decays of the muons produced by the atmospheric $\bar{\nu}_\mu/\nu_\mu$ CC interactions would also be increased by a factor of 5.

Background-only 68.3% confidence interval

Inaccurate 68.3% confidence intervals would be obtained due to the discrete Poisson distribution as shown in Figure 5.20, especially for the low statistics. The background-only

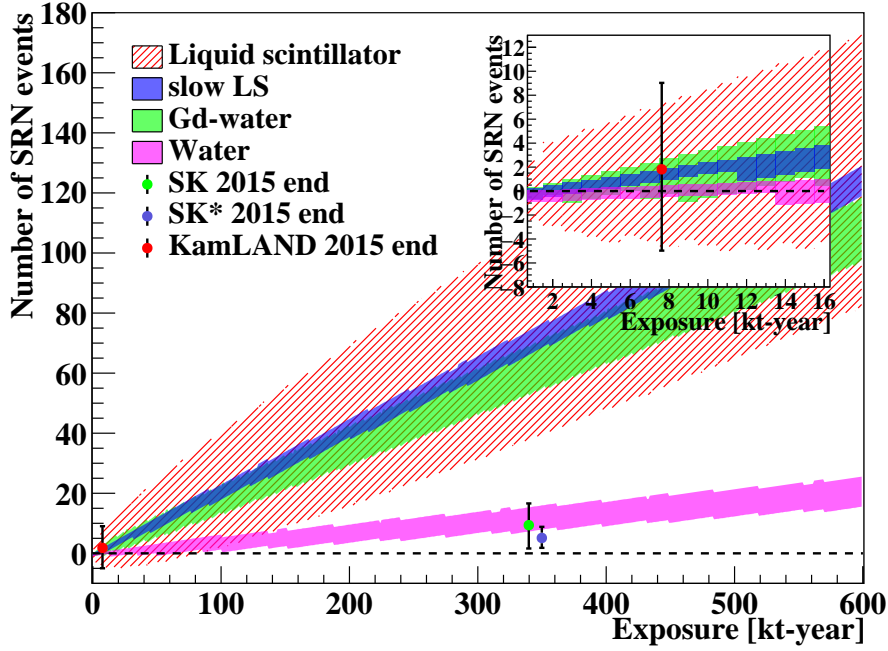


Figure 5.20 The number of SRN events in the neutrino energy region of 10.8-30.8 MeV against the exposure for several different types of detectors. The background-only 68.3% confidence intervals are given. The three points for KamLAND and Super-K with an exposure to the end of 2015 are predicted according to their publications. The SK* point for the SRN neutrino in 15-30 MeV has the same exposure with the SK point. The region with small exposures is zoomed in. See text for more details.

68.3% confidence interval is defined as

$$\sum_{i=\mu_{\text{bkg}}-\sigma_{\text{up}}}^{\mu_{\text{bkg}}+\sigma_{\text{low}}} \text{Poisson}(i, \mu_{\text{bkg}}) \geq 68.3\%, \quad (5-16)$$

where μ_{bkg} is the mean value of the background, and $\sigma_{\text{low/up}}$ correspond to the lower/upper limits of the minimum set of the most probable integers $\{x \in \mathbb{Z} \mid \mu_{\text{bkg}} - \sigma_{\text{up}} \leq x \leq \mu_{\text{bkg}} + \sigma_{\text{low}}\}$ that satisfies Equation (5-16). As drawn in Figure 5.20, $\sigma_{\text{low/up}}$ could be asymmetric.

From the definition above, the variation of $(S + \mu_{\text{bkg}}) - (\mu_{\text{bkg}} \pm \sigma_{\text{low/up}}) = S \pm \sigma_{\text{up/low}}$ results in the sensitivity, S/σ_{low} .

We conclude that, with a kiloton-scale LAB detector at Jinping, a 99.95% confidence-level (same definition as Equation (5-16) and $\sim 3.5\sigma$ assuming a Gaussian distribution) discovery of SRN within [10.8, 30.8] MeV will be obtained with an exposure of 20 kton-years.

The 90% C.L. upper limit provided by a Gd-doped water Cherenkov detector at Jinping is estimated to be comparable with the SRN flux predicted by the HBD model with an exposure of 20 kt-years.

For the SRN detection in the 10-15 MeV range, the background in liquid scintillator (water Cherenkov) detectors would be reduced by a factor of 2 (10) at Jinping with respect to that at Kamioka.

5.9 Supernova neutrino burst sensitivity

Referring to Chapter 3 and Chapter 4, a search for supernova neutrino bursts (online or offline) can also be performed at Jinping with one or several kiloton scale detectors, which have a lower energy threshold and a clean signal against backgrounds.

The selection efficiency of supernova burst electron anti-neutrinos is estimated to be $\sim 90\%$ which results from the common selection criteria for IBD events. A prompt signal energy cut can be 1-100 MeV to fully cover the supernova burst neutrino energy region (model-independent). The lower energy limit is contingent upon the accidental background originating from the natural radioactivity in reality.

Due to the thoroughly removed cosmic-ray muon-induced background (see Section 5.3) and the ultra-low reactor neutrino background ($\sim 10^{-5}$ /kiloton/s) at Jinping^[110], a supernova trigger is assumed to be issued when more than or equal to 2 IBD candidates are observed in a 10-second window. The detection probability is shown in Figure 5.21.

For the detection of the low energy supernova neutrinos, e.g., below 3.5 MeV, the purity of the detector target material and the reduction of the natural radiation of the supporting structure is crucial to lower the energy background.

Due to the deep rock cover, only small detectors may be allowed in Jinping; however, the ultra-low background at Jinping maximizes the detection probability of a detector. The detection probability shown in Figure 5.21 remains at 100% throughout 100 kpc using kiloton scale detectors, and this is comparable to the 22.5-kt Super-Kamiokande water Cherenkov detector^[70].

With 2-3 kiloton of slow LS, the pointing of the supernova neutrino burst could be achieved by identifying the direction of the Cherenkov light from the electrons produced by neutrino-electron scattering interactions. The resolution is roughly estimated to be 8-10° from the pointing ability (in Ref. [63]) of water Cherenkov detectors with an efficient neutron tagging.

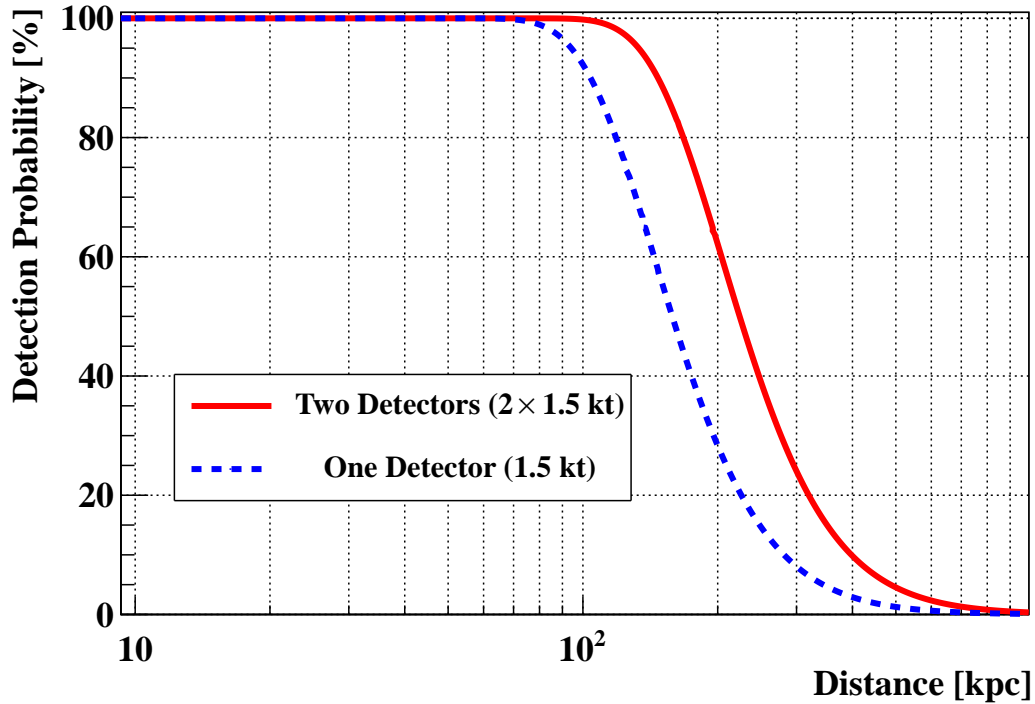


Figure 5.21 The red curve corresponds to two 1.5-kt liquid scintillator detectors and the blue curve corresponds to one 1.5-kt liquid scintillator detector.

5.10 Conclusion and outlook

A computational study on supernova relic neutrino detection was carried out for the proposed Jinping neutrino experiment which seems to be an ideal site for supernova relic neutrino detection. Because of the negligible cosmic-ray muon-induced backgrounds, the SRN detection would be improved significantly at Jinping.

Based on the ability of separating the Cherenkov light and scintillation light in the slow liquid scintillator, e.g., LAB, the most challenging atmospheric neutrino backgrounds for the current SRN detection could be reduced dramatically. Therefore, the discovery potential for supernova relic neutrinos at Jinping can be maximized.

In the future, Gd-doped water Cherenkov detectors^[81,101], liquid scintillator detectors with the pulse shape discrimination of the scintillation light to suppress the NC backgrounds^[103,105], and liquid argon time projection chamber detectors^[47,107,108] may come online to do the SRN study. Compared with them, roughly the same sensitivity would be obtained by a LAB detector at Jinping, however, with one order of magnitude smaller exposure. The sensitivity to supernova neutrino bursts is also one order of magnitude better. The Jinping neutrino experiment is promising to make the first discovery of supernova relic neutrinos.

A better slow liquid scintillator with much higher scintillation light yield is promising in the future which is now under R&D. Such a slow liquid scintillator detector would cover more physics opportunities, especially for low energy neutrino physics, e.g., solar neutrino and geo-neutrino physics.

Chapter 6 Summary

Three experimental studies on supernova neutrino detection are presented in this thesis. The first two studies which rely on the Daya Bay experiment are about an online recognition and an offline search for supernova neutrino bursts based on the detection of supernova burst neutrinos. The last study is a computational study for supernova relic neutrino discovery potential at Jinping.

1) An online supernova trigger system was designed, implemented, tested, and installed in the Daya Bay experiment. The unique feature that multiple ADs are deployed in three separate experimental halls allows a rapid trigger algorithm with an effective suppression of the false-alert rate as well as a gain in the sensitivity to the core-collapse supernovae. This online supernova trigger system is a very prompt (possibly the world's most prompt) supernova trigger system with the lowest energy threshold, and is fully sensitive to core-collapse supernovae throughout the Milky Way. This system was installed at Daya Bay in August 2013 and officially integrated into the worldwide Supernova Early Warning System (SNEWS) in November 2014. It has been smoothly running up to now with an operational efficiency of $\sim 97\%$.

2) An offline search for supernova neutrino bursts has been presented in this chapter using ~ 621 days of data in the Daya Bay experiment. The detection channels include the commonly-used IBD interaction as well as the newly-used neutrino neutral-current excitation of ^{12}C . The latter channel basically increases the fiducial target mass of the Daya Bay detector by which the mineral oil (γ shielding on purpose) could contribute to the neutrino detection.

The search for supernova neutrino bursts was based on any increases observed in the multi-AD signals within the sliding 10-second windows and a rate of fake supernova neutrino bursts imitated by background fluctuations (consistently defined using the false-alert rate threshold which is used for the online supernova trigger) was set to be 1 per century in this search. Two types of analyses were also performed in the search: a high energy threshold (> 10 MeV, IBD channel plus NC- ^{12}C channel) analysis and a low energy threshold (0.7 MeV for IBD nGd signals and 3.5 MeV for IBD nH signals) analysis.

The high energy threshold analysis has a high sensitivity to the ccSN (typical model) which retains 100% out to 25 kpc covering the whole Milky Way and the sensitivity is increased by a factor of 2 for the extragalactic region compared with the online supernova trigger. Since no supernova neutrino burst was observed in this analysis, a 90% C.L. upper limit of the ccSN (including failed CCSN) rate within the Milky Way was estimated to be 1.5 yr^{-1} . As the offline search covered the whole data set before the online trigger system was installed, this upper limit is lowered to 0.53 yr^{-1} considering no supernova trigger has been confirmed from the running online trigger system to date.

The low energy threshold analysis was intended to be a model-independent search covering $<10 \text{ MeV}$ neutrino energy region with the lowest energy threshold in the world (0.7 MeV). As a result, no neutrino burst was found with a false-alert rate threshold of 1 per century but two candidate bursts were observed with a false-alert rate threshold of 1 per year. In terms of the occurrence rate and the energy spectrum, the two candidates are most likely attributable to the background. The detailed information of the two candidates (with an average energy of $\sim 4 \text{ MeV}$) are provided after the checks to rule out the high possibility of being unphysical, accidental, or muon-induced. No coincident supernova was found by two supernova catalogs.

In addition, two exotic searches for coincident neutrino signals with the so far closest type Ia SN2014J and the first discovered gravitational wave event GW150914. There is no positive evidence of any coincident neutrino signals. Corresponding upper limits on neutrino fluence and total energy are given for GW150914.

3) A computational study on supernova relic neutrino detection was carried out for the proposed Jinping neutrino experiment which tends to be an ideal site for supernova relic neutrino detection. Because of the negligible cosmic-ray muon-induced backgrounds, the SRN detection would be improved significantly at Jinping.

Based on the ability of separating the Cherenkov light and scintillation light in the slow liquid scintillator, e.g., LAB, the most challenging atmospheric neutrino backgrounds for the current SRN detection could be reduced dramatically. Therefore, the discovery potential for supernova relic neutrinos at Jinping can be maximized.

In the future, Gd-doped water Cherenkov detectors^[81,101], liquid scintillator detectors with the pulse shape discrimination of the scintillation light to suppress the NC backgrounds^[103,105], and liquid argon time projection chamber detectors^[47,107,108] may

come online to do the SRN study. Compared with them, roughly the same sensitivity would be obtained by a LAB detector at Jinping; however, with one order of magnitude smaller exposure. The sensitivity to supernova neutrino bursts is similarly better. The Jinping neutrino experiment is promising to make the first discovery of supernova relic neutrinos.

A better slow liquid scintillator with much higher scintillation light yield is promising for the future which is now under R&D. Such a slow liquid scintillator detector would cover more physics opportunities, especially for low energy neutrino physics, e.g., solar neutrino and geo-neutrino physics.

References

- [1] A. Burrows. *Supernova explosions in the Universe*. Nature, 2000, 403:727–733.
- [2] A. Burrows. *Neutrinos from supernova explosions*. Annu. Rev. Nucl. Part. Sci., 1990, 40:181–212.
- [3] H.-T. Janka, K. Langanke, A. Marek, G. Martinez-Pinedo, and B. Mueller. *Theory of Core-Collapse Supernovae*. Phys. Rept., 2007, 442:38–74.
- [4] P. Dina. *An Introduction to the Theory of Stellar Structure and Evolution*. Cambridge University Press, 2000.
- [5] S. Woosley, A. Heger, and T. Weaver. *The evolution and explosion of massive stars*. Rev. Mod. Phys., 2002, 74:1015–1071.
- [6] C. Giunti and C. Kim. *Fundamentals of Neutrino Physics and Astrophysics*. Oxford University Press, 2007.
- [7] G. Raffelt. *Neutrinos and the stars*. Neutrino Physics and Astrophysics, volume 182 of *Proceedings of the International School of Physics "Enrico Fermi"*. IOS press. 61–143 [arXiv:1201.1637 [astro-ph.SR]].
- [8] W.P. Wright, G. Nagaraj, K. Scholberg, *et al.* *Neutrinos from type Ia supernovae: The deflagration-to-detonation transition scenario*. Phys. Rev. D, 2016, 94:025026.
- [9] W.P. Wright, J.P. Kneller, K. Scholberg, *et al.* *Neutrinos from Type Ia Supernovae: The Gravitationally Confined Detonation Scenario*. arXiv:1609.07404 [astro-ph.HE].
- [10] K. Kotake, K. Sato, and K. Takahashi. *Explosion mechanism, neutrino burst and gravitational wave in core-collapse supernovae*. Rep. Prog. Phys., 2006, 69:971–1143.
- [11] Y.-Z. Qian, P. Vogel, and G. J. Wasserburg. *Diverse Supernova Sources for the r-Process*. Astrophys. J., 1998, 494:285–296.
- [12] G. Raffelt. *Muon-neutrino and tau-neutrino spectra formation in supernovae*. Astrophys. J., 2001, 561(2):890–914.
- [13] K. Nakazato, K. Sumiyoshi, H. Suzuki, and S. Yamada. *Oscillation and future detection of failed supernova neutrinos from a black-hole-forming collapse*. Phys. Rev. D, 2008, 78:083014.
- [14] T. Fischer, S. Whitehouse, A. Mezzacappa, *et al.* *The neutrino signal from protoneutron star accretion and black hole formation*. Astron. Astrophys., 2009, 499:1.
- [15] C. Lunardini. *Diffuse Neutrino Flux from Failed Supernovae*. Phys. Rev. Lett., 2009, 102:231101.
- [16] H.T. Janka. *Explosion Mechanism of Core-Collapse Supernovae*. Annu. Rev. Nucl. Part. Sci., 2012, 62:407–451.
- [17] P. Antonioli, *et al.* *SNEWS: the SuperNova Early Warning System*. New J. Phys., 2004, 6:114 [astro-ph/0406214].
- [18] K. Scholberg. *The SuperNova Early Warning System*. Astron. Nachr., 2008, 329:337 [arXiv:0803.0531 [astro-ph]].

-
- [19] G. Pagliaroli, F. Vissani, E. Coccia, and W. Fulgione. *Neutrinos from Supernovae as a Trigger for Gravitational Wave Search*. Phys. Rev. Lett., 2009, 103:031102.
- [20] I. Leonor, *et al.* *Searching for prompt signatures of nearby core-collapse supernovae by a joint analysis of neutrino and gravitational-wave data*. Classical and Quantum Gravity, 2010, 27:084019.
- [21] V. Re for the GW-neutrinos working group. *Joint Search for Gravitational Waves and Neutrinos From Core-collapse Supernovae*. The Thirteenth Marcel Grossmann Meeting. WORLD SCIENTIFIC, 2015. 2007–2008.
- [22] R. Mohapatra, P. Pal. *Massive neutrinos in Physics and Astrophysics*. World Scientific Publishing Co. Pte. Ltd., 2004.
- [23] S. Mikheev, A. Smirnov. *Resonance Amplification of Oscillations in Matter and Spectroscopy of Solar Neutrinos*. Sov. J. Nucl. Phys., 1985, 42:913–917.
- [24] L. Wolfenstein. *Neutrino Oscillations in Matter*. Phys. Rev. D, 1978, 17:2369–2374.
- [25] C. Lunardini, A. Smirnov. *Probing the neutrino mass hierarchy and the 13-mixing with supernovae*. JCAP, 2003, 06(009).
- [26] P. Serpico, S. Chakraborty, T. Fischer, *et al.* *Probing the neutrino mass hierarchy with the rise time of a supernova burst*. Phys. Rev. D, 2012, 85:085031.
- [27] H. Duan, *et al.* *Simulation of coherent nonlinear neutrino flavor transformation in the supernova environment: Correlated neutrino trajectories*. Phys. Rev. D, 2006, 74:105014.
- [28] H. Duan, *et al.* *Coherent Development of Neutrino Flavor in the Supernova Environment*. Phys. Rev. Lett., 2006, 97:241101.
- [29] K. Hirata, *et al.* *Observation of a neutrino burst from the supernova SN1987A*. Phys. Rev. Lett., 1987, 58:1490.
- [30] K. Hirata, *et al.* *Observation in the Kamiokande-II detector of the neutrino burst from supernova SN1987A*. Phys. Rev. D, 1988, 38:448.
- [31] R. Bionta, *et al.* *Observation of a neutrino burst in coincidence with supernova 1987A in the Large Magellanic Cloud*. Phys. Rev. Lett., 1987, 58:1494.
- [32] C. Bratton, *et al.* *Angular distribution of events from SN1987A*. Phys. Rev. D, 1988, 37:3361.
- [33] E. Alekseev, *et al.* *Possible detection of a neutrino signal on 23 February 1987 at the Baksan underground scintillation telescope of the Institute of Nuclear Research*. JETP Lett., 1987, 45:589.
- [34] E. Alekseev, *et al.* *Detection of the neutrino signal from SN 1987A in the LMC using the INR Baksan underground scintillation telescope*. Phys. Lett. B, 1988, 205:209.
- [35] S. Horiuchi, J. Beacom, and E. Dwek. *Diffuse supernova neutrino background is detectable in Super-Kamiokande*. Phys. Rev. D, 2009, 79:083013.
- [36] J. Lattimer, M. Prakash. *Neutron Star Observations: Prognosis for Equation of State Constraints*. Phys. Rept., 2007, 442:109–165.
- [37] L. Hüdepohl, B. Müller, H.-T. Janka, A. Marek, and G. Raffelt. *Neutrino Signal of Electron-Capture Supernovae from Core Collapse to Cooling*. Phys. Rev. Lett., 2010, 104:251101; (E) *ibid.* 105 (2010) 249901.

- [38] M. Keil, G. Raffelt, and H.-T. Janka. *Monte Carlo Study of Supernova Neutrino Spectra Formation*. *Astrophys. J.*, 2003, 590:971 [astro-ph/0208035].
- [39] I. Tamborra, B. Müller, L. Hüdepohl, H.-T. Janka, and G. Raffelt. *High-resolution supernova neutrino spectra represented by a simple fit*. *Phys. Rev. D*, 2012, 86:125031 [arXiv:1211.3920 [astro-ph.SR]].
- [40] J. Gava, and J. Kneller, and C. Volpe. *Dynamical Collective Calculation of Supernova Neutrino Signals*. *Phys. REv. Lett.*, 2009, 103:071101.
- [41] K. Scholberg. *Supernova Neutrino Detection*. *Annu. Rev. Nucl. Part. Sci.*, 2012, 62:81–103.
- [42] P. Vogel, J. Beacom. *Angular distribution of neutron inverse beta decay, $\bar{\nu}_e + p \rightarrow e^+ + n$* . *Phys. Rev. D*, 1999, 60:053003.
- [43] H. Watanabe, H. Zhang, *et al.* (Super-Kamiokande Collaboration). *First study of neutron tagging with a water Cherenkov detector*. *Astropart. Phys.*, 2009, 31:320–328.
- [44] J. Beacom, W. Farr, and P. Vogel. *Detection of supernova neutrinos by neutrino-proton elastic scattering*. *Phys. Rev. D*, 2002, 66:033001.
- [45] A. Drukier, L. Stodolsky. *Principles and applications of a neutral-current detector for neutrino physics and astronomy*. *Phys. Rev. D*, 1984, 30:2295.
- [46] C. Horowitz, K. Coakley, and D. McKinsey. *Supernova observation via neutrino-nucleus elastic scattering in the CLEAN detector*. *Phys. Rev. D*, 2003, 68:023005.
- [47] R. Acciarri, *et al.* (DUNE Collaboration). *Long-Baseline Neutrino Facility (LBNF) and Deep Underground Neutrino Experiment (DUNE) : Volume 1: The LBNF and DUNE Projects*. arXiv:1601.05471 [physics.ins-det].
- [48] R. Acciarri, *et al.* (DUNE Collaboration). *Long-Baseline Neutrino Facility (LBNF) and Deep Underground Neutrino Experiment (DUNE) : Volume 2: The Physics Program for DUNE at LBNF*. arXiv:1512.06148 [physics.ins-det].
- [49] J. Strait, *et al.* (DUNE Collaboration). *Long-Baseline Neutrino Facility (LBNF) and Deep Underground Neutrino Experiment (DUNE) : Volume 3: Long-Baseline Neutrino Facility for DUNE June 24, 2015*. arXiv:1601.05823 [physics.ins-det].
- [50] R. Acciarri, *et al.* (DUNE Collaboration). *Long-Baseline Neutrino Facility (LBNF) and Deep Underground Neutrino Experiment (DUNE) : Volume 4 The DUNE Detectors at LBNF*. arXiv:1601.02984 [physics.ins-det].
- [51] C. Duba, *et al.* *HALO: The helium and lead observatory for supernova neutrinos*. *J. Phys. Conf. Ser.*, 2008, 136:042007.
- [52] K. Zuber for the HALO collaboration. *HALO, a supernova neutrino observatory*. *Nucl. Part. Phys. Proc.*, 2015, 265-266:233–235.
- [53] A. Strumia, F. Vissani. *Precise quasielastic neutrino/nucleon cross section*. *Phys. Lett. B*, 2003, 564:42–54.
- [54] A. Mirizzi, I. Tamborra, H.-T. Janka, N. Saviano, K. Scholberg, R. Bollig, L. Hüdepohl, S. Chakraborty. *Supernova Neutrinos: Production, Oscillations and Detection*. *Riv. Nuovo. Cim.*, 2016, 39(1-2):1–112.
- [55] Supernova Early Warning Systems (SNEWS).

-
- [56] F. Halzen, J. Jacobsen, E. Zas. *Possibility that high energy neutrino telescopes could detect supernovae*. Phys. Rev. D, 1994, 49:1758.
- [57] F. Halzen, J. Jacobsen, E. Zas. *Ultrasensitive Antarctic ice as a supernova detector*. Phys. Rev. D, 1996, 53:7359–7361.
- [58] R. Abbasi *et al.* (IceCube Collaboration). *IceCube Sensitivity for Low-Energy Neutrinos from Nearby Supernovae*. Astron. Astrophys., 2011, 535:A109.
- [59] A. Aguilar-Arevalo, *et al.* (The MiniBooNE Collaboration). *Search for core-collapse supernovae using the MiniBooNE neutrino detector*. Phys. Rev. D, 2010, 81:032001.
- [60] M. Soderberg for the MicroBooNE collaboration. *MicroBooNE: A New Liquid Argon Time Projection Chamber Experiment*. AIP Conf. Proc., 2009, 1189:83–87.
- [61] J. Beacom, P. Vogel. *Can a supernova be located by its neutrinos?* Phys. Rev. D, 1999, 60:033007.
- [62] V. Fischer, T. Chirac, T. Lasserre, *et al.* *Prompt directional detection of galactic supernova by combining large liquid scintillator neutrino detectors*. JCAP, 2015, 1508:032.
- [63] R. Tomàs, D. Semikoz, G. Raffelt, M. Kachelrieß, and A. Dighe. *Supernova pointing with low- and high-energy neutrino detectors*. Phys. Rev. D, 2003, 68:093013.
- [64] K. Abe, *et al.* (Hyper-Kamiokande proto-collaboration). *Hyper-Kamiokande Design Report*. KEK Preprint, 2016-21. ICRR-Report-701-2016-1.
- [65] T. Mühlbeier, H. Nunokawa, and R. Zukanovich Funchal. *Revisiting the triangulation method for pointing to supernova and failed supernova with neutrinos*. Phys. Rev. D, 2013, 88:085010.
- [66] K. Scholberg, A. Burgmeier, and R. Wendell. *Obtaining supernova directional information using the neutrino matter oscillation pattern*. Phys. Rev. D, 2010, 81:043007.
- [67] S. Ando, J. Beacom, and H. Yüksel. *Detection of Neutrinos from Supernovae in Nearby Galaxies*. Phys. Rev. Lett., 2005, 95:171101.
- [68] N. Agafonova, *et al.* (The LVD Collaboration). *Implication for the core-collapse supernova rate from 21 years of data of the Large Volume Detectors*. Astrophys. J., 2015, 802:47.
- [69] H. Wei, L. Lebanowski, F. Li, Z. Wang, and S. Chen. *Design, characterization, and sensitivity of the supernova trigger system at Daya Bay*. Astropart. Phys., 2016, 75:38–43.
- [70] M. Ikeda, *et al.* (The Super-Kamiokande Collaboration). *Search for supernova neutrino bursts at Super-Kamiokande*. Astrophys. J., 2007, 669:519–524.
- [71] I. Karachentsev, V. Karachentseva, W. Huchtmeier, and D. Makarov. *A Catalog of Neighboring Galaxies*. Astron. J., 2004, 127(4):2031–2068.
- [72] S. Ando, K. Sato. *Relic neutrino background from cosmological supernovae*. New J. Phys., 2004, 6:170.
- [73] G. Bisnovatyi-kogan, Z. Seidov. *Supernovae, Neutrino Rest Mass, and the Middle-Energy Neutrino Background in the Universe*. Ann. N. Y. Acad. Sci., 1984, 422:319.
- [74] L. Krauss, S. Glashow, and D. Schramm. *Antineutrino astronomy and geophysics*. Nature, 1984, 310:191–198.
- [75] S. Woosley, J. Wilson and R. Mayle. *Gravitational collapse and the cosmic antineutrino background*. Astrophys. J., 1986, 302:19.

-
- [76] T. Totani, K. Sato and Y. Yoshii. *Spectrum of the Supernova Relic Neutrino Background and Evolution of Galaxies*. *Astrophys. J.*, 1996, 460:303.
- [77] R. Malaney. *Evolution of the cosmic gas and the relic supernova neutrino background*. *Astropart. Phys.*, 1997, 7:125.
- [78] D. Hartmann and S. Woosley. *The cosmic supernova neutrino background*. *Astropart. Phys.*, 1997, 7:137.
- [79] M. Kaplinghat, G. Steigman, and T. Walker. *Supernova relic neutrino background*. *Phys. Rev. D*, 2000, 62:043001.
- [80] S. Anto, K. Sato, and T. Totani. *Detectability of the supernova relic neutrinos and neutrino oscillation*. *Astropart. Phys.*, 2003, 18:307.
- [81] J. Beacom, M. Vagins. *Antineutrino Spectroscopy with large water Cerenkov detectors*. *Phys. Rev. Lett.*, 2004, 93:171101.
- [82] C. Lunardini. *Diffuse supernova neutrinos at underground laboratories*. *Astrop. Phys.*, 2016, 79:49–77.
- [83] T. Gaisser, T. Stanev, and G. Barr. *Cosmic-ray neutrinos in the atmosphere*. *Phys. Rev. D*, 1988, 38:85.
- [84] M. Honda, *et al.* *Improvement of low energy atmospheric neutrino flux calculation using the JAM nuclear interaction model*. *Phys. Rev. D*, 2011, 83:123001.
- [85] P. Huber. *On the determination of anti-neutrino spectra from nuclear reactors*. *Phys. Rev. C*, 2011, 84:024617.
- [86] Th. Mueller, *et al.* *Improved Predictions of Reactor Antineutrino Spectra*. *Phys. Rev. C*, 2011, 83:054615.
- [87] S. Li, J. Beacom. *First calculation of cosmic-ray muon spallation backgrounds for MeV astrophysical neutrino signals in Super-Kamiokande*. *Phys. Rev. C*, 2014, 89:045801.
- [88] S Abe, *et al.* (KamLAND Collaboration). *Production of radioactive isotopes through cosmic muon spallation in KamLAND*. *Phys. Rev. C*, 2010, 81:025807.
- [89] Y. Zhang, *et al.* (Super-Kamiokande Collaboration). *First measurement of radioactive isotope production through cosmic-ray muon spallation in Super-Kamiokande IV*. *Phys. Rev. D*, 2016, 93:012004.
- [90] B. Aharmim, *et al.* *A search for astrophysical burst signals at the Sudbury Neutrino Observatory*. *Astrop. Phys.*, 2014, 55:1–7.
- [91] K. Tolich for the KamLAND collaboration. *Supernova detection with KamLAND*. *Nucl. Phys. Proc. Suppl.*, 2011, 221:355.
- [92] K. Asakura, *et al.* (KamLAND Collaboration). *KamLAND Sensitivity to Neutrinos from Pre-Supernova Stars*. *Astrophys. J.*, 2016, 818(1):91.
- [93] <http://www.ucl.ac.uk/mathematical-physical-sciences/news-events/maps-news-publication/maps1405>.
- [94] B.P. Abbott, *et al.* (LIGO Scientific Collaboration and Virgo Collaboration). *Observation of Gravitational Waves from a Binary Black Hole Merger*. *Phys. Rev. Lett.*, 2016, 116:061102.

- [95] K. Bays, *et al.* (Super-Kamiokande Collaboration). *Supernova relic neutrino search at Super-Kamiokande*. Phys. Rev. D, 2012, 85:052007.
- [96] H. Zhang, *et al.* (Super-Kamiokande Collaboration). *Supernova relic neutrino search with neutron tagging at Super-Kamiokande-IV*. Astropart. Phys., 2015, 60:41–46.
- [97] A. Gando, *et al.* (KamLAND Collaboration). *A study of extraterrestrial antineutrino sources with the KamLAND detector*. Astrophys. J., 2012, 745:193.
- [98] B. Aharmim, *et al.* (SNO Collaboration). *A search for neutrinos from the solar hep reaction and the diffuse supernova neutrino background with the Sudbury Neutrino Observatory*. Astrophys. J., 2006, 653:1545.
- [99] G. Bellini, *et al.* (Borexino Collaboration). *Study of solar and other unknown anti-neutrino fluxes with Borexino at LNGS*. Phys. Lett. B, 2011, 696:191–196.
- [100] Y. Zhang. *Experimental Studies of Supernova Relic Neutrinos at Super-Kamiokande-IV*[D]. Beijing, China: Tsinghua University Ph.D. Thesis, 2015.
- [101] T. Mori for the Super-Kamiokande Collaboration. *Status of the Super-Kamiokande gadolinium project*. Nucl. Instrum. Meth., 2013, A732:316–319.
- [102] T. Adam, *et al.* (JUNO Collaboration). *JUNO Conceptual Design Report*. arXiv: 1508:076166 [physics.ins-det].
- [103] F. An, *et al.* (JUNO Collaboration). *Neutrino Physics with JUNO*. J. Phys. G, 2016, 43(3):030401.
- [104] M. Wurm, *et al.* (LENA Collaboration). *The next-generation liquid-scintillator neutrino observatory LENA*. Astropart. Phys., 2012, 35:685–732.
- [105] R. Möllenberg, *et al.* *Detecting the diffuse supernova neutrino background with LENA*. Phys. Rev. D, 2015, 91:032005.
- [106] C. Rubbia. *The liquid argon time projection chamber: a new concept for neutrino detectors*. 1977 Preprint CERN/77-08..
- [107] B. Baller *et al.* *Liquid argon time projection chamber research and development in the United States*. JINST, 2014, 9:T05005.
- [108] A. Cocco, *et al.* *Supernova relic neutrinos in liquid argon detectors*. J. Cosmol. Astropart. Phys., 2004, 12:002.
- [109] A. Ankowski, *et al.* *Supernova Physics at DUNE*. arXiv:1608.07853 [hep-ex].
- [110] J. Beacom, S. Chen, *et al.* (Jinping Collaboration). *Letter of Intent: Jinping Neutrino Experiment*. 2016. arXiv:1602.01733 [physics.ins-det].
- [111] K. J. Kang, *et al.* *Status and prospects of a deep underground laboratory in China*. J. Phys. Conf. Ser., 2010, 203:012028.
- [112] J. Cao, K.-B. Luk. *An overview of the Daya Bay reactor neutrino experiment*. Nucl. Phys. B, 2016, 908:62–73.
- [113] F.P. An, *et al.* (Daya Bay Collaboration). *A side-by-side comparison of Daya Bay antineutrino detectors*. Nucl. Instrum. Meth., 2012, A685:78–97.
- [114] F.P. An, *et al.* (Daya Bay Collaboration). *The Detector System of The Daya Bay Reactor Neutrino Experiment*. Nucl. Instrum. Meth., 2016, A811:133–161.

- [115] M. Grassi. *Seasonal Variation of the Underground Cosmic Muon Flux Observed with the Daya Bay Experiment*. Daya Bay Document 10379, 2016. <http://dayabay.ihep.ac.cn/cgi-bin/DocDB/ShowDocument?docid=10379>.
- [116] F.P. An, *et al.* (Daya Bay Collaboration). *The muon system of the Daya Bay Reactor antineutrino experiment, Daya Bay Collaboration*. Nucl. Instrum. Meth., 2015, A773:8–20.
- [117] F.P. An, *et al.* (Daya Bay Collaboration). *Observation of electron-antineutrino disappearance at Daya Bay*. Phys. Rev. Lett., 2012, 108:171803.
- [118] F.P. An, *et al.* (Daya Bay Collaboration). *Improved measurement of electron antineutrino disappearance at Daya Bay*. Chinese Phys. C, 2013, 37:011001.
- [119] F.P. An, *et al.* (Daya Bay Collaboration). *Spectral Measurement of Electron Antineutrino Oscillation Amplitude and Frequency at Daya Bay*. Phys. Rev. Lett., 2014, 112:061801.
- [120] F.P. An, *et al.* (Daya Bay Collaboration). *Independent measurement of the neutrino mixing angle 13 via neutron capture on hydrogen at Daya Bay*. Phys. Rev. D, 2014, 90:071101(R).
- [121] F.P. An, *et al.* (Daya Bay Collaboration). *New Measurement of Antineutrino Oscillation with the Full Detector Configuration at Daya Bay*. Phys. Rev. Lett., 2015, 115:111802.
- [122] F.P. An, *et al.* (Daya Bay Collaboration). *New measurement of 13 via neutron capture on hydrogen at Daya Bay*. Phys. Rev. D, 2016, 93:072011.
- [123] S. Parke. *What is Δm_{ee}^2 ?* Phys. Rev. D, 2016, 93:053008.
- [124] F.P. An, *et al.* (Daya Bay Collaboration). *Measurement of the Reactor Antineutrino Flux and Spectrum at Daya Bay*. Phys. Rev. Lett., 2016, 116:061801.
- [125] F.P. An, *et al.* (Daya Bay Collaboration). *Improved Measurement of the Reactor Antineutrino Flux and Spectrum at Daya Bay*. arXiv:1607.05378.
- [126] F.P. An, *et al.* (Daya Bay Collaboration). *Search for a Light Sterile Neutrino at Daya Bay*. Phys. Rev. Lett., 2014, 113:141802.
- [127] F.P. An, *et al.* (Daya Bay Collaboration). *Improved Search for a Light Sterile Neutrino with the Full Configuration of the Daya Bay Experiment*. Phys. Rev. Lett., 2016, 117:151802.
- [128] P. Adamson, *et al.* (Daya Bay and MINOS Collaborations). *Limits on Active to Sterile Neutrino Oscillations from Disappearance Searches in the MINOS, Daya Bay, and Bugey-3 Experiments*. Phys. Rev. Lett., 2016, 117:151801.
- [129] F.P. An, *et al.* (Daya Bay Collaboration). *Study of the wave packet treatment of neutrino oscillation at Daya Bay*. arXiv:1608.01661.
- [130] F. Li, X.L. Ji, X.N. Li, and K.J. Zhu. *DAQ Architecture Design of Daya Bay Reactor Neutrino Experiment*. IEEE Trans. Nucl. Sci., 2011, 58:1723.
- [131] MySQL. <http://www.mysql.com/>.
- [132] S.H. Zhang, Y.F. Wang, M. Ye, *et al.* *Detector control system for Daya Bay Reactor Neutrino Experiment*. SCIENCE CHINA Technological Sciences, 2013, 56(8):1966–1973.
- [133] Distributed Information Management System (DIM). <http://dim.web.cern.ch/dim>.
- [134] Q. Zhao. *Flashers in P12C Part2*. Daya Bay Document 8486, 2012. <http://dayabay.ihep.ac.cn/cgi-bin/DocDB/ShowDocument?docid=8486>.

- [135] L. Cadonati, F.P. Calaprice, and M.C. Chen. *Supernova neutrino detection in Borexino*. *Astrop. Phys.*, 2002, 16:361–372.
- [136] J.A. Formaggio, G.P. Zeller. *From eV to EeV: Neutrino cross sections across energy scales*. *Rev. Mod. Phys.*, 2012, 84:1307.
- [137] B. Bodmann, *et al.* (KARMEN Collaboration). *First observation of the neutral current nuclear excitation $^{12}\text{C}(\nu, \nu)^{12}\text{C}^*(1+, 1)$* . *Phys. Lett. B*, 1991, 267:321–324.
- [138] B. Zeitnitz, *et al.* (Collaboration). *KARMEN: neutrino physics at ISIS*. *Prog. Part. Nucl. Phys.*, 1994, 32:351–373.
- [139] B. Armbruster, *et al.* (KARMEN Collaboration). *Measurement of the weak neutral current excitation $^{12}\text{C}(\nu(\mu) \nu'(\mu))^{12}\text{C}^*(1+, 1, 15.1\text{-MeV})$ at $E(\nu(\mu)) = 29.8\text{-MeV}$* . *Phys. Lett. B*, 1998, 423:15–20.
- [140] F.P. An, *et al.* (Daya Bay Collaboration). *Measurement of electron antineutrino oscillation based on 1230 days of operation of the Daya Bay experiment*. arXiv:1610.04802.
- [141] J. Isern, *et al.* *Gamma-ray emission from SN2014J near maximum optical light*. *Astron. Astrophys.*, 2016, 588:A67.
- [142] O.L. Caballero, G.C. McLaughlin, and R. Surman. *NEUTRINO SPECTRA FROM ACCRETION DISKS: NEUTRINO GENERAL RELATIVISTIC EFFECTS AND THE CONSEQUENCES FOR NUCLEOSYNTHESIS*. *Astrophys. J.*, 2012, 745:170.
- [143] O.L. Caballero, T. Zielinski. *Black hole spin influence on accretion disk neutrino detection*. *Phys. Rev. D*, 2016, 93:123015.
- [144] V. Connaughton, *et al.* *FERMI GBM OBSERVATIONS OF LIGO GRAVITATIONAL-WAVE EVENT GW150914*. *Astrophys. J. Lett.*, 2016, 826:L6.
- [145] High-energy neutrino follow-up search of gravitational wave event GW150914 with ANTARES and IceCube. *S. Adrian-Martinez, et al. (ANTARES Collaboration, IceCube Collaboration, LIGO Scientific Collaboration, and Virgo Collaboration)*. *Phys. Rev. D*, 2016, 93:122010.
- [146] A. Gando, *et al.* (KamLAND Collaboration). *Search for electron antineutrinos associated with gravitational wave events GW150914 and GW151226 using KamLAND*. *Astrophys. J. Lett.*, 2016, 829:L34.
- [147] K. Abe, *et al.* (The Super-Kamiokande Collaboration). *SEARCH FOR NEUTRINOS IN SUPER-KAMIOKANDE ASSOCIATED WITH GRAVITATIONAL-WAVE EVENTS GW150914 AND GW151226*. *Astrophys. J. Lett.*, 2016, 830:L11.
- [148] B. Baret, *et al.* *Bounding the time delay between high-energy neutrinos and gravitational-wave transients from gamma-ray bursts*. *Astrop. Phys.*, 2011, 35:1–7.
- [149] G. Feldman, R. Cousins. *A Unified approach to the classical statistical analysis of small signals*. *Phys. Rev. D*, 1998, 57:3873–3889.
- [150] G. Cowan, K. Cranmer, E. Gross, and O. Vitells. *Asymptotic formulae for likelihood-based tests of new physics*. *Eur. Phys. J. C*, 2011, 71:1554.
- [151] Q. Yue, *et al.* (CDEX Collaboration). *Limits on light weakly interacting massive particles from the CDEX-1 experiment with a p-type point-contact germanium detector at the China Jinping Underground Laboratory*. *Phys. Rev. D*, 2014, 90:091701 (R).

-
- [152] W. Zhao, *et al.* (CDEX Collaboration). *Search of low-mass WIMPs with a p-type point contact germanium detector in the CDEX-I experiment.* Phys. Rev. D, 2016, 93:092003.
- [153] X. Xiao, *et al.* (PandaX Collaboration). *Low-mass dark matter search results from full exposure of the PandaX-I experiment.* Phys. Rev. D, 2015, 92:052004.
- [154] A. Tan, *et al.* (PandaX-II Collaboration). *Dark Matter Results from First 98.7 Days of Data from the PandaX-II Experiment.* Phys. Rev. Lett., 2016, 117:121303.
- [155] Y.-Ch. Wu, *et al.* *Measurement of cosmic ray flux in the China JinPing underground laboratory.* Chinese Phys. C, 2013, 37(8):086001.
- [156] International Atomic Energy Agency. <http://www.iaea.org/>.
- [157] C. Andreopoulos, *et al.* *The GENIE neutrino Monte Carlo generator.* Nucl. Instrum Meth., 2010, A614:87–104.
- [158] M. Yeh, *et al.* *A new water-based liquid scintillator and potential applications.* Nucl. Instrum Meth., 2011, A660:51–56.
- [159] J. Alonso, *et al.* *Advanced Scintillator Detector Concept (ASDC): A Concept Paper on the Physics Potential of Water-Based Liquid Scintillator.* BNL-106082-2014-JA. arXiv: 1409.5864 [physics.ins-det].
- [160] M. Li, *et al.* *Separation of scintillation and Cherenkov lights in linear alkyl benzene.* Nucl. Instrum. Meth., 2016, A830:303–308.
- [161] C. Aberle, *et al.* *Measuring Directionality in Double-Beta Decay and Neutrino Interactions with Kiloton-scale Scintillation Detectors.* JINST, 2014, 9:P06012.
- [162] J. Birks. *Scintillations from Organic Crystals: Specific Fluorescence and Relative Response to Different Radiations.* Proc. Phys. Soc. A, 1951, 64:874.
- [163] S. Agostinelli, *et al.* *Geant4 – a simulation toolkit.* Nucl. Instrum. Meth., 2003, A506:250–303.
- [164] J. Goett, *et al.* *Optical attenuation measurements in metal-loaded liquid scintillators with a long-pathlength photometer.* Nucl. Instrum Meth., 2011, A637:47–52.
- [165] S. Agarwalla, Y. Kao, and T. Takeuchi. *Analytical approximation of the neutrino oscillation matter effects at large θ_{13} .* JHEP, 2014, 04:047.
- [166] C. Giunti, C.W. Kim, M. Monteno. *Atmospheric neutrino oscillations with three neutrinos and a mass hierarchy.* Nucl. Phys., 1998, B521:3–36.
- [167] D.L. Anderson. *Theory of the Earth.* Blackwell Scientific Publications, 1989.
- [168] C. Patrignani, *et al.* (Particle Data Group). *The Review of Particle Physics (2016).* Chinese Phys. C, 2016, 40:100001.
- [169] M. Alam, *et al.* *GENIE Production Release 2.10.0.* FERMILAB-FN-1006-CD. arXiv:1512.06882 [hep-ph].

Acknowledgments

Firstly, I would express my sincere gratitude to my supervisor Prof. Shaomin Chen and Assoc. Prof. Zhe Wang. Many thanks to them for guiding me in my PhD study and life. They provided me a deep insight into the profound physical universe and taught me how to do scientific researches. I shall cherish their meticulous care and edification forever.

Secondly, i really appreciate the fruitful and constructive suggestions and solid help in many aspects from Prof. Yuanning Gao, Assoc. Prof. Zhenwei Yang, and Assoc. Prof. Xianglei Zhu during my PhD life. I would also thank the comrades in the Center for High Energy Physics, Tsinghua University, the Daya Bay collaborators, and Prof. Kate Scholberg from SNEWS.

Then, i feel like expressing my great respect and gratitude to my parents and my wife. Without their infinite understanding and selfless support, i could not stand here and make my today's achievements.

Finally, i would like to tell my seven-months-old son: thank you for accompanying me and inspiring me to write my PhD thesis, I love you.

Declaration

本人郑重声明：所呈交的学位论文，是本人在导师指导下，独立进行研究工作所取得的成果。尽我所知，除文中已经注明引用的内容外，本学位论文的研究成果不包含任何他人享有著作权的内容。对本论文所涉及的研究工作做出贡献的其他个人和集体，均已在文中以明确方式标明。

签 名： _____ 日 期： _____

Appendix A Statistics in overlapping windows

A.1 Probability distribution of N_{IBD} in sliding 10-second windows

The probability distribution of N_{IBD} in sliding 10-second windows is not a trivial mathematical problem. In general, the classical probability is defined as the frequency of one event among the infinite tests with one precondition that the infinite tests are mutually independent. The sliding 10-second windows as shown in Figure A.1 have overlapping, thus obviously correlated to some extent. For the derivation below, the sliding 10-second windows are divided into 10 parts – A, B, C, ..., J. Each part has its own independent 10-second windows.

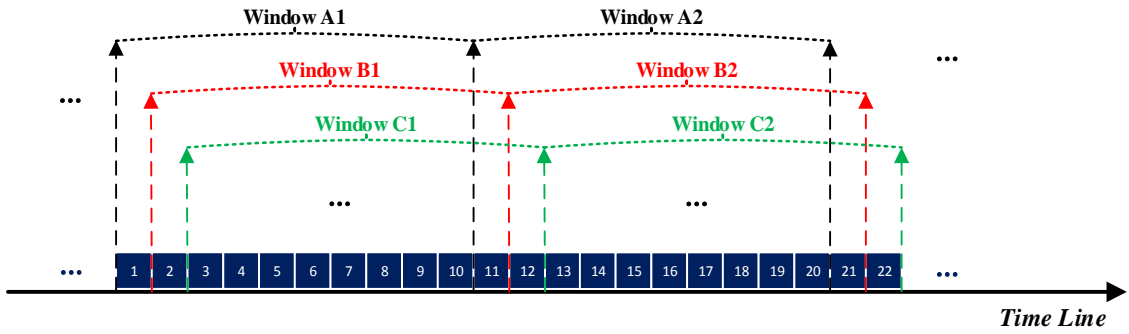


Figure A.1 A division of the sliding 10-second windows. Each number represents one second on the time line.

From the frequentist definition of the probability, the probability of $N_{IBD} = i$ (P'_i) in sliding 10-second windows can be expressed as,

$$P'_i = \frac{\sum_{d=1}^{10} P_i^d \cdot N_{\text{window}}^d}{N_{\text{window}}^{\text{total}}}, \quad (\text{A-1})$$

where N_{window} is the number of windows, and the superscript d represents the d th part (A, B, C, ..., J) of the sliding 10-second windows. P_i^d is the key point here and naturally P_i^d just follows the poisson distribution (poisson(i)) hypothesizing only the d th part exists. A proof of contradiction follows below. For windows B and windows A, window B_i is always 1 second later than window A_i (it is easy to calculate that the correlation between window B_i and window A_i is 0.9 for N_{IBD} since 9 seconds are shared). Assuming P_i^2 for windows B is $>$ ($<$) P_i^1 for windows A, then $P_i^3 >$ ($<$) P_i^2 must be satisfied. By this

analogy, P_i^{11} is $>$ ($<$) P_i^{10} $>$ ($<$) P_i^1 while P_i^{11} (beginning with window A2) is equal to P_i^1 (beginning with window A1). This contradiction proves that $P_i^d = \text{poisson}(i)$. As a result, $P_i' = \text{poisson}(i)$. Q.E.D.

A.2 Statistical uncertainty of the occurrence rate

Recall that the online supernova trigger is determined every second from the N_{IBD} in a 10-second window (see Figure 3.15) and the sliding 10-second windows are divided into 10 parts for a better elaboration (see Figure A.1). The definitions in these two figures will be commonly used.

poisson variable For a poisson variable N_{IBD} in the 10-second window, the correlation between the i th part and j th part of the sliding 10-second windows can be calculated.

$$\begin{aligned}
 & Cov(\sum_{i=1}^{10} N_i, \sum_{j=2}^{11} N_j) \\
 &= Cov(N_2, N_2) + Cov(N_3, N_3) + \dots + Cov(N_{10}, N_{10}) \\
 &= 9 \times Var(N_i) \\
 &= 0.9 \times \sigma(\sum_{i=1}^{10} N_i) \cdot \sigma(\sum_{j=2}^{11} N_j),
 \end{aligned} \tag{A-2}$$

where N_i denotes the number of IBD events in the i th second and apparently the correlation coefficient is 0.9. By this analogy, the correlation between any two windows can be calculated.

A more complicated case, for example, the correlation between the part - windows A and the part - windows B, is introduced here. The N_{IBD} in the i th window belonging to windows A (B) is represented by A_i (B_i).

$$\begin{aligned}
 & Cov(\sum_i A_i, \sum_j B_j) \\
 &= Cov(A_1, B_1) + \{Cov(A_2, B_1) + Cov(A_2, B_2)\} + \dots \\
 &\quad + \{Cov(A_i, B_{i-1}) + Cov(A_i, B_i)\} + \dots \\
 &= (0.9 + (0.1 + 0.9) + \dots + (0.1 + 0.9) + \dots) \times \sigma(A_i) \cdot \sigma(B_j) \\
 &= \frac{0.9 + N_w - 1}{N_w} \cdot \sigma(\sum_i A_i) \cdot \sigma(\sum_j B_j),
 \end{aligned} \tag{A-3}$$

where N_w is the number of windows in each part. If N_w approaches infinity, the correlation coefficient is 1. This is actually a trivial conclusion which means the IBD event rate is the same for both windows A and windows B. This equation is useful for the derivation later.

Bernoulli variable In terms of occurrence rate r_i , the corresponding combination is actually a Bernoulli event in an individual 10-second window: ‘1’ means it happened and ‘0’ not.

First, consider the case of one AD. Define the Bernoulli event as the occurrence that the number of IBD events in a 10-second window $N_{IBD} = i$, then the correlation between the two Bernoulli variables of window A1 and window B1 is,

$$Cov = P(i, i) \cdot 1 \cdot 1 - P(i) \cdot P(i) = P(i, i) - P(i)^2, \quad (A-4)$$

where $P(i, i)$ ($P(i)$) represents the probability of $N_{IBD} = i$ in both window A1 and window B1. If $i=0$, then the correlation is easily calculated to be

$$\rho = \frac{P(0, 0) - P(0)^2}{P(0)(1 - P(0))} = \frac{e^{-10R_{IBD}} \cdot e^{-R_{IBD}} - e^{-20R_{IBD}}}{e^{-10R_{IBD}}(1 - e^{-10R_{IBD}})}. \quad (A-5)$$

where $P(0, 0) = P(0) \cdot P(N_{11} = 0 | N_{A1} = 0)$ (conditional probability, N_{11} (N_{A1}) means the number of IBD events in the 11th second (window A1)) and R_{IBD} is the IBD event rate in unit of Hz. Notice that, if R_{IBD} is $\ll 1$, then

$$\rho = \frac{-11R_{IBD} - (-20R_{IBD})}{-10R_{IBD}} = 0.9, \quad (A-6)$$

this is the same as the case of poisson variables.

Since it is difficult to derive the correlation for any value of i in an analytical way, a numerical simulation was performed to investigate the correlation between the two Bernoulli variables mentioned above. A conclusion was obtained from the simulation that the correlation is smaller for a smaller probability of the Bernoulli variable ‘1’ (a larger value of i). This is understandable if we look at window A1 and window B1 in Figure A.1, where the 11th second will play a more important role if the value of i is larger, hence a smaller correlation will be there since the 11th second is an independent second of window B1 with those of window A1. As a consequence, the correlation between window A1 and window B1 has an upper limit expressed by Equation (A-5).

Multiple Bernoulli variables The real supernova trigger is determined from the combination of N_{IBD} from all the ADs, this means multiple Bernoulli variables have to be ‘1’ for all the ADs in terms of a combination. For two independent ADs, the Bernoulli variable

is defined as \mathcal{B} which is '1' only if $N_{AD1} = i$ and $N_{AD2} = j$. Assume the correlation of the two sub Bernoulli variables ($\mathcal{B}_{1/2}^{A1}$ and $\mathcal{B}_{1/2}^{B1}$) for AD1 ($\mathcal{B}_1: N_{AD1} = i$)/AD2 ($\mathcal{B}_2: N_{AD2} = j$) in window A1 and window B1 is ρ_1/ρ_2 , the covariance of the two newly defined Bernoulli variables (\mathcal{B}^{A1} and \mathcal{B}^{B1}) in window A1 and window B1 can be calculated as follows. Notice that if the probability $P(\mathcal{B}_{1/2} = 1) = p_1/p_2$, $\mathcal{B} = p_1p_2$.

$$\begin{aligned} Cov(\mathcal{B}^{A1}, \mathcal{B}^{B1}) &= Cov(\mathcal{B}_1^{A1}\mathcal{B}_2^{A1}, \mathcal{B}_1^{B1}\mathcal{B}_2^{B1}) \\ &= E(\mathcal{B}_1^{A1}\mathcal{B}_2^{A1}\mathcal{B}_1^{B1}\mathcal{B}_2^{B1}) - E(\mathcal{B}_1^{A1}\mathcal{B}_2^{A1})E(\mathcal{B}_1^{B1}\mathcal{B}_2^{B1}). \end{aligned} \quad (A-7)$$

Since \mathcal{B}_1 and \mathcal{B}_2 are independent (assuming two ADs are independent), then

$$\begin{aligned} &Cov(\mathcal{B}^{A1}, \mathcal{B}^{B1}) \\ &= E(\mathcal{B}_1^{A1}\mathcal{B}_1^{B1})E(\mathcal{B}_2^{A1}\mathcal{B}_2^{B1}) - E(\mathcal{B}_1^{A1})E(\mathcal{B}_2^{A1})E(\mathcal{B}_1^{B1})E(\mathcal{B}_2^{B1}) \\ &= (Cov(\mathcal{B}_1^{A1}, \mathcal{B}_1^{B1}) + E(\mathcal{B}_1^{A1})E(\mathcal{B}_1^{B1}))(Cov(\mathcal{B}_2^{A1}\mathcal{B}_2^{B1}) + E(\mathcal{B}_2^{A1})E(\mathcal{B}_2^{B1})) \\ &\quad - E(\mathcal{B}_1^{A1})E(\mathcal{B}_2^{A1})E(\mathcal{B}_1^{B1})E(\mathcal{B}_2^{B1}) \\ &= Cov(\mathcal{B}_1^{A1}, \mathcal{B}_1^{B1})Cov(\mathcal{B}_2^{A1}\mathcal{B}_2^{B1}) + p_2^2Cov(\mathcal{B}_1^{A1}, \mathcal{B}_1^{B1}) + p_1^2Cov(\mathcal{B}_2^{A1}\mathcal{B}_2^{B1}) \\ &= \rho_1\rho_2p_1p_2(1-p_1)(1-p_2) + \rho_1p_1(1-p_1)p_2^2 + \rho_2p_2(1-p_2)p_1^2 \\ &= p_1p_2(\rho_1\rho_2(1-p_1)(1-p_2) + \rho_1(1-p_1)p_2 + \rho_2p_1(1-p_2)). \end{aligned} \quad (A-8)$$

Then, the correlation coefficient of \mathcal{B}^{A1} and \mathcal{B}^{B1} is,

$$\rho = (\rho_1\rho_2(1-p_1)(1-p_2) + \rho_1(1-p_1)p_2 + \rho_2p_1(1-p_2))/(1-p_1p_2). \quad (A-9)$$

Considering the upper limit of both ρ_1 and ρ_2 is ρ_{up} , ρ can be re-expressed as,

$$\rho = k \cdot \rho_{up}^2 + (1-k) \cdot \rho_{up}. \quad (A-10)$$

Several approximations of ρ can be obtained according to the values of p_1 and p_2 , which are summarized in Table A.1.

Table A.1 Approximations of ρ according to the values of p_1 and p_2 .

	$p_1 \sim 1$	$p_1 \ll 1$
$p_2 \sim 1$	$\rho_{up} (k=0)$	$\rho_{up} (k=0)$
$p_2 \ll 1$	$\rho_{up} (k=0)$	$\rho_{up}^2 (k=1)$

From Table A.1, it is easy to extrapolate ρ for multiple ADs. Based on the measured R_{IBD} 's for each AD, the probability of $N_{\text{IBD}} = 0$ is ~ 1 , and the probability of $N_{\text{IBD}} \neq 0$ is $\ll 1$. Therefore, a conservative deal with ρ for multiple ADs is

$$\rho = \begin{cases} \rho_{up}^n & (n \geq 2), \\ \frac{1}{2}\rho_{up}^2 + \frac{1}{2}\rho_{up} & (n = 1), \\ \rho_{up} & (n = 0). \end{cases} \quad (\text{A-11})$$

where n is the number of ADs which have non-zero N_{IBD} 's. Considering the probability $\prod_i^{\text{AD}} p_i$ would be $\ll 1$ during the extrapolation from one AD to multiple ADs, there should be a correction (in the form of $k \cdot \rho_{up} + (1 - k)$ which is less than 1) to ρ but ignored here so that Equation (A-11) is a conservative solution, especially for $n = 0$.

Final uncertainty by error propagation For the occurrence rate of a combination (r), the statistical uncertainty can be calculated by an error propagation with the correlation matrix for the 10 parts of the sliding 10-second windows (see Figure A.1). Since the probability of the combination is equal to the value of r (in a unit of Hz), the statistical uncertainty (σ_i) of the counts (n_i) of the combination for the i th part is a binomial uncertainty $\sqrt{N_w r(1-r)}$ where N_w is the number of 10-second windows in each part. The derivation of the final uncertainty of the total counts of the combination ($\sum_{i=1}^{10} n_i$) follows below.

$$\text{Var}(\sum_{i=1}^{10} n_i) = \begin{pmatrix} \sigma_1 & \dots & \sigma_{10} \end{pmatrix} \cdot \begin{pmatrix} 1 & \dots & \rho_{ij} \\ \vdots & \ddots & \vdots \\ \rho_{ji} & \dots & 1 \end{pmatrix} \cdot \begin{pmatrix} \sigma_1 \\ \vdots \\ \sigma_{10} \end{pmatrix}. \quad (\text{A-12})$$

Since $\rho_{i,j} = \rho_{j,i}$ and $\rho_{i,j} = \rho_{i+1,j+1}$,

$$\begin{aligned} & \text{Var}(\sum_{i=1}^{10} n_i) \\ &= \sum_{j=1}^{10} \rho_{1,j} \cdot 10 \cdot N_w \cdot r \cdot (1-r) \\ &= \sum_{j=1}^{10} \rho_{1,j} \cdot N_{\text{total}} \cdot r \cdot (1-r), \end{aligned} \quad (\text{A-13})$$

where j corresponds to the j th part in Figure A.1, e.g. $j = 1$ corresponds to windows A and $j = 2$ to windows B.

The correlation matrix can be obtained following the idea in Equation (A-3), Equation (A-6), and Equation (A-11). The results of $\rho_{1,j}$ where j is from 2 to 6 are presented in Table A.2. Define the factor $\sum_{j=1}^{10} \rho_{1,j}$ multiplied by the binomial uncertainty is g .

Table A.2 $\rho_{1,j}$ for $j = 2, 3, 4, 5, 6$ in various cases of n . n is the number of non-zero N_{IBD} from all the ADs. $g = \sum_{j=1}^{10} \rho_{1,j}$, where $\rho_{1,j} = \rho_{1,12-j}$ for j from 7 to 10.

	$j=2$	3	4	5	6	
$n = 0$	1(=0.9+0.1)	1(=0.8+0.2)	1 (=0.7+0.3)	1	1	$g = 10$
$n = 1$	0.92	0.84	0.79	0.76	0.75	$g = 8.4$
$n = 2$	0.82 (=0.9 ² +0.1 ²)	0.68 (=0.8 ² +0.2 ²)	0.58	0.52	0.5	$g = 6.7$
$n = 3$	0.73 (=0.9 ³ +0.1 ³)	0.52	0.37	0.28	0.25	$g = 5.0$
$n = 4$	0.66	0.41	0.25	0.16	0.13	$g = 4.1$
$n = 5$	0.59	0.33	0.17	0.09	0.06	$g = 3.4$
$n = 6$	0.53	0.26	0.12	0.05	0.03	$g = 3.0$
$n = 7$	0.48	0.21	0.08	0.03	0.02	$g = 2.6$
$n = 8$	0.43	0.17	0.06	0.02	0.01	$g = 2.4$

We can in principle calculate a more stringent upper limit of g for any case, however, it is too complicated and there is unknown uncertainty with ρ_{up} . In a validation, the predicted occurrence rates were compared with the measured ones and the differences were also quantified by the estimated uncertainties (see Figure. 3.11).

A.3 Number of consecutive supernova triggers

This section is to present the estimation of an upper limit of the average number of consecutive supernova triggers, \bar{N} , which is the only factor in the conversion from the real false-alert rate to the Daya Bay trigger threshold for trigger decision (see Equation 3-13).

Suppose T_i indicates that a trigger is issued for the i th 10-second window and \bar{T}_i is that the contrary is true. The probability of a supernova trigger in the i th 10-second window is $P(T_i)$, which is equal to P_{DYB} . Supposing a sequence of consecutive 10-second windows, \bar{N} can be expressed by conditional probabilities:

$$\begin{aligned}
 \bar{N} &= 1 \cdot P(\bar{T}_2|T_1) + 2 \cdot P(T_2\bar{T}_3|T_1) + \dots + \\
 &\quad i \cdot P(T_2 \cdots T_i \bar{T}_{i+1}|T_1) + \dots \\
 &= 1 \cdot P_1 + 2 \cdot P_2 + \dots + i \cdot P_i + \dots,
 \end{aligned} \tag{A-14}$$

where $P_i = P(T_2 \cdots T_i \bar{T}_{i+1} | T_1) = P(T_1 \cdots T_i \bar{T}_{i+1}) / P(T_1)$. Since T_{i+10} is independent with T_i , $P(T_1 \cdots T_{11} \bar{T}_{12}) < P(T_1 T_{11})$ (no requirements of other windows) $= P_{\text{DYB}}^2$. Moreover, \bar{N} can be expressed in the form:

$$\begin{aligned}
 \bar{N} &= \mathcal{O}(P_{\text{DYB}}) + \mathcal{O}(P_{\text{DYB}}^2) + \mathcal{O}(P_{\text{DYB}}^3) + \dots \\
 &= \mathcal{O}(P_{\text{DYB}} + P_{\text{DYB}}^2 + P_{\text{DYB}}^3 + \dots) \\
 &= \mathcal{O}\left(\lim_{n \rightarrow \infty} \frac{P_{\text{DYB}}(1 - P_{\text{DYB}}^n)}{1 - P_{\text{DYB}}}\right) \\
 &= \mathcal{O}(P_{\text{DYB}}) \text{ (because } P_{\text{DYB}} \ll 1\text{)}.
 \end{aligned} \tag{A-15}$$

According to this new expression, the terms containing T_i with $i > 10$ can be ignored.

By symmetry, $P_1 = P(T_1 \bar{T}_2) / P(T_1) = P(T_2 \bar{T}_3) / P(T_1)$. Since $P(T_2 \bar{T}_3) / P(T_1) > P(T_1 T_2 \bar{T}_3) / P(T_1) = P_2$, so $P_1 > P_2$. Similarly, $P_i > P_{i+1}$, thus $P_1 > P_2 > \cdots > P_{10}$. Because $\sum_{i=1}^{\infty} P_i = 1$, $\sum_{i=1}^{10} P_i < 1$ and such that $P_{10} < 0.1$. Then an upper limit of \bar{N} can be achieved assuming $P_1 = P_2 = \cdots = P_{10} = 0.1$ and $\sum_{i=1}^{10} P_i = 1$:

$$\begin{aligned}
 \bar{N} &\cong 1 \cdot P_1 + 2 \cdot P_2 + \dots + 10 \cdot P_{10} \\
 &< 1 \cdot 0.1 + 2 \cdot 0.1 + 3 \cdot 0.1 + \dots + 10 \cdot 0.1 = 5.5.
 \end{aligned} \tag{A-16}$$

To understand why it is an upper limit, define $P_i = P(i)$ as the probability distribution function of an integer random variable i , with a value space from 1 to 10. Since $P(i)$ is a monotony decrease function (recall that $P_1 > P_2 > \cdots > P_{10}$), the mean value (\bar{N}) is maximized under the condition that larger values have larger probability. And the limit is reached if $P_1 = P_2 = \cdots = P_{10} = 0.1$, in which case $\bar{N} = 5.5$.

\bar{N} is set to be 3, which is roughly the average of the upper limit 5.5 and the lower limit 1.

An interesting digression is described below. Recall that in the estimation of the occurrence rate uncertainty, a factor g shows up besides the binomial uncertainty also due to the overlapping of 10-second windows. From the uncertainty,

$$\frac{\sqrt{g \cdot np(1-p)}}{n} = \sqrt{\frac{p(1-p)}{\frac{n}{g}}},$$

one can see that the factor g has a similar meaning to \bar{N} .

Resume and Publications

个人简历

1989年1月9日出生于河南省南阳市。

2001年9月进入河南省南阳市第十三中学学习。

2004年9月考入河南省南阳市第一中学学习。

2007年9月考入清华大学工程物理系核工程与核技术专业，2011年7月本科毕业并获得工学学士学位。

2011年9月免试进入清华大学工程物理系攻读物理学博士学位至今。

发表的学术论文

- [1] Hanyu Wei, *et al.*, *Design, characterization, and sensitivity of the supernova trigger system at Daya Bay*, *Astroparticle Physics* **75**, 38-43 (2016)
- [2] Hanyu Wei for the Daya Bay Collaboration, *Highlight on Supernova Early Warning at Daya Bay*, *Physics Procedia* **61**, 802-806 (2015)
- [3] F. P. An *et al.* (Daya Bay Collaboration), *New measurement of θ_{13} via neutron capture on hydrogen at Daya Bay*, *Phys. Rev. D* **93**, 072011 (2016)
- [4] F. P. An, *et al.* (Daya Bay Collaboration), *Independent measurement of the neutrino mixing angle θ_{13} via neutron capture on hydrogen at Daya Bay*, *Phys. Rev. D* **90**, 071101(R) (2014)
- [5] F. P. An, *et al.* (Daya Bay Collaboration), *Measurement of electron antineutrino oscillation based on 1230 days of operation of the Daya Bay experiment*, arXiv:1610.04802 [hep-ex]
- [6] A. V. Artamonov, *et al.* (E949 Collaboration), *Search for heavy neutrinos in $K^+ \rightarrow \mu^+ \nu_H$ decays*, *Phys. Rev. D* **91**, 052001 (2015)
- [7] F. P. An, *et al.* (JUNO Collaboration), *Neutrino physics with JUNO*, *J. Phys. G* **43**, 030401 (2016)
- [8] J. Beacom, *et al.*, *Letter of intent: Jinping Neutrino Experiment*, accepted by Chinese Physics C, arXiv:1602.01733 [physics.ins-det]